The Principal Axes of the Directional Energy Distribution of Cosmic Rays Measured with the Pierre Auger Observatory

vorgelegt von

Diplom-Physiker

Tobias Winchen

aus Leverkusen

Contents

Contents

1 Introduction

About half of the natural ionizing radiation observed on the Earth's surface does not originate from decay of radio active elements in the crust [1], but is generated by extraterrestrial particles hitting the atmosphere [2]. These 'cosmic rays' are charged particles [3], mainly protons [4, 5] but also heavier nuclei [6, 7]. They are observed with energies ranging from below $1\,\mathrm{GeV}$ up to an energy of $3 \times 10^{20}\,\mathrm{eV}$ [8, 9], the so far highest energetic particle observed. Although cosmic rays have been intensively studied in the last 100 years (for a historical review see, e.g., reference [10]), several aspects of the phenomenon remain unclear. Among the open questions are in particular the identification of the sources and the acceleration mechanism of cosmic rays, the chemical composition of the cosmic ray flux, and the separation of the cosmic ray flux that originate from within the Milky Way from an extragalactic component (e.g. references [11–17]).

Addressing these questions is a challenging task. The decrease of the flux of cosmic rays with increasing energy makes it necessary to study high energetic cosmic rays by the particle cascades they induce in the atmosphere, as the size of the detectors needed for a direct observation becomes impracticable. Still, at the highest energies the currently largest available detector, at the Pierre Auger Observatory [18, 19], detects only dozens of particles per year. The center-of-mass energy of collisions of these particles with the atmosphere exceeds the energies achieved in nowadays man-made accelerators [20]. The models for the particle cascade thus have to rely on an extrapolation of the standard model of particle physics to higher energies. Cosmic rays are deflected in cosmic magnetic fields, which obscures the position of their sources. The strength and structure of the cosmic magnetic fields are only poorly understood, their origin and formation mechanism are also under debate (e.g. references [21–24]).

All questions concerning cosmic rays are tightly entangled. Identifying the sources and knowing the composition, the magnetic fields could be measured. Knowing the composition and magnetic fields, the sources could be identified. Nevertheless, these questions can be addressed by comparison of observations with predictions from model scenarios using appropriate observables. Continuous progress is made by development and measurement of observables characterizing the energy and arrival distribution of cosmic rays [25–37], while comparing the measurements with results from simulations of propagation scenarios [38–55].

In this thesis we characterize the energy dependency of the distribution of arrival directions of cosmic rays in selected regions in the sky. For this we measure the principal axes of the directional energy distribution in regions around events with an energy $E > 60\,\mathrm{EeV}$ observed with the Pierre Auger Observatory, and quantify the strength of the collimation of events along these axes. The measurement is compared with the

results of simulations of scenarios, modeling an extragalactic origin of the cosmic rays considered in this study. From a statistical analysis of the measured and simulated data, constraints on the strength of the deflection in extragalactic magnetic fields as a function of the source density within the tested scenarios are set.

The thesis is structured as follows. In the remaining sections of the introduction we describe the development of particle cascades from the primary particles of the cosmic radiation and summarize measurements of the energy spectrum of the cosmic ray flux and its mass composition. We restate the prevailing interpretation of the measurements and further motivate this work. In the second chapter the prevailing models for the cosmic rays considered in this thesis are summarized, with focus on their origin and propagation through galactic and extragalactic magnetic fields.

To generate data from pseudo experiments which incorporate these propagation effects, we developed the simulation software PARSEC presented in chapter 3. Using this software we adopt a set of observables from high-energy physics to usage in astroparticle physics in chapter 4, which yields the principal axes of the cosmic ray energy distribution and the strength of collimation of events along these axes. The Pierre Auger Observatory and the detector components used to detect the cosmic rays considered in this study are described in chapter 5. In chapter 6, the used data set and the measurement of the observables is presented.

The reproducibility of the axes in subsamples of the data as criterion for the non-triviality of the map of axes is discussed in chapter 7. An interpretation of the measurement is given as limit on the strength of the deflection in the extragalactic magnetic field in chapter 8. The conclusions drawn from this work are summarized in chapter 9 and are followed by appendices containing details to calculations, computer software and alternative methods developed in course of this work.

1.1 Cosmic Ray Induced Air Showers

A cosmic ray hitting Earth interacts with the molecules of the atmosphere and produces a cascade of secondary particles called 'air shower'. The cascade initiated by a vertical 10^{19} eV proton contains more than 10^{10} particles at sea-level and stretches over several kilometers [14]. To emphasize the size of the spatial extent of the air showers initiated by high energy cosmic rays, they are sometimes attributed as 'extensive'. The secondary particles produced in an air shower move towards ground level with the speed of light in a 'disc' or 'shower front' of particles with a thickness in order of meters. The geometry of an air shower is depicted in figure 1.1 (a). It depends on the zenith angle θ, energy E_0, and mass of the primary particle.

Following a selection of reviews of the subject [14, 58–60], the particles in the shower are grouped into three components, based on the characteristic of their further interaction (see figure 1.1 (b)). Electrons, positrons*, and photons, form an 'electromagnetic component'. In further interactions, these particles increase in number by initiating

---

*As in reference [59], we refer in the following to both, electrons and positrons, only as electrons.
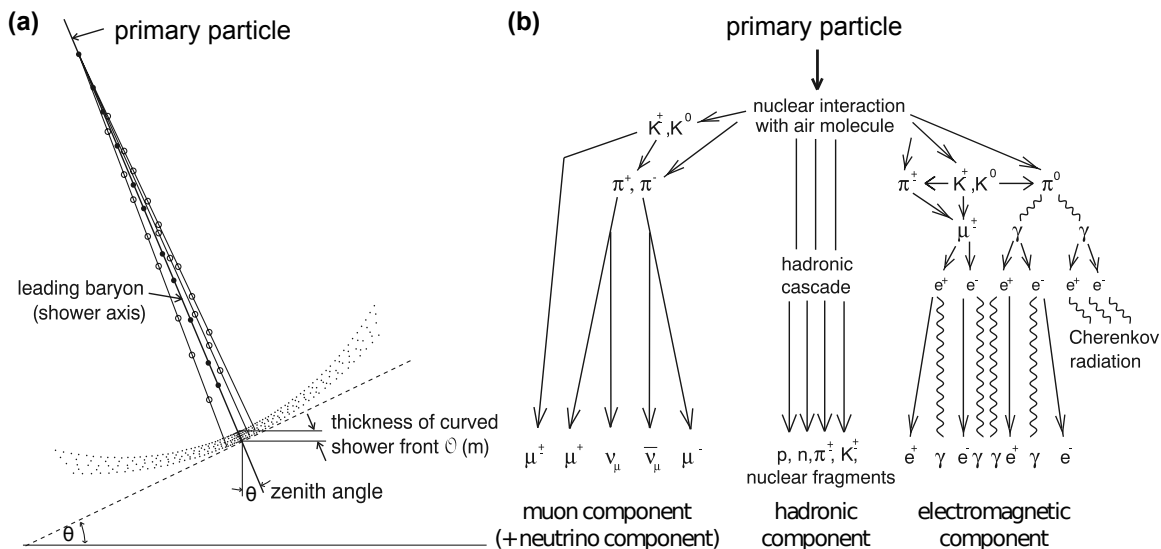
Figure 1.1: Sketches of an extensive air shower (modified from references [56, 57]). **(a)** Lateral section of the shower. **(b)** Main process in a shower separated by components.

new electromagnetic sub-showers. Similarly to the electromagnetic component, a 'hadronic component' is formed consisting to $\sim 90\%$ of pions and $\sim 10\%$ of kaons [61]. The hadrons not only initiate hadronic cascades but also feed the electromagnetic component and create a 'muonic component' and a 'neutrino component' by their decay products.

In contrast to the particles in the other two components, muons and neutrinos are unlikely to interact further once they are created. Also muon decay can be neglected, as the decay length of the muons in the shower is larger than the depth of the atmosphere up to zenith angles of $\theta = 80°$ [56]. In the following, we summarize the properties of the electromagnetic and hadronic cascades, which are used in typical detectors to get informations on the primary particle. Effects relevant only for showers with zenith angles $\theta > 60°$ are omitted here, as events with larger zenith angles are not used in this thesis.

1.1.1 Electromagnetic Cascade

In a simple analytical model introduced by Heitler [62], electrons above a critical energy lose energy due to bremsstrahlung and photons lose energy due to pair-production. Energy losses due to other processes are neglected. The cross sections of both processes are treated as equal and independent from the energy. The cascade thus forms a binary tree.

At every node of the tree, the energy of the parent particle E_0 is distributed evenly on two children. Photons create an electron-positron pair, whereas electrons emit one photon by bremsstrahlung and survive. At depth n the tree has $N = 2^n$ leafs, each

representing a particle with energy $E_n = E_0/N$. The cascade stops when the energy of the leaf particles drops below a critical energy E_c as the energy losses are hereafter dominated by ionization processes; in air $E_c \sim 80\,\text{MeV}$ [14, 63].

This model does not account for the generation of multiple photons in the bremsstrahlung and also overestimates the interaction length of electrons. Therefore, in this model N_{max} is overestimated by a factor two to three and also two times more electrons than photons are generated; in detailed simulations about six times more photons than electrons are found.

Nevertheless, several other properties of the cascade can be derived that agree qualitatively with results from simulations [14] or more sophisticated cascade theories (see references given in [62]). Of interest here are in particular the maximum number of particles N_{max} and the atmospheric depth at which this maximum is reached.

The maximum of the shower development is reached here at the end of the cascade. The number of particles is thus proportional to the energy of the initial particle of the cascade

$$N_{\text{max}} \propto \frac{E_0}{E_c}. \tag{1.1}$$

As the maximum is reached after n steps of length d, the slant-depth of the shower maximum is $X_{\text{max}} = n \cdot d + X_0$ with X_0 beeing the depth of the starting point of the cascade. With $d = \lambda_r \ln 2$ and radiation length $\lambda_r = 37\,\text{g}\,\text{cm}^{-2}$ in air this reads

$$X_{\text{max}} = X_0 + \lambda_r \ln\left(\frac{E_0}{E_c}\right). \tag{1.2}$$

The slant-depth of the maximum of the electromagnetic cascade thus depends logarithmically on the energy of the initial particle.

1.1.2 Hadronic Cascade

Analog to the electromagnetic cascade in the previous section, the hadronic cascade can be modeled also as tree [63]. Here, the tree has a constant branch length $d = \lambda_I \ln 2$ with hadronic interaction length in air $\lambda_I = 120\,\text{g}\,\text{cm}^{-2}$ constant for all particles.

In contrast to the electromagnetic cascade, the hadrons are in every step not split into two particles, but into several particles; the number of secondary particles increases with increasing center-of-mass energy of the collision. In the model discussed here, in every step of the cascade a constant number of $N_{ch} = 10$ charged pions and $\frac{1}{2}N_{ch}$ neutral pions are created; all child-particles carry the same fraction of the energy. The neutral pions decay into two photons in the same step which in turn immediately initiate electromagnetic showers. The charged pions continue the hadronic cascade in the next step. The cascade stops when the energy of the charged pions drops below the critical energy E_c^H, and the pions decay into muons and neutrinos; in air $E_c^H = 20\,\text{GeV}$. The model is adapted to nuclei with atomic number A by modelling the nuclei as superposition of A nucleons with energy E_0/A.

As for the electromagnetic cascade, this simple model yields results that can be qualitatively confirmed by simulations. First, the number of muons in the shower is

proportional to the energy of the initial particle and the multiplicity N_{ch} as

$$N_\mu = \left(\frac{E_0}{E_c^H}\right)^\beta \tag{1.3}$$

with $\beta = \frac{\ln N_{ch}}{\ln 3/2 N_{ch}}$. For nuclei we get

$$N_\mu = A\left(\frac{E_0/A}{E_c^H}\right)^\beta = \left(\frac{E_0}{E_c^H}\right)^\beta A^{1-\beta}. \tag{1.4}$$

Second, the energy of the primary particle is distributed between the electromagnetic and hadronic sub-showers, thus $E_0 = E_{em} + E_H$. With $E_H = N_\mu E_c^H$ given by the number of muons in eq. 1.4 we get

$$\frac{E_{em}}{E_0} = 1 - \left(\frac{E_0}{E_c^H}\right)^{\beta-1} A^{1-\beta} \tag{1.5}$$

for the fraction of energy in the electromagnetic cascade.

Third, the maximum of the shower development $X_{\max}(A = 1)$, i.e. the atmospheric depth at which the number of particles in the electromagnetic cascade reaches its maximum, depends on the cross section, the multiplicity, and the mass and the energy of the primary particle. If we only consider the electromagnetic cascade stated in the first hadronic interaction, this reads

$$X_{\max}(A = 1) = X_0 + \lambda \ln \frac{E_0}{3N_{ch}E_C^H}, \tag{1.6}$$

for protons and

$$X_{\max}(A) = X_{\max}(A = 1) - \lambda_r \ln A \tag{1.7}$$

for nuclei.

The model reproduces qualitatively the observed shower development, but is based on an incorrect view on the hadronic interaction. In a hadronic interaction only single constituents of the hadrons participate. As each constituent carries only a fraction of the particles energy, only the fraction κ of the total energy is available to generate new particles in every step of the cascade. The fraction $1 - \kappa$ of the energy is carried away by the other constituents as 'leading particle' in the shower. The parameter κ, named 'inelasticity' in high-energy physics, depends on the energy and the mass of the particles. The inelasticity in high energy proton-air collisions is estimated to be in the range $0.4 \lesssim \kappa \lesssim 0.9$ [64]. As the model above assumes $\kappa = 1$, the depth of the shower maximum is underestimated by approximately $100\,\mathrm{g\,cm^{-2}}$.

Given the relationships derived from the analytical models above, the direction, energy and mass of the primary particle can be derived from observations of the shower. The shower development is symmetric towards the axis along the arrival direction of the primary particle. The direction of the primary particle can thus be estimated from the arrival time of the secondary particles at the ground and the distribution of

particles in the shower front. Based on eq. 1.4 and eq. 1.5, the energy of the particle and also the primary mass can be estimated by observations of the number of electrons and muons in the shower. The mass of the primary particle can also be derived from the atmospheric depth of the shower maximum (cf. eq. 1.7).

1.2 Energy Spectrum and Mass Composition

From the energy E and number N of cosmic rays observed in an experiment, the differential flux

$$J(E) = \frac{d^4N}{dE\ dA\ d\Omega\ dt} \tag{1.8}$$

is calculated using the sensitive area A, sensitive solid angle Ω, and exposure time t of the experiment. In figure 1.2 the differential flux as reported by several experiments [8, 65–67, 69–77] is shown as a function of the energy E. The range of observations covers approximately 13 orders of magnitude in the energy from below $1\,\mathrm{GeV}$ up to the so far highest energetic particle observed with an energy of $E = 3 \times 10^{20}\,\mathrm{eV}$ [8, 9]. With increasing energy, the intensity of the flux drops more than 33 orders of magnitude from 10^4 events per square-meter and second at $E = 1\,\mathrm{GeV}$ down to less than one event per km^2 and century above $E \approx 70\,\mathrm{EeV}$.

Data points below $E \approx 100\,\mathrm{TeV}$ are from experiments using relatively small detectors mounted on balloons or satellites. Above $E \gtrsim 100\,\mathrm{TeV}$, the detectors required for a direct measurement with sufficient statistic would become too large to be mounted on a carrier. The data points are thus from experiments that detect air showers as discussed in the previous section.

Below $E_S \approx 10\,\mathrm{GeV}$ the cosmic ray flux is subject to modulation during the solar-cycle [60, 79]. Above E_S the energy spectrum of the flux is described by a power-law

$$J(E) \propto E^\gamma \tag{1.9}$$

with spectral index $\gamma < 0$ nearly uniform over E.

Based on direct observations, the cosmic ray flux below $E \approx 100\,\mathrm{TeV}$ is composed to $\sim 98\%$ of nuclei and $\sim 2\%$ of electrons. Above $E \approx 5\,\mathrm{GeV}$ the flux of electrons is strongly suppressed due to synchrotron losses from deflections in the galactic magnetic field. The nuclei are to $\sim 79\%$ protons, $\sim 15\%$ helium nuclei, and $\sim 7\%$ heavier nuclei [60]. The abundances of elements roughly follows the abundances in the interstellar matter. Any deviation is consistent with effects from spallation and inelastic scattering during the propagation [79].

The spectral index changes slightly only at distinguished positions in the energy range. To point this out in the spectrum, figure 1.2 (b) shows the flux $J(E)$ stretched with a factor $E^{2.7}$. As the shape of the spectrum in this visualization shows some resemblance with a human leg, the points where changes in γ occur are called 'knee' and 'ankle'. Consequently, the fine-structure at the high-energy end of the spectrum is sometimes referred to as 'toes' (e.g. [80]).
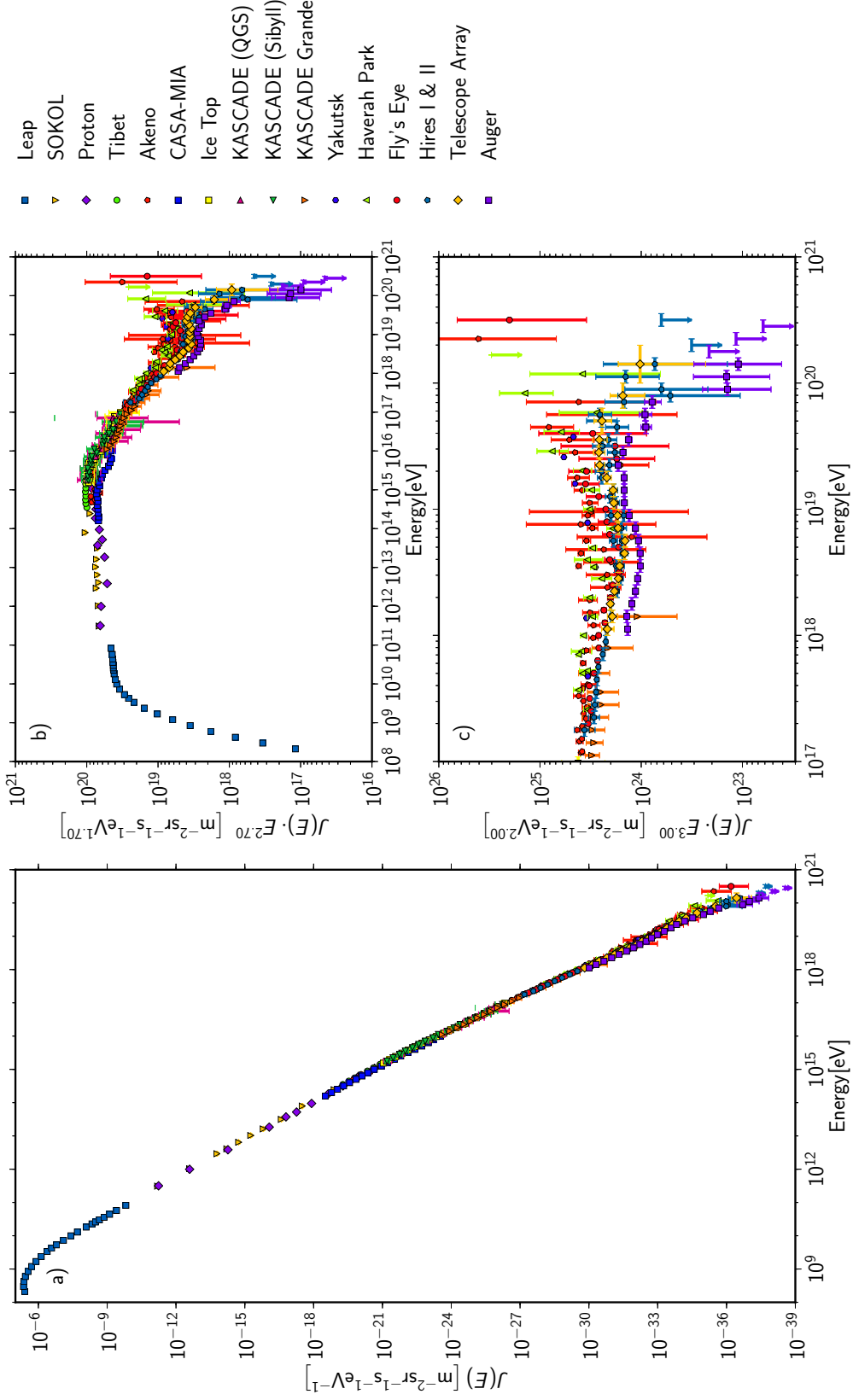
Figure 1.2: **(a)** All-particle energy spectrum of cosmic rays from direct observations [65–67] and measurements of extensive air-shower [8, 68–77] (based on reference [78]). **(b)** Same as in (a) but flux multiplied with a factor $E^{2.7}$. **(c)** End of the energy-spectrum; the flux is multiplied with a factor $E^{3.0}$.
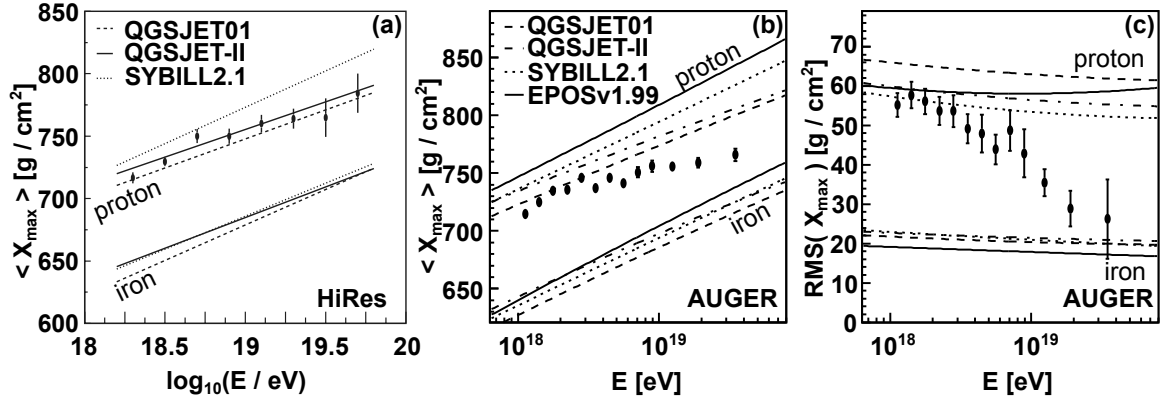
Figure 1.3: Measurement of the average depth of shower maximum (X_{max}) by **(a)** the HiRes experiment [85] and **(b)** the Pierre Auger Observatory [86]. **(c)** Magnitude of the shower-to-shower fluctuations of the depth of maximum $RMS(X_{\mathrm{max}})$ measured by the Pierre Auger Collaboration [86]. The data points from the individual experiments are compared with results from air shower simulations using different hadronic interaction models and primary particles. The legend for the curves given in (c) is the same given in (b). The text of the original plots has been replaced to be readable here.

Below the knee at $E_{knee} \approx 10^{15}$ eV the spectral index is $\gamma \approx -2.7$. Above E_{knee} a steeper spectrum with $\gamma \approx -3.1$ is reported [59, 81]. The change of the flux at the knee can be attributed to a steepening in the spectra of light elements [72]. An increase of the mean logarithmic mass is observed by several experiments from measurements of the depth of shower maximum and the ratio of the number of muons and electrons at ground level [59].

A further steepening at $E_{2nd.\ knee} \approx 8 \times 10^{16}$ eV was reported recently. As for the knee, this feature can be attributed to a steepening of the flux of heavier elements [82]. At an energy of 1×10^{17} eV, measurements of the depth of shower maximum indicate that the flux is dominated by a mixture of heavy nuclei [8, 59].

Below the ankle a transition to lighter elements is indicated by the data. At the ankle at $E_{ankle} \approx 3$ EeV observations of the depth of shower maximum are consistent with a proton dominated flux [16] and the energy spectrum becomes again harder with spectral index $\gamma \approx -2.7$ [8].

The high-energy end of the observed spectrum is shown in figure 1.2 (c). The differences among the fluxes reported by the individual experiments are comparable to the systematic uncertainties of $\Delta E_{sys} \approx 20\% - 30\%$ [75, 83] in the individual measurements. However, only few events with energies above 100 EeV have been reported so far; a suppression of the flux compared with a simple power law above $E_{cut} = 4 \times 10^{19}$ eV is evident with high significance [75, 84].

Although all experiments report consistent results on the composition up to approximately 3 EeV, at energies beyond the ankle the results of individual experiments appear not consistent. On the one hand, measurements of the depths of shower maxima

reported by the HiRes [85] and Telescope Array [87] experiments are consistent with a composition dominated by protons up to approximately 50 EeV. But on the other hand, data recorded at the Pierre Auger Observatory [86] indicates a transition from light to heavier elements in this energy range [88].

The measurements reported by HiRes collaboration and the Pierre Auger Collaboration are displayed in figure 1.3. However, direct comparison of the results is hindered as only the data reported by the Pierre Auger Collaboration is corrected for known systematics [86]. The data reported by the HiRes collaboration is reported uncorrected and the detector simulation is instead applied to the simulated showers used for the interpretation [85].

The inconsistency of the two results cannot be explained by the systematic uncertainties in the energy scale, as the flux reported by the Pierre Auger Collaboration is lower than the flux observed by the HiRes experiment. Simply shifting the energy scale of one experiment towards the other one would fortify either conclusion.

1.3 Arrival Directions

Cosmic rays are deflected in magnetic fields and thus point not directly back to their source. The field strength inside the galactic disc is in the order of $\sim 3\,\mu G$ (see section 2.4.2 for a detailed description of the galactic magnetic field) resulting in a gyro radius of $\sim 0.4\,pc$ for a $1 \times 10^{15}\,eV$ proton. Small scale anisotropies at low energies are thus not expected.

Nevertheless, anisotropies have been observed at energies ranging from 0.8 TeV to 2 PeV by several experiments [59, 89–94]. Localized regions of increased cosmic ray flux ('hot spots') are found on both hemispheres at TeV energies with significances up to $12\,\sigma$. Additionally, the experiments report a dipole structure with amplitudes at the 10^{-3} level. The strength of this large scale anisotropy seems to become stronger at higher energies. Above 2 PeV no dipole has been observed yet. An upper limit is set on the amplitude of a dipole of 2% at 1 EeV and 10% at 10 EeV [35, 37]. At the same energies, the amplitude of a quadrupole is limited to lower than 3%, respectively 10% [35]. Reports of an excess at $\sim 1\,EeV$ energies towards the galactic center have not been confirmed [95].

Above 56 EeV an isotropic distribution of UHECR has been rejected by the Pierre Auger Collaboration with at least 99% confidence [96, 97]. In the analysis, a correlation of the arrival direction of cosmic rays with the position of active galactic nuclei (AGN) closer than 75 Mpc from the Véron-Cetty and Véron (VCV) catalogue was studied as follows. First, the maximum angular distance between the direction of cosmic ray and the position of the closest AGN ψ, the lower energy cut for the cosmic rays E_{th}, and the maximum redshift of the AGN $z_{\max}$ have been optimized using data recorded in a first 'search' period. The strongest correlation was found for cosmic rays with $E_{th} > 56\,EeV$, $\psi = 3.1°$, and $z_{\max} = 0.018$ with 12 events out of 15 correlating with AGN. Using this prescription on independent data from a second period, an isotropic distribution could be rejected as 8 out of 13 observed cosmic rays fulfilled the correlation criteria while
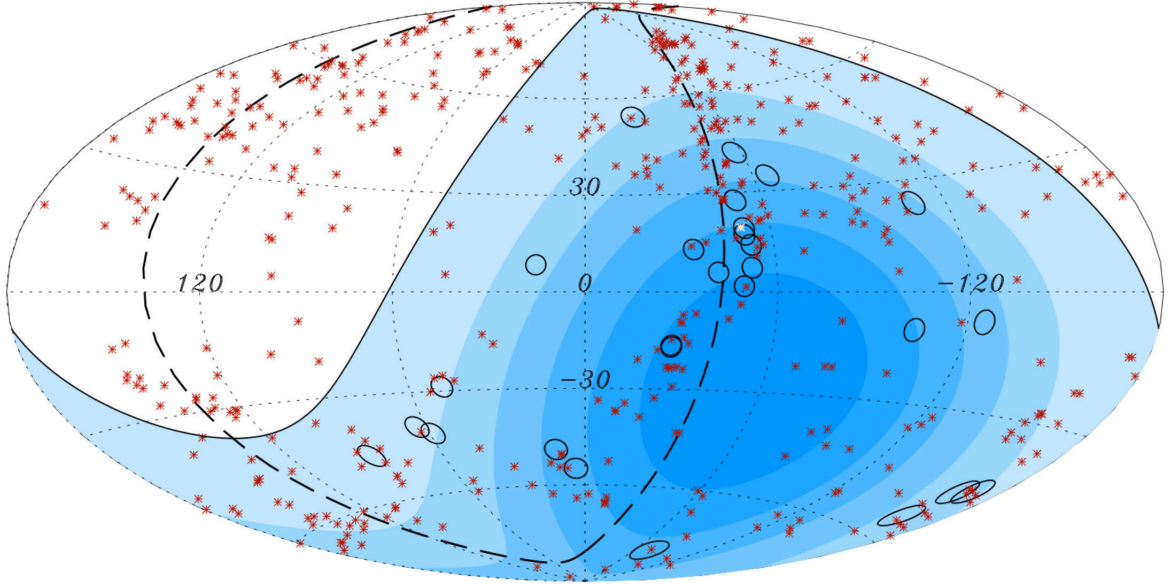
Figure 1.4: Sky-map of the arrival directions of cosmic rays with energy $E > 57\,\text{EeV}$ (black circles) and nearby AGN (red stars) in galactic coordinates. The circles mark a region with radius $\psi = 3.2°$. Blue shading indicates the exposure of the direction with the Pierre Auger Observatory; the black line marks its field of view. The black dashed line indicates the super-galactic plane. The white star marks the position of Centaurus A [96, 97].

only 2.7 were expected from an isotropic distribution.

After rejecting an isotropic distribution with this analysis, the cuts have been optimized using the full data set. A maximum correlation in the complete data is found with $E_{th} > 57\,\text{EeV}$, $\psi = 3.2°$ and $z_{\max} = 0.017$ with 20 out of 27 UHECR events correlating with AGN positions while expecting 5.6 from an isotropic distribution of UHECR. A map of these events is shown in figure 1.4.

In data recorded in a third period, the degree of correlation decreased from $69^{+11}_{-13}\%$ to $38^{+7}_{-6}\%$. A 21% correlation would be expected from an isotropic distribution of cosmic rays [98]. Data from the HiRes [99] and Telescope Array [100] experiments are compatible with an isotropic distribution of the arrival directions in the same analysis, but cannot reject the correlation hypothesis either. No significant correlation with nearby matter was also found in a meta-analysis of cosmic rays from multiple experiments [101].

Besides correlations with astrophysical objects and over-densities on large scales, also intrinsic properties of the distribution of arrival directions of UHECR can be used to compare the observations with model expectations. In particular, correlations among the arrival directions of the highest energetic events [30, 34] and energy dependent structures in the arrival distributions [33, 102, 103] have been studied. None of these analysis have observed a significant deviation from an isotropic distribution of cosmic rays.

1.4 Astrophysical Interpretation

Given the observations presented in the previous sections, the following picture emerges (e.g. references [16, 59, 79]). Cosmic rays with energies approximately up to the energy of the ankle are evidently of galactic origin. The gyro radius for a $1\,\mathrm{EeV}$ proton can be compared to the thickness of the galactic disk. Cosmic rays with energy $E \ll 1\,\mathrm{EeV}$ are thus bound to the galactic magnetic field; An increases of the number of cosmic rays towards the galactic center has been observed.

From the fractions of radioactive isotopes, a propagation time of $\sim 10^7\,\mathrm{yr}$ is deduced. The analysis of meteorites yields that the cosmic ray flux has been approximately constant over the past $4 \times 10^9\,\mathrm{yr}$. Cosmic rays can therefore not be the remnants of a singular event, but the cosmic ray flux within the galaxy is constantly renewed with an energy input of $\sim 40\ \mathrm{erg}^*\mathrm{s}^{-1}$, so that the major part of the cosmic ray flux is in a steady state within the galaxy.

Cosmic rays are accelerated in a non-thermal process, as indicated by the power-law shape of the energy spectrum. The environment needed for acceleration of cosmic rays is provided within supernova remnants (SNR), which can also account for the needed energy input. For a summary of the implications of the 'SNR paradigm' see reference [104].

The change of the spectral shape at the knee, the second knee, and the change of composition are consistent with a rigidity dependency of galactic cosmic rays as described by the 'poly-gonato' model [105, 106]. This rigidity dependency can be attributed to a leakage of cosmic rays out of the galaxy (leaky-box model), or to a maximum energy of the acceleration mechanism. For an overview on the involved models see [107]. Further constraints on the distribution of galactic sources and the magnetic field are expected from interpretations of the TeV to PeV anisotropies (e.g. reference [108]).

Nevertheless, the maximum energy of cosmic rays from SNR is surely below $1\,\mathrm{EeV}$. Furthermore, cosmic rays with energies above the ankle cannot be confined by the galactic magnetic field and their arrival directions are, in contrast to cosmic rays at TeV energies, remarkably isotropic; both is expected from an extragalactic origin of UHECR.

Consequently, the change in the shape of the energy spectrum and the composition around the ankle has been interpreted as on-set of the extragalactic component of cosmic rays. However, it remains yet unclear whether galactic sources dominate the cosmic ray flux up to energies $\sim \mathrm{EeV}$ and the ankle marks the transition [109, 110], or if the ankle is a feature of the second component [111, 112] and the transition is the origin of the second knee.

The correlation of UHECR with AGN as extragalactic objects found by the Pierre Auger Collaboration provides evidence for an extragalactic origin of UHECR. It does not imply that AGN are the sources of UHECR, as AGN follow the large scale structure of the matter distribution in the universe and the cosmic rays are deflected in magnetic

---

$^*1\,\mathrm{erg} = 1 \times 10^{-7}\,\mathrm{J}$.

fields. Furthermore, a reanalysis of the objects from the VCV catalogue showed that one-third of the objects that showed correlation with UHECR are not AGN [113]. The cosmic rays from the same dataset also show a correlation with the positions of nearby AGN observed with the Fermi satellite [114] and the local distribution of matter using various catalogues [25, 98]. Further analysis of UHECR data is thus needed to test the models for UHECR origin.

But UHECR are not only messengers from their sources, they are also affected by the environment they traverse. In particular, they lose energy during propagation and are deflected by magnetic fields; from analysis of UHECR observations, models for cosmic magnetic fields can thus be tested. The prevailing models for the origin and propagation of extragalactic cosmic rays are summarized in the next chapter.

2 Extragalactic Cosmic Rays

2.1 Sources

2.1.1 Acceleration Mechanisms

In the prevailing interpretation, UHECR are protons or nuclei accelerated in extragalactic objects. Alternative hypotheses (a review is included e.g. in reference [115]) that UHECR are not accelerated ('bottom-up') but relics from other processes ('top-down') are strongly disfavoured by limits on the fraction of photons in the UHECR flux [116, 117].

Two acceleration mechanisms for cosmic rays are predominantly discussed in the literature, 'direct' or 'one-shot' acceleration in electric fields and 'stochastic' or 'statistical' acceleration in multiple steps in magnetized plasma. A detailed description of these and other acceleration mechanisms as well as references to the original papers can be found in detailed reviews on UHECR (e.g. references [16, 17, 115]).

Direct acceleration in electrical fields is considered unlikely, as the resulting predictions for the energy spectrum are hard to bring in agreement with the observations. Furthermore, large differences in the electric potential in space cannot exist for long times as they are quickly canceled by plasma movements. Nevertheless, under special conditions, e.g. in neutron stars and accretion disks of black holes, strong electrical fields are generated from rotating magnetic fields which might accelerate UHECR before the potential difference is canceled. Details on the one-shot mechanism in such sources are given in section 2.1.3.

Both objections to direct acceleration do not hold for the stochastic acceleration in magnetic fields. First, magnetic fields are omnipresent in the universe. Second, any stochastic acceleration yields a power law with a spectral index depending on the properties of the acceleration environment [118]. In every step of the stochastic acceleration, the particle gains energy $\Delta E = \xi E_0$; after n steps it has the energy

$$E_n = E_0(1 + \xi)^n. \tag{2.1}$$

In every step, the particle has a probability p_{esc} to escape the accelerating region. The probability that the particle has not escaped after n steps is therefore $p_n = (1 - p_{\mathrm{esc}})^n$; the number of particles above an energy E_n is thus

$$N(\geq E_n) \propto \sum_{i=n}^{\infty} (1 - p_{\mathrm{esc}})^i = \frac{(1 - p_{\mathrm{esc}})^n}{p_{\mathrm{esc}}}. \tag{2.2}$$

With $n = \frac{\ln(E_n/E_0)}{\ln(1+\xi)}$ from eq. 2.1 this yields the power-law

$$N(\geq E) \propto \exp\left(\ln(1 - p_{\text{esc}})\frac{\ln E/E_0}{\ln(1+\xi)}\right) = \left(\frac{E}{E_0}\right)^\alpha \tag{2.3}$$

with spectral index $\alpha = \ln\xi - p_{\text{esc}}$.

The first idea for stochastic acceleration by scattering in magnetic fields was proposed by Enrico Fermi [119]. In this model, a particle gains or loses energy from the collisions with moving clouds depending on the speed of the cloud β measured in units of the speed of light c. As head-on collisions are more frequent than tail-on collisions, the particle in total gains energy; detailed calculation yields that the energy gain is $\Delta E/E \propto \beta^2$, resulting in its nowadays name 'second order Fermi mechanism'. Nevertheless, for non-relativistic motions with $\beta \ll 0.1$ the mechanism is not efficient enough to accelerate particles to ultra-high energies [120].

A more efficient 'first order Fermi mechanism' is derived from diffusive scattering in shocks. For a basic understanding we consider a planar wave running through a plasma with non-relativistic velocity v_s. If $v_s > c_s$, with c_s velocity of sound in the plasma, the wave forms a shock front, as the material ahead of the front cannot react on the wave before it arrives. Consequently the shock front marks two regions with different density in the plasma, the 'unshocked' or 'upstream' region and 'shocked' or 'downstream' region.

A particle that crosses the shock front is reflected at magnetic scattering centers in the plasma and is eventually reflected back into its original region. On each crossing, the particle faces a head-on collision with the opposite media, resulting in a net energy gain of $\Delta E/E \propto \beta$, with speed of the scattering centers β. For a detailed discussion of acceleration in diffusive non-relativistic and relativistic shocks see e.g. references [121–123].

The acceleration of particles in diffusive shocks has been directly observed in the bow shock of the solar wind in the magnetic field of the Earth (see e.g. [121] and references therein) and shocks in merging galaxy clusters [124]. Nevertheless, several details of the diffusive shock acceleration model for UHECR remain unclear. In particular, the accelerated particles need to be injected into the plasma with a velocity larger than the shock velocity v_s to allow crossing of the shock front, making the nature of the 'pre-accelerator' a new question. A summary of theoretical challenges to UHECR acceleration in shocks is given in references [13, 16]. Nevertheless, the acceleration models still allow to formulate requirements for UHECR sources.

2.1.2 Source Requirements

A necessary geometric condition for stochastic accelerating sources of cosmic rays is that any source of cosmic rays with an energy E has to confine particles with lower energy. With the size of the acceleration region R and strength of the magnetic field B this gives a maximum energy of

$$\left(\frac{E_{\text{max}}}{1\,\text{EeV}}\right) = 2 \cdot 1.08 \cdot Z \cdot \left(\frac{B}{1\,\upmu\text{G}}\right)\left(\frac{R}{1\,\text{kpc}}\right) \tag{2.4}$$
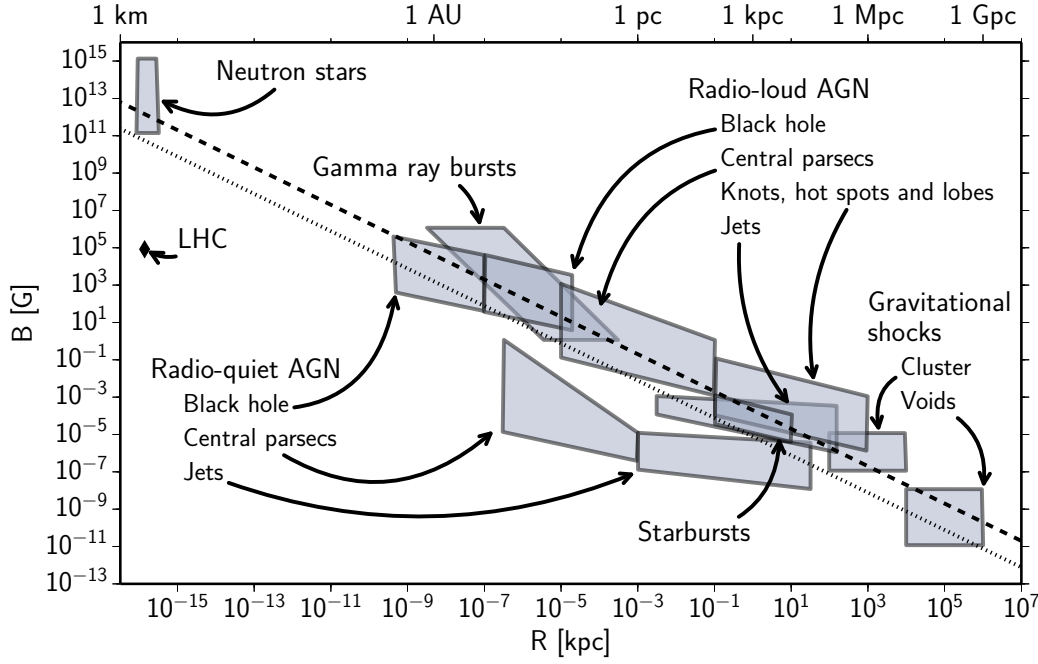
Figure 2.1: Size and magnetic field strength of possible UHECR accelerators after an idea of Hillas [126]. The dashed (dotted) line corresponds to the acceleration of protons (iron nuclei) with $E = 100\,\text{EeV}$ and $\beta = 1$. As comparison, the LHC as largest artificial accelerator is also included in the plot (figure modified from [127]).

for particles with charge number Z from this source [125].

A tighter constraint than eq. 2.4 has been derived by Hillas [126]. The so called 'Hillas constraint'* is valid for acceleration in diffusive shocks and also one-shot acceleration in electric fields generated from rotating magnetic fields. The maximum energy is given as

$$\left(\frac{E_{\max}}{1\,\text{EeV}} \right) = 2 \cdot 1.08 \cdot Z \cdot \beta \cdot \left(\frac{B}{1\,\mu\text{G}} \right) \left(\frac{R}{1\,\text{kpc}} \right) \tag{2.5}$$

with dimensionless factor β specific to the acceleration mechanism.

For stochastic acceleration β is the velocity of the scattering centers, respectively the velocity of the shock front given in units of the speed of light c. For relativistic shocks with $\beta \approx 1$ the Hillas criterion converges to the geometric criterion. However, in relativistic shocks the size of the accelerating region is reduced by the Lorentz factor $\Gamma = \sqrt{1-\beta^2}^{-1}$ to R/Γ, which changes the Hillas criterion [16]. In one-shot acceleration in electric fields generated from rotating magnetic fields, R is the size of the rotating region and $\beta = \frac{\omega R}{c}$ the rotation velocity [126, 128].

A visualization of the Hillas criterion is given in figure 2.1. Following an idea of Hillas [126], classes of possible accelerators are marked as boxes depending on the size

---

*Sometimes also the geometric criterion given in eq. 2.4 is referred to as Hillas criterion (cf. e.g. references [16, 127] and reference [125]).

of the accelerating region R, assuming $\Gamma \approx 1$, and magnetic field strength B. Here conservative ranges for the size and strength of the magnetic field of the objects are used [127]. Diagonal lines mark the requirement for the acceleration of proton and iron nuclei to a maximum energy $E_{\max} = 100\,\mathrm{EeV}$ with $\beta = 1$. Sources below the line do not fulfill this condition.

Additional constraints on source candidates are set from peculiarities of the source environment based on three arguments (e.g. references [13, 16, 125, 127]). First, while accelerating, particles also lose energy due to synchrotron radiation in the magnetic field of the source and interactions with radiation fields [127]. In particular, acceleration environments containing a strong magnetic field also contain strong radiation fields due to synchrotron emission of light particles. Second, the time needed for accelerating the particles has to be smaller than the lifetime of the accelerator. Third, constraints to the sources can be set by the observed chemical composition [129]. The sources have not only to provide the necessary elements to match the observed chemical composition, the acceleration environment must also allow an escape of the elements before they are disintegrated by interaction with photon fields (cf. section 2.3). Based on these requirements, several classes of astrophysical objects have been considered as candidates for UHECR sources.

2.1.3 Source Candidates

The astrophysical objects fulfilling the necessary geometrical requirement for UHECR acceleration as visualized in figure 2.1 are brought to mind in this section. An analysis of the details of the acceleration mechanism in the individual object-classes is given in references [127, 128] and the references cited below. The sources can be classified into continuous or transient emitters. Owing to the time delay of UHECR only continuous sources can be observed with both, cosmic rays and other messengers. We will thus focus here on the statistical properties of the individual classes of objects instead of individual objects; a summary of properties of the types of source candidates is given in table 1.

Two properties of the source candidates are of particular interest in the context of this work. First, the spatial distribution of all source candidates is correlated to the large scale structure of the distribution of matter in the universe. Classes of source candidates differ in spatial density ρ; from the source density thus inferences on the source candidates are possible. Second, the sources accelerate UHECR with a specific composition depending on the abundances of elements in the source and details of the acceleration mechanism.

Neutron stars

Neutron stars (see e.g. reference [130] for a general review) are objects with a mass of about 1.5 solar masses but with only a radius of $\sim 12\,\mathrm{km}$. They are formed in supernova explosions and consist mainly of densely packed neutrons. Nevertheless, the crust of the star consists of protons, heavier ions, and electrons. As neutron stars host the strongest magnetic fields so far observed in the universe, which can

Table 1: Properties of source candidates for UHECR acceleration.

Type	Mechanism	Visibility	$\rho(z=0)$ [Mpc^{-3}]	Element Abundances
Neutron Stars	one-shot	transient	—	heavy
Active Galactic Nuclei				
Radio loud	stochastic[b]	continuous	$10^{-9} - 10^{-4}$	solar
Radio quiet			$10^{-4} - 10^{-3}$	
Gamma ray bursts	stochastic	transient	—	light[d]
Starbursts	stochastic	continuous[c]	10^{-4}	heavy
Gravitational shocks	stochastic	continuous	$10^{-4} - 10^{-3}$ [a]	solar

[a] Number density of galaxy cluster [135].
[b] One-Shot in black hole accretion disk.   [c] Transient for distant sources.
[d] Synthesis of heavy elements in acceleration proposed [136].

achieve strengths of $B \sim 10^{11}$ G in normal neutron stars and $B > 10^{14}$ G in so called 'magnetars' [131], they have been considered as UHECR source shortly after their discovery (see reference [128] and references therein).

The proposed acceleration mechanism for cosmic rays requires rotating neutron stars called 'pulsars'. Owing to their rotation, pulsars emit a relativistic outflow or 'wind', in which the strong magnetic field induces an electric field that accelerates particles. After acceleration, the cosmic rays have to escape the surrounding SNR, in which energy losses are likely; the maximum energy achievable by acceleration in pulsars is thus tightly constraint [127]. Nevertheless, it has been speculated, that the accelerating winds 'shred' the SNR, so that high energy losses are circumvented [132].

The conditions to accelerate particles to energies above 1×10^{20} eV exist for only a few days after the formation of a pulsar or magnetar [115, 133, 134]. As the star spins down, the maximum energy of the accelerated particles decreases. The energy spectrum of cosmic rays emitted by a young pulsar follows a power-law with a maximum energy of few EeV after a few days. The particles are thus not emitted continuously, but in a transient burst. Pulsars and magnetars are formed in every galaxy with massive stars. Their formation rate and energy output can easily account for the observed flux, even if only $\sim 0.01\%$ of pulsars or respectively $\sim 10\%$ of magnetars provide the necessary conditions [132, 134].

Gamma Ray Bursts

Bursts of gamma radiation (GRB) of 30 ms to 100 s duration appear roughly once a day with an isotropic distribution on the sky. In every burst a total energy of $\sim 10^{51}$ erg is emitted, making GRB the highest energetic events known today. The radiation bursts are believed to be emitted in the formation of a black hole from rotating objects like e.g. binary neutron stars; for a general review on GRB see reference [137].

Several models consider the acceleration of UHECR in winds emitted from the GRB
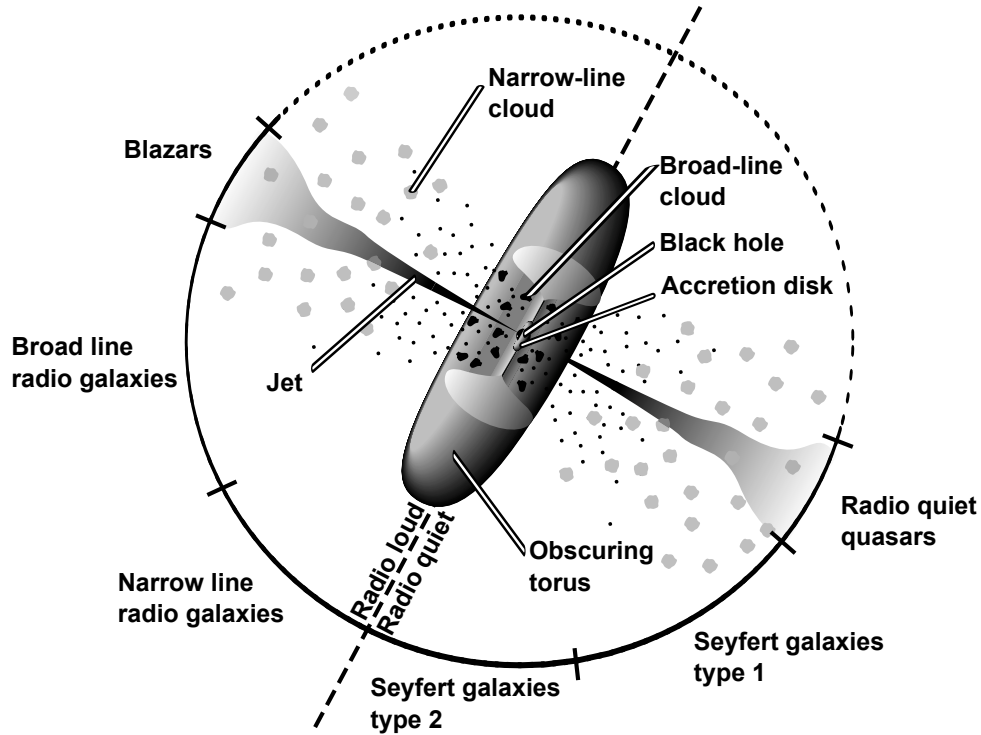
Figure 2.2: Unification model for radio-loud and radio-quiet AGN [144, 145]. Marked arcs denote the classification of the object depending on the viewing angle. The graphic is not to scale (based on reference [145]).

by Fermi's original mechanism (e.g. [138]) or shocks (e.g. [139]). The initial models considered only protons [128, 138] as GRB are believed to require young host galaxies with metallicities lower than in the Milky Way [140, 141]. Nevertheless, mechanisms that allow acceleration of heavy nuclei have been proposed recently, either assuming low-luminosity GRB with high metallicity [139] or that elements with mass numbers up to $A \approx 200$ are synthesized in the accelerating wind [136].

Active Galactic Nuclei

About 10% of all galaxies emit radiation with high luminosity from their central region, called 'galactic nucleus'. These 'active galactic nuclei' (AGN) [142] have been phenomenologically categorized into several subtypes. However, a unified model can describe the observations based on only two types, AGN with strong radio emission ('radio-loud') and AGN without strong radio emission ('radio-quiet'). About 15%–20% of all AGN are radio loud [143]. For reviews on the unification of radio-loud and radio-quiet AGN see references [144, 145].

A sketch of AGN in the unified model is given in figure 2.2. In the center of both types of AGN is a super massive black hole, that accretes matter. It is surrounded by a torus or warped disc of matter, that obscures the view on the central part of the nucleus. The accretion disk emits ultraviolet and perhaps soft X-ray radiation, as the

matter heats up from friction during accretion. Clouds of heated gas orbit above the disc and emit a line spectrum of radiation. The velocity of clouds closer to the black hole is higher; their emission lines are broadened by the Doppler effect. Relativistic particles are emitted in jets parallel to the rotation axis of the accretion disc.

The jets of radio-loud AGN emit stronger radiation than the jets of radio-quiet AGN and can extend beyond their termination shock ('lobe'). The emission is particularly strong in shocked regions ('knots') and the termination region ('hot spot'). These features are absent in jets of radio-quiet AGN [127, 128].

Depending on the viewing angle, the central black hole and the broad line clouds, or only the central black hole is obscured; eventually the jets partly point to the observer. Consequently, these objects are classified depending on the viewing angle as corresponsding AGN subtype.

The remaining variability in the luminosities of the AGN is attributed to the variability of the masses of the central black holes. With increasing mass the AGN becomes brighter and the surrounding magnetic fields larger and stronger. AGNs with low luminosity are more common than AGNs with high luminosity; AGNs of the highest luminosity class have only a number density $\rho \sim 10^{-9}\,\mathrm{Mpc}^{-3}$ [16, 146].

The acceleration of UHECR in shocks in the central region, in shocks in the jets and lobes [16, 127, 128], and in rotationally induced electric fields in the vicinity of the black hole [147] has been proposed. Compared with radio-quiet AGN, radio-loud AGN are typically larger and have stronger magnetic fields, and can thus accelerate particles to higher energies. Nevertheless, acceleration in the central regions is disfavoured, as the strong radiation results in high energy losses [115]. The density of photons in the jets and lobes is much lower than the density of photons in the central parsecs, making UHECR acceleration in jets and lobes more likely than acceleration in the central regions.

The abundances of chemical elements in AGN are comparable to the solar system with a trend to higher metallicities in objects with a higher luminosity [148]. A composition of accelerated UHECR comparable to the solar abundances is thus expected.

Starbursts

Regions with an enhanced star formation rate are called 'starburst regions' or short 'starbursts'. In these regions massive stars are abundant, the supernova rate is increased, and strong infrared and radio emission is produced. From the regions a wind of plasma is emitted that terminates with a strong shock. Galaxies containing starbursts are called 'starburst galaxies' or also short 'starbursts' [128]. Starbursts last less than $\sim 10^8\,\mathrm{yr}$; the number density of post-starburst galaxies, i.e. galaxies that hostet a starburst within $1\,\mathrm{Gyr}$, is $1 \times 10^{-4}\,\mathrm{Mpc}^{-3}$ [149].

The strong radiation inside the starburst result in high energy losses and makes them thus an unlikely source for UHECR. Nevertheless, an acceleration in a two step process has been proposed that avoids high energy losses [150]. First, cosmic rays are accelerated in SNR in the region up to energies of $\sim 10^{15}\,\mathrm{eV}$ depending on their charge number Z. The cosmic rays are then quickly transported out of the region with the wind by convection instead of diffusion, so that disintegration is avoided. Finally,

the particles are accelerated in a second step in the termination shock of the wind to ultra-high energies.

Gravitational Accretion Shocks

In the gravitational structure formation on large scales, the intergalactic matter can be shocked with shock speeds of a few thousand $\mathrm{km\,s^{-1}}$. The magnetic field strength in clusters of galaxies is $\sim \mathrm{\mu G}$, in voids between $\sim 10^{-15}\,\mathrm{G}$ and $\sim 10^{-8}\,\mathrm{G}$ (cf. section 2.4). A radio relic of a acceleration shock of $2\,\mathrm{Mpc}$ size has been detected that provides evidence for the acceleration of particles in shocks [16]. In this radio relic, an acceleration of protons up to $\sim 10^{19}\,\mathrm{eV}$, and consequently iron nuclei up to $\sim 3 \times 10^{20}\,\mathrm{eV}$, is possible [124]. However, for shock speeds of a few thousand $\mathrm{km\,s^{-1}}$, simulations suggest that the energy of protons cannot exceed $1 \times 10^{20}\,\mathrm{eV}$ if energy losses during acceleration are included in the calculation.

2.2 Effects from Cosmology

From the expansion of the universe four consequences arise that have to be considered for the discussion of extragalactic cosmic rays. Here and in the following we only consider a flat universe with ΛCDM cosmology with Hubble parameter

$$H(z) = H_0 \sqrt{\Omega_{m,0}(1+z)^3 + \Omega_{\Lambda,0}} \qquad (2.6)$$

(e.g. references [151, 152]). We use for the current dark energy density $\Omega_{\Lambda,0} = 0.7$, the current matter density $\Omega_{m,0} = 0.3$, and the Hubble constant $H_0 = 0.72 \times 100\,\mathrm{km\,s^{-1}\,Mpc^{-1}}$, as measured by the WMAP satellite [153].

First, the density ρ of the sources is not constant but changes during the evolution of the universe as space was smaller at higher z and also sources form with a non-constant rate. The source density is usually parametrized as $\rho(z) = F(z)\rho(z = 0)$ using the source evolution factor $F(z)$. Of the sources listed in the previous section, the source evolution of neutron stars and starbursts follows the star formation rate (e.g. [154, 155]). A parametrization of the star formation rate

$$F_{\mathrm{SFR}}(z) = \begin{cases} (1+z)^{3.4} & 0 \leq z < 1, \\ f_1^{\mathrm{SFR}}(1+z) & 1 \leq z < 4.5, \\ f_1^{\mathrm{SFR}} f_2^{\mathrm{SFR}}(1+z)^{-7} & 4.5 \leq z \end{cases} \qquad (2.7)$$

can be fitted for different redshift regions, with parameters f_1^{SFR} and f_2^{SFR} so that F_{SFR} is a continuous function [156]. For GRB a stronger evolution $F_{\mathrm{GRB}} = (1+z)^{1.4} \cdot F_{\mathrm{SFR}}$ is assumed as the formation of a GRB may require a low metallicity [141]. The formation rate of AGN is dependent on the luminosity of the AGN; at higher z high-luminous AGN are more frequent. The density of AGN with the highest luminosity evolves as

$$F_{\mathrm{AGN}} = \begin{cases} (1+z)^{7.1} & 0 \leq z < 1.7, \\ f_1^{\mathrm{AGN}} & 1.7 \leq z < 2.7, \\ f_1^{\mathrm{AGN}} 10^{-0.43(z-2.7)} & 2.7 \leq z \end{cases} \qquad (2.8)$$
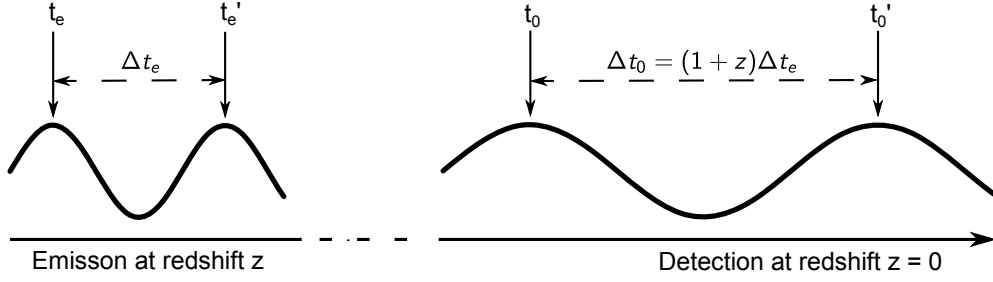
Figure 2.3: Cosmic time dilation. Two particles emitted with a time difference Δt_e are at time z a distance $x_z = c\Delta t_e$ apart from each other. At present time $z = 0$ the distance between the two particles is $x_0 = (1 + z)x_z$, the time interval between detection of the two particles thus a factor $(1 + z)$ longer.

with f_1^{AGN} so that F_{AGN} is a continuous function [157].

Second, the time interval between the observation of two events increases with increasing distance. This is illustrated in figure 2.3; as the time interval between the detection of particles from distant sources increases with respect to the time interval between the injection of the particles, the observed luminosity $L(z)$ of a source with luminosity L_0 in distance z is $L(z) = L_0/(1 + z)$.

Third, cosmic rays lose energy by the adiabatic expansion of the universe. With $E(z) = (1 + z) \cdot E(z = 0)$ we get

$$\frac{dE}{dx} = E_0 \frac{dz}{dx} = E_0 \frac{dz}{dt} \frac{dt}{dx} \tag{2.9}$$

for the adiabatic energy loss. As dz/dt is continuous and monotonic we can use $dz/dt = (dt/dz)^{-1} = (1 + z)H(z)$ and thus define an adiabatic energy loss length

$$L_{ad} = \left(\frac{1}{E} \frac{dE}{dx} \right)^{-1} = \frac{c}{H(z)} \tag{2.10}$$

depending on the evolution of the Hubble parameter.

Fourth, the density of photons changes with increasing z. The rate of interactions with photons as described in the next section thus also depends on the redshift.

2.3 Interaction with Photon Fields

During propagation cosmic rays lose energy, and if they are nuclei also mass, in the interaction with photon backgrounds. Interactions with other particles than photons are negligible due to their low density in space. A detailed discussion of UHECR interactions with photons is given in reference [158], here only the dominant effects are summarized.

In the rest frame of the cosmic ray background photons are blue shifted, so that $E_{\mathrm{CMB}} \sim 10^{-4}\,\mathrm{eV}$ photons of the 'cosmic microwave background' (CMB) have sufficient energy to induce interactions. Besides the CMB, contributions from the 'cosmic infrared
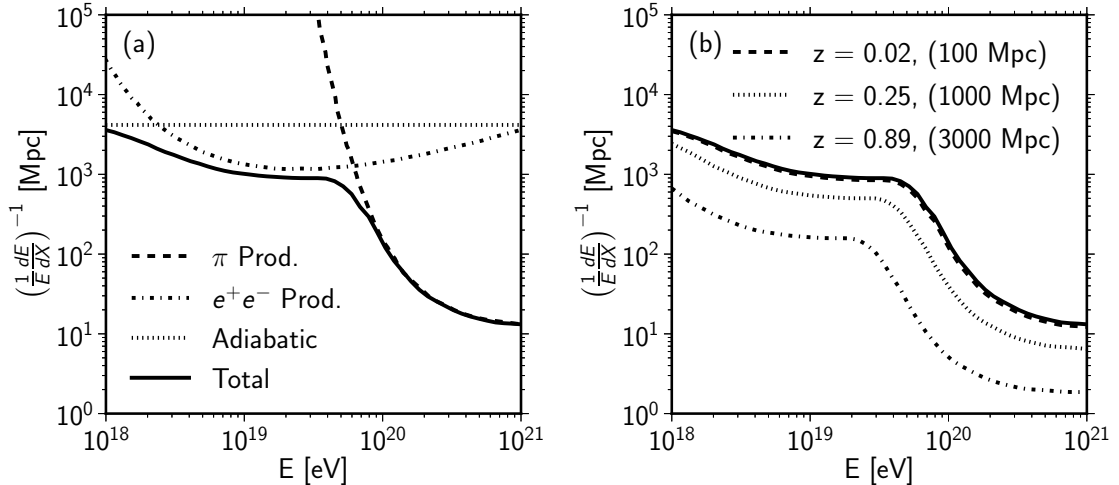
Figure 2.4: Energy loss lengths for protons based on reference [112]. **(a)** Energy loss lengths separated by processes and resulting total energy loss length at $z = 0$. **(b)** Total energy loss length at different redshifts and corresponding current proper distances.

background' (CIB) and 'cosmic ultraviolet and optical background' (CUVOB), together also referred to as 'extragalactic background light' (EBL) (e.g. [159]), have to be considered [160]. However, compared to the CMB the energy density of the EBL is more than ten times smaller [161], making interactions with the CMB the dominant process, if energetically possible.

The density of the photon backgrounds and the photon energy change with the evolution of the universe. As relic of the big bang, the density of CMB photons increases as $\rho_\gamma^{\text{CMB}}(z) = (z+1)^3 \cdot \rho_\gamma^{\text{CMB}}(z = 0)$. The photons are subject to adiabatic energy loss so that $E_\gamma^{\text{CMB}}(z) = (z+1) \cdot E_\gamma^{\text{CMB}}(z = 0)$. In contrast to the CMB, the EBL is generated by astrophysical objects; its density and energy distribution thus reflects the history of the emission in the universe. A review of current limits and models for the EBL is given in references [162, 163].

Individual interactions are characterized by a mean free path length $L(E, z)$ that depends on the energy E of the cosmic ray and its red shift z. An exact calculation of the processes requires detailed Monte Carlo simulations; the cross sections of the processes are accessible by experiment. However, a 'continuous energy loss approximation' (CEL) allows an instructive analytic treatment of the individual processes. For every individual process i, the energy loss length

$$\left(\frac{1}{E} \frac{dE}{dX} \right)_i = L_i^{-1} \tag{2.11}$$

allows to calculate the average energy of particles after propagation of a distance X. The total energy loss length including processes $i = 1 \dots N$ is given by $L_{\text{tot}}^{-1} = \sum_i^N L_i^{-1}$.
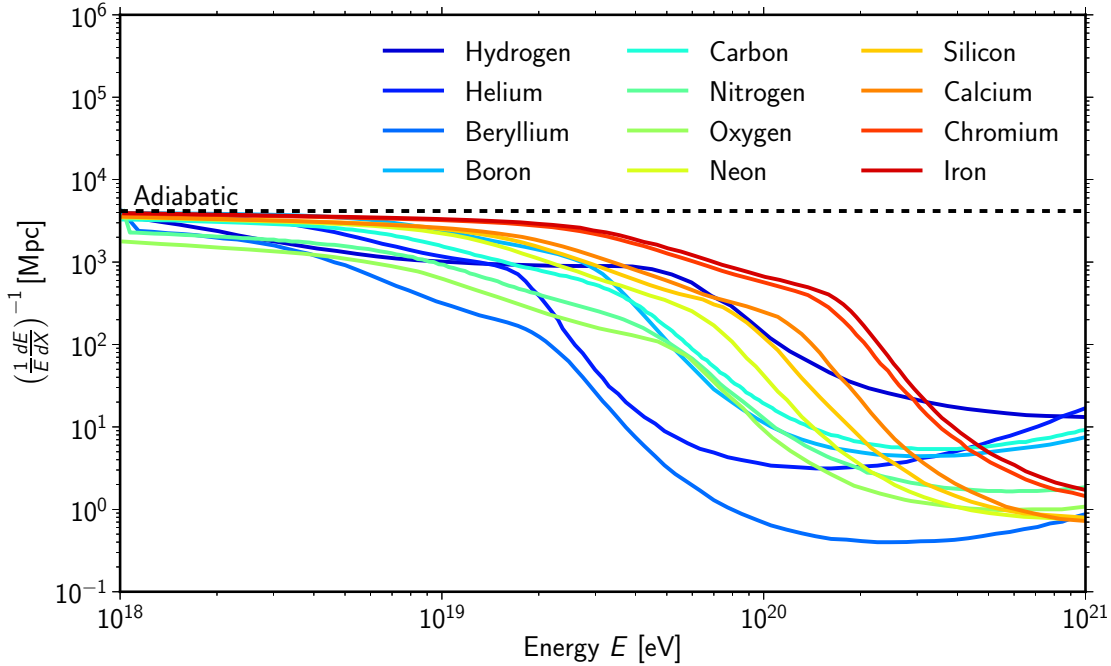
Figure 2.5: Total energy loss length for photon interactions of several elements based on simulations [177] and adiabatic energy losses at $z = 0$ following eq. 2.10.

The CEL approximation has been successfully used for the analysis of the propagation of protons [112, 164–167] and also heavier nuclei [168–172].

The total energy loss length and the energy loss length for the relevant processes for the interactions of UHE protons are shown in figure 2.4. Below $E \approx 2\,\text{EeV}$ the total energy loss at $z = 0$ is dominated by the adiabatic expansion as given in eq. 2.10. Between $E \approx 2\,\text{EeV}$ and $E \approx 60\,\text{EeV}$ the energy loss is dominated by electron pair production [173]

$$p + \gamma \longrightarrow p + e^+ + e^-. \tag{2.12}$$

For higher energies, photo-meson production [158, 174–176], with channels

$$\begin{aligned}
p + \gamma &\longrightarrow p + \pi^0 \\
p + \gamma &\longrightarrow n + \pi^+ \\
p + \gamma &\longrightarrow \Delta^+ \qquad \longrightarrow p + \pi^0 \\
p + \gamma &\longrightarrow \cdots
\end{aligned} \tag{2.13}$$

decreases the energy loss length to $L_{\text{tot}} \approx 10\,\text{Mpc}$. This has been first recognized by Greisen [175] and independently Zatsepin and Kuzmin [176], who consequently predicted a cut-off of the spectrum beyond $E_{\text{GZK}} \approx 50\,\text{EeV}$.

Like protons, heavier nuclei also lose energy by electron pair production [178]. However, at high energies, their energy loss is not due to the creation of massive

particles but due to the fragmentation of the nucleus by photodisintegration [175, 179–181]

$$^Z_A X + \gamma \longrightarrow {}^{Z-Z'}_{A-A'}\hat{X} + {}^{Z'}_{A'}X'. \tag{2.14}$$
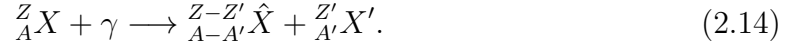
The dominant effect can be understood as excitation of the 'giant dipole resonance'. The nucleus behaves here as consisting of two penetrating fluids of neutrons and protons. Photons with an energy above $\sim 8\,\mathrm{MeV}$ in the rest frame of the nucleus can excite a vibration of the fluids with a characteristic resonance frequency. It de-excites by the emission of a typically small fragment with $A' \lesssim 4$. All nucleons approximatly carry the fraction $\frac{1}{A}E_0$ of the total energy E_0 of the nucleus; the heavier fragment thus carries the major part of the energy $E = \frac{A-A'}{A}E_0$.

The energy loss lengths for several elements is shown in figure 2.5. As for protons, the energy loss length of all nuclei decreases drastically at energies above few times $10^{19}\,\mathrm{eV}$. Here, the threshold energy for the excitation of the giant dipole resonance is reached by CMB photons. Consequently a cut-off similar to the GZK effect is expected also for cosmic rays being nuclei.

An accurate treatment of nuclei propagation has to include all disintegration paths in the nuclear table and also the decay of radioactive isotopes (e.g. reference [182]). Nevertheless, a simplified analytical treatment considering only a single disintegration path without nuclear decays is in good agreement with the results from full simulations [168, 183].

2.4 Cosmic Magnetic Fields

Magnetic fields are ubiquitous in the universe [184] and in particular permeate the galactic and extragalactic space traversed by UHECR. Nevertheless, there is no commonly accepted theory about their formation and in particular their origin [21, 23, 24, 185–190]. Cosmic magnetic fields are shaped by the plasma they permeate. But in the framework of magnetohydrodynamics, magnetic fields can only be amplified and shaped, but not be created (e.g. [186]). The magnetic fields observed today are thus formed out of initial 'seed fields' by dynamo processes and plasma motion during the structure formation process. For a review of dynamo processes for the origin of galactic magnetic fields see references [21, 191] and reference [24] for a general summary on plasma mechanics.

Several models for the seed fields have been proposed, either hypothesizing an origin in astrophysical objects (e.g. [192–194]) or in primordial processes (e.g. [195, 196]). If of primordial origin, the magnetic field might allow conclusion on structure formation [197–201], baryon asymmetry [202], and inflation (e.g. [203, 204]). For reviews on mechanisms that might generate a primordial magnetic field and its effects see references [22–24, 187, 190, 205], for a summary on the generation in astrophysical objects see reference [24].

These generation scenarios yield discriminative expectations for the extragalactic, i.e. outside of galaxies, magnetic field (EGMF). Strong extragalactic magnetic fields have

to be generated early in the universe, whereas weak extragalactic magnetic fields can be easily formed after the structure they permeate. Early seed fields can, e.g., be the result of ejecta of protogalaxies [194], or the remnant of a primordial magnetic field. If of primordial origin the observed magnetic fields can be coherent on large scales, which is not expected from an origin in astrophysical objects. The key observables are thus the strength and the characteristic length scale of the extragalactic magnetic field, in particular in the voids and filaments.

However, cosmic magnetic fields, in particular in voids and filaments, are hard to measure. For a review of methods and a summary of observations see reviews [184–186, 188, 189]. But cosmic magnetic fields might be an important factor for UHECR propagation, as they obscure the position of the sources and elongate the propagation distance of the cosmic rays. Extragalactic cosmic rays can therefore also be considered probes of the field they traverse; UHECR measurements thus contribute to the understanding of magnetic fields [102, 206–208].

2.4.1 The Extragalactic Magnetic Field

Observations established magnetic fields with a strength in order of µG in the atmosphere of galaxy clusters. At localized positions in the core, the magnetic field can reach levels of up to 40 µG [209]. Between galaxy clusters that are 40 Mpc apart, a 'bridge' of radio emission has been observed, that suggest a magnetic field of 0.3-0.6 µG in filaments [210]. Nevertheless, magnetic fields in filaments have not been observed with synchrotron emission, leaving the field strength uncertain [24].

An overview of observational limits on the strength of the magnetic fields in voids depending on the coherence length of the field is given in figure 2.6. An upper limit on the EGMF independent on the coherence length results from the observation of the 21 cm absorption line of the light from distant quasars. The light emitted by the quasar excites the 21 cm energy level of hydrogen in intergalactic space. In presence of a magnetic field, the absorption line is split according to the Zeeman effect. Tighter upper limits on the EGMF at specific coherence lengths are derived from the analysis of Faraday rotations of distant quasars [213].

Lower limits are from the non-observation of GeV γ-ray from a TeV γ-ray source [212, 215–218]. The technique uses that the initial TeV γ-rays will create an electromagnetic cascade. The charged particles are deflected in the magnetic field, creating an extended halo of GeV γ-rays around a TeV γ-ray source. However, the assumptions included in these limits [217, 218] might be too optimistic, which potentially reduces the lower limits [219]. Evidence for a GeV halo around a TeV source has been recently found. The interpretation of this measurement results in a strength of the field in voids of $\sim 10^{-15}$ G [220], but is subject to the same assumptions.

Magnetohydrodynamic simulations of the formation of large scale structures are able to reproduce the magnetic fields observed in galaxy clusters assuming an origin of the field in AGN ejecta [221] or initial seed fields [24, 46, 222]. The corresponding values for the magnetic field in filaments range from 1 µG [222] to 1 nG [46] and below. From the amplification in structure formation, a field strength that correlates with matter
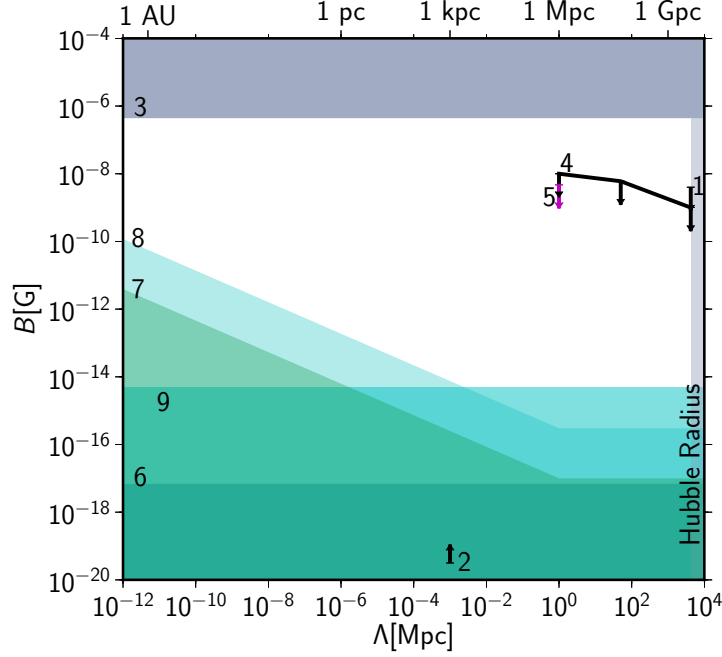
Figure 2.6: Observational limits on the extragalactic magnetic field in voids. Shaded regions are excluded. Points marked as 1 and 3 are taken from [211], 2: [212], 4: [213], 5: [214], 6: [215], 7: [216], 8:[217], 9: [218] (idea and initial collection from reference [211], supplemented with additional publications.).

density and field lines following the large scale structure are expected. The field is modulated by local turbulences [222]. The field strength in voids is roughly two orders of magnitude smaller than in the field strength in filaments [24, 46].

Independently of the origin of the seed fields, the structure of the magnetic field observed nowadays is expected to be the result of turbulent dynamo processes [24]; the resulting magnetic field energy is distributed on eddies of different size.

In a sufficient homogeneous and isotropic region, the turbulent magnetic field can be described by Kolmogoroff's theory of turbulence. Here, the energy distribution on scales k is described by a power law $dE/dk \propto k^n$ with spectral index $n = -5/3$ between minimum and maximum length scales $L_{\min}$ and $L_{\max}$. For the magnetic field $\vec{B}(\vec{x})$ with zero mean and root mean square (rms) B, a correlation length Λ can be defined [223] by integration

$$\int_{-\infty}^{\infty} dL \langle \vec{B}(0)\vec{B}(\vec{x}(L))\rangle = \Lambda B^2 \tag{2.15}$$

reading

$$\Lambda = \frac{1}{2}L_{\max}\frac{n-1}{n}\frac{(1-L_{\min}/L_{\max})^n}{1-(L_{\min}/L_{\max})^{n-1}} \tag{2.16}$$

for a power law spectrum.

For a cosmic ray with rigidity E/Z that propagates a distance D through a turbulent field with coherence length Λ four regimes of propagation can be identified depending on the strength of the deflection σ [223]. If the deflections are small ($\sigma \ll \Lambda/D$), the variation among the trajectories of cosmic rays with similar initial conditions is small, so that all cosmic rays seen by an observer have traversed the same magnetic field structures. If $\sigma \sim \Lambda/D$, several separated groups of trajectories can become possible, resulting in multiple images of the same source appearing to an observer. With further increasing deflection strength, the trajectories become more and more chaotic, resulting in a blurring of the image of a source. In this scenario, the average strength of the deflection, given by the root mean square of the distribution of angles between the line of sight to the source and the arrival direction of the cosmic ray, σ is calculated as

$$\sigma = \frac{37.5°}{\sqrt{3}} \sqrt{\frac{D_k}{\Lambda}} \left(\frac{\Lambda}{\text{Mpc}}\right) \left(\frac{B}{\text{nG}}\right) \left(\frac{E/Z}{\text{EeV}}\right)^{-1} \tag{2.17}$$

in the limit of small deflections and under the neglect of energy losses. Within this approximation, the trajectories of the cosmic rays are longer by a distance

$$r = 116 \text{ kpc} \left(\frac{B}{\text{nG}}\right)^2 \left(\frac{D_k}{\text{Mpc}}\right)^2 \left(\frac{E/Z}{\text{EeV}}\right)^{-2} \left(\frac{\Lambda}{\text{Mpc}}\right) \tag{2.18}$$

compared with the linear distance D [224]. The prefactors of eq. 2.17 and eq. 2.18 have been modified compared with the original references [223, 224] to use the definitions of the angle and coherence length given above.

For large deflections ($\sigma \gg \Lambda/D$) the cosmic rays lose all information about their original direction; UHECR propagation can be modeled as diffusion process [225, 226]. In particular, it has been shown that if the deflection is comparable to or larger than the angular distance between sources, the energy spectrum assumes an universal form [227]. In particular, the spectrum is independent on the distribution of sources and the strength of deflection in the magnetic field. The cosmic rays are 'bound' to their sources by the magnetic field; the cosmic ray density near the source is increased compared with linear propagation. The maximum propagation distance of UHECR is thus limited by the magnetic field resulting in a 'magnetic horizon' (e.g. [228]).

2.4.2 The Magnetic Field of the Milky Way

The magnetic field of the Galaxy is deduced from measurements of starlight polarization, polarization of thermal dust emissions, Zeemann splitting, diffuse synchrotron emission, and measurements of Faraday rotation. An overview of the methods and measurements is given e.g. in references [188, 189, 229]. As in other spiral galaxies, the magnetic field lines are aligned with the spiral arms in the disc; the field is not unidirectional on the complete arm, but shows field reversals. At the position of the sun, the field strength is $(2.1 \pm 0.3)\,\mu\text{G}$ on a $(8.5 \pm 4.7)\,\text{kpc}$ scale; the strength of the vertical component is approximately $0.2\,\mu\text{G}$. The large scale field is modulated by a small scale random field with 4-6 μG strength on a 10-100 pc scale. In region of the galactic center, observations
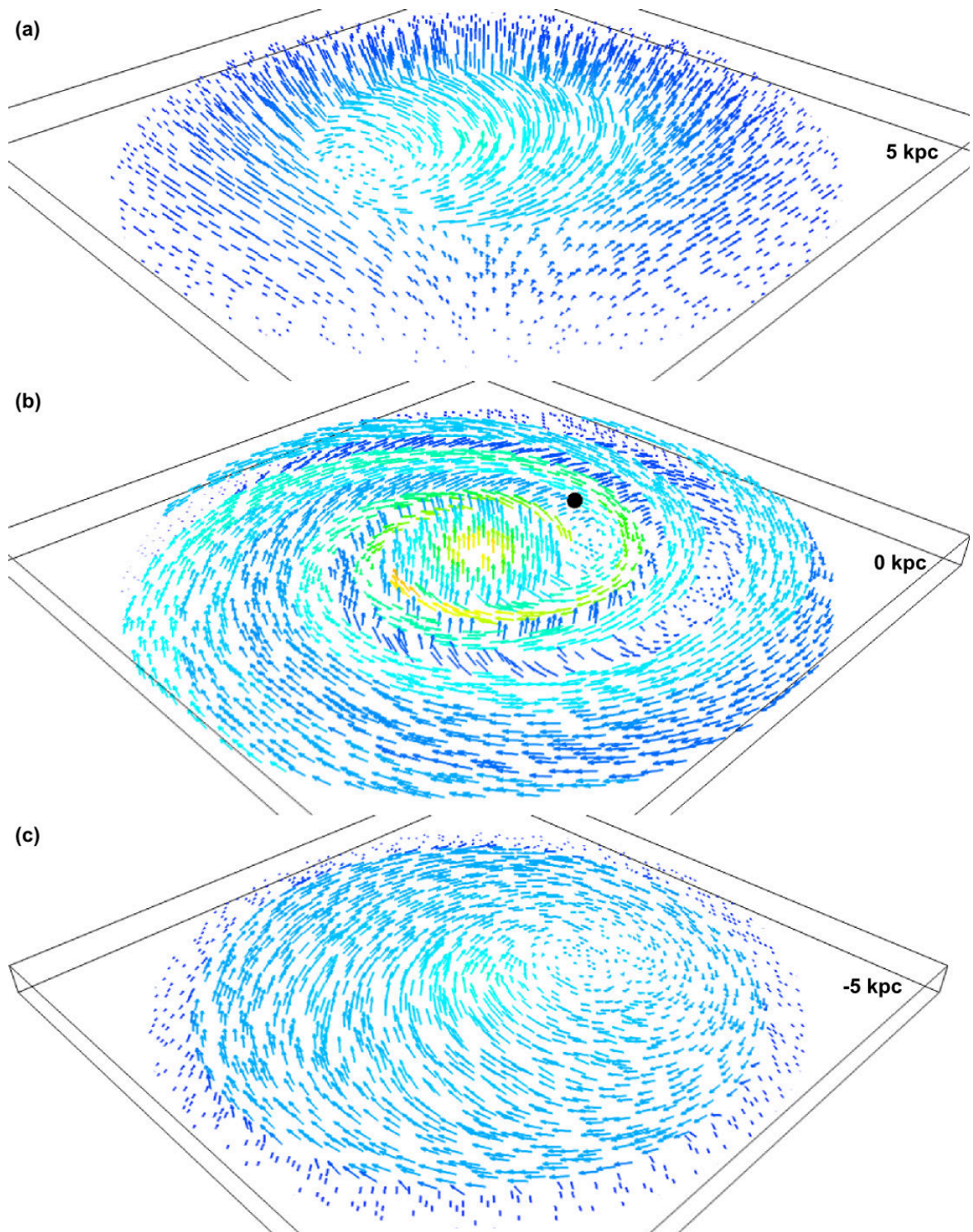
Figure 2.7: Slices through the JF 2012 regular field calculated with the CRT software [53]. **(a)** 5 kpc above the galactic plane, **(b)** in the galactic plane, **(c)** 5 kpc below the galactic plane. The color of the vectors denote the fieldstrength. The outline has the dimensions $20\,\mathrm{kpc} \times 20\,\mathrm{kpc} \times 2\,\mathrm{kpc}$ and is centered around the plane. The black dot in (b) denotes the position of the Sun.

sugest a toroidal field configuration [230]. The field strength increases towards the galactic center and reaches at least 50 µG on a 400 pc scale at the center [231]. Outside the galactic disc, rotation measurements show an antisymmetry towards the disc, consistent with reversed field directions at the disc.

Numerous models have been proposed to describe the field structure. Most prominent are a simple ring model and axisymmetric (ASS) and bisymmetric (BSS) models [80, 232]. In the ring model the magnetic field simply points in the azimuthal direction with no radial component and also no spiral arms. In the ASS and BSS models, a field structure following the spiral arms is included. In the axisymmetric models the field in all spiral arms points in the same direction whereas in the bisymmetric models the fields direction in the arms is reversed. Depending on the extension outside the disc, the ASS and BSS model are suffixed as (A)BSS_S or (A)BSS_A, model, indicating a symmetry or antisymmetry of the field towards the galactic plane. Nevertheless, these simple models are not divergence-free and none of the models describe the observational data significantly better than any of the other [233].

Improved models fit combinations of the simple models with additional field components to observational data [234–238]. The JF2012 model [237, 238] is based on a divergence free field structure fitted to full sky observational data. It models the field with three different components, a large scale regular field, a 'striated' random field and small scale random fields. The three components can be fitted separately to the observations.

The large scale regular field consists of a disc-component, a toroidal halo component, and a poloidal halo component. The disk component sections the galactic plane in rings at 3 kpc, 5 kpc and 20 kpc distance from the galactic center. Between 3-5 kpc the field is azimuthal with a strength of 0.1 µG. Beyond 5 kpc the field is modeled along eight spiral arms with different field strength in each arm. The strength of the toroidal component decreases exponentially in z; the transition between the disk and the halo field is modeled by the logistic function. Both fields are superposed with an X-shaped out-of-plane component motivated by observations of other galaxies. The JF2012 regular field in the galactic plane and 5 kpc above and below the galactic plane is displayed in figure 2.7. The strength of the striated field is scaled with the strength of the large-scale regular field. The striated field is aligned randomly parallel or anti-parallel to the regular field on a scale of ~ 100 pc.

The trajectory of cosmic rays propagating through the field depends on the configuration of the random field, and the starting point and direction of the trajectory. To model the effect of the field on the observed cosmic rays on earth, the individual trajectories have to be calculated numerically.

3 Simulation of UHECR Propagation

To compare the scenarios discussed in the previous chapter with observations, the generation of simulated data as 'pseudo experiments' is needed. The simulation has to combine models for four different aspects of UHECR propagation:

1. A model describing position, spectrum, and relative luminosity of the sources,

2. A model for the deflection in extragalactic magnetic field,

3. A model describing the composition and the corresponding energy loss of the particles, and

4. A model describing the deflection in the galactic magnetic field.

Beside the composition of the UHECR flux, the most uncertain components are here the unknown sources and the extragalactic magnetic field. To test hypotheses on the density of sources and strength of the magnetic fields, a fast generation of sufficiently large data samples at every point of the parameter-space is required.

The most obvious approach for a UHECR Monte-Carlo generator allowing detailed simulations of individual physics processes is to follow the trajectories of individual particles from the source to the observer and account for energy losses and deflections during the propagation. This forward-propagation is for example implemented in the CRPropa program [48, 239]. In this approach the, compared to intergalactic distances, small size of the observer makes the generation of large Monte-Carlo data sets highly challenging. Furthermore, forward simulations so far do not include cosmological effects, as the simulation of the temporal evolution of the UHECR flux would challenge even further the required computing resources.

A different approach aiming at UHECR mass production is to backtrack particles starting at the observer and associate them to the objects in the source model. This approach is well understood and documented in the literature (e.g. [53, 240]). However, it requires huge trajectory databases (e.g. [47]) and the trajectories are associated to sources only at the end of the simulation.

To make the parameters of the models listed above testable, we designed the 'PARameterized Simulation Engine for Cosmir rays' (PARSEC) software. In the following, we summarize the simulation methods and physical models used in PARSEC and discuss selected aspects of the simulated datasets. An overview on technical details of design and implementation of the PARSEC software as well as a benchmark of the computing performance is given in appendix A.

3.1 Simulation Methods

In our approach, we first explicitly calculate the probability distribution to observe a particle with an energy E from a given direction (ϕ, θ). Simulated datasets of arbitrary number of individual UHECR within the scenario are then generated based on this calculation in a separate step.

We interpret the probability to observe a particle from a discrete direction $(\phi, \theta)_j$ on a pixellated sky as an element j of a vector $\mathbf{p}_{obs}$ resembling the probability distribution. For every energy range $E_i^l \leq E_i < E_i^r$ a separate vector is calculated, leaving the total probability distribution $\mathcal{P}$ from which individual cosmic rays are later generated as a set of vectors $\mathcal{P}_{obs} = \{\mathbf{p}_{obs}^i\}$. For the pixels, we use the 'Hierarchical Equal Area isoLatitude Pixelization' (HEALPix) discretization scheme [241]. To achieve an angular resolution of better than 1°, HEALPix order 6 resulting in 49 152 pixels is needed.

For every energy range i, the observed probability vector $\mathbf{p}_{obs}^i$ is calculated in two steps: First, 'extragalactic' probability vectors $\mathbf{p}_{eg}^i$ for the expected distribution including all effects except the galactic magnetic field are calculated. In a second step this probability vector is transformed to account for deflections in the galactic magnetic field, yielding $\mathbf{p}_{obs}^i$.

3.1.1 Extragalactic Propagation

The discrete probability distribution $\mathbf{p}_{eg}^i$ is calculated by the sum of the contributions of every individual source S_k of a source model $\{S_1 \cdots S_N\}$ to every pixel p_j^i. We separate the contribution of S_k to p_j^i into three factors:

1. A factor f_S including the source distance and luminosity,

2. A factor f_E describing the source energy spectra and energy loss effects, and

3. A factor f_B distributing the flux from one source on multiple pixels to account for the deflection in magnetic fields.

With these ingredients the probability to observe a particle with energy E_i in pixel j can be written as

$$p_j^i = \Gamma_i \cdot \sum_k f_S f_B f_E \tag{3.1}$$

where Γ_i denotes a normalization factor ensuring $\sum_{i,j} p_j^i = 1$.

Energy Losses

A particle emitted by source S_k with the energy E_{inj} propagates a distance τ within the extragalactic magnetic field model, and is then observed with energy E_i. The probability to observe the particle therefore depends on the source spectra, the energy loss of the particle and the propagation distance, which is summarized in f_E. For source spectra following a power law described with spectral index γ this corresponds to

$$f_E = \frac{1}{1 + z_g} \left(E_{inj,r}^{\gamma+1} - E_{inj,l}^{\gamma+1} \right) \tag{3.2}$$

where the scaling factor $(1 + z_g)^{-1}$ of the universe at the cosmological epoch of particle injection accounts for cosmological time dilation. The range of injection energies $E_{inj,l/r}$ is calculated with the continuous energy loss approximation by numerically integrating

$$\left(-\frac{1}{E}\frac{dE}{dx} \right) = \frac{1}{L(z, E)} \tag{3.3}$$

with the total energy loss length defined as $L(E, z)^{-1} = L_{ad}(z)^{-1} + L_\gamma(E, z)^{-1}$. Here $L_{ad}(z)$ is the adiabatic energy loss given in eq. 2.10.

For protons the energy loss lengths for interactions in background photon fields $L_\gamma(E, z = 0)$ as published in references [112, 165] are implemented. As an extension, we also implemented a simplistic model for the observed UHECR being iron nuclei. For this we also use a continuous energy loss approximation with an attenuation length given by the maximum of the nuclei calculated in reference [177]. Here, the 'iron nuclei' do not disintegrate but keep a charge number of $Z = 26$. The propagation of secondary particles is not included. As the cosmic rays thus have maximum range and deflections, this model yields a minimum anisotropy-signal for the simulated parameters. From the energy loss length of photon interactions at redshift $z = 0$ the energy loss length at z is derived from scaling using

$$L_\gamma(E, z) = (1 + z)^{-3}L_\gamma\left((1+z)E, z = 0 \right) \tag{3.4}$$

to account for the increase of the energy and density of the CMB background photons.

Scattering around Sources

The effects of the extragalactic magnetic field are parametrized assuming a turbulent field in which the particles perform a random walk. The flux of a single source S_k is distributed over several pixels p_j^i.

For small scattering angles, the rms of the deflection is given by eq. 2.17. This parametrization for the rms of the deflection angle does not include energy losses. To derive a first order approximation including energy losses, we first differentiate eq. 2.17 with respect to the source distance x

$$\frac{d\sigma}{dx} = \frac{37.5°}{\sqrt{3}} \sqrt{\frac{\Lambda}{x}} \frac{B}{E(x)} \left(1 - \frac{x}{E}\frac{dE}{dx} \right). \tag{3.5}$$

Assuming $(dE/dx) \cdot (x/E)$ being small for the ultra-high energies considered here the second term of eq. 3.5 can be neglected. Integrating eq. 3.5 to the source distance

$$\sigma = \frac{37.5°}{\sqrt{3}} \sqrt{\frac{\Lambda}{x}} B \int_0^{D_k} \frac{1}{E(x)} dx \tag{3.6}$$

then yields the rms of the deflection for particles from source S_k.

If the particles perform a random walk, the distribution of the angles $\alpha_{j,k}$ between the direction of source S_k and the center of pixel p_j^i follows a Fisher distribution [242],
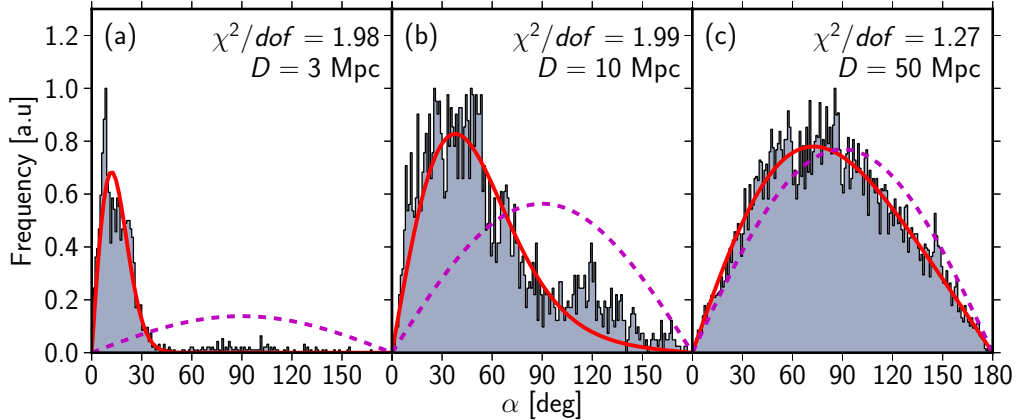
Figure 3.1: Distribution of angles between arrival direction of cosmic rays with $E = 10\,\mathrm{EeV}$ and line of sight to the source in distance D after propagation through a turbulent field with $B = 3\,\mathrm{nG}$ and $\Lambda = 5.2\,\mathrm{Mpc}$. The solid line shows a fit of a Fisher distribution; the dashed line correspond to an isotropic distribution of directions.

which can be regarded as normal distribution on a sphere. The second factor f_B of eq. 3.1 thus reads

$$f_B(\alpha_{j,k}, \kappa) = \frac{\kappa}{4\pi \sinh(\kappa)} e^{\kappa \cdot \cos \alpha_{j,k}} \tag{3.7}$$

with concentration parameter κ.

A fit of eq. 3.7 to data simulated with CRPropa [48] is shown in figure 3.1 for different source distances and thus different strength of the deflection. For propagation distances D smaller or in the order of a few coherence lengths Λ, individual particles traverse the same magnetic field. The distribution of arrival directions is thus not normal, but shows structures characteristic to the local field structure.

For small deflections, the Fisher distribution can be approximated by a Rayleigh distribution. For the concentration parameter κ and the root mean square (rms) σ of the deflection for small angles it is

$$\kappa = 1/\sigma^2. \tag{3.8}$$

Here we use the so defined κ with σ as in eq. 3.6 for all values of E, D, Λ and B.

A comparison of this parametrization with results from forward simulations using the CRPropa software [239] is shown in figure 3.2 (a) and (b) for two choices of the observed energy and the coherence length. In all simulations the strength of the magnetic field is $B = 1\,\mathrm{nG}$. In the forward simulations we assumed a spectral index of the sources of $\gamma = -2.7$. The expectation value for angles θ described by a Fisher distribution with concentration parameter κ is calculated using computer algebra software [243] as

$$\langle \theta \rangle = \frac{\pi}{2 \sinh \kappa} \cdot (I_0(\kappa) - e^{-\kappa}) \tag{3.9}$$
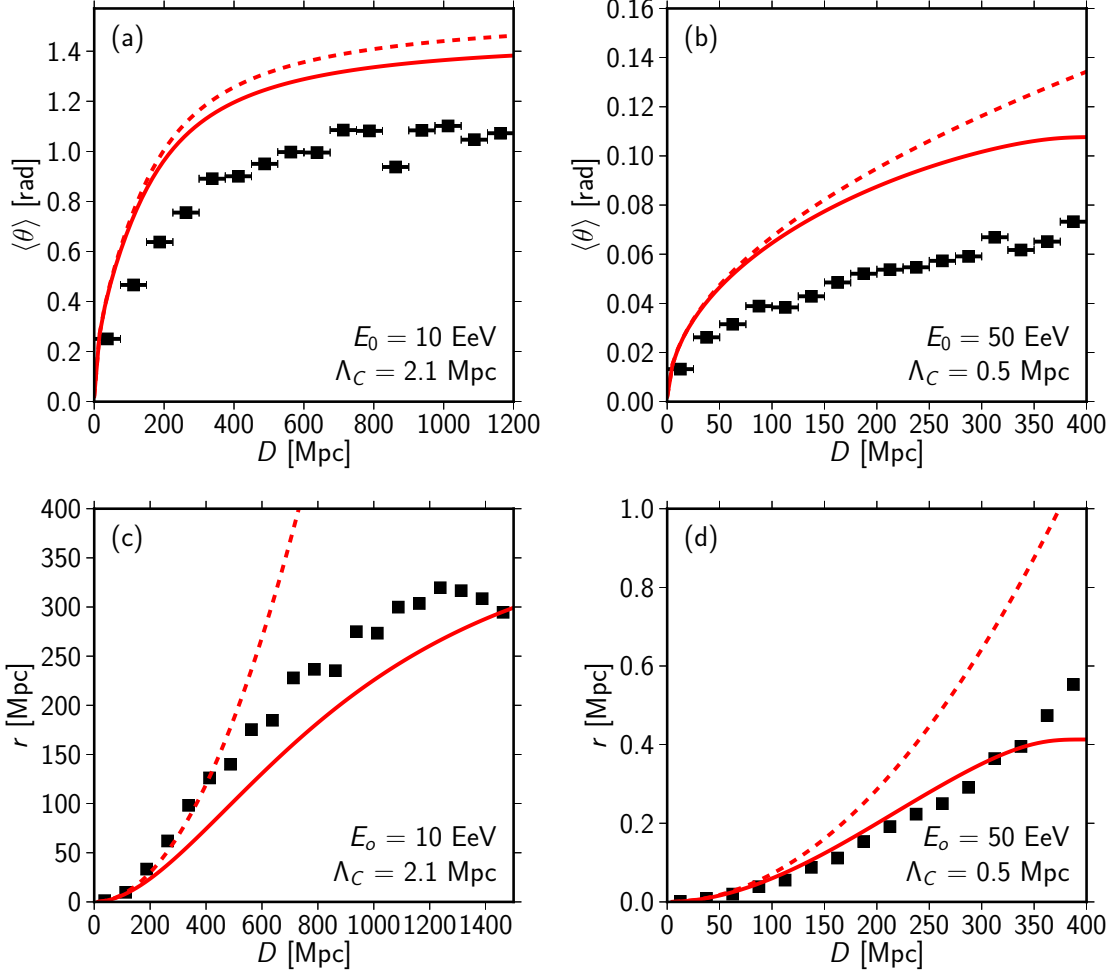
Figure 3.2: Comparison of the parametrizations of **(a,b)** mean deflection angle given θ and **(c,d)** elongation of propagation path r used in parsec (solid lines) with forward simulated data (square markers). Dashed line shows parametrization without energy losses as given by eq. 2.17 respectively eq. 2.18.

with I_0 representing the modified Bessel function of order 0. An expectation value of $\langle\theta\rangle = \frac{\pi}{2}$ corresponds to isotropic arrival directions and is reached for $\kappa \to 0$.

The plots selected for figure 3.2 exhibit the maximum deviation within the simulated combinations of parameters E_o, B, Λ. Including the energy losses in the parametrization as given by eq. 3.6 improves the description of the average deflection for high energies. The approximation overestimates the strength of the deflections by less than a factor two.

Elongation of Propagation Time

Due to deflection in magnetic fields, the length of the trajectory of the particles $c\tau = D_k + r$ from sources in distance D_k is elongated by an extra distance r. The parametrization for r given in eq. 2.18 does not include energy losses. To account for

energy losses in the extended propagation length we write eq. 2.18 for infinitely small dx reading

$$dr \propto \left(\frac{2xB^2\Lambda Z^2}{E^2}dx - \frac{2B^2x^2\Lambda Z^2}{E^3}\frac{dE}{dx}dx \right) \quad (3.10)$$

with $0 < x \leq D_k$. Assuming again $(dE/dx) \cdot (x/E)$ to be small, the second term of eq. 3.10 can be neglected. The result can be written as a Riemann sum

$$r \propto \sum_i^N \frac{B^2\Lambda Z^2}{E\left(x_i + \frac{(x_i - x_{i-1})}{2}\right)^2}(x_i^2 - x_{i-1}^2) \quad (3.11)$$

with $x_N = D_k$. Eq. 3.11 is solved iteratively for every individual source S_k.

A comparison of the two parametrizations with results from forward simulations is shown in figure 3.2 (c) and (d) for two choices of the observed energy and the coherence length. In all simulations the strength of the magnetic field is $B = 1\,\mathrm{nG}$. Without inclusion of energy losses the path elongation r is overestimated. For small deflections the parametrization in eq. 3.11 matches the forward simulations.

Increase of Particle Density

The factor $f_S(S_k)$ accounts for the relative individual luminosity L_k of source S_k and the density of particles at the position of the observer in current proper distance D_k. If the particles propagate on a straight line, the flux from a source is distributed on a sphere with radius of the current proper distance D_k of the source resulting in $f_S(S_k) = L_k/D_k^2$.

Nevertheless, in the presence of magnetic fields the density of UHECR is higher compared with the densities obtained in linear propagation scenarios. At some distance
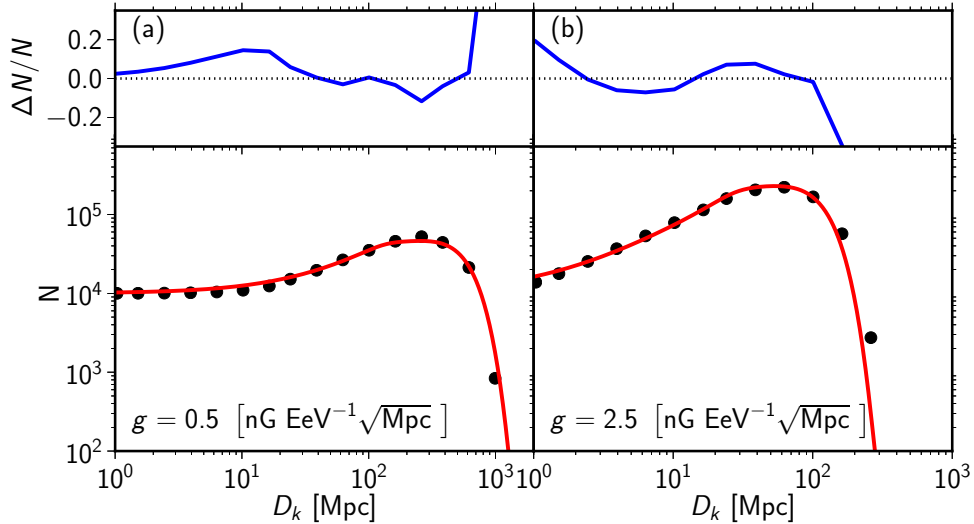
Figure 3.3: Comparison of the parametrization in eq. 3.12 to forward simulated data for two choices of $g = \frac{B}{E}\sqrt{\lambda}$. The upper panel shows the relative difference between simulation and parametrization $\Delta N/N$.

to the source all information about the origin of the UHECR is lost, and instead of a directed random walk the density is described according to a Wiener process. To model this transition we simulated the trajectories of individual UHECR from one source in a turbulent magnetic field with a modified version of the CRPropa software [239]. Using $g = \frac{B}{E}\sqrt{\Lambda}$, we found that the density of UHECR in distance D_k can be approximately described by

$$f_S = \frac{L_k}{D_k^2} \left((1 + p_1 \cdot g^2 \cdot D_k)(1 - T) + T \cdot p_2 \cdot g \cdot e^{-\frac{1}{2}\left(\frac{D_k}{x_1} \cdot g - 1\right)^2} \right) \qquad (3.12)$$

with

$$T = \frac{1}{1 + \left(\frac{D_k \cdot g}{x_t}\right)^{-s}}. \qquad (3.13)$$

and parameters as listed in table 2.

Table 2: Results of the fit of eq. 3.12 to UHECR densities in forward simulations.

Parameter	Value	Unit
p_1	0.1	$\mathrm{nG}^{-2}\,\mathrm{EeV}^2\,\mathrm{Mpc}^{-2}$
s	5	—
x_t	70	$\mathrm{nG}\,\mathrm{EeV}^{-1}\,\mathrm{Mpc}^{3/2}$
p_2	9	$\mathrm{nG}^{-1}\,\mathrm{EeV}\,\mathrm{Mpc}^{-1/2}$
x_1	140	$\mathrm{nG}\,\mathrm{EeV}^{-1}\,\mathrm{Mpc}^{3/2}$

For two choices of g the parametrization is shown together with the simulated data in figure 3.3. The relative difference between simulated and parametrized particle numbers $\Delta N/N$ depending on the distance X is shown in the upper panel. For $0.1 < g \cdot \mathrm{nG}^{-1}\,\mathrm{EeV}\,\mathrm{Mpc}^{-1/2} < 2.5$ the deviation of eq. 3.12 from the simulations is typically below $\sim 20\%$.

The propagation theorem [227] states, that the observed spectrum does not depend on the magnetic field, if the separation between sources is much smaller than all characteristic propagation lengths. This is a consequence of the increase of particle density in presence of magnetic fields compared to linear propagation. For a homogeneous distribution of sources the spectrum calculated with PARSEC agrees within 20% with the 'universal spectrum' expected by the propagation theorem.

3.1.2 Propagation in the Milky Way

To model particle propagation in the magnetic field of the Milky Way, we neglect energy losses during the relatively short galactic propagation. The effects of the galactic magnetic field can thus be addressed as magnetic lensing [80, 244]. As there is no random process in this model, a particle with energy E_i entering the galaxy at a point
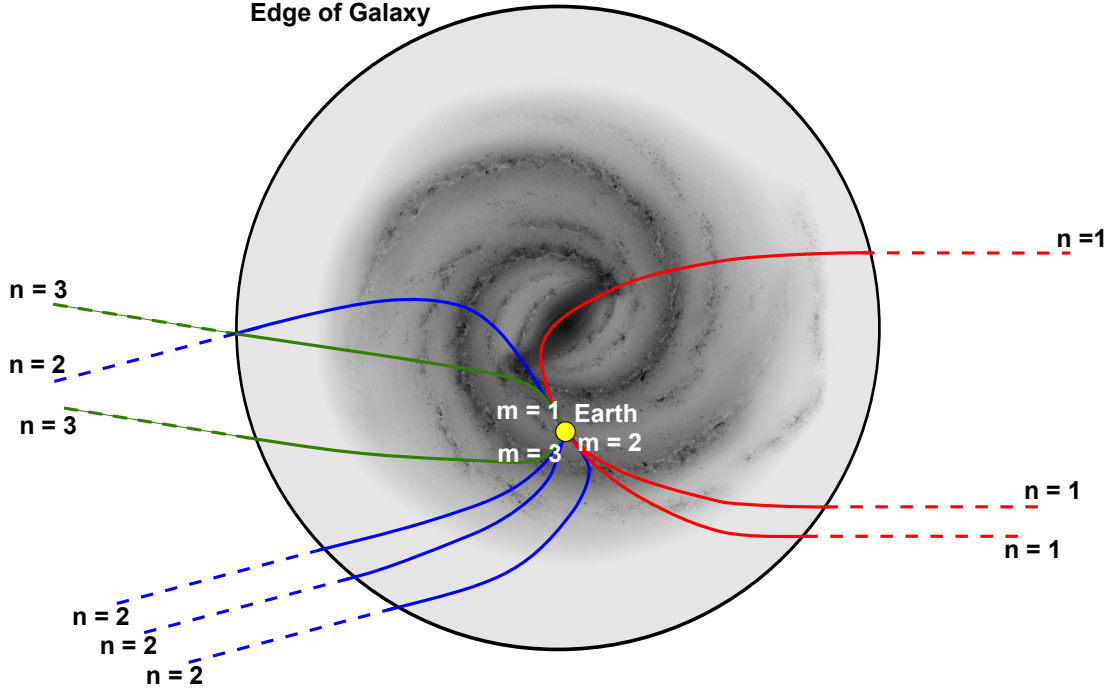
Figure 3.4: Sketch of the creation of a galactic lens from backtracking data. Cosmic rays are emitted from earth in three directions indexed with m. The directions in which the rays leave the galaxy are indexed with n.

$\vec{C}$ on the surface of the galaxy in a direction denoted with index n is at a fixed point $\vec{O}$ always observed from a direction denoted with index m.

The sources considered here are generally in a large distance compared with the size of the galaxy, which reduces the galaxy to a point in view of the source. The directions of entry n for particles with energies E_i can therefore be averaged over all points of entry $\vec{C}$. Thus a particle with energy E_i entering the galaxy from direction n can be deflected into several observed directions m. The probability of observing a particle on Earth from direction m that entered the galaxy from direction n is $l_{m,n}$. The $l_{m,n}$ form a matrix $\boldsymbol{\mathcal{L}}_i$ which represents the galactic lens for energy E_i. The magnetic lensing can thus be written as a matrix-vector equation which transforms the extragalactic probability vector $\mathbf{p}_{eg}^i$ as described in the previous subsection reading

$$\boldsymbol{\mathcal{L}}_i \cdot \mathbf{p}_{eg}^i = \mathbf{p}_{obs}^i. \tag{3.14}$$

The model for the galactic field is hence completely described by a set of matrices $\{\boldsymbol{\mathcal{L}}_1 \cdots \boldsymbol{\mathcal{L}}_N\}$ with the energy index $i = 1 \ldots N$.

Generation of the Matrices from Backtracking

The individual matrices $\boldsymbol{\mathcal{L}}_i$ can be generated by backtracking cosmic rays with isotropic starting directions from the earth with the following technique. The starting directions of backtracked particles are binned in N pixels indexed by m. The directions

in which the cosmic rays leave the galaxy are binned into N pixels indexed by n. Counting all trajectories leads to a matrix $\tilde{\mathcal{L}}_i$ with elements $\tilde{l}_{m,n}$. We normalize $\tilde{\mathcal{L}}_i$ by the maximum of unity norms $\|\tilde{\mathcal{L}}_i\|_1$ of all lenses reading

$$\mathcal{L}_i = \frac{1}{\max \|\tilde{\mathcal{L}}_i\|_1} \tilde{\mathcal{L}}_i. \tag{3.15}$$

Each element $l_{m,n}$ of $\mathcal{L}_i$ is the probability that a particle entering the galaxy in pixel n is observed in direction m.

For three directions and nine backtracked particles the procedure is illustrated in figure 3.4. The resulting matrices are

$$\tilde{\mathcal{L}} = \left. \right|_m \left(\overset{\displaystyle \overrightarrow{n}}{\begin{matrix} 1 & 1 & 1 \\ 2 & 1 & 0 \\ 0 & 2 & 1 \end{matrix}} \right) \quad \text{and} \quad \mathcal{L} = \begin{pmatrix} 1/4 & 1/4 & 1/4 \\ 2/4 & 1/4 & 0 \\ 0 & 2/4 & 1/4 \end{pmatrix} \tag{3.16}$$

in this example.

As a consequence of Liouville's theorem, that the phase space along trajectories that satisfy the Hamiltonian equations is constant, an isotropic distribution of cosmic rays outside the galaxy is observed as an isotropic distribution at any point of the galaxy [244–246]. This important property of the galactic field is correctly modeled by this technique, if the directions m are uniformly sampled in the backtracking, respectively the unity norm $\|.\|_1$ of all row vectors $\mathbf{l}_m$ are identical.

In general the galactic field modifies the energy spectrum of cosmic rays depending on the positions of the sources S_k as the flux from individual regions in the sky is suppressed or enhanced [244].

Uncertainty of the Matrices

Galactic lenses, generated from backtracking Monte-Carlo data in the described way, introduce an uncertainty in the observed probability distribution $\delta\mathbf{p}$. This uncertainty depends on the extragalactic model, as the density of directions, in which the backtracked cosmic rays leave the galaxy, is not constant. In directions where fewer backtracked cosmic rays leave the galaxy, the relative fluctuations between individual realizations are stronger than in denser regions. Nevertheless, to discuss the energy dependency of the uncertainty, we first assume that the uncertainty $\hat{\delta\mathbf{p}}$ on the probability distribution is isotropic reading $\hat{\delta\mathbf{p}} = \epsilon \cdot \hat{\mathbf{p}}_o$. An upper limit for ϵ on the uncertainty can be estimated, from two realizations of the matrices $\mathcal{L}_1$ and $\mathcal{L}_2$ of the same model for the magnetic field as

$$\epsilon \leq \frac{1}{2} \max_n \left(\|\delta\mathbf{L}_n\|_1 + \left| \|\mathcal{L}_1\|_1 - \|\mathcal{L}_2\|_1 \right| \right) \tag{3.17}$$

with $\delta\mathcal{L} = \mathcal{L}_1 - \mathcal{L}_2$ and $\delta\mathbf{L}_n$ n-th column vector of $\delta\mathcal{L}$. The derivation of eq. 3.17 is given in appendix B; it can be easily generalized to more than two realizations of $\mathcal{L}$.

The uncertainty in the individual directions can be reduced by applying a smoothing kernel $\mathcal{G}$ reading

$$\mathcal{L} \cdot \mathcal{G} \cdot \mathbf{p}_{eg} = \mathbf{p}_{ob}. \tag{3.18}$$
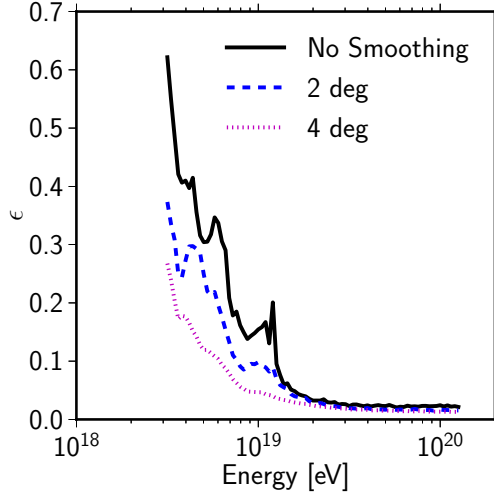
Figure 3.5: Upper limit on the uncertainties ϵ on the probability vector after transformation with the lenses depending on the energy without smoothing and after application of a 2° and 4° smoothing kernel.

We can calculate the uncertainty using the same formalism as in eq. 3.17 but substituting the matrices $\mathcal{L}_{1,2}$ with the product $\mathcal{L}_{1,2} \cdot \mathcal{G}$.

For two realizations of the BSS_S magnetic field with $1\,000\,000$ backtracked cosmic rays in every energy bin, the upper bound on the relative uncertainty calculated with eq. 3.17 depending on the energy is shown in figure 3.5 without smoothing and two different strengths of a spherical normal smoothing kernel. The maximum uncertainty decreases with increasing energy, as the strength of the deflection decreases and the simulated particles are distributed on fewer pixels. For vanishing deflections, $\epsilon \to 0$, as the matrix becomes diagonal. In this example, we found a maximum upper bound on the uncertainty of 62% for a UHECR energy of $10^{18.5}$ eV. The maximum uncertainty above energies of $10^{19.5}$ eV is less than 3%.

The uncertainty in an individual direction $\epsilon_{m,m} = \mathbf{e}_m^T \mathcal{E} \mathbf{e}_m$, defined as $\hat{\delta}\mathbf{p} = \mathcal{E} \cdot \hat{\mathbf{p}}_o$, can be estimated (see appendix B for the derivation) as

$$|\epsilon_{m,m}| \leq \frac{1}{2}\|\mathbf{e}_m^T \cdot \hat{\boldsymbol{\delta}\mathcal{L}}\|_1 = \frac{1}{2}\max_n \hat{\delta}\mathbf{l}_{\mathbf{m}}^{\mathbf{T}} \tag{3.19}$$

with m-th row vector $\hat{\delta}\mathbf{l}_m^T$ of $\hat{\mathcal{L}}$. Maps of this uncertainty are given in figure 3.6 for two different energies, each unsmoothed and after application of a 4° spherical normal smoothing kernel. The typical uncertainty $\epsilon_{m,m}$ in a pixel is about 0.6% with a maximum of 1.2% at $10^{18.5}$ eV. In particular at the lowest energies without smoothing, the structure of the final state of the backtracked particles become visible and resemble a characteristic pattern for the BSS_S field model (cf. reference [247]).
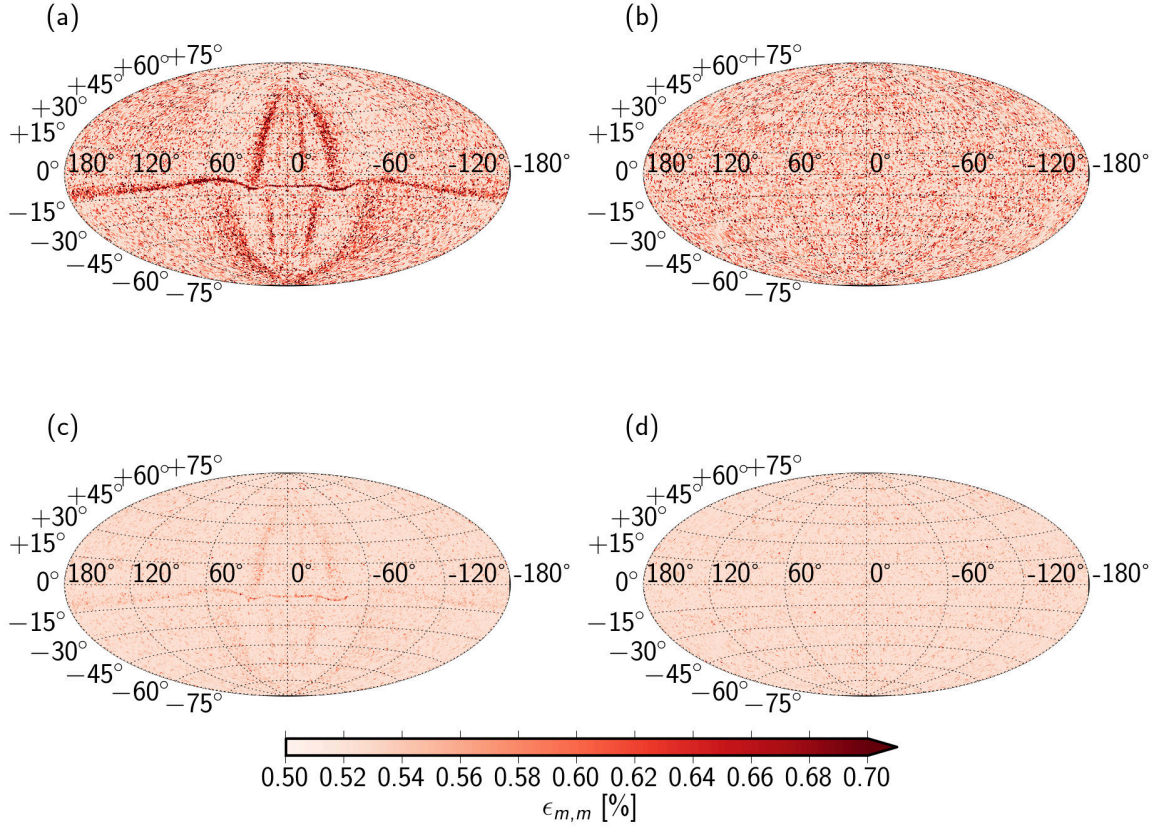
Figure 3.6: Maps of the uncertainity $\epsilon_{m,m}$. **(a)** Unsmoothed map at $E = 5\,\mathrm{EeV}$, **(b)** unsmoothed map at $E = 50\,\mathrm{EeV}$, **(c)** 4° smoothed map at $E = 5\,\mathrm{EeV}$, **(d)** 4° smoothed map at $E = 50\,\mathrm{EeV}$.

3.2 Properties of the Simulation

3.2.1 Energy spectrum

The energy spectrum of cosmic rays is a key distribution for comparisons of models with observations. From PARSEC simulations the energy spectra $dN/dE(E_i)$ are calculated using $dN/dE(E_i) = \hat{L} \cdot \|\mathbf{p}_i\|_1$ with normalization factor $\hat{L}$ representing the absolute scale to the relative luminosities L_k of the sources in eq. 3.1.

In figure 3.7 energy spectra obtained with the PARSEC program are compared with the observed energy spectra of the Pierre Auger Observatory [248] and the HiRes experiment [75]. In subfigure (a) mean and spread of the energy spectra of 50 realizations with different source positions are shown for two different injection spectra. The sources are homogeneously distributed with a density $\rho = 1 \times 10^{-5}\,\mathrm{Mpc}^{-3}$. The strength of the extragalactic magnetic field in the simulations was $B = 1\,\mathrm{nG}$; the coherence length of the magnetic field $\Lambda = 1\,\mathrm{Mpc}$. The normalization factor $\hat{L}$ has been set to match the result from the Pierre Auger Collaboration at an energy of $22\,\mathrm{EeV}$. As comparison, in subfigure (b) the spectrum calculated from simulations of an infinite
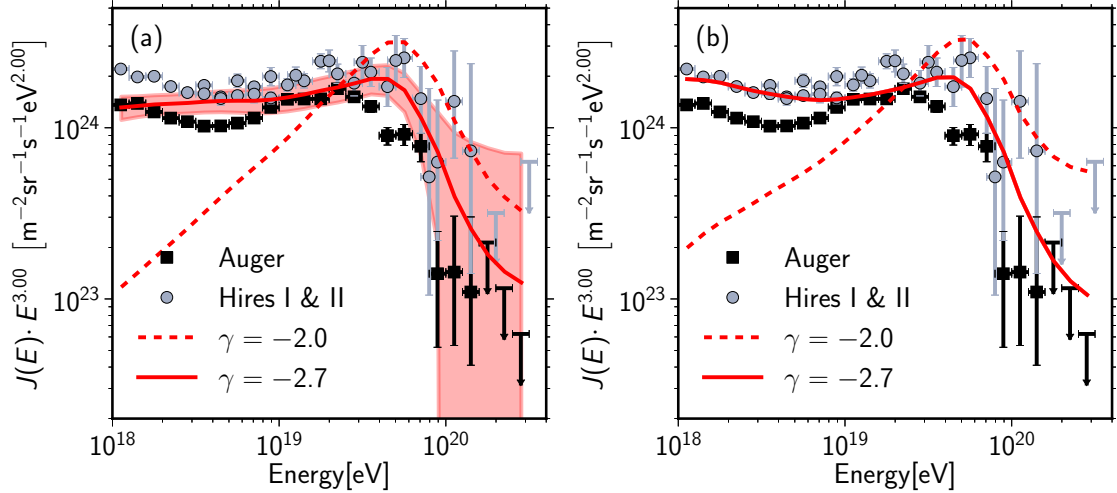
Figure 3.7: Energy spectra of UHECR generated by PARSEC and observed spectra reported by the Pierre Auger Observatory [248] and the HiRes experiment [75]. **(a)** Obtained from simulations of sources with density $\rho = 1 \times 10^{-5}\,\mathrm{Mpc}^{-3}$, spectral indices $\gamma = -2.7$ and $\gamma = -2.0$ in an extragalactic magnetic field with $B = 1\,\mathrm{nG}$ and $\Lambda = 1\,\mathrm{Mpc}$. The shaded regions indicate the spread in the simulations for $\gamma = -2.7$. **(b)** Universal spectrum from homogeneously distributed sources.

number of homogeneously distributed sources with PARSEC is shown with the same normalization as in (a); this corresponds to the universal spectrum described in the propagation theorem (cf. section 2.4). The spectrum does not match the observations of the Pierre Auger Observatory, but is in good agreement with the HiRes results. This is a known feature of the model implemented here [249].

3.2.2 Particle Horizons

From the maximum injection energy E_{max} and the model of the energy loss, a particle horizon can be derived that corresponds to the maximum linear distance a particle can originate from. Following eq. 3.11 this horizon depends on the extragalactic magnetic field model and the observed particle energy. In figure 3.8 (a) the horizon for different field strengths is shown as a function of the energy for sources with a maximum injection energy of $E_{\mathrm{max}} = 5 \times 10^{21}\,\mathrm{eV}$. Distances are given in comoving coordinates.

The horizon for cosmic rays with energies below approx. $100\,\mathrm{EeV}$ depends on the model for the extragalactic field due to the elongation of the trajectories by deflections in the extragalactic fields. In contrast to a horizon defined as the distance in which a given fraction of UHECR above a threshold energy is produced, a horizon as defined above does not decrease for lower energies in case of zero magnetic field. The displayed decrease of the horizon for low energies in case of non-zero magnetic fields is
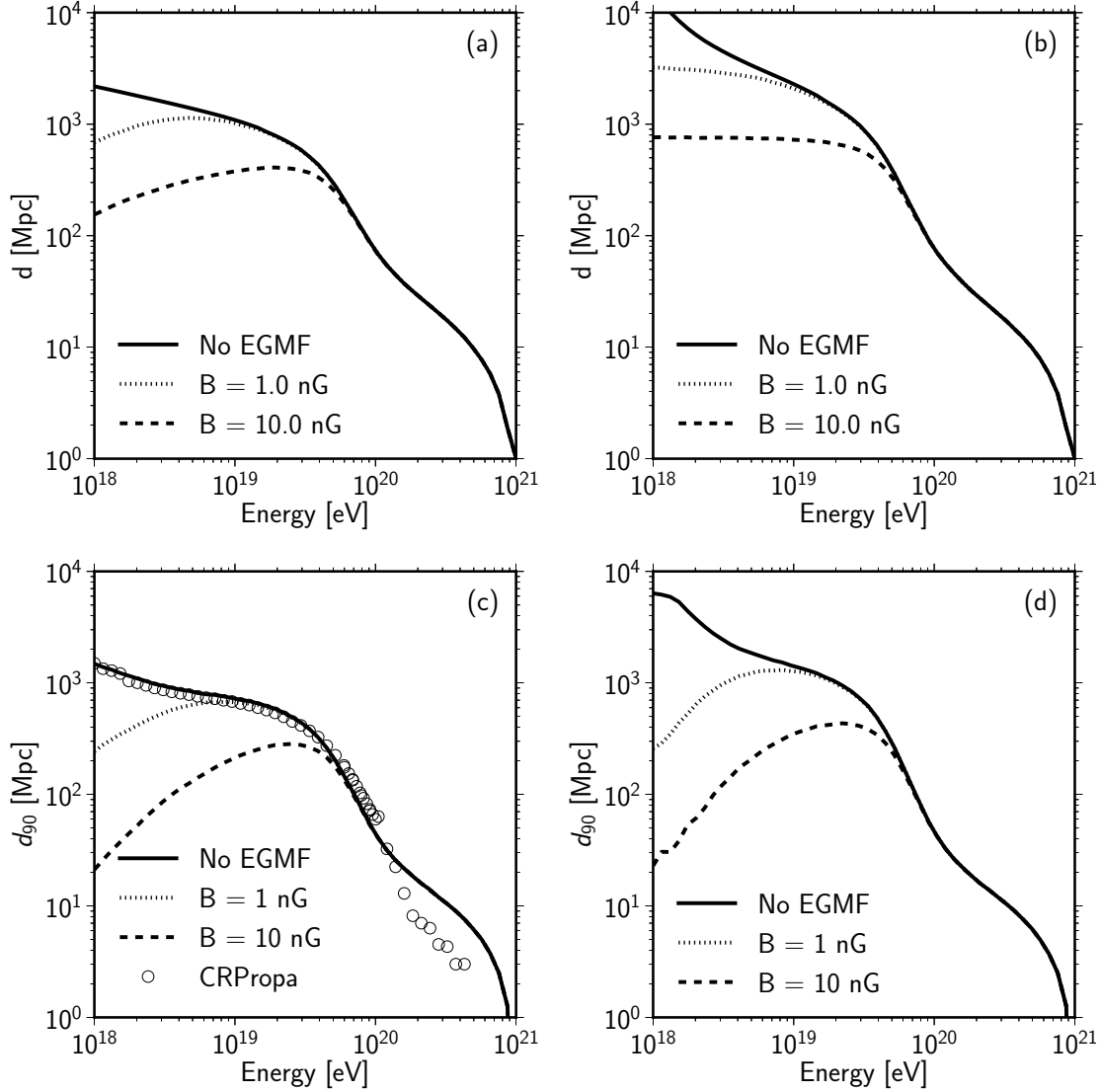
Figure 3.8: Particle horizon for protons calculated with PARSEC with different strength of the EGMF B depending on the observed energy E for sources with a maximum energy $E_{\max} = 5 \times 10^{21}$ eV. **(a)** Maximum horizon d from continuous energy loss approximation, including cosmological effects; **(b)** As (a) but without cosmological effects; **(c)** Linear distance d_{90} from within 90% of the flux originates, including cosmological effects; **(d)** As (c) but without cosmological effects.

a consequence of the decreasing energy loss length with increasing z and the elongation of the propagation time due to deflections in the magnetic fields. The horizon without inclusion of cosmological effects is displayed in figure 3.8 (b).

In figure 3.8 (c,d) the equivalent plots for a horizon d_{90}, defined as linear distance from within 90% of the UHECR flux originates from, are displayed. Between 60 EeV and 130 EeV the horizons calculated with PARSEC are up to $\approx 30\%$ lower than

the result obtained from simulations with CRPropa. This is a known feature of the continuous energy loss approximation [250].

3.2.3 Mean Deflection in Magnetic Fields

The mean deflection in the extragalactic magnetic field can be calculated for the parameters of the magnetic field and source model using eq. 3.9. The mean deflections $\bar{\Theta}$ in the galactic field can be directly calculated from the lens $\mathcal{L}_i$ as

$$\bar{\Theta} \propto \sum_n \sum_m l_{m,n} \arccos{(\vec{e}_m \cdot \vec{e}_n)} \tag{3.20}$$

with $\vec{e}_n, \vec{e}_m$ being the unit vectors in the direction of pixel m, respectively n. In general the mean deflection in the galactic field depends on the source configuration because of the suppression of individual regions by the galactic lens and the direction-dependent deflection patterns. To get a mean deflection that is independent of the source configuration, we independently normalized every column n of $\mathcal{L}_i$ for the calculation of the mean deflection so that $\|(\mathcal{L}_i)_n\|_1 = 1$.

In figure 3.9 (a) the mean deflection of protons from a source at 10 Mpc distance in extragalactic magnetic fields with three different strengths and a coherence length $\Lambda = 1$ Mpc are shown as a function of the energy as calculated from eq. 3.9 and eq. 3.6. A mean deflection of 90° corresponds to an isotropic arrival distribution of the UHECR. In figure 3.9 (b) the mean deflection from lenses for the JF Model [237] and the BSS_S model [80, 232] of the galactic field are displayed. For the BSS_S
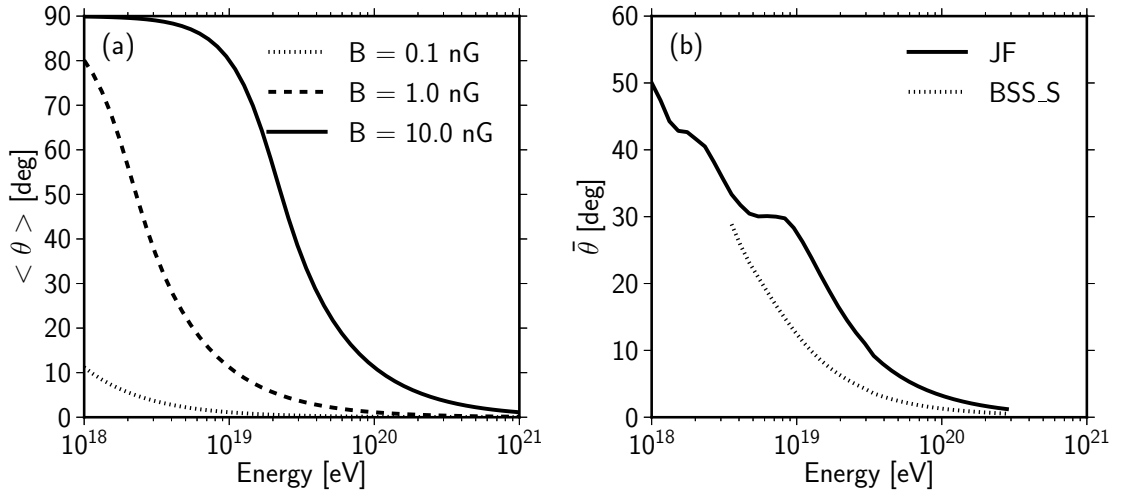
Figure 3.9: Mean deflection of protons in **(a)** turbulent extragalactic magnetic fields with $\Lambda = 1$ Mpc from a source in distance $D = 10$ Mpc and **(b)** BSS_S [80, 232] and JF [237] model for the galactic magnetic field.

model a field normalization of $B_0 = 0.48\,\mu G$ and scale heights of $z_1 = 0.95\,kpc$ and $z_2 = 40.0\,kpc$ were chosen.

3.2.4 Simulation Example

Probability Maps of VCV Sources

To demonstrate the capabilities of PARSEC we generated a simulation as example with source positions taken from the 12th edition of the catalogue of quasars and active galactic nuclei (AGN) by Véron-Cetty and Véron [251]. Every AGN of the catalogue up to a distance of 1000 Mpc has been considered. For the extragalactic field we chose a field strength $B = 3$ nG and a correlation length of $\Lambda = 1$ Mpc. The resulting probability maps from the extragalactic propagation $\mathbf{p}_{eg}^i$ are shown in the top row of figure 3.10 for the two different energies $E_1 = 5$ EeV (figure 3.10 (a) and $E_2 = 75$ EeV (figure 3.10 (b)).
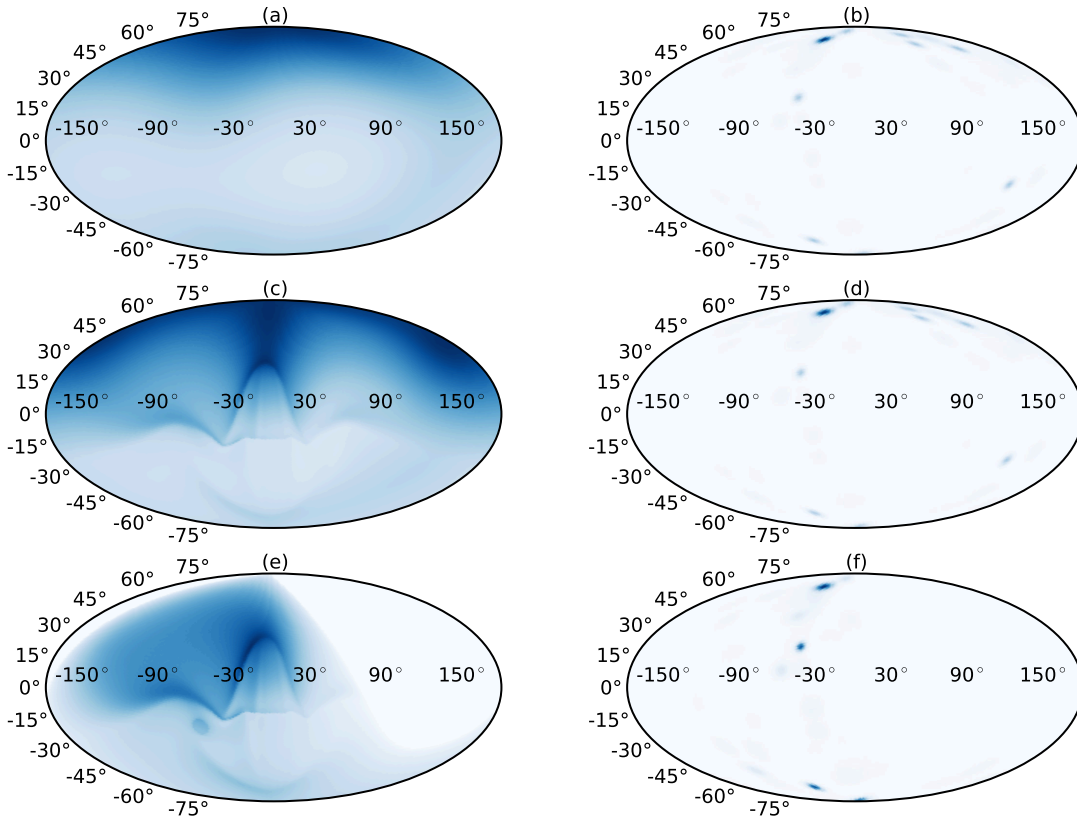
Figure 3.10: Hammer projected probability density maps for an observed energy of $E = 5\,EeV$ (left column) and $E = 75\,EeV$ (right column) in galactic coordinates. Blue indicates higher, white lower probability on an arbitrary scale. From top to bottom the panels show: Probability density before applying the galactic lens (a,b), probability density after application of the galactic lens (c,d), probability density after application of a typical detector acceptance (e,f).

The second row of figure 3.10 (c,d) displays the same probability maps after application of the galactic lenses for a BSS_S model of the galactic field with a normalization of $B_0 = 0.48\,\mu G$ and scale heights of $z_1 = 0.95\,kpc$ and $z_2 = 4.0\,kpc$. The lenses have been created by backtracking 10^6 protons with the CRT program [53] for 100 log-linear spaced mono-energetic simulations from $10^{18.5}$ eV to $10^{20.5}$ eV. The lenses and probability vectors have been discretized into 49 152 equal area pixels following the scheme presented in [241].

The third row of figure 3.10 (e,f) shows the probability map after application of a purely geometric detector acceptance of a typical earth-bound observatory [252].

Map of UHECR from Isotropic Point Sources

In figure 3.11 sky maps of 10 000 UHECR protons generated in simulations with homogeneously distributed point sources are shown. The left panel shows a simulation with a source density $\rho = 1 \times 10^{-5}\,Mpc^{-3}$ and strength of the extragalactic magnetic field $B = 0.1\,nG$; the right panel a simulation with source density $\rho = 1 \times 10^{-4}\,Mpc^{-3}$ and strength of the extragalactic magnetic field $B = 5\,nG$.

The closest source in both simulations is in a distance of 8.5 Mpc at galactic coordinates $(l = 81°, b = 27°)$. In this simulation it is identifiable by eye via the clustering of
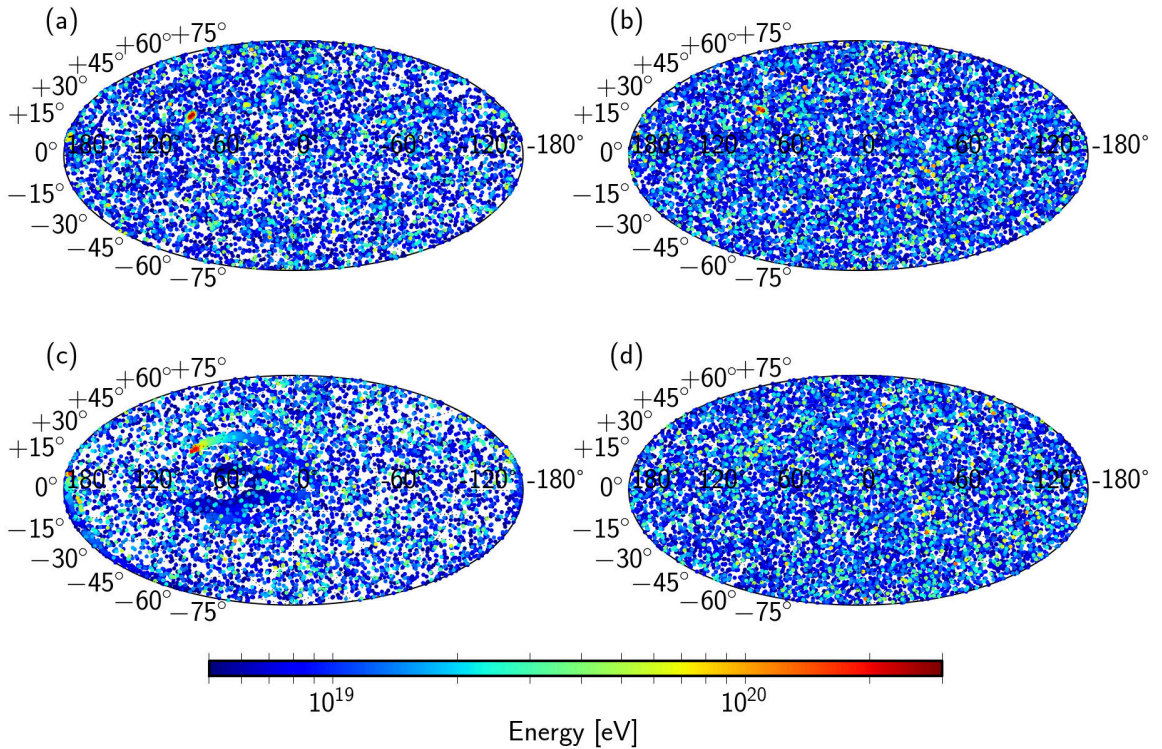
Figure 3.11: Sky Maps of simulated UHECR in galactic coordinates. **(a)** $\rho = 1 \times 10^{-5}\,Mpc^{-3}$ and $B = 0.1\,nG$ without galactic magnetic field, **(b)** $\rho = 1 \times 10^{-4}\,Mpc^{-3}$ and $B = 5\,nG$ without galactic magnetic field, **(c)** as in (a) but with JF galactic magnetic field, and **(d)** as in (b) but with JF galactic magnetic field. The sources in (a,c) are a subset of the sources in (b,d).

events with high energies.

Deflection patterns arising from the galactic magnetic fields are exemplified by comparison of (a,b) and (c,d). In particular, a 'tail' and multiple extended images at low energies are created from the closest source in (c). The structures are degenerated in (d) because of the weaker extragalactic anisotropy. Patterns from deflections are in (d) only hardly visible by eye. Suitable observables are therefore needed to find and characterize these patterns.

4 The Principal Axes of the Directional Energy Distribution

The energy-dependent patterns arising from deflection in cosmic magnetic fields can be abstracted as symmetric 'blurring' from multiple scattering in turbulent fields and threadlike structures from deflection in coherent fields. Both effects have been investigated in prior studies. In particular a search for linear structures of events with increasing energies, so called 'multiplets' [33], and an analysis of energy-energy correlations [102] are sensitive to individual aspects of the patterns, but neither study found significant structures in the directional energy distribution of UHECR.

Here we characterize the directional energy distribution by the collimation of energy along the principal axes of the distribution in a localized region in the sky. The method is sensitive to both aspects of the expected deflection patterns and thus provides a consistent description of both types of energy dependent deflection patterns.

4.1 The Thrust Observables

Definition

To derive the principal axes and quantify the collimation of energy along these axes, we use here the 'thrust observables' that were first used in high energy physics to characterize the energy distribution in particle collisions [253]. The expectation values of the thrust observables in a particle collision can be calculated from perturbative QCD [254], allowing a measurement of the strong coupling constant α_S.

The three thrust observables $T_{k=1,2,3}$ quantify the strength of the collimation of the particle momenta along each of the three axes $\vec{n}_{k=1,2,3}$ of the principal system. The principal axes and the corresponding observables T_k are successively determined by maximizing T_k with respect to the axis $\vec{n}_k$ using

$$T_k = \max_{\vec{n}_k} \left(\frac{\sum_i |\vec{p}_i \vec{n}_k|}{\sum_i |\vec{p}_i|} \right) \tag{4.1}$$

with $\vec{p}_i$ being the momentum of the individual particles. For $k = 1$ the quantity T_1 is called 'thrust' and consequently the first axis of the principal system $\vec{n}_1$ is called 'thrust axis'. For the second axis the additional side condition $\vec{n}_1 \perp \vec{n}_2$ is used in eq. 4.1. The resulting value T_2 is denoted as 'thrust major', the axis as 'thrust major axis'. Finally, the third quantity T_3 is called 'thrust minor' with corresponding 'thrust minor axis'. For the thrust minor axis $\vec{n}_3$ it is $\vec{n}_1 \perp \vec{n}_2 \perp \vec{n}_3$ which renders the maximization in eq. 4.1 trivial.
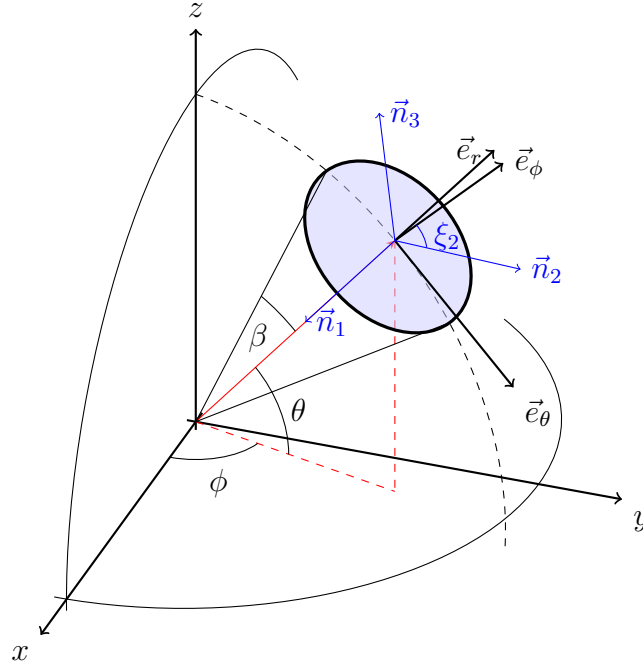
Figure 4.1: Sketch of the geometry of a region of interest (blue shaded area) in spherical coordinates. The thrust axes $\vec{n}_{1,2,3}$ are defined in the local spherical coordinate system $(\vec{e}_r, \vec{e}_\phi, \vec{e}_\theta)$. Here $\vec{n}_1$ points from the center of the ROI to the origin.

Interpretation of Axes

To use this observables in astroparticle physics, we calculate them from the momenta $\vec{p}_i$ of all events in a bounded region of the sky, further on denoted as region of interest (ROI). A sketch of the geometry of a ROI in the spherical coordinate system with corresponding definitions of vectors and angles is given in figure 4.1.

A schematic distribution of cosmic rays inside such a region resulting from coherent and turbulent deflections with the successively derived thrust axis is shown in figure 4.2. As all observed cosmic rays approach the observer centered in the coordinate system, the thrust axis points to the barycenter of the energy distribution in this region (figure 4.2 (a)).

The thrust axis is anti-parallel to the radial unit vector $\vec{e}_r$ pointing to the local barycenter of the energy distribution. The thrust major and thrust minor axis can therefore be written as linear combinations of the unit vectors $\vec{e}_\phi$ and $\vec{e}_\theta$ reading

$$\vec{n}_{2,3} = \cos \xi_{2,3} \cdot \vec{e}_\phi + \sin \xi_{2,3} \cdot \vec{e}_\theta \tag{4.2}$$

with $\xi_3 = 90° + \xi_2$. Using this together with eq. 4.1, T_2 becomes maximal if $\vec{n}_2$ is aligned to a linear distribution of UHECR. The thrust major axis thus points along threadlike structures in the energy distribution of UHECR as illustrated in figure 4.2 (b).

As the thrust minor axis $\vec{n}_3$ is chosen perpendicular to $\vec{n}_1$ and $\vec{n}_2$ it has no physical meaning beyond its connection to the thrust major axis (figure 4.2 (c)). The thrust major (minor) value is invariant under rotation of the thrust major (minor) axis by
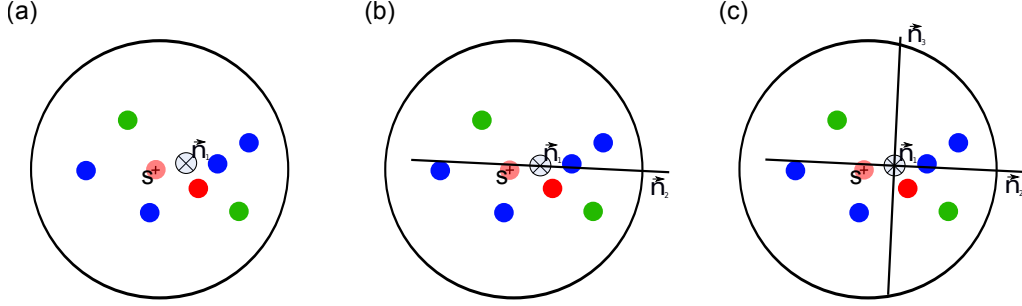
Figure 4.2: Successive calculation of the thrust observables $T_{1,2,3}$ and axes $\vec{n}_{1,2,3}$ in three steps (a–c). Dots mark arrival directions of UHECR with energy denoted by the color.

180°; the pointing of the axes is only introduced by convention and thus omitted in figures 4.2 and in the following.

Expectation Values

The thrust value is a measure for the energy-weighted strength of clustering of the events in this region. For no dispersion of the particles in the region it is $T_1 = 1$. For an isotropic distribution of an infinite number of particles with arbitrary energy spectrum in a circular region of size β, the thrust axis is anti-parallel to the unit vector $\vec{e}_r$ pointing to the center of the region. The expectation value $\langle \tilde{T} \rangle$, with $\vec{n}_1$ fixed to the center of the region, is calculated (see appendix C.1 for the calculation) analytically to

$$\langle \tilde{T}_1 \rangle = \frac{1}{2} \frac{\sin^2 \beta}{1 - \cos \beta}. \tag{4.3}$$

It depends only on the size of the region of interest and is in particular independent of the energy spectrum of the UHECR.

With a finite number of isotropically distributed cosmic rays, the barycenter of the distribution deviates from the center of the region by a value related to the variance of the thrust in the region (cf. appendix C.2). The variance is governed by the energy spectrum of the UHECR. An analog behavior is expected for the expectation values of the thrust major and the thrust minor, given the similarity of the equations.

4.2 Sensitivity to Typical Deflection Patterns

Toy Monte Carlo to Generate Deflection Patterns

To demonstrate the sensitivity of the observables to the expected patterns from deflections in magnetic fields, we simulate several simple scenarios of UHECR in coherent and turbulent fields. Here we model the distribution of UHECR in a region around the source as superposition of both effects. Events in this region of interest are
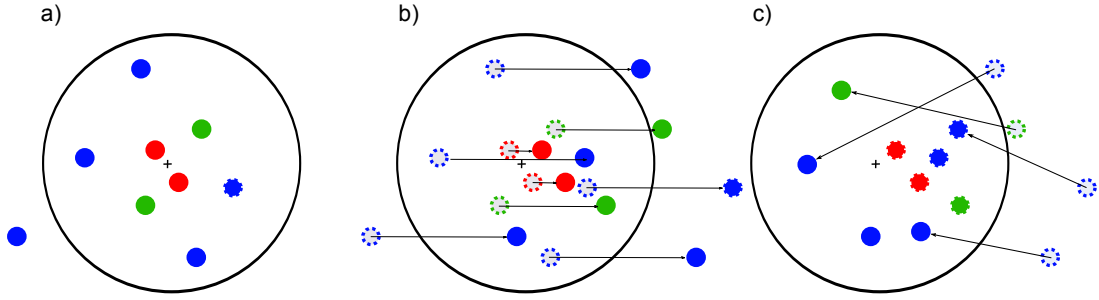
Figure 4.3: Generation of anisotropically distributed UHECR in a region of interest. **(a)** First, UHECR are distributed symmetrically around the center of the ROI using a Fisher distribution with energy dependent concentration parameter according to eq. 4.4. **(b)** The UHECR are then deflected in one direction using eq. 4.5. **(c)** UHECR deflected outside of the ROI are moved to a random position inside the region.

generated in three steps as sketched in figure 4.3. First, the UHECR are distributed around the center of the ROI following a Fisher distribution with probability density as given by eq. 3.7. The concentration parameter κ is chosen in dependence of the energy to emulate deflection in turbulent magnetic fields as

$$\kappa = C_T^{-2} E^2. \tag{4.4}$$

with deflection strength C_T summarizing the source distance and properties of the magnetic field in eq. 2.17. A value of $C_T = 1\,\mathrm{rad\,EeV}$ is equivalent to a RMS of the deflection angle $\delta_{\mathrm{RMS}} = 5.7°$ for $10\,\mathrm{EeV}$ particles. This corresponds to the expected deflection of $10\,\mathrm{EeV}$ protons from a source in distance $D \approx 16\,\mathrm{Mpc}$ propagating through a turbulent magnetic field with coherence length $\Lambda \approx 1\,\mathrm{Mpc}$ and strength $B \approx 4\,\mathrm{nG}$.

Second, in a simple model for the deflection in coherent magnetic fields the UHECR are 'shifted' by an energy dependent angle as illustrated in figure 4.3 (b). Here, the arrival direction is rotated around an axes perpendicular to the center of the region of interest using the relationship in eq. 4.4. The angle of the rotation α depends on the energy of the particles with

$$\alpha = C_C E^{-1} \tag{4.5}$$

where the parameter C_C is used to model the strength of the coherent deflection.

Third, particles deflected outside the region of interest are added as isotropic background to keep the number of particles in this setup constant (cf. fig. 4.3 (c)).

Behavior of the Thrust Observables

With this toy MC, we generated 100 ROI of size $\beta = 0.25\,\mathrm{rad}$ with 300 UHECR each for several choices of $C_T = 0.1\text{-}10\,\mathrm{rad\,EeV}$ and $C_C = 0\,\mathrm{rad\,EeV}$, i.e. no coherent deflection, $C_C = 0.5\,\mathrm{rad\,EeV}$, and $C_C = 1.0\,\mathrm{rad\,EeV}$. The mean and spread of the thrust observables $T_{1,2,3}$ are shown depending on C_T in figure 4.4 (a–c).
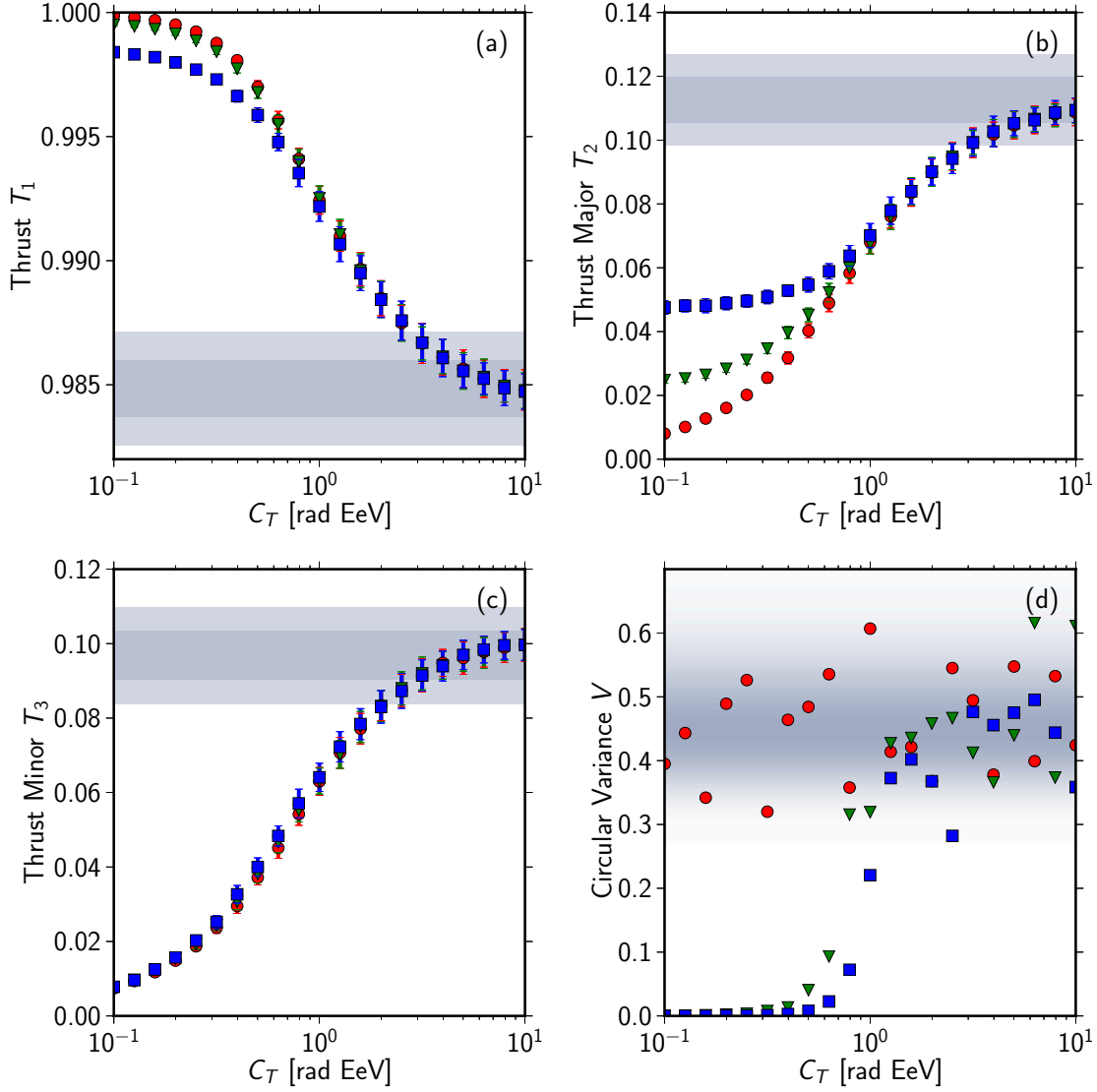
Figure 4.4: Response of the thrust observables to the toy MC. **(a–c)** Mean and spread of the observables $T_{1,2,3}$ as a function of the strength of the deflection in turbulent magnetic fields C_T. Red circles correspond to no directed deflection, green triangles to $C_C = 0.5\,\mathrm{rad\,EeV}$ and blue squares to $C_C = 1.0\,\mathrm{rad\,EeV}$. Shaded areas correspond to the 1σ and 2σ expectation of the observables for an isotropic distribution of cosmic rays. **(d)** Circular variance of the thrust major axis calculated with the toy MC in 100 ROI. Gray shading corresponds to the probability density of the expectation value of the circular variance of uniform distributed directions.

All three observables are sensitive to a symmetric blurring of the source, with expectation values of the observables for an isotropic distribution of UHECR depending approximately only on the angular size β of the ROI. For increasing C_T the distribution of cosmic rays in the ROI becomes isotropic, and the observables approach the expectation value for an isotropic distribution. The expectation value of the thrust major and thrust minor is below the isotropic expectation, as the toy model contains no background and the particles are thus concentrated in the center of the ROI. The thrust minor, displayed in figure 4.4 (c), does not depend on the strength of coherent deflection, as the width of the blurring is determined here only by the strength of C_T.

The thrust major axes points parallel to the direction of the coherent deflection, if the strength of the blurring is not too strong. We quantify the concentration of the directions by the variability among the axes using the circular variance V derived in the specialized statistics for directional data (e.g. [255, 256]). The direction of the thrust major axis $\vec{n}_2^{\,i}$ in a region of interest i is defined by the angle θ_i of the axes to the local unit vector $\vec{e_\phi}$ in spherical coordinates with $\theta_i \in [0 \cdots \pi)$. To calculate the circular variance V from the n observations θ_i on a periodic interval $\theta_i \in [0 \cdots \frac{2\pi}{l}]$, first the θ_i are transformed to angles on the full-circle by $\theta_i^* = l \cdot \theta_i$. For the thrust major axis thus $l = 2$.

With

$$C = \sum_{i=1}^{n} \cos \theta_i^*, \qquad S = \sum_{i=1}^{n} \sin \theta_i^* \tag{4.6}$$

the resultant length R is then defined as

$$R = \sqrt{C^2 + S^2}. \tag{4.7}$$

Based on the resultant length R in eq. 4.7 the circular variance V of a sample of size n is defined as

$$V = 1 - \left(\frac{R}{n}\right)^{1/l^2}. \tag{4.8}$$

In contrast to the variance in linear statistics, the circular variance V is limited to the interval $[0 \ldots 1]$. It is a consistent measure for the concentration of observations θ_i on periodic intervals with $V = 0$ for data from a single direction and $V = 1$ for perfectly dispersed data. For a limited set of random directions, both cases $V = 0$ and $V = 1$ are unlikely. The expectation value of V depends on the number of observations.

For the 100 simulations of the toy MC, the circular variance among the axes of the simulated ROI is shown in figure 4.4 (d). Gray shading denotes the probability distribution for V of 100 uncorrelated directions. In case of zero coherent deflection, and also in case of strong blurring of the sources, no stable axes is found. For small blurring of the sources, zero variance among the directions indicates the alignment of the thrust axis with the direction of deflection.

Here we have demonstrated, that the thrust observables $T_{1,2,3}$ and in particular the thrust major axis $\vec{n}_2$ are sensitive to the deflection patterns simulated in this toy model. In the next sections, we further develop an analysis based on this observables using the simulation software discussed in chapter 3.

4.3 Sensitivity in Propagation Simulations

To test the response of the observables in a more realistic scenario, we generated an example scenario using the PARSEC software described in chapter 3. We simulated 20 000 UHECR protons from homogeneously distributed point sources with a density $1 \times 10^{-5} \,\mathrm{Mpc}^{-3}$ in simulations with two strengths of the extragalactic magnetic field $B = 0.1 \,\mathrm{nG}$ and $B = 5 \,\mathrm{nG}$. The galactic magnetic field is modeled using a lens for the regular component of the JF2012 [237] magnetic field. The position of the sources is identical in both simulations. All sources are simulated with equal luminosity, a power law spectrum with spectral index $\gamma = -2.7$, and a maximum energy of $1000 \,\mathrm{EeV}$. Regions of interest with a size $\beta = 0.25 \,\mathrm{rad}$ are set to the closest 50 sources in the simulations .

In figure 4.5 the region around the closest source in the simulations is shown. A magenta star marks the direction of the thrust axis and a black line denotes the direction of the thrust major axis. For the weak extragalactic magnetic field shown in figure 4.5 (a), a tail of UHECR from the source resulting from coherent deflection is visible. The thrust major axis points along this structure. Because of the stronger deflections in the extragalactic magnetic field, the structure is not visible by eye in figure 4.5 (b). Nevertheless, the thrust major axis points in a similar direction in this example, indicating the preferred direction of deflection in the magnetic field. The values of thrust observable T_1 calculated in both cases deviates from the isotropic
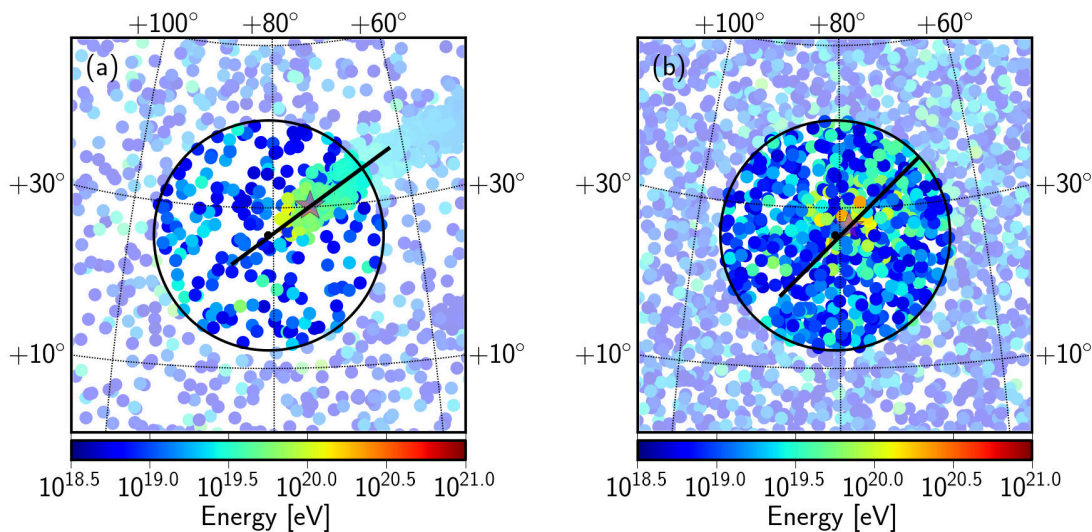
Figure 4.5: Region of interest around the closest source in two simulations with different strength of the EGMF $B = 0.1 \,\mathrm{nG}$ (left panel) and $B = 5 \,\mathrm{nG}$ (right panel). Colored dots denote arrival direction and energy of the UHECR. Source position, source density, and galactic magnetic field model are identical in both simulations. The thrust axis in the regions is denoted by a magenta star; the thrust major axis in this region is denoted by a black line.
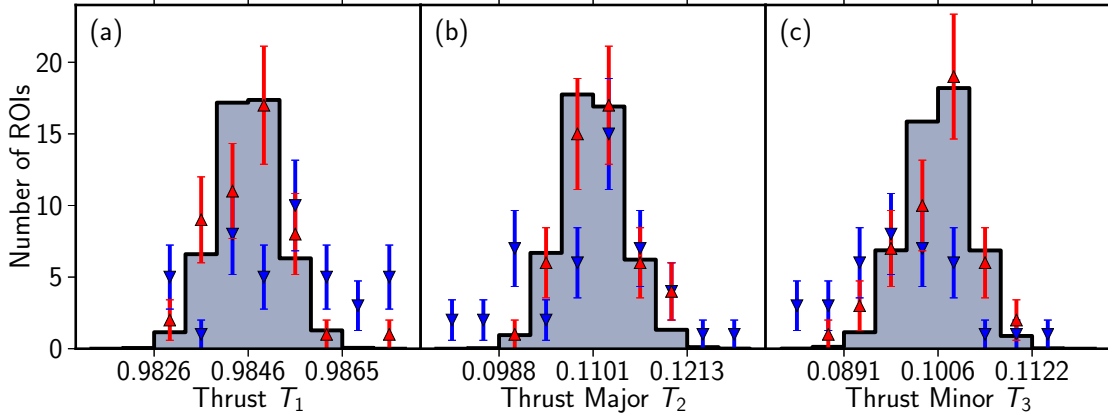
Figure 4.6: Mean distribution of observables $T_{1,2,3}$ in the example scenario with $B = 0.1\,\mathrm{nG}$ (blue downward triangles), and $B = 5\,\mathrm{nG}$ (red upward triangles). The gray histogram corresponds to the average of the observables from 100 simulations with isotropically distributed UHECR.

expectations by more than three times the spread of the corresponding isotropic distribution.

In figure 4.6 the distribution of the observables $T_{1,2,3}$ of the two simulations above are show together with the mean of 100 simulations with isotropically distributed UHECR. For weak extragalactic magnetic fields, the distribution for $T_{1,2,3}$ deviate considerably in several ROI from the expectation for isotropically distributed UHECR. For $B = 5\,\mathrm{nG}$, in this example only the thrust of a single ROI deviate from the isotropic expectation. Additional probability distribution of the observables $T_{1,2,3}$ for several values of B and ρ are given in appendix D.

The thrust observables remain their sensitivity in simulations that model all known effects relevant to UHECR propagation. With increasing number of sources and increasing strength of the deflection in extragalactic magnetic fields, the number of exceptional regions and the strength of the deviation of the observables from the expectation for isotropically distributed UHECR is reduced. However, before applying the method to observational data, the choice of the values for the free parameters in the analysis have to be optimized.

4.4 Optimization of Free Parameters

In the previous two sections, we calculated the observables in regions centered to the sources of UHECR. As the sources of UHECR are, however, yet unknown, this is not possible in the analysis of measured data. Instead, we could analyze regions around source candidates based on catalogues of astronomical objects or scan the entire sky. However, if an astronomical catalogue is used, the incompleteness and the selection bias of the catalogue has to be accounted for in the analysis. Furthermore, this allows only

to test a single or few assumption on the source candidates, as with increasing number of repetitions of the analysis, the significance of a deviation from the null-hypothesis in a single analysis is reduced. In a scan of the entire sky, no additional assumptions are included, but as we expect no deviations from an isotropic distribution of UHECR in most parts of the sky, a scan introduces a high number of ROI that are compatible with the null hypothesis in the analysis.

To avoid extrinsic assumptions in the analysis and simultaneously maximize the power to discriminate between isotropic and anisotropic UHECR distributions, we choose regions around the highest energetic events in the analysis. By this we assume, that these events are least deflected from their sources and thus are tracers of interesting regions in the sky. Events that 'seeded' a ROI are removed from the analysis in this ROI to avoid a possible bias by including a single high energetic event exactly in the center of the region; the seed-particles are included in the analysis of other ROI they participate in.

With this selection of ROI, the analysis has three free parameters:

1. The minimum energy of the seed particle E_{seed} used to define a region of interest,

2. The size of the regions of interest β,

3. The minimum energy E_{min} of particles included in the calculation of T_k in eq. 4.1.

The optimal choice for these parameters is determined by maximizing the ability of this method to distinguish simulations of anisotropic cosmic ray skies from isotropic distributions using Monte Carlo simulations. As anisotropic UHECR distributions we simulated 100 data sets consisting of 10 000 UHECR each, using the PARSEC program described in chapter 3 with isotropically distributed point sources. All sources have equal luminosity, a maximum energy of 1000 EeV and a power-law energy spectrum with spectral index $\gamma = -2.7$. The source density is fixed to $\rho = 10^{-4}\,\text{Mpc}^{-3}$ and a HMR BSS_S type galactic magnetic field [80] with $1\,\mu\text{G}$ normalization is used in the simulation. For 21 values of the strength of the extragalactic field ranging from $B = 0.1\,\text{nG}$ to $B = 10\,\text{nG}$ we varied one of the three parameters in the analysis while keeping the others fixed.

We discriminate between the isotropic hypothesis as null-hypothesis $\mathcal{H}_0$ and an alternative hypothesis $\mathcal{H}_B$ given a PARSEC simulation with strength of the EGMF B as above using a likelihood-ratio test on the binned distributions of the observables 'measured' in the simulations. The probability in empty bins of the distributions is set to the inverse of the number of entries in the histogram. With $p_i^{\mathcal{H}_x}$ probability that under hypothesis $\mathcal{H}_x$ an observable T_k has a value in bin i, the likelihood to observe r_i out of N ROI in that bin given $\mathcal{H}_x$ is thus

$$\mathcal{L}_{\mathcal{H}_x} = \prod_i \binom{N}{r_i} (p_i^{\mathcal{H}_x})^{r_i} (1 - p_i^{\mathcal{H}_x})^{N-r_i}. \tag{4.9}$$

With the likelihood ratio

$$Q = -2\ln \frac{\mathcal{L}_{\mathcal{H}_1}}{\mathcal{L}_{\mathcal{H}_0}} \tag{4.10}$$
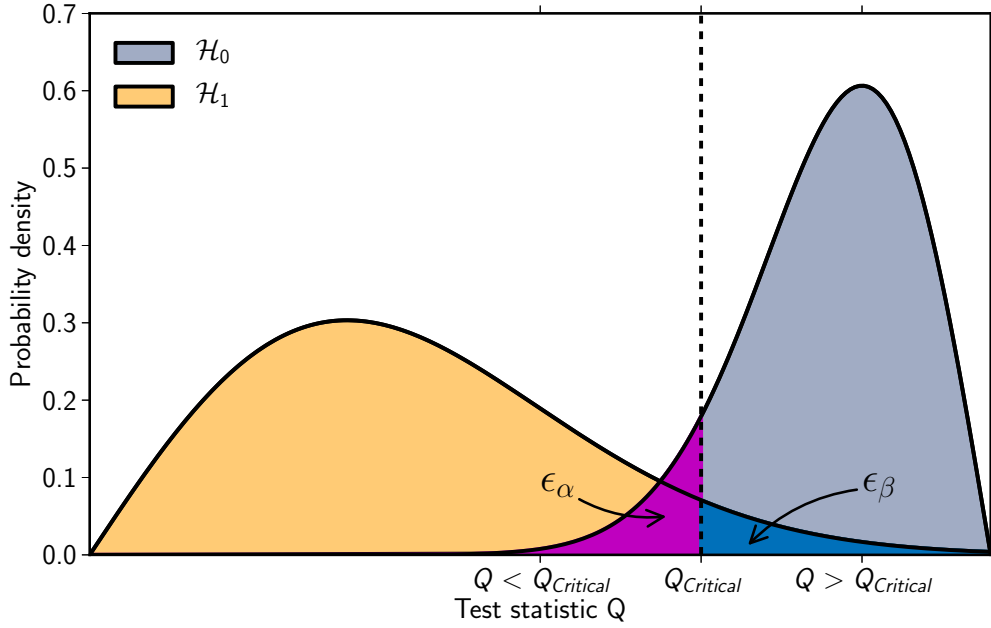
Figure 4.7: Illustration of the significance $1 - \epsilon_\alpha$, probability for an error of first kind ϵ_α, probability for an error of second kind ϵ_β, and the test power $1 - \epsilon_\beta$ given the test statistic Q for two hypothesis $\mathcal{H}_0$ and $\mathcal{H}_1$.

we refuse $\mathcal{H}_0$ at confidence level $1 - \epsilon_\alpha$ if $Q < Q_{\text{crit.}}(\epsilon_\alpha)$ with critical value $Q_{\text{crit.}}(\epsilon_\alpha)$. The statistical test power $1 - \epsilon_\beta$ at significance level $1 - \epsilon_\alpha$ is then given by the probability to correctly reject $\mathcal{H}_0$. These definitions are illustrated in figure 4.7.

The resulting test power for the scan with significance level $1 - \epsilon_\alpha = 95\%$ for each of the three observables and free parameters is show in figure 4.8. The general structure of the dependence of the test power on the free parameters is the same for all observables, allowing to choose the same value for all three observables.

The test power increases with an increasing size of the ROI. However, smaller cone sizes are preferable to increase the angular resolution. As the increase of the test power slows down above a cone size of about 0.2 rad, we choose a cone size of $\beta = 0.25$ rad.

From the second column of figure 4.8 it becomes clear that the inclusion of events with an energy as low as possible is preferable. We choose a lower energy limit of 5 EeV as UHECR with this or higher energy are expected to be of extra galactic origin.

From the third column of figure 4.8 (c,f,i) we see that the minimum energy of the seed particle for the regions of interest has only a small influence on the test power within the scanned range. We set this value to 60 EeV, which compares to the lower energy used in the AGN correlation study [97].
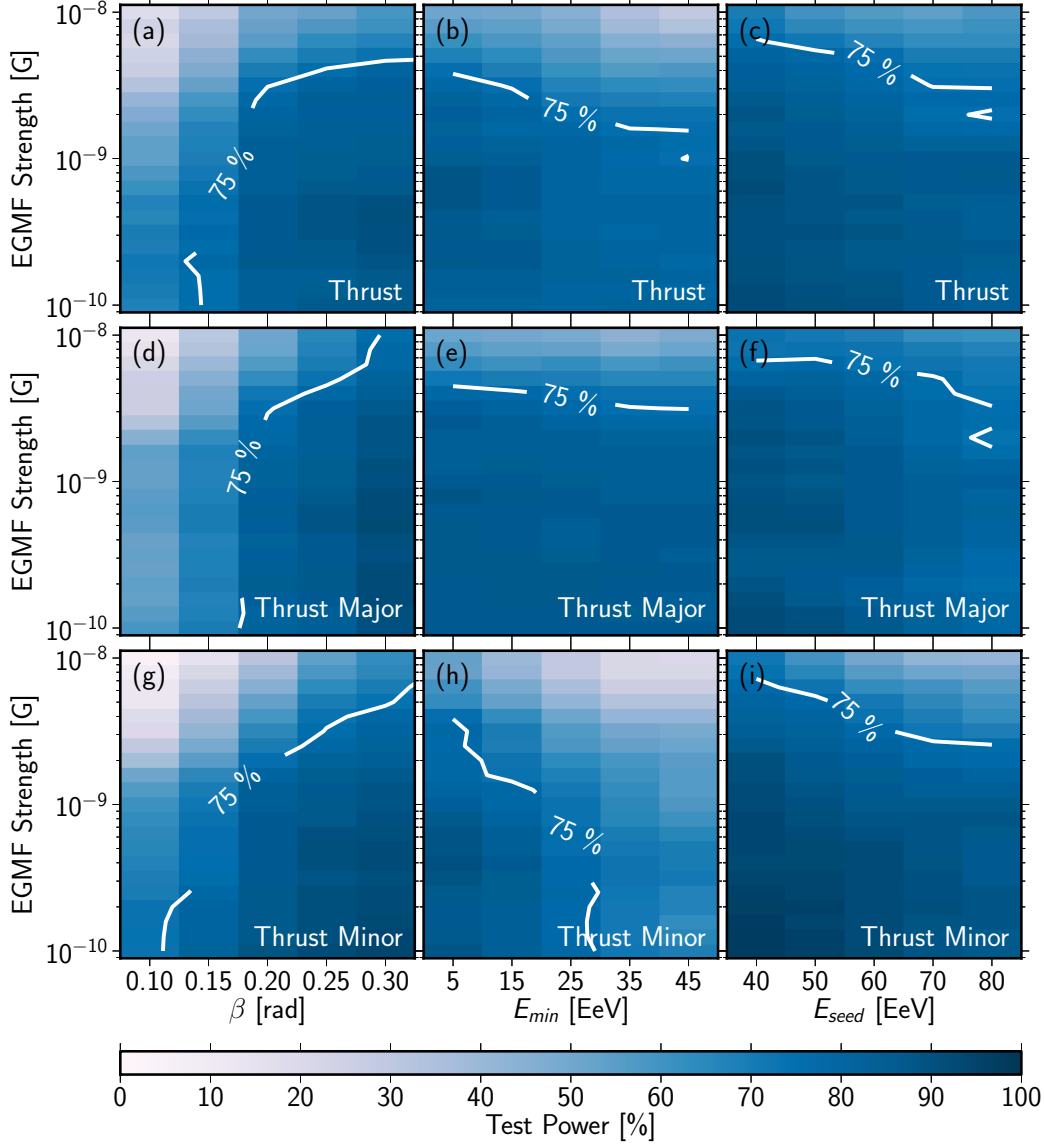
Figure 4.8: Test power using the distribution of the thrust **(a–c)**, thrust major **(d–f)** and thrust minor **(g–i)** observable for various choices of the cone radius (left column), lower energy cut (middle column) and seed energy (right column) and strength of the extragalactic magnetic field. Contour lines at 75% test power are given to guide the eye. The unmodified values are set to $\beta = 0.25\,\text{rad}$, $E_{\text{seed}} = 60\,\text{EeV}$, and $E_{\text{min}} = 5\,\text{EeV}$.

5 The Pierre Auger Observatory

The Pierre Auger Observatory [257–259] is the currently largest experiment dedicated to the investigation of the highest energetic particles. It is located in the Pampa Amarilla in the south of the Province of Mendoza in Argentina at an altitude of approximately 1300-1400 m above sea level. A map showing the location of the observatory in South America and of the observatory site is displayed in figure 5.1.

The observatory is constructed as a hybrid of two complementary detector systems. The 'surface detector' (SD) consists of more than 1600 water Cherenkov stations arranged in a hexagonal grid with 1.5 km spacing covering a total area of 3000 km². The 'fluorescence detector' (FD) is build out of 24 telescopes stationed at 4 sites surrounding the surface detector array. A photography taken at the observatory showing several detector components is printed as figure 5.2.

While the surface detector measures the secondary particles in an extensive air shower at ground level, the fluorescence detector detects the fluorescence light emitted by nitrogen molecules excited by the electrons in an extensive air shower. With an absolute calibration, the FD enables superior energy measurements compared with the
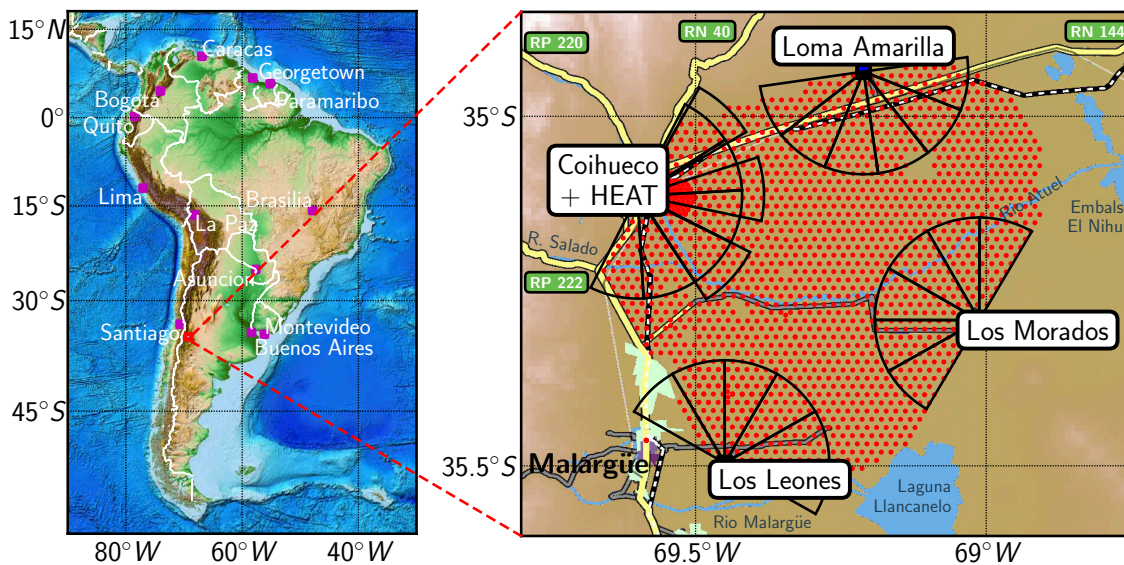
Figure 5.1: Location of the Pierre Auger Observatory near Malargüe in Argentina (left) and map of the observatory (right). Red dots denote positions of surface detector stations, black wedges the field of view of the fluorescence telescopes (map data is taken from references [260–263]; plotting routines for the Observatory is from reference [264].)
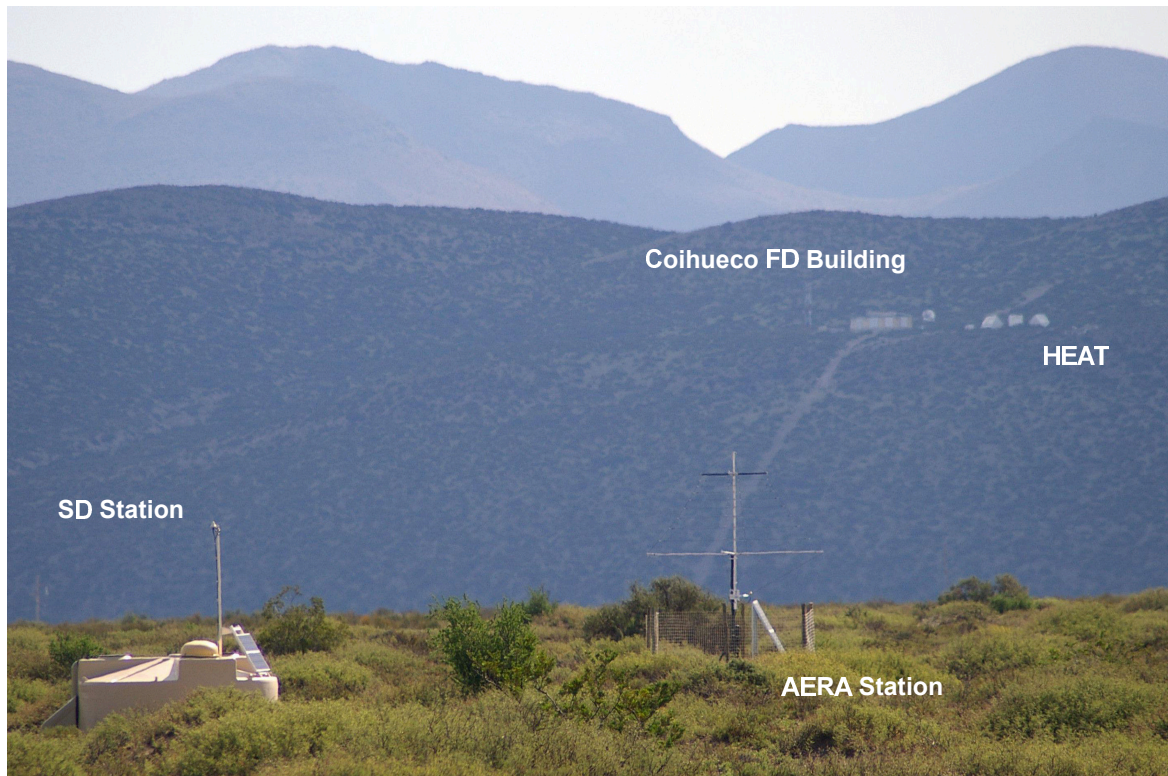
Figure 5.2: Photography taken at the Pierre Auger Observatory near Malargüe in March 2011 showing several detector components. In the front a surface detector station and an 'Black Spider' antenna [265] of the 'Auger Engineering Radio Array' (AERA) is visible. On the right side on the hill in the back the building housing the six telescopes of the Coihueco site (left) as well as the three additional 'High Elevation Telescopes' (HEAT) [266] can be seen together with equipment for atmospheric measurements.

SD. Furthermore, observation of an air shower in the FD allows for a measurement of the depth of the shower maximum X_{max} as the longitudinal shower profile is measured directly. However, it operates only in clear and moonless nights resulting in an average uptime of about 13% of the total time [259]. In contrast to the FD, the SD can operate without principle timing constraints and thus covers the sky uniformly in right ascension each day. Events reconstructed independently in both detector components, so called 'hybrid' events, are used for an energy calibration of the SD detector.

Beside those two main detector components, several additional detectors and experiments are operated by the Pierre Auger Collaboration at the Malargüe site. Some of them extend the experiment to lower energies [266, 267] to investigate models for the transition from galactic to extragalactic cosmic rays. Other extensions are to improve the determination of the composition [267] or to investigate new methods for the detection of showers (e.g. [268, 269]). In the following the two main detector components are described with emphasis on the reconstruction of the energy and direction of the cosmic rays used for the measurement described in chapter 6.

5.1 Fluorescence Detector

At each of the four sites of the fluorescence detector [259] (eyes), a building houses six telescopes. Each individual telescope has a field of view of $30° \times 30°$ so that the system of six telescopes has 180° coverage. The telescopes are separated into individual 'bays' by curtains to avoid stray light from neighboring bays. A schematic view of a telescope bay and a photograph taken inside a bay is shown in figure 5.3.

The band-width of the detector is limited to photons with wavelengths of 300-410 nm by a UV filter window. The wavelength range includes almost all of the fluorescence emission lines of nitrogen. A $13\,\text{m}^2$ segmented mirror reflects the light on a camera of 440 photo multiplier (PMT). Each of the PMT has 1.5° field of view. A 'corrector ring' at the filter window is used to get a small spot size of 15 mm respectively 0.5°, despite the large aperture of 2.2 m. With the same spot size, but without the corrector ring, the telescope would have only approximately half of the aperture.

The PMT of the camera are read out with 10 MHz frequency, which allows a spatial and temporal resolution of the light emission of the shower. The detector is triggered in three hierarchical levels. The first level is triggered if the voltage of an individual PMT excesses a moving average. The threshold voltage is continuously adjusted so that a constant trigger rate of 100 Hz per pixel is maintained. The second level trigger (SLT) selects events with 5 coincident FLT, which spatial arrangement on the camera matches 1 out of 108 patterns consistent with an air shower. A third level trigger (TLT) filters out events triggered by lightning by rejecting events based on FLT multiplicity,
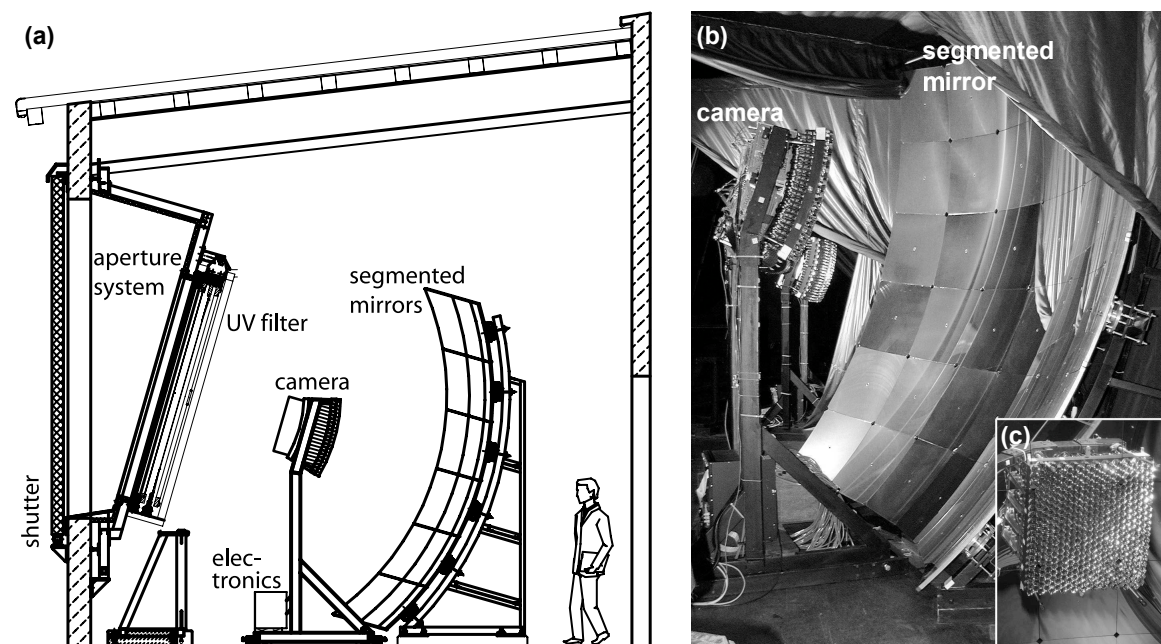
Figure 5.3: **(a)** Schematic view of a fluorescence telescope [259]. **(b)** Photography of a flourescence telescope and **(c)** close up of the reflection of the camera in the mirror [270].
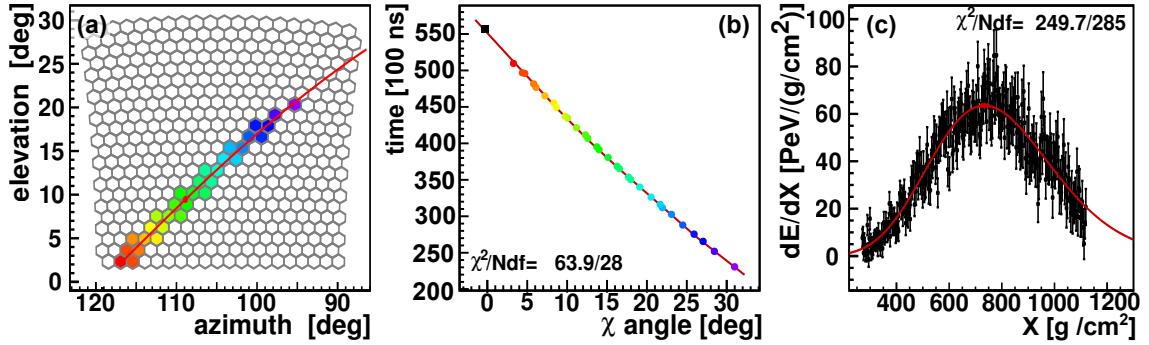
Figure 5.4: Cosmic ray induced air shower detected in a single FD telescope. **(a)** Trace of camera pixel triggered by the fluorescence light. Each hexagon corresponds to a PMT. The color of the pixel denotes the detection time of the signal; white hexagons detected no signal. The red line indicates the reconstructed shower axis. **(b)** Timing depending on the angle χ in the shower-detector plane and additional information of a SD station (black square). **(c)** Reconstructed energy deposition of the shower depending on atmospheric depth X. The red line shows the fit of a Gaisser-Hillas profile as given by eq. 5.1.

number of triggered pixels, and noise in the PMT traces.

If an event passes the TLT, the data of the camera is stored and also a 'T3-trigger' (see section 5.2) is emitted to read out the data of the surface detector. In figure 5.4 (a) the trace of a shower detected with a single camera is shown.

The geometry for the reconstruction of the shower is defined in the 'shower-detector plane' (SDP), i.e. the plane containing the shower axis as given by the triggered pixels and the center of the eye. A sketch of the geometry is given in figure 5.5. From the timing information of the individual pixels t_i, the pointing-direction of the pixels ξ_i, and the timing information of the triggered SD stations, the shower axis is reconstructed by finding the optimal angle χ_0 and distance R_p that describe the data. In figure 5.4 (b) the result of the fit for the trace in figure 5.4 (a) is displayed.

The accuracy of the geometry-reconstruction of a shower observed in only one telescope depends greatly on the arrival direction with respect to the telscopes field of view. The geometry dependency is reduced and the quality of the reconstruction is greatly improved if additional timing information from the surface detector is available. Events that are detected with the FD and also at least one station of the SD can be reconstructed with an accuracy of the shower core of 50 m and an accuracy of the direction of 0.6° [259].

With known shower geometry, the amount of fluorescence light as a function of the atmospheric depth is derived using corrections for the attenuation of the signal in air, the current weather, contributions of Cherenkov light, and multiple-scattered light. The number of emitted photons per area density and wavelength is proportional to the energy deposition per area density in the traversed material. With the corresponding proportionality factor, the 'fluorescence yield', the energy deposit depending on the atmospheric depth of the shower $\frac{dE}{dX}(X)$ is deduced (cf. section 1.1). A typical
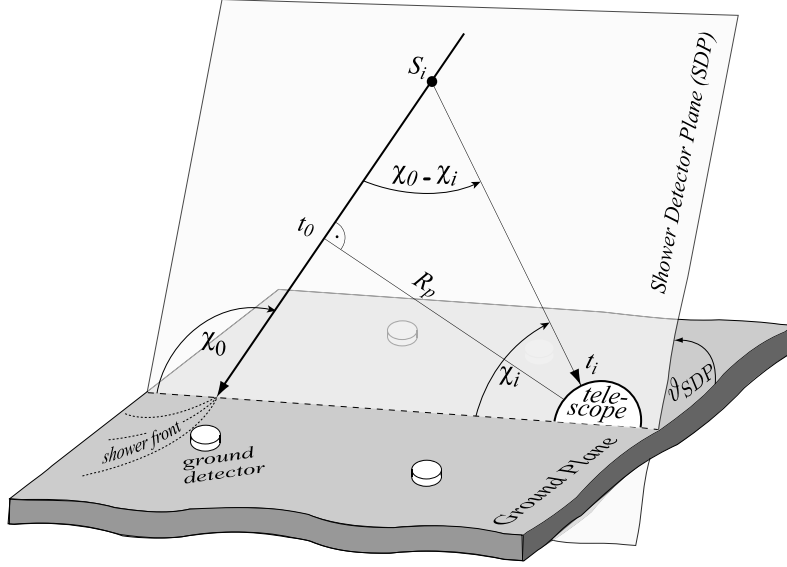
Figure 5.5: Geometry of the shower-detector plane used in the FD reconstruction (taken from reference [259], originally from reference [271]).

measurement of the energy deposit per atmospheric depth is given in figure 5.4 (c).

The energy deposit depending on the atmospheric depth in an cosmic ray induced air shower can be described by the Gaisser-Hillas function [272] reading

$$\frac{dE}{dX}(X) = \frac{dE}{dX}(X_{\max})\left(\frac{X - X_0}{X_{\max} - \lambda}\right)^{\frac{X_{\max} - \lambda}{\lambda}} \exp\left(-\frac{X - X_0}{\lambda}\right) \tag{5.1}$$

with $\lambda = 70\,\mathrm{g\,cm^{-2}}$. From a fit of eq. 5.1 to the data the calorimetric energy is derived by integration reading

$$E = \int_{-\infty}^{\infty} \frac{dE}{dX}(X)dX \tag{5.2}$$

yielding the energy of the primary particle after an correction for invisible energy. The statistical uncertainty in this measurement is less than 10%. Systematic uncertainties arise from the detector calibration, invisible energy in the shower, the reconstruction method, atmospheric effects, and in particular the fluorescence yield, which is known from laboratory experiments within 14% accuracy. All effects sum up to a total systematic uncertainty on the FD energy scale of 22% [273].

5.2 Surface Detector

The individual surface detector stations [258] consist of a robust cylindrical polyethylene tank containing $12\,\mathrm{m^3}$ of ultra pure water. The tank is lined with 'Tyvek', a special polyethylene fiber; the liner prevents the water from contamination, provides additional light shielding, and reflects Cherenkov light created by particels traversing the water to three photo multiplier tubes (PMT) mounted at the top of the station. The SD
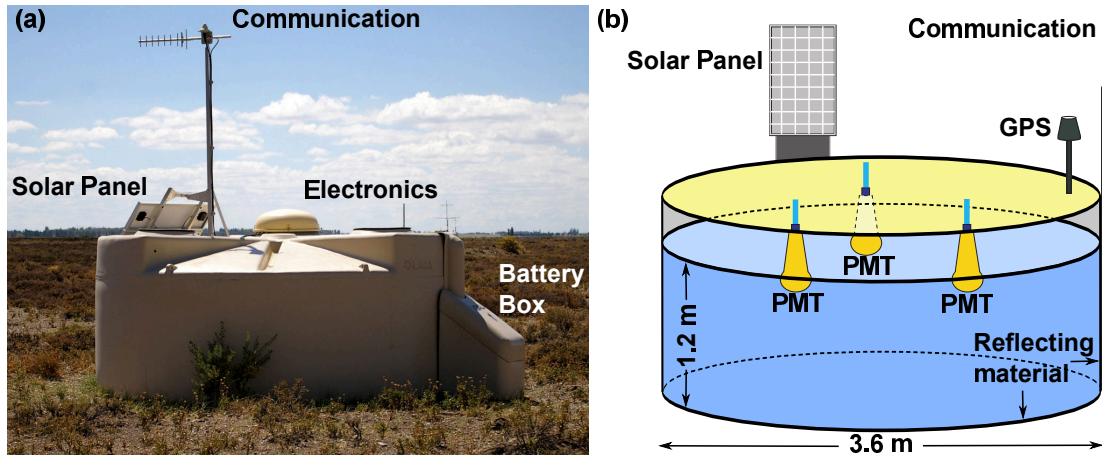
Figure 5.6: SD Detecor station. **(a)** Photography of an SD station in the Argetninian Pampa, March 2010. **(b)** Schematic of the SD station design (modified from [57]).

station is powered with two 55 W* solar panel and designed to work fully autonomous with minimum maintenance for 20 years. A photography and a schematic sketch of a SD station is shown in figure 5.6.

Data read out of the SD stations is triggered using three hierarchical levels (T1-T3) [19]. The first two levels are formed on the individual station from the amount of light detected by the PMT. The signal strength in the PMT is measured here in equivalents of the signal produced by the vertical and central passage of a single muon, abbreviated as 'vertical-equivalent muon' (VEM) [274].

A T1 can be formed from two independent conditions, corresponding to the muonic and electromagnetic component of the shower. The first condition is fulfilled by a coincident signal of at least 1.75 VEM in each PMT (threshold trigger). It triggers on large but short signals as primarily induced by the muons of a shower. The second condition is fullfilled if the level in at least two PMTs is above a threshold of 0.2 VEM for more than 325 ns within a sliding window of 3 µs ('time-over-threshold' (ToT)); the trigger detects prolonged small signals as primarily induced by the electromagnetic component of a shower. Signals passing the T1 level are stored for 10 s in the SD station.

If the T1 is a ToT, or the coincident signal was stronger than 3.2 VEM, the second level (T2) is triggered and the time-stamp and information about the cause of the T2 are sent to the central data acquisition system (CDAS). If the CDAS receives at least three T2 from stations with location and timing compatible with an air shower, the third level is triggered and data from stations that have at least a T1 within 30 µs of the T3 is send to the CDAS.

For all T3 candidate events a T4 'physics trigger' separates remaining noise from cosmic ray induced air showers. A T4 is achieved if two conditions are met. First, either three neighboring stations in a triangular pattern had a T2-ToT trigger (3ToT)

---

*At standard solar irradiation.
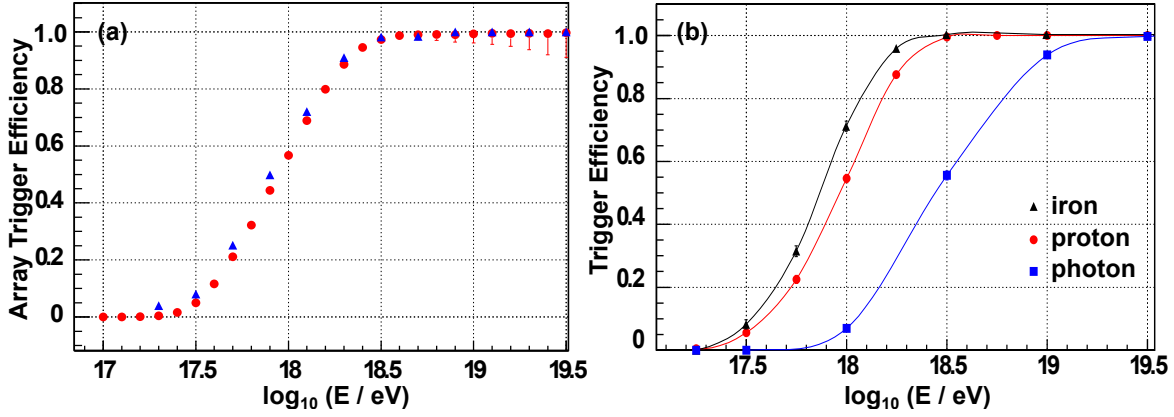
Figure 5.7: SD Trigger Efficiency **(a)** Trigger efficiency derived from SD data (triangles) and hybrid data (circles). **(b)** Trigger efficiency in Monte Carlo simulations for proton, iron nuclei, and photon primaries (taken from reference [19]; labels have been adjusted to remain readable here).

or the event had at least four neighboring stations with a T2 (4C1). Second, the timing of the stations is consistent with a planar shower front moving at the speed of light.

The trigger efficiency has been investigated using measured fluctuations in single showers observed with 'twin stations', hybrid data, and Monte Carlo simulations [19]. The trigger efficiency as a function of the energy from the three analysis is shown in figure 5.7. In all three analysis, the SD array has $\approx 100\%$ selection efficiency up to zenith angles of 60° for showers induced by protons or iron nuclei with energy above 3 EeV.

Every event at T4 level is considered an air shower induced by a cosmic ray and is reconstructed with the Auger Offline Software [275], and complementary also the CDAS software [257]. The employed reconstruction method depends on the zenith angle θ, as showers with a stronger inclination traverse more atmosphere before detection. Here we restate only the reconstruction of events with $\theta < 60°$ using the Offline software based on reference [276]. Details for the reconstruction of showers with zenith angles $\theta > 60°$ can be found in reference [56]. A event with $\theta = 48°$ and $E = 35$ EeV detected with the SD is shown in figure 5.8 (a) as example.

Reconstruction of the properties of the primary particle is done in three steps. First, 'the shower core', i.e. the intersection point of shower axis and ground plane, is estimated as barycenter of the signal strengths of the SD stations. Assuming a planar shower front, a first estimate of the direction of the air shower is derived. Second, the 'lateral density function' (LDF), i.e. a model for the signal distribution of the shower on the ground, is fitted to the signal data. The signal of a station in distance r is here parametrized as $S(r) = S_{1000} \cdot f_{\text{LDF}}(r)$ with LDF shape based on the Nishimura-Kamata-Greisen (NKG) function

$$f_{\text{NKG}}(r) \propto \left(\frac{r}{r_M}\right)^{s-2}\left(\frac{r}{r_M}+1\right)^{s-4.5} \tag{5.3}$$

with Molière radius r_M [277, 278]. Details of the LDF parametrization used in the
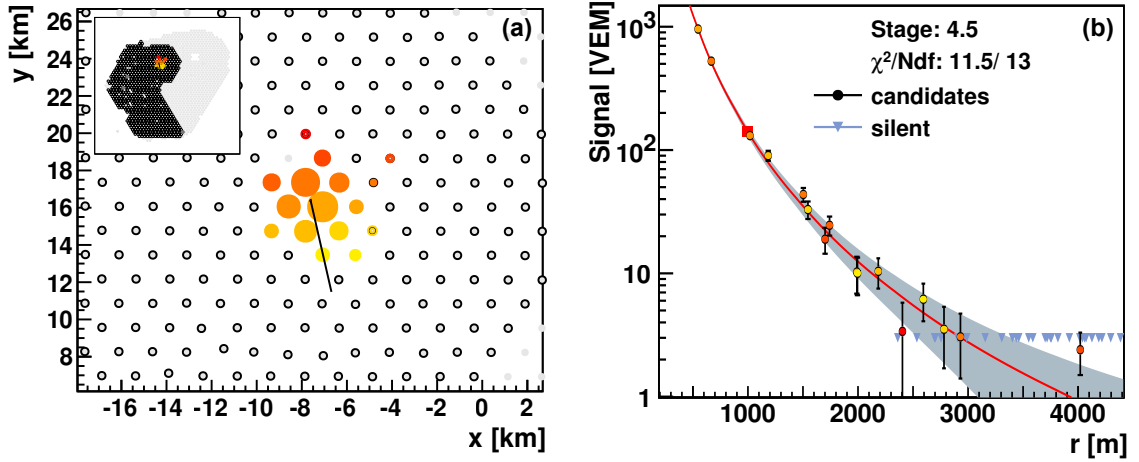
Figure 5.8: Exemplary SD event. **(a)** Spatial signal distribution. Black circles mark SD stations without T1, the colored circles SD stations with at least T1 trigger level. The size of the circles indicate the signal strength and the color the trigger time (red is late). The black line denotes the reconstructed shower axis. **(b)** Signal strength of the stations in (a) depending on the distance to the shower core with identical color code. Stations without signal are marked by triangles. The fitted LDF is indicated by the red line, the gray area marks the uncertainty of the fit. The S_{1000} energy estimator is marked with a red square.

Offline reconstruction can be found in reference [279]. The normalization of the LDF is given by the parameter S_{1000}, i.e. the estimated signal strength at a distance of 1000 m from the shower core. It has been shown that at 1000 m distance, the uncertainty from the choice of parameters in the LDF model is minimal for an array with 1500 m spacing [280].

The LDF fit is repeated two times. From the first pass the final core position is taken and shower axis and LDF fitted again, yielding the final shower direction (θ, ϕ) and estimator S_{1000}. The result of the LDF fit to the spatial signal distribution of the shower given in figure 5.8 (a) is shown in panel (b) of the same figure.

The achieved angular resolution is defined as the angular radius within 68% of the showers from the true direction are reconstructed. For showers with energy $E > 3$ EeV the angular resolution depending on the zenith angle θ and the number of SD stations is shown in figure 5.9 (a). The angular resolution is better than 1.6° for showers with signals in 3 stations and better than 0.9° for showers with signals in 6 or more stations [281].

As third step, from S_{1000} an energy estimator corrected for the zenith angle dependency of the signal

$$S_{38} = \frac{S_{1000}}{\text{CIC}(\theta)} \tag{5.4}$$

with $\text{CIC}(\theta) = 1 + a(\cos^2\theta - \cos^2 38°) + b(\cos^2\theta - \cos^2 38°)$ with $a = 0.87 \pm 0.04$ and $b = -1.49 \pm 0.20$ is derived [273]. Here, $\text{CIC}(\theta)$ is derived from data using the 'constant-intensity-cut' method assuming an isotropic flux of primary cosmic rays. The
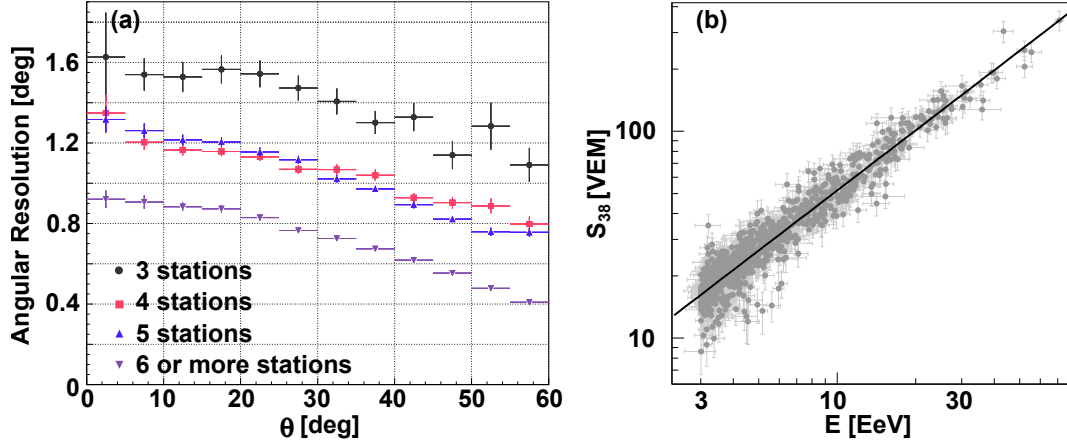
Figure 5.9: Uncertainty of the SD reconstruction. **(a)** Angular resolution of the SD depending on the zenith angle for various station multiplicities [281]. **(b)** SD energy estimator S_{38} depending on FD energy for hybrid events [273] (labels have been adjusted to remain readable here).

estimator S_{38} is calibrated with the energy measured with the FD detector in hybrid events using a power law $E_{\mathrm{FD}} = A \cdot S_{38}^B$. A fit to hybrid events shown in figure 5.9 (b) results in $A = (1.68 \pm 0.05) \times 10^{17}$ eV and $B = 1.035 \pm 0.009$.

The resulting energy resolution of the surface detector is $\sigma_E/E_{\mathrm{SD}} = (15.8 \pm 0.9)\%$ from 3-6 EeV, $\sigma_E/E_{\mathrm{SD}} = (13.0 \pm 1.0)\%$ from 6-10 EeV, and $\sigma_E/E_{\mathrm{SD}} = (12.0 \pm 1.0)\%$ above 10 EeV. The systematic uncertainty of the SD energy measurement is given by the systematic uncertainty of the energy scale of the fluorescence detector of 22% [83].

6 Measurement of the Principal Axes of the Directional Energy Distribution

6.1 Correction for Inhomogeneous Exposure

In the description of the analysis we so far assumed an uniform exposure in the regions of interest. But for a typical earth bound observatory as the Pierre Auger Observatory the relative exposure $w(\delta)$ varies with declination δ depending on the geographical latitude a_0 of the observatory and the maximum zenith angles of the detector θ_m as described in reference [252] reading

$$\omega(\delta) \propto \cos a_0 \cos \delta \sin \alpha_m + \alpha_m \sin a_0 \sin \delta \tag{6.1}$$

with

$$\alpha_m = \begin{cases} 0 & \text{if} \quad \xi > 1 \\ \pi & \text{if} \quad \xi < -1 \\ \cos \xi^{-1} & \text{otherwise} \end{cases} \tag{6.2}$$

and

$$\xi = \frac{\cos \theta_m - \sin(a_0) \sin(\delta)}{\cos a_0 \cos \delta}. \tag{6.3}$$

This introduces an artificial gradient in the directional energy distribution of the UHECR and thus results in a bias for the direction of the principal axes along this gradient. To account for this effect, we weight the momenta of the individual particles in equation 4.1 with the inverse of the observatory's relative exposure ω_i^{-1} in direction of UHECR i, reading

$$T_k = \max_{\vec{n_k}} \left(\frac{\sum_i \omega_i^{-1} |\vec{p_i} \vec{n_k}|}{\sum_i |\vec{p_i} \omega_i^{-1}|} \right). \tag{6.4}$$

For the selected regions we further require, that the complete ROI is in the field of view of the observatory to assure the symmetry of the regions of interest. For a radius of the ROI $\beta = 0.25 \, \text{rad}$ this is identical to the condition that the declination of the center of the ROI is smaller than $0.18 \, \text{rad}$.

6.2 Data Selection

For the measurement of the principal axes and the thrust observables we use data of the Pierre Auger Observatory from January 2004 to November 2012 reconstructed with the Auger Offline Software (version v2r7p7). In this period, $3\,608\,060$ T3 events have

Table 3: Events passing the successive application of the individual cuts of the data selection, separated in energy ranges for the measurement, the error calculation, and ROI seeding events. The cut on the declination is only applied for the seeding of ROI.

Events before November 2012			3 608 060
	$E_{\min} = 5\,\mathrm{EeV}$	$E_{\min} = 3\,\mathrm{EeV}$	$E_{\min} = 60\,\mathrm{EeV}$
$E > E_{\min}$	75 859	169 284	606
$\theta < 60°$	38 886	99 743	88
with 6T5-trigger	25 327	66 654	56
Not tagged as lightning	25 326	66 653	55
Not in bad period	24 242	63 744	55
Not in fake-T5 list	23 657	62 206	54
Declination $< 0.18\,\mathrm{rad}$			53

been recorded with the surface detector. For the measurement, we use only events with a reconstructed energy above 5 EeV, as they are believed to be of extragalactic origin, independently of the transition model (cf. section 1.4). By design, the trigger probability of the SD is approximately 100% at energies above 3 EeV and at zenith angles $\theta < 60°$; we thus limit our analysis to data within this zenith angle range to avoid any bias from uncorrected inhomogeneities in the trigger efficiency by the inclusion of very inclined events.

To further minimize potential bias, we employ several additional quality cuts. First, the reconstruction of the properties of the primary particle, in particular the energy, might be biased, if the shower is detected at the edge of the observatory, or individual stations are not active near the shower core. Therefore, we remove events from the dataset that do not have six active stations around the station with the strongest signal ('hottest' station) in the first step of the reconstruction (6T5-prior), and also events whose reconstructed shower axis is not surrounded by six active stations (6T5-posterior). This '6T5-trigger' or 'fiducial trigger' criteria are described in reference [19]. However, some events satisfy the 6T5 criteria based on stations that are reported active at the time of the event, but are not reported active in second-by-second checks in time intervals surrounding the event. Such events are considered as potentially not fulfilling the 6T5 condition ('fake-T5') and also removed from the analysis [282].

Second, events detected in a period with questionable detector operations are removed. Such 'bad periods' are, e.g., marked based on scheduled maintenance, in particular software updates, or sudden drops in the T5 trigger rate, e.g. due to instabilities in the communications with SD stations during storms [19]. Between 2004-01-01 and 2013-11-01, a cumulative time of approx. 365 days in 465 individual periods is marked as bad. The shortest bad period lasted for 391 s; the longest with a duration of more than a 100 days in the end of 2004 is attributable to a software update of the detector in 2004. After 2008-01-01, 92% of the time is not marked as bad period.

Third, events that pass all prior cuts, but are potentially influenced by lightning are also removed from the data.
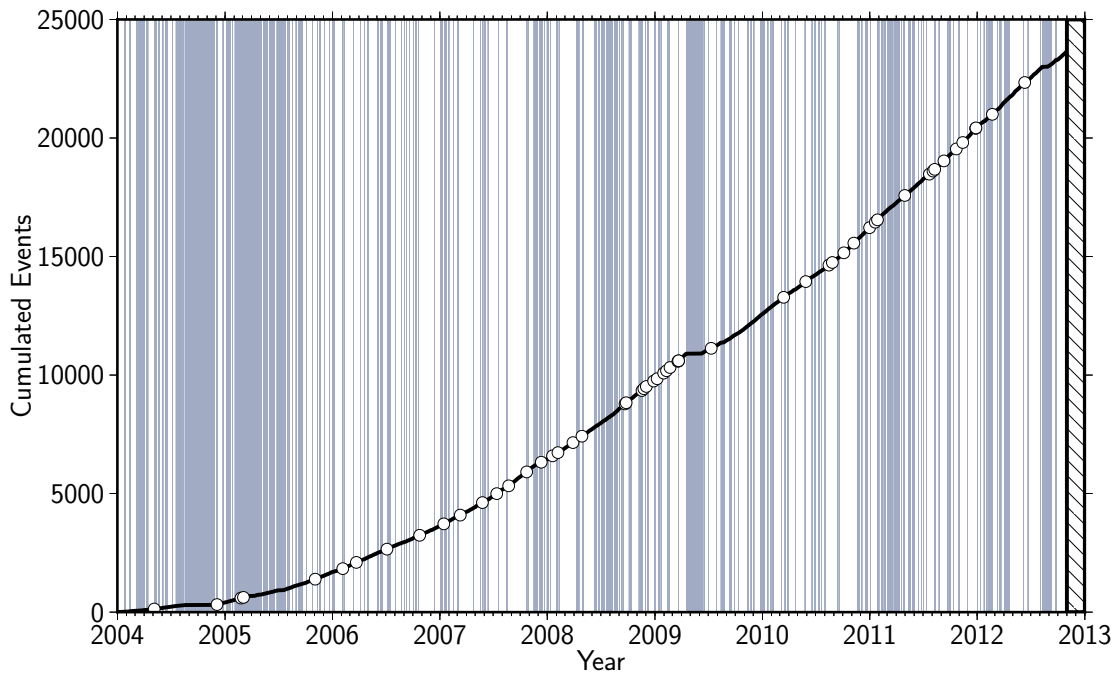
Figure 6.1: Cumulative number of events included in this analysis as a function of time. Gray shaded areas mark bad periods. White circles mark events that seeded a region of interest.

The remaining number of events after the successive application of each of these cuts are listed in table 3 for a threshold energy of 5 EeV, a threshold of 3 EeV, later used for the analysis of the uncertainties, and ROI seeding events with $E > 60$ EeV. On first sight, the zenith angle cut seems to remove a huge number of events with $E > 60$ EeV from the analysis that is inconsistent with the numbers at lower energies. However, the events considered here have not been reconstructed with the necessary corrections for very inclined showers, so that the used energy reconstruction is unreliable at high energies.

In figure 6.1 the cumulative number of events used in this analysis as a function of time is shown. Events that seeds a ROI are marked with white circles. The number of events increases linearly with time since the completion of the detector in the end of 2007. The distribution of time intervals between consecutive ROI-seeding events after 2008-01-01, corrected for bad periods, is compatible with an exponential distribution as expected for a Poisson process.

The differential energy spectrum of the selected events is shown in figure 6.2 (a). The selected data contains 54 events above 60 EeV; 53 are located at a declination smaller than 0.18 rad and thus define a region of interest. The distribution of the number of cosmic rays per region of interest is shown in figure 6.2 (b). The region with the lowest exposure contains 282 UHECR.
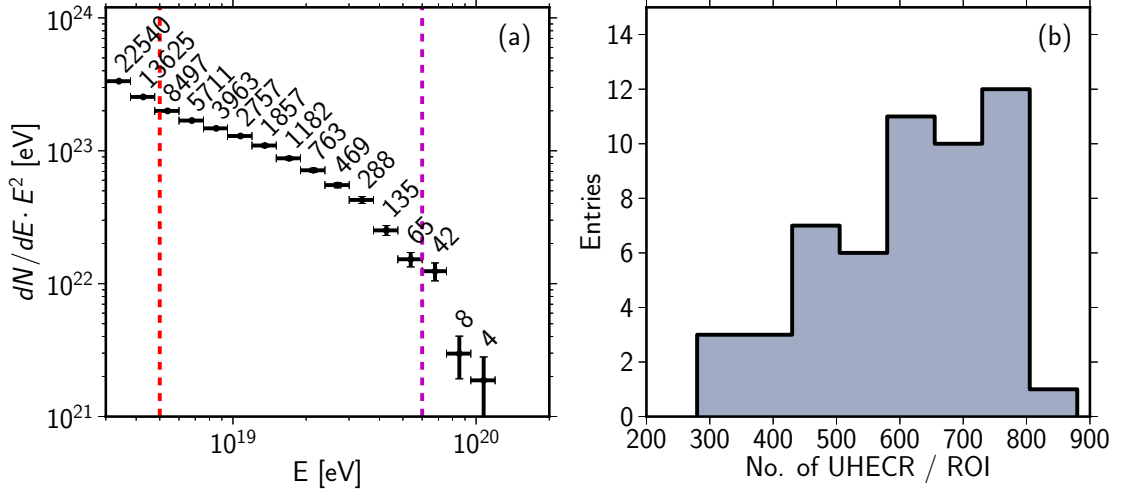
Figure 6.2: (a) Differential energy spectrum of selected events. Dashed lines indicate the threshold energy for the measurement $E_{\min} = 5\,\mathrm{EeV}$ and the seed energy for regions of interest $E_{\mathrm{seed}} = 60\,\mathrm{EeV}$. The seed energy is not identical with a bin edge in the histogram. **(b)** Distribution of the number of cosmic rays per region of interest.

6.3 Measurement and Uncertainties

Uncertainties in the reconstructed arrival direction and energy of the individual cosmic rays need to be considered here. The systematic uncertainty of the energy reconstruction is dominated by a 20% uncertainty on the energy scale as discussed in chapter 5. The observables $T_{1,2,3}$ as defined by eq. 4.1 are invariant under a linear recalibration of the detector energy scale $E_i \to c \cdot E_i$. The choices for the energy threshold of the measurement and the seed energy of the ROI are motivated by the spectrum, and would thus change accordingly. For the data selection as described above, systematic uncertainties in the reconstruction of the arrival direction of the UHECR and the exposure are small in comparison with the detector resolution.

To estimate the uncertainty on this analysis arising from the direction and energy resolution of the detector, we repeat the analysis 100 times on datasets with arrival directions and energies of the individual cosmic rays varied according to the uncertainties discussed in chapter 5. To allow an estimation of the uncertainty of the thrust values in the individual regions of interest, we use the ROI defined by the initial dataset in all repetitions; the positions of the ROI are not modified in the repetitions.

Fluctuations of events below or above the lower energy cut $E_{\min} = 5\,\mathrm{EeV}$ are taken into account by varying all events with $E > 3\,\mathrm{EeV}$ and applying the lower energy cut in every repetition of the analysis. Given the 16% energy-resolution of the detector in this energy range, fluctuations from events approximately 4 standard deviations below the lower energy cut are included here. Because of the steep energy spectrum,
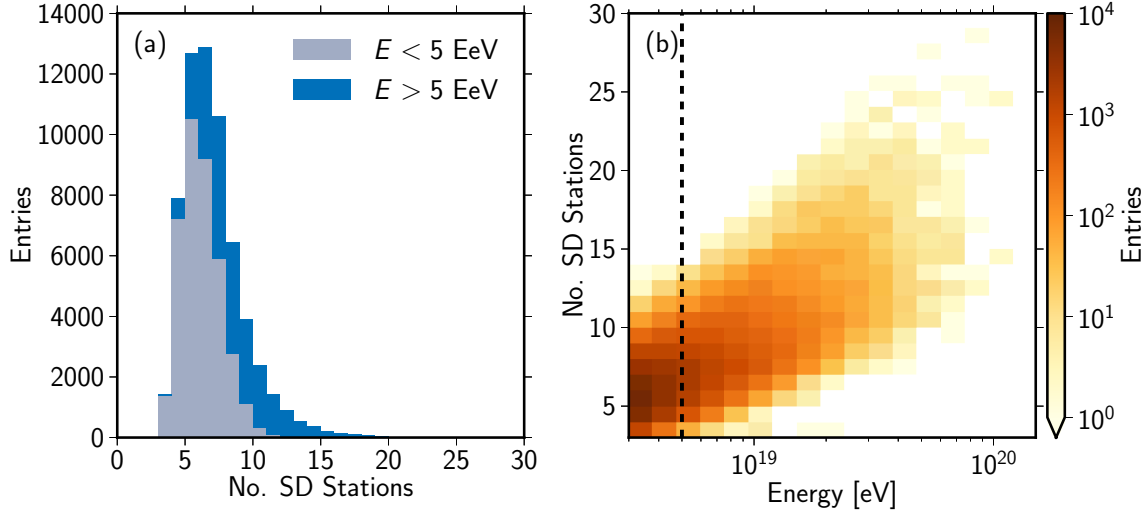
Figure 6.3: (a) Stacked distributions of the number of triggered SD stations in the selected data for events with $E < 5\,\text{EeV}$ and $E > 5\,\text{EeV}$. **(b)** Number of triggered SD stations for seperate energy ranges. The dashed line indicates the lower energy cut at $5\,\text{EeV}$.

more events fluctuate from lower to higher energies than vice versa, which increases the number of events in the datasets for the uncertainty analysis compared to the original dataset. To keep the number of events fixed in the analysis, a set of randomly selected events is removed from the analysis in every repetition.

The statistical uncertainty on the reconstructed directions depends on the number of stations triggered by the event as described in chapter 5. For the events selected here, the distribution of the number of triggered SD stations is shown in figure 6.3 (a) for all energies, and depending on the energy in figure 6.3 (b). 88% of the events above $5\,\text{EeV}$ and 99% of the events above $10\,\text{EeV}$ triggered more than 6 stations; the uncertainties of the direction of these events is thus better than $0.9°$. The variation of the arrival direction is done in galactic coordinates; fluctuations of events from zenith angles $\theta > 60°$ to lower zenith angles and vice versa are thus not included in the estimation of the uncertainty. However, only 2.2% of the events are within $1°$ of the maximum zenith angle in this analysis, so that we only expect a negligible increase of the uncertainty of the measured observables from this effect.

The result of the measurement of the thrust observables $T_{1,2,3}$ is displayed in figure 6.4. Panels in the top row (a–c) shows the distribution of the mean of the observables from the measurement in all regions of interest. The gray distribution corresponds to the expectation from isotropically distributed cosmic rays. In the bottom row (d–f) the result for the individual regions of interest with an arbitrary numbering scheme of the ROI is shown. Black squares denote the result from the initial selection, red dots and error bars denote mean and spread of the results from repeated measurements in datasets with cosmic rays varied by their energy and direction uncertainties. The gray shaded areas mark the 1σ, 2σ and 3σ intervals of the normal distribution with mean
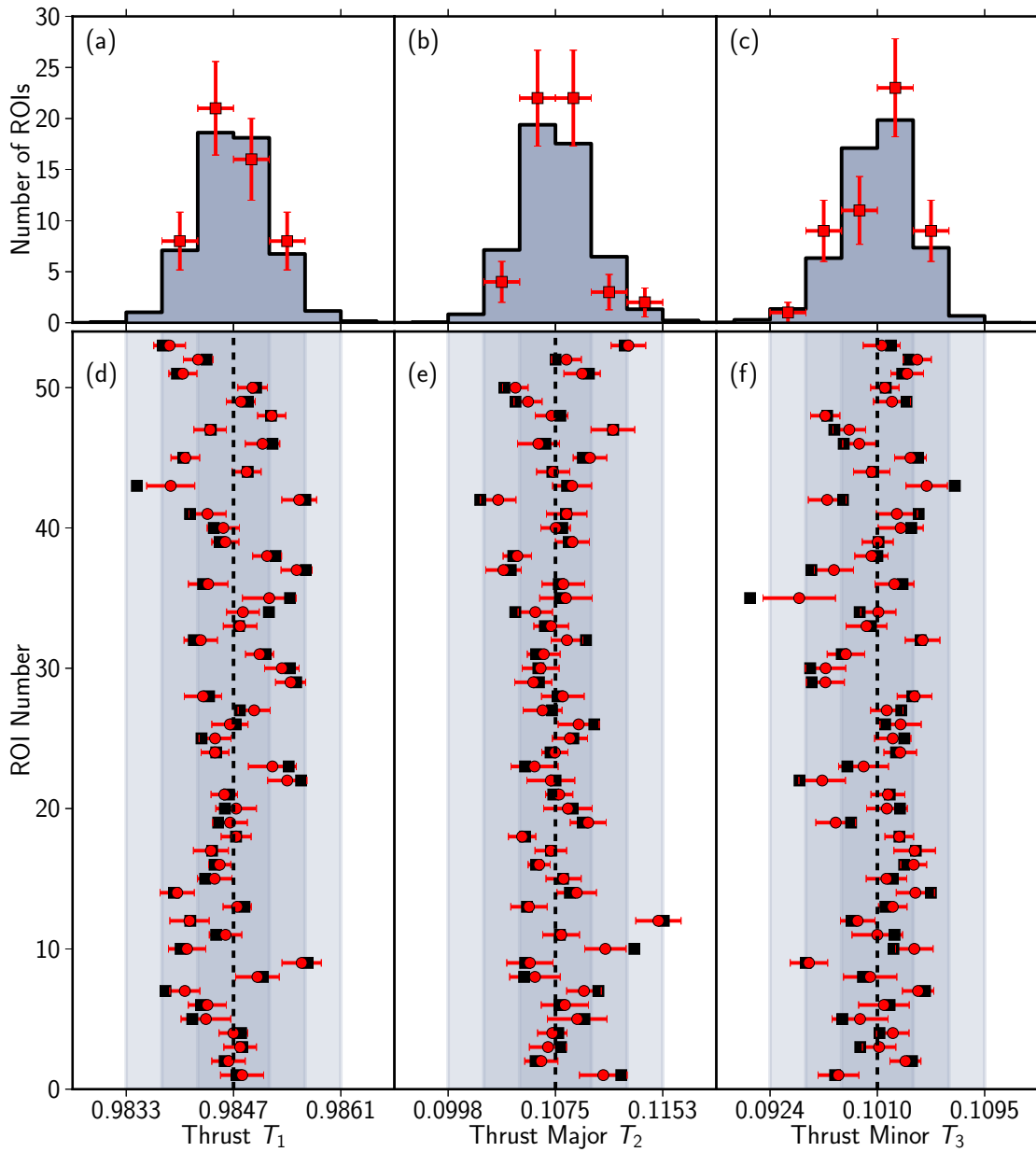
Figure 6.4: Measurement of the thrust observables. **(a–c)** Datapoints represent the distribution of the measured observables and the variation from the uncertainty of the measurement. The gray shaded histograms indicate the result from simulations of isotropically distributed UHECR. **(d–f)** Measured values in the individual regions of interest. Black squares denote the directly observed values. Red circles and error-bars the mean and spread of repetitions of the measurement with energy and direction of the UHECR varied according to their individual uncertainties. Gray shaded areas indicate the spread of the observables in isotropic simulations.
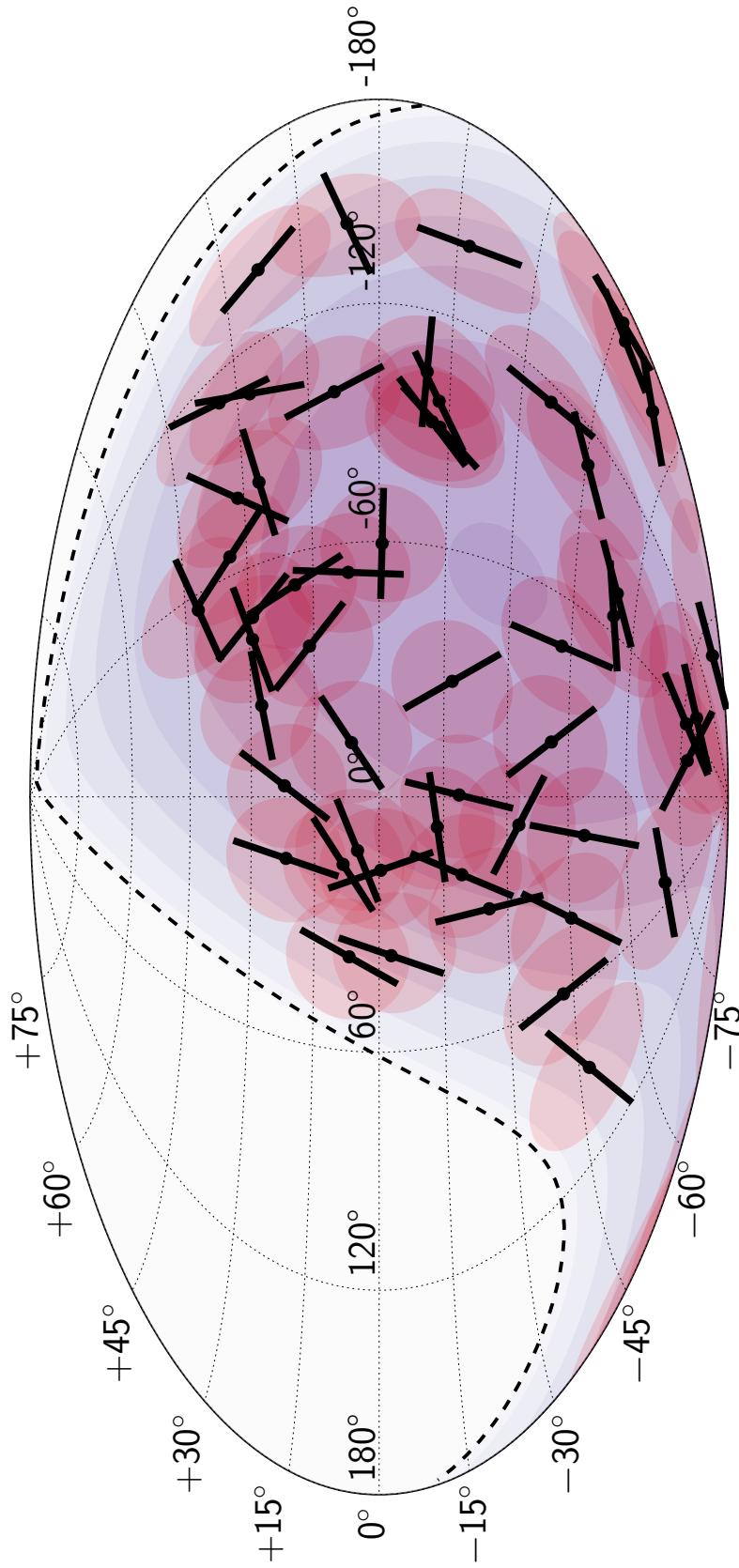
Figure 6.5: Hammer projection of the map of principal axes of the directional energy distribution in galactic coordinates. The red shaded areas represent the regions of interest. Black lines denote the second principal axes (thrust major axes) $\vec{n}_2$, black dots mark the positions of the thrust axes $\vec{n}_1$. The blue shading indicates the exposure of the Pierre Auger Observatory; the dashed line marks its field of view.

and spread according to isotropic distributed cosmic rays. A map of the regions of interest and directions of thrust major axes $\vec{n}_2$ is shown in figure 6.5.

The resulting average relative uncertainties for the thrust observables are $\overline{\Delta T_1/T_1} = 0.02\%$, $\overline{\Delta T_2/T_2} = 1.2\%$, and $\overline{\Delta T_3/T_3} = 1.3\%$. In figure 6.6 (a) the measured observables $T_{1,2,3}$ are shown in units of the respective average measurement $\bar{T}_{1,2,3}$ as a function of the exposure. The distributions of the thrust T_1 and thrust major T_2 are compatible with being independent of the relative exposure $\omega(\delta)$ as defined in eq. 6.1. The thrust minor has a trend to lower than average values in regions with a low exposure. The dependency becomes insignificant if the five regions with the lowest values for the exposure are excluded.

In figure 6.6 (b), the uncertainties of the measurements ΔT_k relative to the width of the distribution σ_{T_k} are shown as a function of the exposure. In regions with high exposure the uncertainties are lower compared to regions with low exposure owing to the number of cosmic rays in the regions. The average values are $\overline{\Delta T_1}/\sigma_{T_1} = 51\%$, $\overline{\Delta T_2}/\sigma_{T_2} = 63\%$, and $\overline{\Delta T_3}/\sigma_{T_3} = 60\%$; the uncertainty of the measurement in the individual regions is thus smaller than the spread among the individual regions respectively the expected spread from isotropically distributed cosmic rays.

The uncertainty of the direction of the axes $\vec{n}_k$, quantified by the circular variance V among the axes from the varied datasets (cf. p. 54), is shown as a function of the exposure of the center of the ROI in figure 6.6 (c). With increasing exposure, the circular variance, and thus the uncertainty of the axes measurement, decreases, also owing to the increasing number of cosmic rays in the regions. The thrust axes $\vec{n}_1$ are measured with higher accuracy than the thrust major or thrust minor axes. 68% of the thrust axes $\vec{n}_1$ in the varied datasets are closer to the average thrust axes of the ROI than 0.06°. The average angle between the thrust vector $\vec{n}_1$ and the center of the region of interest is 0.4°.

Without variation of the thrust, the variance among the thrust minor axes would be identical to the thrust major axes as $\vec{n}_3 = \vec{n}_2 \times \vec{n}_1$. Here however, the tangential plane in which $\vec{n}_2$ and $\vec{n}_3$ are located is slightly different for each individual repetition. As the variance among the sets is calculated from the vectors regardless of the plane, the variances are not identical.

For the thrust major axes, the distribution of the angles $\Delta \xi_2$ between the axes in the individual repetition and the average axis is shown in figure 6.6 (d) for all ROI. The accuracy of the measurement of the thrust major axis $\vec{n}_2$, defined as 68% quantile of the distribution of angles between average direction and direction in dataset with varied UHECR energy and direction is 11.8°.

The distribution of the measured observables is compatible with an isotropic distribution of UHECR. In none of the regions of interest a value of $T_{1,2,3}$ that deviates more than 3 standard deviations from the expectation value for an isotropic distribution of cosmic rays is observed, if the uncertainties on the energy and direction of the UHECR are included. A single region deviates more than 3σ from the isotropic reference if the uncertainties are not included.

In chapter 8 we use this non-observation of extraordinary patterns with the thrust observables to constrain parameters of propagation scenarios. However, the map of
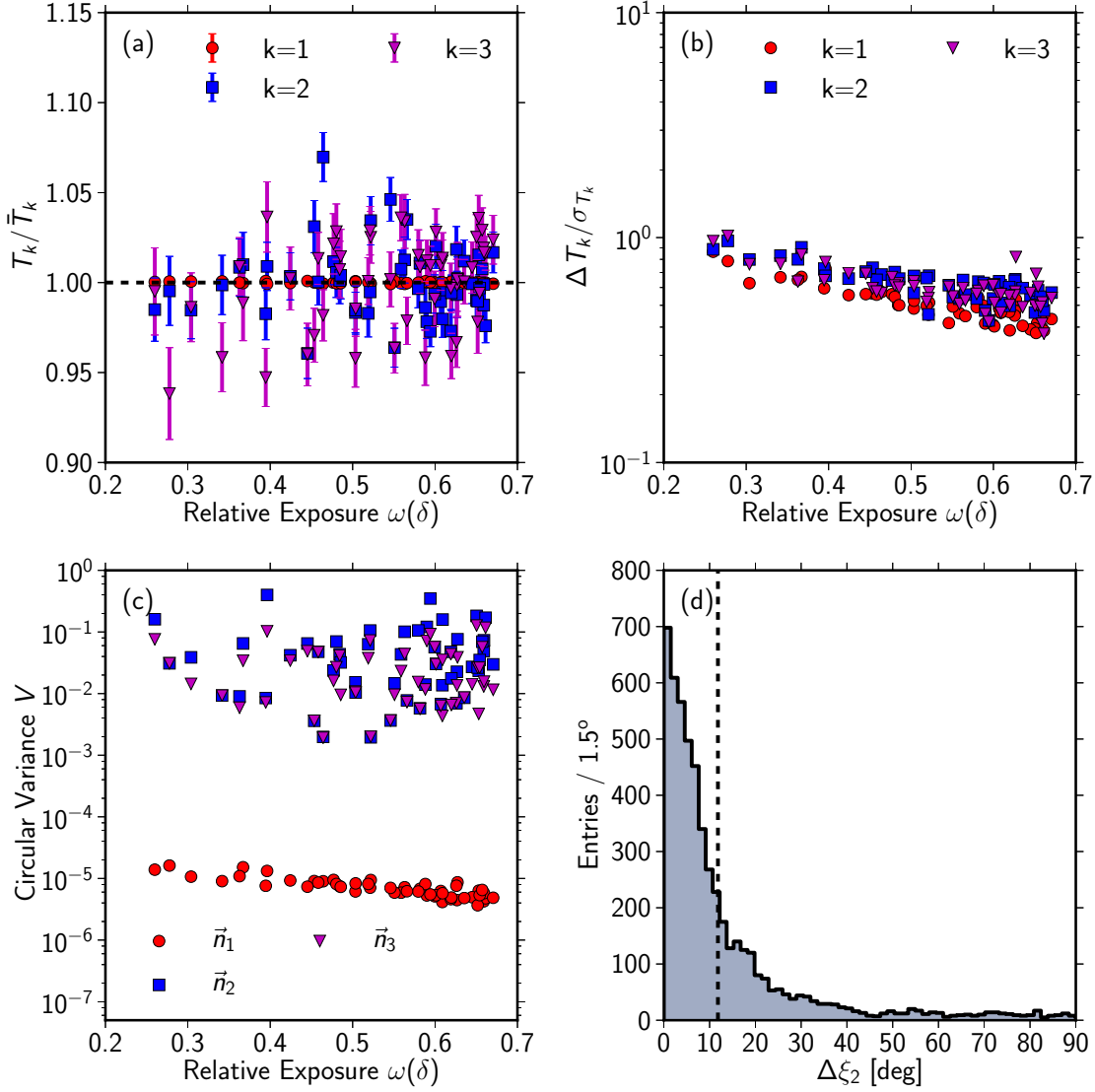
Figure 6.6: **(a)** Observables T_k in the individual ROI relative to the mean of the observations as a function of the relative exposure. **(b)** Relative uncertainty of the observables $T_{1,2,3}$ in the individual ROI as a function of relative exposure. **(c)** Circular variance V of the principal axes $\vec{n}_{1,2,3}$ in the individual ROI as a function of relative exposure. **(d)** Distribution of angles $\Delta\xi_2 = |\bar{\vec{n}}_2 \angle \vec{n}_2^j|$ between thrust major axes in datasets with modified CR $\vec{n}_2^j$ and the average direction $\bar{\vec{n}}_2$ in the individual ROI. The dashed line denotes the 68% quantile at 11.8°.

thrust major axes shown in figure 6.5 features several patterns that appear to the eye hardly compatible with an uniform distribution of the axes. A quantitative analysis of this map based on the reproducibility of the axes in subsamples of the data is discussed in the next chapter.

7 Reproducibility of the Axes Measurement

The thrust major axes $\vec{n}_2$ mapped in figure 6.5 are the result of the maximization of T_2 in equation 6.4 (p. 71). Thus on first sight, a value of the thrust major T_2 that is compatible with isotropy, indicates a trivial direction of the thrust major axis. But the thrust major value, indicates only the strength of the collimation along the thrust major axis, and even with a strength of the collimation that is compatible with isotropy, the direction can be characteristic for the specific scenario. If on the one hand, the thrust major axes carry information characteristic for the simulated scenario, subsequent independent experiments should observe the same directions. If on the other hand the observed axes are trivial, no concentration of directions among the sets of axes from the same region is expected.

We applied this argument to simulations of 100 scenarios using the PARSEC software described in chapter 3 with $B = 7\,\mathrm{nG}$ strength of the extragalactic magnetic field, source density $\rho = 10^{-4}\,\mathrm{Mpc}^{-3}$, JF2012 model for the galactic magnetic field, and experimental exposure as for the Pierre Auger Observatory. For each of the scenarios, we generated $100 \times 20\,000$ UHECR with energies above $5\,\mathrm{EeV}$ following a power law spectrum. One of the resulting maps is shown together with a map derived from isotropically distributed UHECR in figure 7.1.

Within each repetition in an simulated scenario, i.e. identical source positions and identical cosmic magnetic fields, the sets of cosmic rays are drawn from the identical probability distribution. Each individual set constitutes a 'pseudo experiment' in this scenario. Using the UHECR of only the first pseudo experiment in each scenario, we set ROI of size $\beta = 0.25\,\mathrm{rad}$ around these UHECR with $E > 60\,\mathrm{EeV}$. Using this ROI, we then calculate the thrust observables in every pseudo experiment, resulting in a set of 100 thrust major axes $\vec{n}_2^{\,i=1...100}$ for every individual ROI in every scenario. To quantify the degree of concentration among the directions in every ROI, we use the circular variance V introduced in section 4.2 (p. 54).

For all ROI of the simulated scenarios, the circular variance is shown as a function of the mean of the thrust observables $T_{1,2,3}$ observed in the individual pseudo experiments in figure 7.2 using red dots. For comparison, black dots denote the result of the same method applied to isotropically distributed UHECR. Compared with the results of the previous section (fig. 6.4), the spread of the values is smaller, as here the mean of 100 realizations is shown instead of the value of a single realization. Most of the ROI from anisotropic scenarios are compatible with the isotropic reference distributions; several ROI deviate in at least one of the observables $T_{1,2,3}$ from the isotropic reference. Of particular interest here is, that approximately one-third of the ROI with a circular variance below 0.3 have values of $T_{1,2,3}$ compatible within 3 standard deviations of the isotropic reference distribution; the thrust major axis in each of this regions points
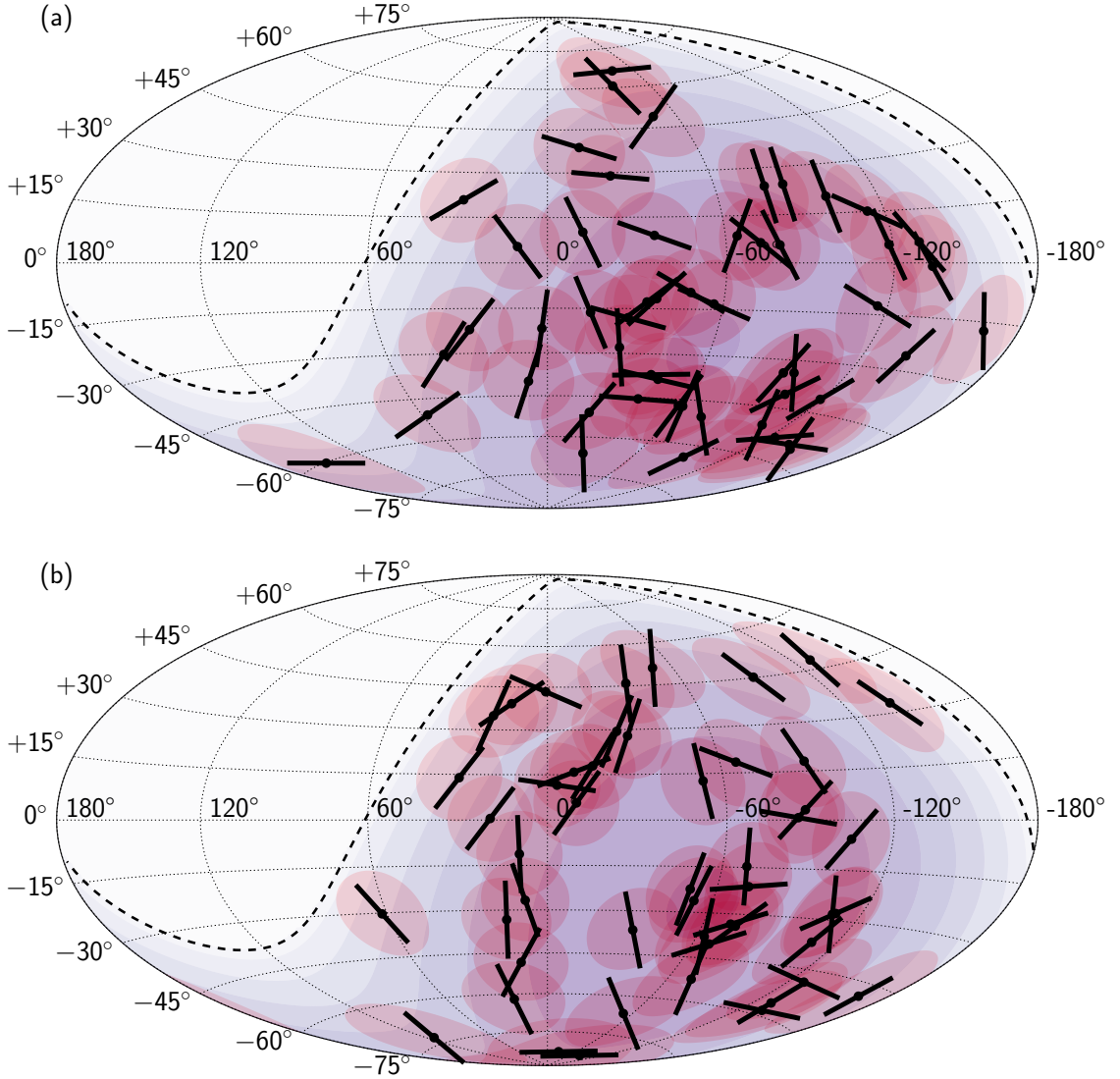
Figure 7.1: Typical skymaps of thrust major axes from **(a)** isotropically distributed UHECR and **(b)** anisotropically distributed UHECR from a PARSEC simulation with $7\,\mathrm{nG}$ extragalactic magnetic field, source density $10^{-4}\,\mathrm{Mpc}^{-3}$, and BSS_S model for the galactic magnetic field.

in the same direction in repeated experiments, even though the values of all three thrust observables in the ROI are compatible with the isotropic distribution. The thrust major axes can therefore be non trivial even if the thrust observables $T_{1,2,3}$ are compatible with the expectation from isotropically distributed UHECR.

Patterns in the map of measured axes in figure 6.5 could thus also be non trivial. However, patterns can be found by eye also in maps of random directions, e.g. in figure 7.1 (a), so that a quantitative analysis of the directions is imperative. We investigated several approaches to quantify structures in the directions of thrust major
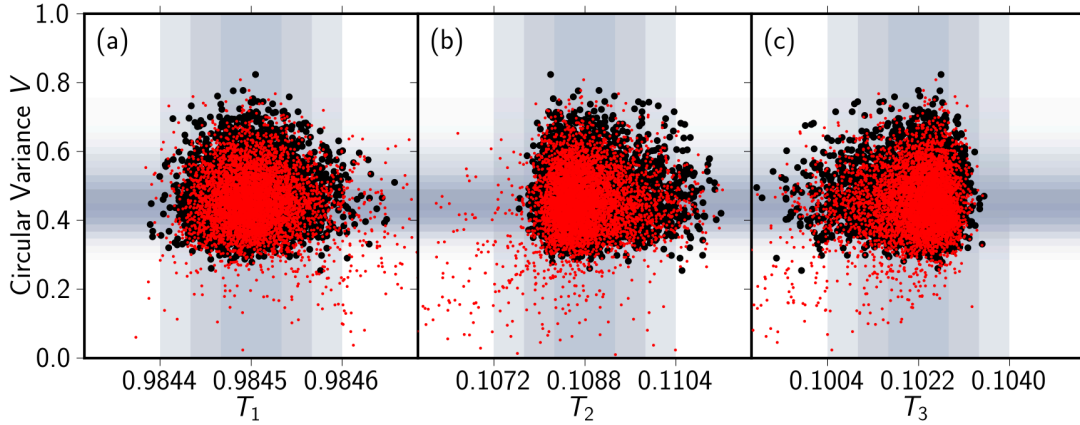
Figure 7.2: Circular variance V among the thrust major axes of 100 repetitions of the analysis in ROI of 100 simulated datasets. Horizontal and vertical gray shading indicates the distributions of V and mean and spread of the distribution of $T_{1,2,3}$ expected from isotropically distributed UHECR.

axes found in simulations, but none of the analysed methods allowed a convincingly powerful test. A brief summary of the methods investigated in course of this work is given in appendix E.

These searches assume, that the deflections of UHECR in coherent magnetic fields lead to structures in the distribution of UHECR on angular scales in order of magnitude of the typical distance of neighbouring regions of interest. However, this might not be the case and structures in the deflection of UHECR might appear only on a smaller scale. In such scenarios, the apparent structures are trivial, but the individual directions may be non-trivial. The analysis strategies for patterns are thus model dependent. Furthermore, as the methods are developed only a posteriori, special care has to be taken to allow conclusions on the significance of the patterns.

Here we therefore investigate the reproducibility of the directions of the axes in subsets of the data. This allows a test of the triviality of the measurement similar to the argument used above, but without repetition of the whole experiment. We first define interesting regions for the measurement with parameters as discussed in chapter 4 using all available data. We then split the dataset into n independent subsamples and compare the directions $\vec{n}_{2,j=1} \cdots \vec{n}_{2,j=n}$ obtained in each subsample for every individual region of interest. A low variability of directions in the subsets of the data provides evidence for a non-triviality of the thrust major axes and consequently for an anisotropic distribution of UHECR. From a high variability though, the triviality of the directions measured with the complete dataset cannot be concluded coercively as the individual subsets contain only parts of the data.

The quantitative treatment of this argument is described in the following sections. We first describe models for the circular variance in regions with and without concentration of axes in subsets of the data. We then formulate a likelihood ratio test to infer if there are regions with a high concentration in a dataset or not, discuss the optimal choice

for the number of subsets to split the data into, and finally apply the method to the measured data.

7.1 Models for the Circular Variance

Isotropic distribution of UHECR

For isotropically distributed UHECR, our null-hypothesis H_0, we expect no correlation among the thrust major axes derived from subsamples of the dataset. The probability density function (p.d.f.) of the circular variance V of a sample of size n of uniform distributed data is derived from eq. 4.8 and the p.d.f. for the resultant length R for uniform distributed data

$$f_u(R) = R \int_0^\infty dt \; J_0(Rt) J_0^n(t) \; t, \tag{7.1}$$

where J_0 denotes the Bessel function of the first kind [255]. From eq. 7.1 the p.d.f. for the circular variance is derived by a transformation of variable $R \to V$ and $V(R) = 1 - \left(\frac{R}{n}\right)^{1/l^2}$ with $l = 2$ for the thrust major reading

$$f_u(V) = \left| \frac{\partial V}{\partial R} \right| f_u(R) = \frac{1}{l^2} \left(\frac{R}{n}\right)^{\frac{1}{l^2}-1} (1-V)^{l^2} \int_0^\infty dt \; J_0\left(n \cdot (1-V)^{l^2} t\right) J_0^n(t) \; t. \tag{7.2}$$

In figure 7.3 this p.d.f. is displayed for sample sizes of $n = 2 \ldots 5$ calculated from eq. 7.2 using numeric integration [283, 284] and derived from Monte Carlo simulations of random directions. For sample sizes $n = 2$ and $n = 3$ the p.d.f. does not decrease for $V \to 0$. For sample sizes $n = 3$ and $n = 4$ the p.d.f. features a discontinuous point. For sample sizes $n \geq 5$ the p.d.f. assumes a smooth shape with increasing mean and decreasing width for increasing n. As for high concentration $V \to 0$, we require $n \geq 4$ here.

Anisotropic distribution of UHECR

If the observed thrust major axes contain information on the deflection of UHECR in coherent fields, we expect a concentration of the thrust major axes derived from independent subsamples of the data. To model such a concentration, we use the von Mises distribution [285] which can be regarded as normal distribution on the circle. The p.d.f. for von Mises distributed directions θ with mean direction μ_0 reads

$$f(\theta, \mu_0, \kappa) = \frac{1}{2\pi I_0(\kappa)} e^{\kappa \cos(\theta - \mu_0)} \tag{7.3}$$

with concentration parameter κ and I_0 denoting the modified Bessel function of first kind and order zero. For $\kappa \to 0$ the distribution converges to the uniform distribution. The von Mises distribution with three choices of κ is visualized in figure 7.4 together with the p.d.f. of the uniform distribution.
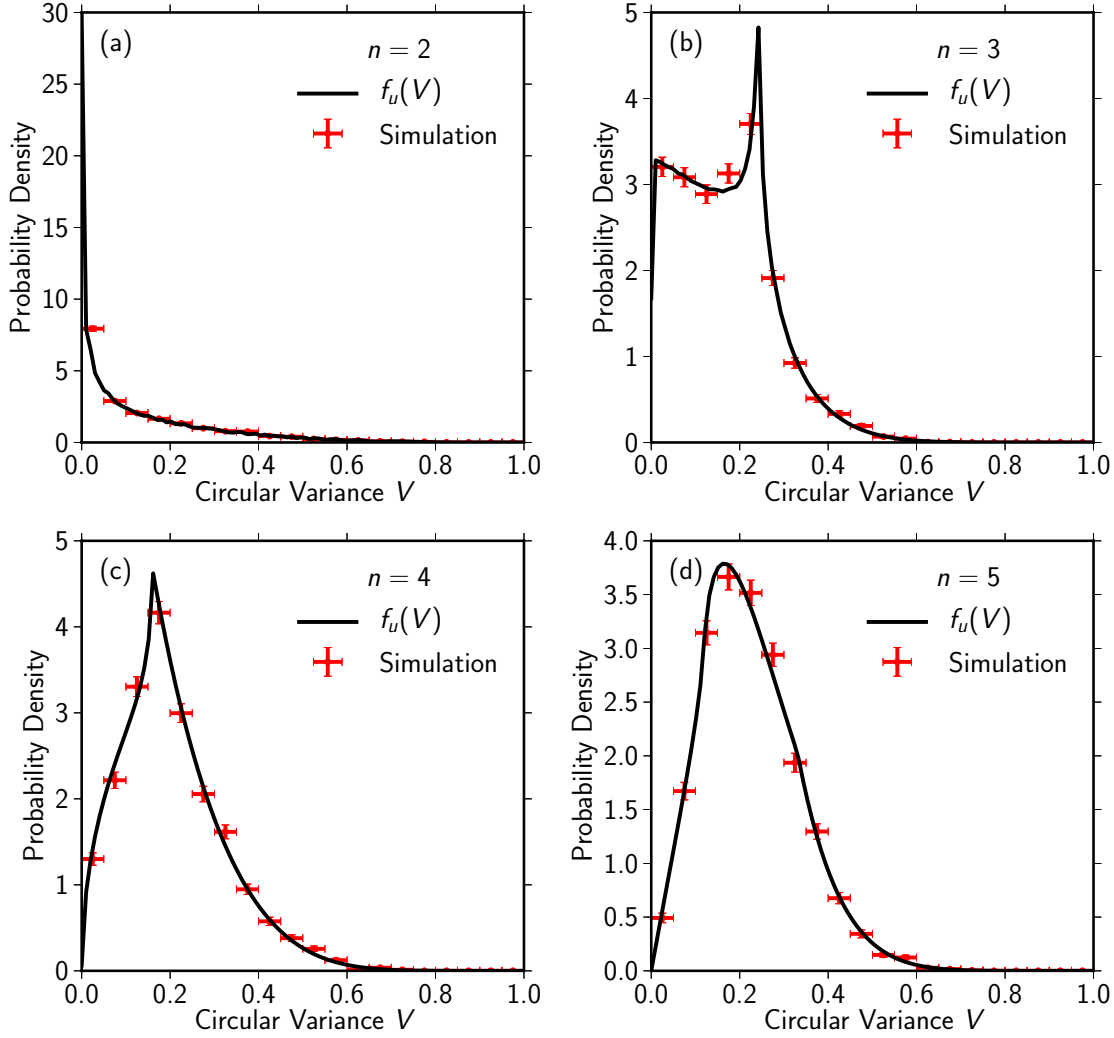
Figure 7.3: Probability density function for the circular variance V of n uniform distributed directions with **(a)** $n = 2$, **(b)** $n = 3$, **(c)** $n = 4$, and **(d)** $n = 5$. The data points are derived from Monte Carlo simulations of random directions, the solid line is derived from eq. 7.2 using numerical integration.

The p.d.f. for the circular variance of n samples from a von Mises distribution with concentration parameter κ is also derived from its p.d.f. of the resultant length

$$f_{CN}(R, \kappa) = \frac{I_0(\kappa R)}{I_0^n(\kappa)} \cdot f_u(R) \tag{7.4}$$

with f_u as in eq. 7.1 being the p.d.f. for the corresponding uniform case [255]. With a transformation of variable we get

$$f_{CN}(V, \kappa) = \frac{I_0(\kappa n(1 - V)^{l^2})}{I_0^n(\kappa)} \cdot f_u(V). \tag{7.5}$$
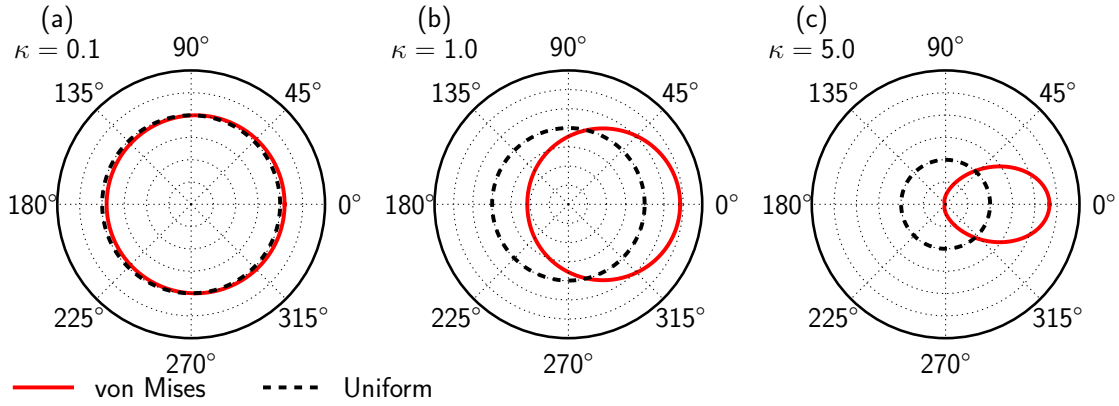
Figure 7.4: Comparison of the von Mises distribution with the uniform distribution for three different choices of the concentration parameter κ. Here $\sqrt{f}$ is shown instead of the p.d.f. f, so that the area in any interval is proportional to the probability, and not to the square of the probability (cf. reference [255]).
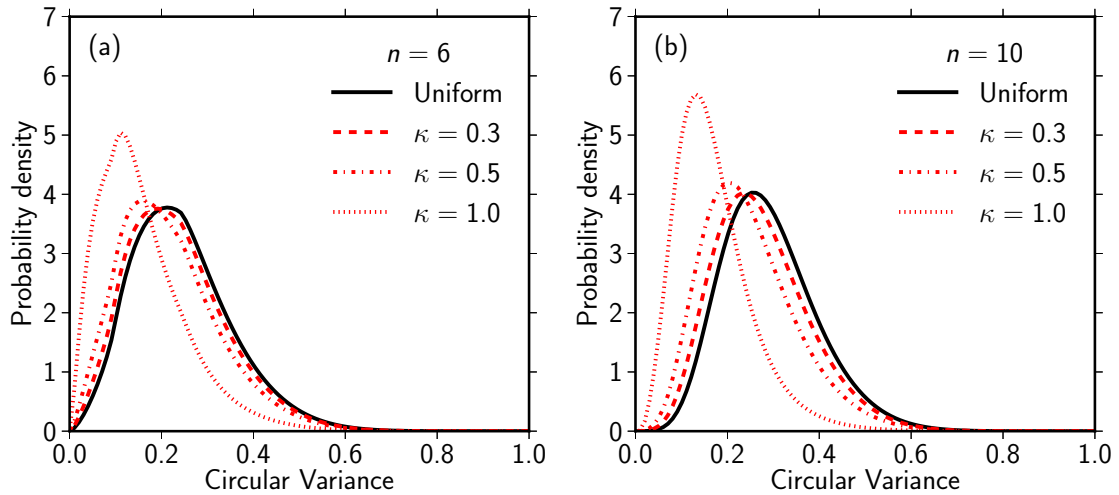
Figure 7.5: Probability density function for the circular variance V for von Mises distributed data with concentration parameter κ in comparison with uniform distributed data for sample sizes of **(a)** $n = 6$ and **(b)** $n = 10$.

as model for the circular variance in regions with anisotropically distributed UHECR.

In figure 7.5 examples for the circular variance of the concentrated distribution are compared with the expected variance from uniform distributed data for two choices of n. For increasing κ, smaller values of V are modeled.

Combined Model

For a map derived from a dataset with N regions of interest, we expect also in anisotropic scenarios only some regions (signal regions) to show a high concentration of

the thrust major axes whereas other regions (background regions) show no concentration. In the following we describe the distribution of the circular variance from all signal regions using only a single concentration parameter κ, although every region of interest could be characterised best by an individual κ_i. This simplification is justified as we are so far interested only in modelling variable degrees of concentration in contrast to an uniform distribution and not a detailed characterization of non-trivial regions.

For N_S signal regions and N_B background regions the combined p.d.f. of the circular variance reads

$$f_C = \frac{N_S}{N} f_{CN} + \frac{N_B}{N} f_u \tag{7.6}$$

and completely describes the alternative hypothesis H_{κ,N_S} for a fixed total number of regions N. A statistical test to discriminate between H_{κ,N_S} or H_0 given data is described in the next section.

7.2 Statistical Method

As test statistic we use the likelihood ratio

$$Q = -2 \ln \frac{\mathcal{L}_{\kappa,N_S}}{\mathcal{L}_0} = -2 \ln \frac{\prod_i f_C(V_i, \kappa)}{\prod_i f_u(V_i)} \tag{7.7}$$

with the likelihood of H_0 calculated from the probability density function f_u as in eq. 7.2 and the likelihood for the alternative hypothesis H_{κ,N_S} calculated using the p.d.f. f_C from eq. 7.6. By insertion of $\frac{f_C}{f_u}$ from eq. 7.6 this first simplifies to

$$Q = -2 \sum_i \ln \left(\frac{N_S}{N} \frac{f_{CN}}{f_u} + \frac{N_B}{N} \right). \tag{7.8}$$

With eq. 7.5 and also $N_B + N_S = N$ the likelihood ratio further simplifies to

$$Q = -2 \sum_i \ln \left(\frac{N_S}{N} \left(\frac{I_0(\kappa n (1 - V_i)^{l^2})}{I_0^n(\kappa)} - 1 \right) + 1 \right) \tag{7.9}$$

and can thus be efficiently computed without numerical integration of the probability density functions in eq. 7.2 and eq. 7.5. The point in parameter space with the lowest

Table 4: Critical values for commonly used levels of significance to exclude H_0. Because of the limited statistics of the simulation the value for 5σ is ill defined. Q_{CL} is approximately independent on the number of splits n for $n > 5$.

Confidence Level	2σ	3σ	4σ	5σ
Probability [%]	95.44997	99.73002	99.99367	99.99994
Q_{CL}		-4.20	-9.29	-16.73	*(-27.45)*

value of $Q(\kappa, N_S)$ gives the best estimate for the concentration parameter κ and the number of signal regions N_S. The value of $\min\left(Q(\kappa, N_S)\right)$ is used to determine the level of confidence in H_0.

To account for the fit of κ and the scanning in N_S (look-elsewhere effect) as well as the small sample bias from the small number of regions of interest $N \lesssim 100$, we derive the critical values Q_{CL} for the test statistic from applying the method described above to Monte Carlo simulations of uniformly distributed thrust major axes in 53 independent regions of interest. The distribution of the resulting values for $\min Q$ is approximately independent on the number of splits n for $n > 5$. The critical values for commonly used confidence levels are listed in table 4.

7.3 Parameter Optimization

Compared with the analysis of the values described in chapter 4, the analysis of the directions described above introduces n, the number of subsamples to split the data into, as additional free parameter. The optimal choice for n is not trivial. On the one hand choosing n as small as possible maximizes the number of signal UHECR in the individual subsamples. On the other hand choosing n as large as possible enhances the separation of the p.d.f. of the circular variance V for the signal and background models (see figure 7.5).

For an optimal choice of n, we investigated the influence of n on the power to exclude an isotropic distribution of UHECR with 2σ confidence using this method,
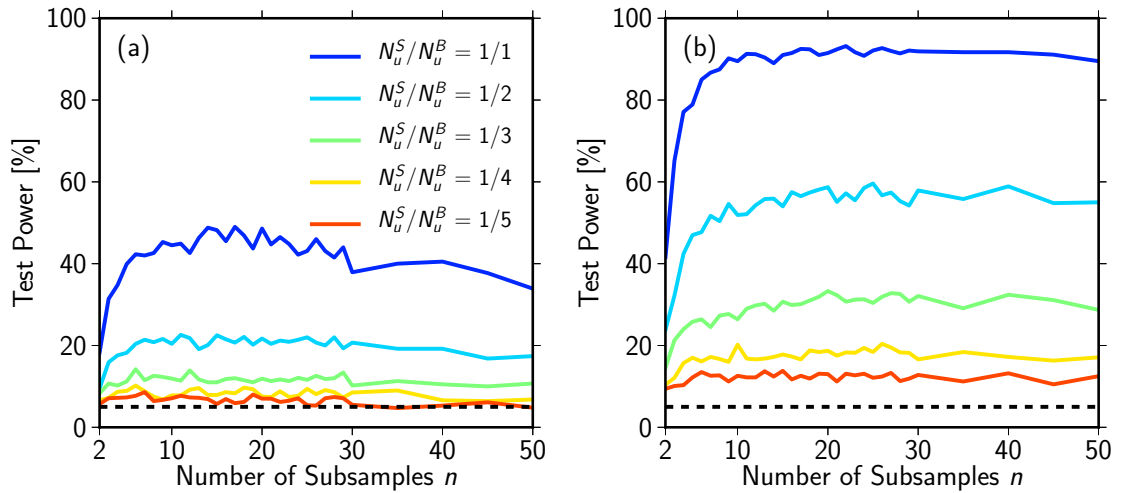
Figure 7.6: Test power of the method for simulations with five different signal to background ratios N_u^S/N_u^B for **(a)** $N_u = 300$ UHECR and **(b)** $N_u = 600$ UHECR in $N = 50$ regions of interest. 15 ROI contain contributions from the signal, 35 ROI include UHECR only from background. The dashed line mark the 5% minimum test power equivalent to the confidence level chosen here.
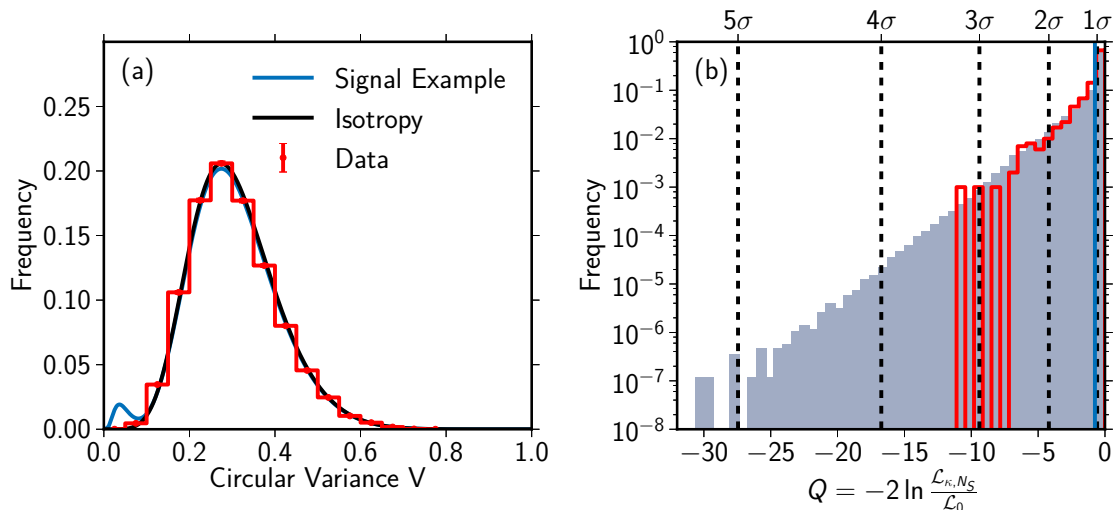
Figure 7.7: Reproducibility of the axes in the measurement. **(a)** Average distribution of circular variance of splits of the data into $n = 12$ parts compared with the expectation for uniform distributed axes and to a signal hypothesis with one regions and a concentration parameter $\kappa = 3$. **(b)** Distribution of likelihood ratios of the individual distributions of V. The result for the data (red) is compared with the results from isotropic simulations (gray). The average likelihood ratio found in data $\bar{Q} = -0.75$ is marked by a blue line. Dashed lines mark commonly used significance level.

from scenarios generated with the toy Monte Carlo described in chapter 4. In every simulated dataset we simulated $N = 50$ regions of interest containing N_u UHECR. We simulated two sets, one with $N_u = 300$ UHECR and one with $N_u = 600$ UHECR. $N_u = 300$ is approximately the number of UHECR in a ROI in a low coverage region; $N_u = 600$ is approximately the typical number of UHECR in a ROI. $N_S = 15$ of the regions were simulated as signal regions, $N_B = N - N_S$ as background regions. The signal regions contain N_u^S UHECR from a point source in the center of the region, smeared with $C_C = 1.5\,\mathrm{rad}\,\mathrm{EeV}$ and $C_T = 0.8\,\mathrm{rad}\,\mathrm{EeV}$, and N_u^B isotropic distributed UHECR. Cosmic rays deflected outside the ROI are re-added as isotropic background, but are not included in N_u^B. The background ROI contain only isotropically distributed UHECR.

In figure 7.6 this test power is displayed depending on the number of splits n for simulations for five signal to background ratios N_u^S / N_u^B in the signal regions. A higher number of UHECR in the regions increases the test power; thus indicating statistical consistency of the procedure. The test power increases up to $n \approx 10$ and stays approximately constant for higher number of subsamples for both choices of N_u. We chose $n = 12$ here to be safely in the regime of constant test power.

7.4 Application to the Measurement

The measured data are split into 12 parts by chance instead of time of data taking to avoid any potential bias of the result by possible effects attributable to detector aging. The procedure described thus has to be applied repeatedly to the measurement, as otherwise the result would depend on the random seed used to split the data. In figure 7.7 (a) the average distribution of the circular variance of 1000 applications of the method is shown together with the null-hypothesis and a hypothetical signal from one signal region with $\kappa = 3$.

The distribution of likelihood values of the repeated applications of the method and the reference distribution of the application of the method to simulations of isotropically distributed UHECR are shown in figure 7.7 (b). From the 1000 repetitions 2 deviated with more than 3σ significance from an uniform distribution of axes. The average likelihood ratio is $\bar{Q} = -0.75$ with a probability to observe a smaller likelihood ratio in sets of isotropically distributed UHECR of $P(\bar{Q} < -0.75) = 28\%$. The observed axes shown in figure 6.5 are thus not reproducible in the individual subsets if the data are split into 12 parts. No evidence for the non-triviality of the axes is thus found with this analysis.

8 Constraints on Astrophysical Scenarios

The measurement of the thrust observables $T_{1,2,3}$ presented in chapter 6 is compatible with an isotropic arrival distribution of UHECR; all scenarios that predict otherwise are excluded by this observation. Variation of the parameters in a simulation of UHECR propagation allows to tune the degree of anisotropic signal in the simulated datasets. By comparison of the simulated results with the observation, thus limits on the simulation parameters can be set using the measurement of the thrust observables. In this chapter, we first discuss the statistical method used here to infer if a model scenario is compatible with the observation, or if it is excluded by the observation. We then apply this method to scenarios simulated with the PARSEC software and set a limit on the strength of the deflection in the extragalactic magnetic field in the simulation.

8.1 Technique of Statistical Inference

To discriminate between two hypothesis using the measurement described in chapter 6, here the likelihood ratio

$$Q = -2 \ln \frac{\mathcal{L}_{\mathcal{H}_{\mathbf{X}}}}{\mathcal{L}_{\mathcal{H}_0}} \tag{8.1}$$

is used as test statistic. The calculation of the confidence in $\mathcal{H}_0$ based on Q is discussed in section 4.4. Here, we discuss the exclusion of the alternative hypothesis $\mathcal{H}_{\mathbf{X}}$.

In frequentist interpretation, $P(Q > Q_{\text{obs}}|\mathcal{H}_{\mathbf{X}})$ is the frequency of occurrence of $Q > Q_{\text{obs}}$ in repeated experiments if $\mathcal{H}_{\mathbf{X}}$ is true. If, as illustrated in figure 8.1 (a), both hypotheses are clearly distinguishable in the analysis, $P(Q > Q_{\text{obs}}|\mathcal{H}_{\mathbf{X}})$ provides a good estimator for the confidence in the alternative hypothesis. If, however, the hypotheses are only marginally distinguishable, a fluctuation of Q_{obs} to a large value results in low confidence in the alternative hypothesis if the confidence is estimated as above. This is illustrated in figure 8.1 (b). A derivation of limits on parameter $\mathbf{X}$ with this method thus prematurely excludes scenarios, to which the analysis is not sensitive.

To avoid this in frequentist inference, a modified likelihood ratio can be used instead to calculate the confidence in the signal hypothesis [286, 287]. This CL_S method is, e.g., used to exclude mass ranges for the Higgs Boson at the LEP [288], Tevatron [289], and LHC [290, 291] experiments. Here, the confidence in the signal hypothesis $\mathcal{H}_{\mathbf{X}}$ is defined as

$$CL_S = \frac{P(Q > Q_{\text{obs}}|\mathcal{H}_{\mathbf{X}})}{P(Q > Q_{\text{obs}}|\mathcal{H}_0)}. \tag{8.2}$$

This corresponds to a weighting of the probability to get Q_{obs} if $\mathcal{H}_{\mathbf{X}}$ is true, with the confidence in the background-only hypothesis $\mathcal{H}_0$; points in parameter space with,
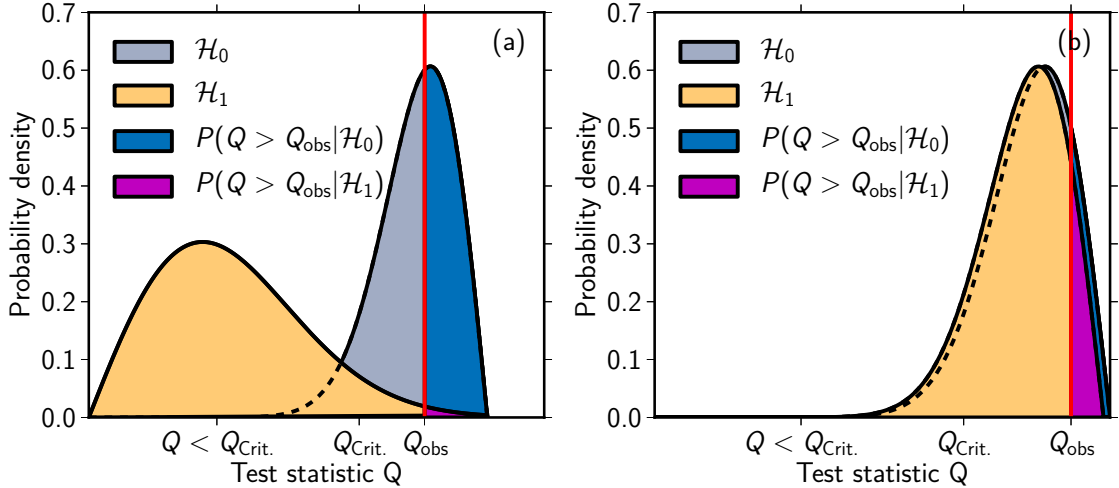
Figure 8.1: Statistical inference based on the test statistics Q for two hypothesis $\mathcal{H}_0$ and $\mathcal{H}_1$ given the observed value Q_{obs}. **(a)** Clear discrimination between $\mathcal{H}_0$ and $\mathcal{H}_1$ in the analysis. **(b)** The analysis cannot discriminate between $\mathcal{H}_0$ and $\mathcal{H}_1$.

e.g., $CL_S < 0.05$ are excluded at 95% confidence. Limits given by CL_S are considered as conservative, i.e. not excluding hypotheses that would be excluded by alternative approaches.

8.2 Limit on the Deflection Strength in the Extragalactic Magnetic Field

Assuming point sources, anisotropy in the arrival distribution of UHECR is reduced for increasing number of sources contributing to the observed flux and increasing strength of the deflection of the UHECR in magnetic fields. We describe deflections in the galactic magnetic field here using the regular component of the JF2012 model, which allows to set a limit on the deflection outside the galaxy in the simulated scenarios.

The number of sources contributing to the flux depends on the source density and the maximum distance up to which sources contribute to the observed UHECR flux. The maximum distance depends on the energy losses of the UHECR and the deflections; we thus use the density of point sources as additional free parameter here, and formulate the limit on the strength of the deflection in extragalactic magnetic field as a function of the source density. All other parameters are regarded here as nuisance parameters. To obtain a robust lower limit, we set the nuisance parameters in the simulations to values that mostly diminishes any anisotropic signal, as discussed in the following.

For a given number of sources, the anisotropic signal is stronger, if the sources are clustered than if they are distributed homogeneously. We thus simulate here homogeneous distributions of point sources, although the distribution of the proposed

sources (cf. chapter 2) correlates with the large scale distribution of matter in the universe.

The maximum distance up to which sources contribute to the observed UHECR flux is given by the energy loss of the particles in cosmic photon fields. Here, we discuss both types of energy losses that can be simulated with the PARSEC software separately. This results in a lower limit assuming protons, and a lower limit assuming the minimum anisotropic signal expected from nuclei propagation. In this scenario, the maximum propagation distance is modeled by assuming a constant charge $Z = 26$ and minimum interactions in photon fields. In both scenarios the photon densities are scaled with $\sim (1 + z)^3$. As this underestimates the non-CMB backgrounds, the propagation distance of the UHECR is here larger than expected from a realistic model (cf. section 2.3 and chapter 3).

The sources are modeled with a maximum energy of $E_{\max} = 1000\,\mathrm{EeV}$ and a spectral index of the sources of $\gamma = -2.7$; this choice of the spectral index results in an observed spectrum for the proton scenario best fitting to the spectrum measured with the Pierre Auger Observatory. However, to reduce sensitivity on the spectrum, the energies of the simulated UHECR are not chosen according to the simulated spectrum. Instead, UHECR with energies exactly matching the observed UHECR are distributed according to the simulated probability density maps. All sources are modeled with equal luminosity; the luminosity of the individual sources increases with redshift as $\sim (1 + z)^7$, the strongest expected increase for all source candidates (cf. section 2.2).

We scanned the parameter space at source densities $\rho = 10^{-6} - 10^{-3.5}\,\mathrm{Mpc}^{-3}$ in 31 logarithmically spaced steps. This range of source densities probes a wide range of densities of radio loud AGN (cf. section 2.1.3). For lower densities, it becomes unlikely to have a source in the simulations that is close enough to the Milky Way, to provide UHECR in the simulations with the highest energies observed. We could artificially select only simulations with a close source, but for source densities lower than $\sim 10^{-6}\,\mathrm{Mpc}^{-3}$ the closest source would always be the dominant source of UHECR as shown in figure 8.2. Lower source densities are thus not distinguishable by this analysis, and the limit obtained for $\sim 10^{-6}\,\mathrm{Mpc}^{-3}$ is therefore also approximately valid for lower source densities.

The strength of the extragalactic magnetic field in the PARSEC simulations is scanned from $B = 10^{-10} - 10^{-8}\,\mathrm{G}$ in the proton simulation and $B = 10^{-12} - 10^{-10}\,\mathrm{G}$ in the iron simulation; the correlation length of the extragalactic magnetic field is always set to $\Lambda = 1\,\mathrm{Mpc}$. This ranges for the magnetic field probe approximately the allowed range for the strength of the extragalactic magnetic field (cf. figure 2.6) and the angular resolution of the PARSEC simulations.

For the isotropic reference scenarios, the selected UHECR from data are scrambled by selecting a random right ascension while keeping the declination fixed. Thus, any declination dependent detector effect is still included in the simulated isotropic scenarios.

At every point in the parameter space, 200 independent realizations of $\mathcal{H}_{B,\rho}$ are simulated; for $\mathcal{H}_0$, 1000 realizations are created. The expected distributions of the observables for the anisotropic simulations are compared with the measurement and
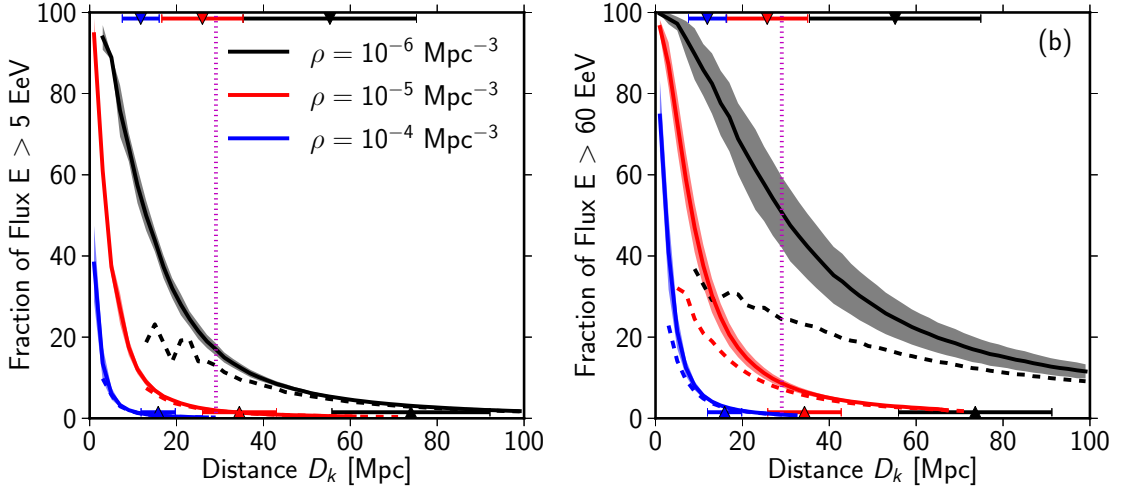
Figure 8.2: Fraction of UHECR above energy E that originate from the closest source (solid lines) and second closest source (dashed lines) with **(a)** $E > 5\,\text{EeV}$ and **(b)** $E > 60\,\text{EeV}$ in PARSEC simulations without magnetic fields for three choices of the source density ρ. Shaded areas denote the spread of the fraction from the closest source. Downward triangles at the top mark the average position of the closest source; upward triangles at the bottom mark the average position of the second closest source. The horizontal dotted line denotes the horizon for $200\,\text{EeV}$ protons (cf. section 3.2.2).

the isotropic distribution in figure 8.3 for selected points of the scanned parameter range.

The observed distribution of T_2 contains less signal-like regions than expected from isotropic simulations. Consequently, the observed likelihood ratio Q_{obs} is larger than the average Q expected from isotropic simulations; a high number of simulations are thus necessary for an accurate calculation of CL_S. To reduce the number of necessary computations, we calculate the probabilities $P(Q > Q_{\text{obs}}|\mathcal{H}_{\mathbf{X}})$ and $P(Q > Q_{\text{obs}}|\mathcal{H}_0)$ not using the simulated distributions of $T_{1,2,3}$ directly. Instead, we create $10\,000$ additional pseudo experiments by bootstrapping [292], i.e. sampling 53 random values of all simulated values of $T_{1,2,3}$ in every step of the bootstrap. The resulting distribution of likelihood ratios are shown in figure 8.4 for the distributions of $T_{1,2,3}$ shown in figure 8.3.

Within PARSEC, the deflections in the extragalactic magnetic field are assumed to be symmetric around the sources, resulting from long propagation distances through unstructured magnetic fields. For structured magnetic fields, and also for turbulent fields with short propagation distances, this overestimates the deflection strength. As the extragalactic magnetic field is likely structured, we report here primarily limits on
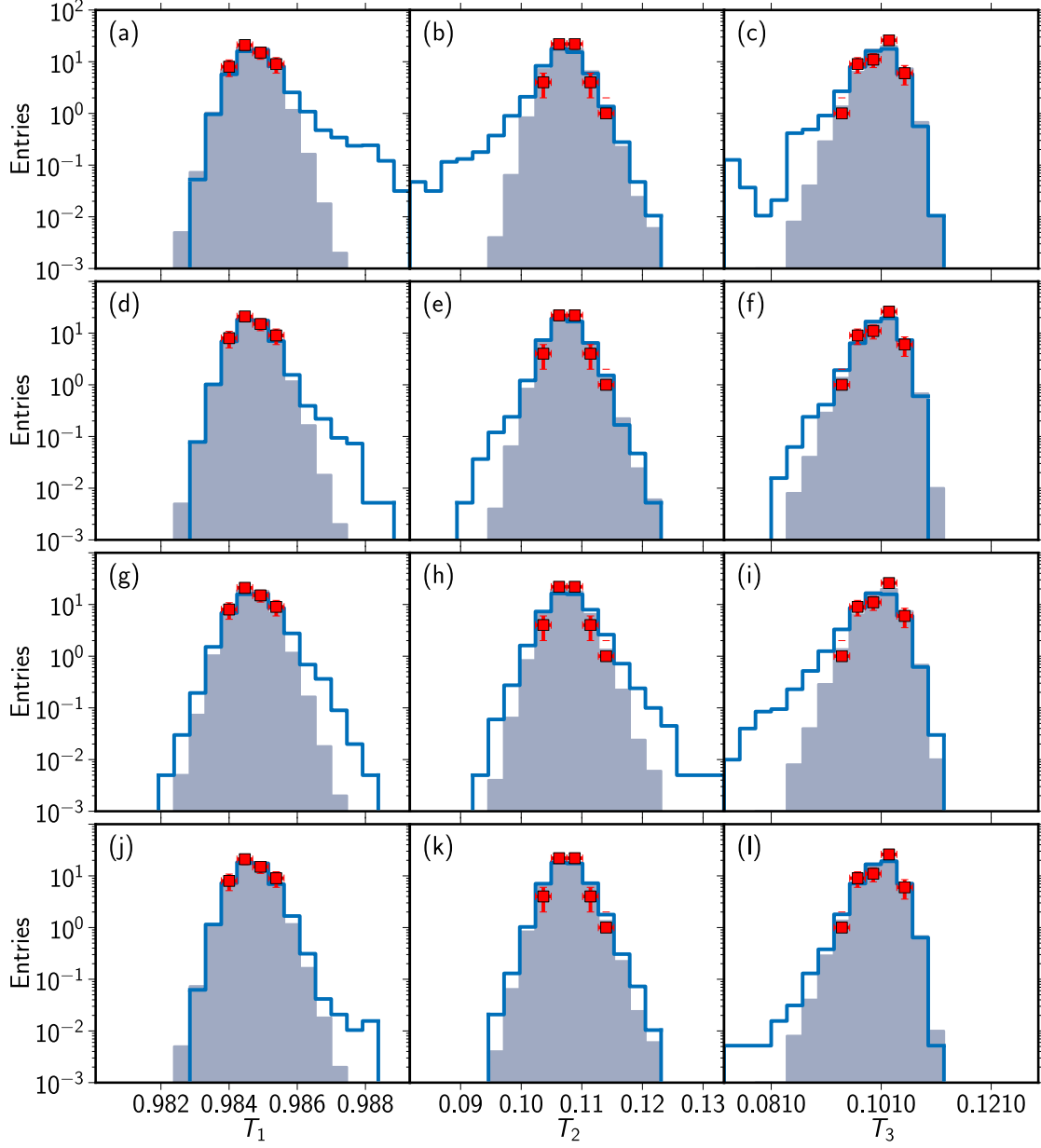
Figure 8.3: Observed distribution of the thrust T_1, thrust major T_2, and thrust minor T_3 (datapoints) compared with expected distribution of the observables in simulations at selected $\mathcal{H}_{B,\rho}$ (blue) and compared to $\mathcal{H}_0$ (gray). **(a-c)** Proton model with $B = 10^{-8.5}\,\text{G}$ and $\rho = 10^{-5.0}\,\text{Mpc}^{-3}$; **(d-f)** Proton model with $B = 10^{-8.3}\,\text{G}$ and $\rho = 10^{-3.7}\,\text{Mpc}^{-3}$; **(g-i)** Minimum anisotropy model with $B = 10^{-11}\,\text{G}$ and $\rho = 10^{-6.0}\,\text{Mpc}^{-3}$; **(j-l)** Minimum anisotropy model with $B = 10^{-11}\,\text{G}$ and $\rho = 10^{-5.0}\,\text{Mpc}^{-3}$.
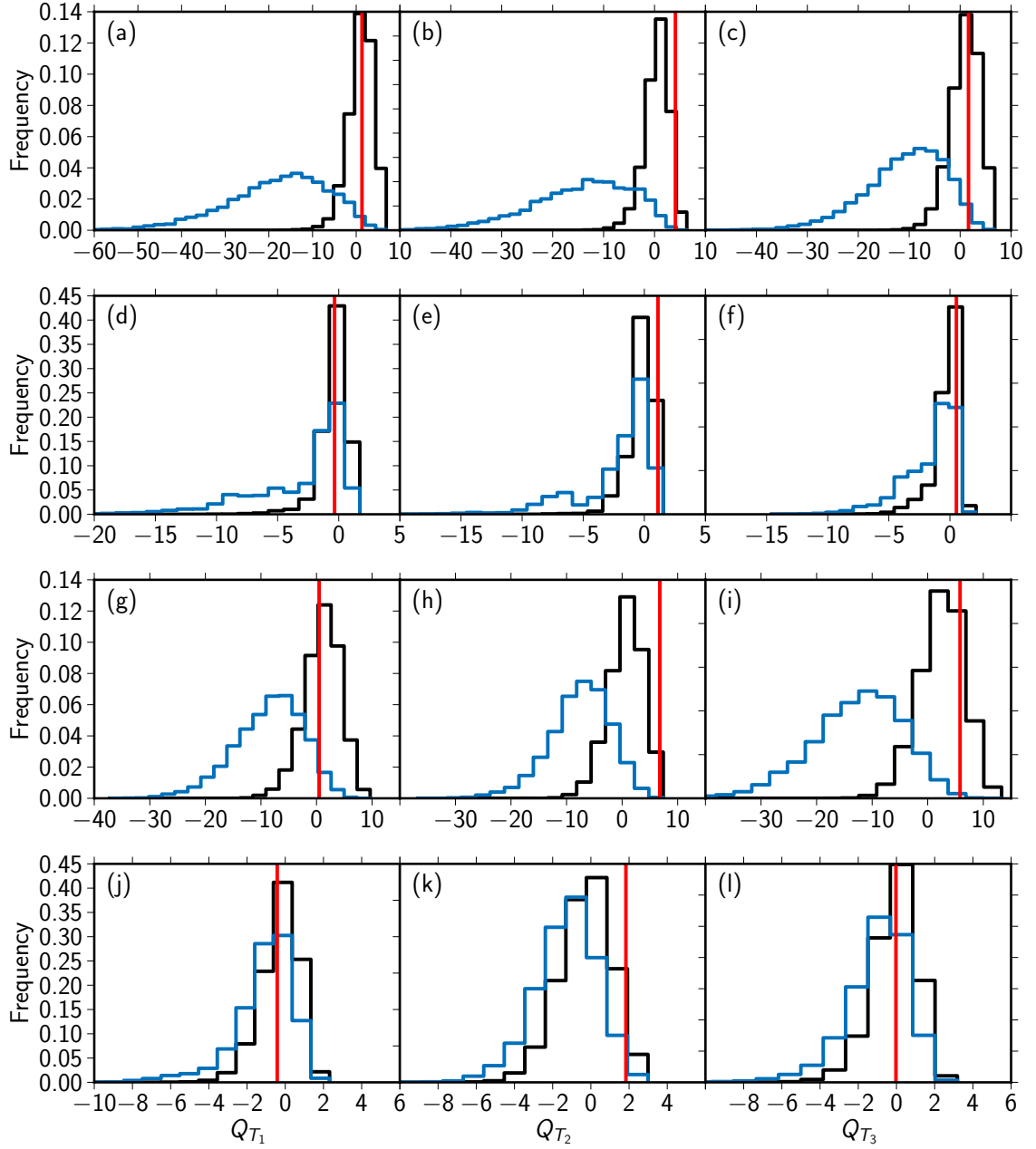
Figure 8.4: Distribution of likelihood ratios at selected (B, ρ) if $\mathcal{H}_{B,\rho}$ is true (blue), if $\mathcal{H}_0$ is true (black), and observed likelihood ratio Q_{obs} (red line). **(a-c)** Proton model with $B = 10^{-8.5}$ G and $\rho = 10^{-5.0}$ Mpc^{-3}; **(d-f)** Proton model with $B = 10^{-8.3}$ G and $\rho = 10^{-3.7}$ Mpc^{-3}; **(g-i)** Minimum anisotropy model with $B = 10^{-11}$ G and $\rho = 10^{-6.0}$ Mpc^{-3}; **(j-l)** Minimum anisotropy model with $B = 10^{-11}$ G and $\rho = 10^{-5.0}$ Mpc^{-3}.
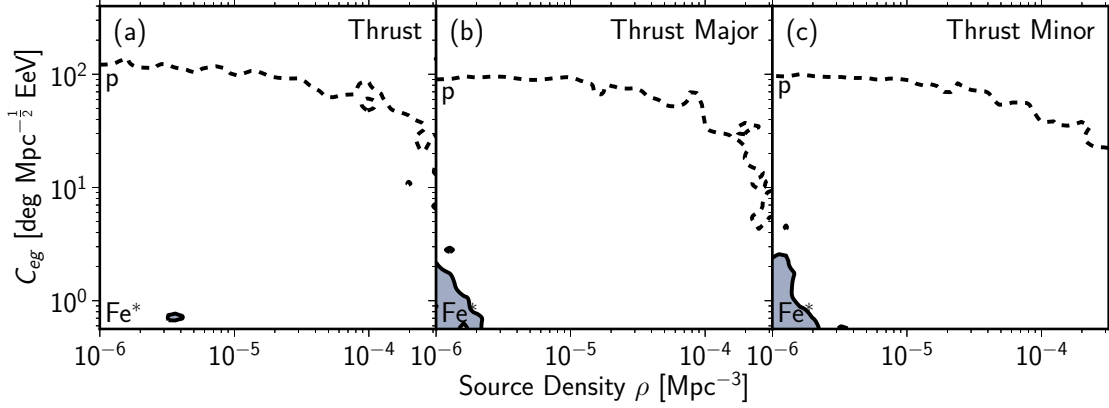
Figure 8.5: Lower limits ($CL_S < 0.05$) on the strength of the deflection in extragalactic magnetic fields C_{eg} and the density of point sources assuming a JF2012 galactic magnetic field. The dashed line marked with p assumes UHECR to be protons, the shaded area marked with Fe^* assumes minimum energy losses of all stable nuclei up to iron resulting in a maximum propagation distance and $Z = 26$ resulting in a maximum deflection in the galactic magnetic field.

the strength of the deflection C_{eg} with average deflection

$$\delta = C_{eg}\sqrt{\frac{D}{\mathrm{Mpc}}}\left(\frac{E}{\mathrm{EeV}}\right)^{-1} \tag{8.3}$$

for UHECR with energy E from a source in distance D (cf. eq. 2.17).

The resulting limits on the density of point sources ρ and the strength of deflection in extragalactic magnetic fields C_{eg} at $CL_S \leq 0.05$ are are shown in figure 8.5, independently for each of the three observables; discontinuities in the contours and isolated areas are attributable to the limited number of original simulations. The limits on the deflection strength are displayed as a function of the density of point sources for the simulation assuming protons as a dashed line marked with the letter 'p', and as gray shaded area marked with 'Fe*' for the minimum anisotropy model (cf. p. 33); all combinations of C_{eg} and ρ below these lines are excluded by this analysis.

If the UHECR are protons, the limits obtained from the individual observables are roughly identical. For a combined limit of all three observables, model dependent correlations of the observables need to be considered. However, here we conservatively exclude a scenario, if it is excluded in at least one observable, instead of combining the individual tests. Consequently, deflections lower than $20\,°\,\mathrm{Mpc}^{-1/2}\,\mathrm{EeV}$ outside the Milky Way are excluded by the measurement of T_3, even at the highest source density considered here. If sources occur only once per $1 \times 10^{-6}\,\mathrm{Mpc}^{-3}$ or less, deflections stronger than $100\,°\,\mathrm{Mpc}^{-1/2}\,\mathrm{EeV}$ are needed to simulate UHECR distributions compatible with the measurement.

The measurement of the thrust observable T_1 does not allow to set a robust lower limit using the minimum anisotropy signal scenario. By the analysis of the thrust
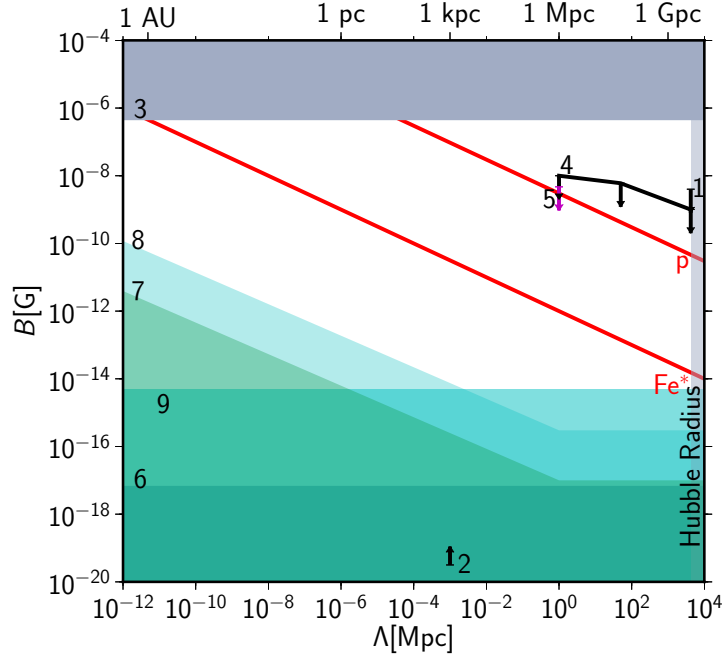
Figure 8.6: Comparison of the limits on the deflection strength obtained in this analysis (red lines) with other observational limits on the strength of the extragalactic magnetic field assuming an unstructured turbulent extragalactic magnetic field. Upper limits marked with '4' are from Faraday rotation measurements [213]. References to the other limtits are give in the caption of figure 2.6, p. 26.

major and thrust minor, deflections smaller than $\sim 2\,^\circ\,\mathrm{Mpc}^{-1/2}\,\mathrm{EeV}$ in the extragalactic magnetic field are excluded, if the density of sources is $\sim 1 \times 10^{-6}\,\mathrm{Mpc}^{-3}$ or less. For a source in the distance of $25\,\mathrm{Mpc}$ and UHECR with an energy $E = 5\,\mathrm{EeV}$, this strength of the deflection compares to the angular resolution of the simulation. Here thus only scenarios are excluded, in which the majority of UHECR are concentrated on few pixel of the extragalactic simulation.

Assuming that the extragalactic magnetic field is an unstructured turbulent field as described by Kolmogorov's theory of turbulence, the magnetic field strength in the PARSEC software can be compared with with observational limits on the field strength in voids [212–218] as shown in figure 8.6. For the proton simulations, the field strength has to be larger than $1\,\mathrm{nG}$ assuming a source density of $10^{-3.5}\,\mathrm{Mpc}^{-3}$ and a coherence length of $1\,\mathrm{Mpc}$. Thus only a small range of the field strengths B and the coherence length Λ is not excluded by the observations. In the minimum anisotropy simulation, the limit on the deflection corresponds to a lower limit of approximately $1 \times 10^{-12}\,\mathrm{G}$ for a coherence length of $1\,\mathrm{Mpc}$, assuming a source density of less than $10^{-6}\,\mathrm{Mpc}^{-3}$. The exclusion limit derived from this analysis is thus 2–3 orders of magnitude higher than the best lower limit resulting from Blazar observations. Here, of course, the assumption of an unstructured extragalactic magnetic field reduces the validity of these
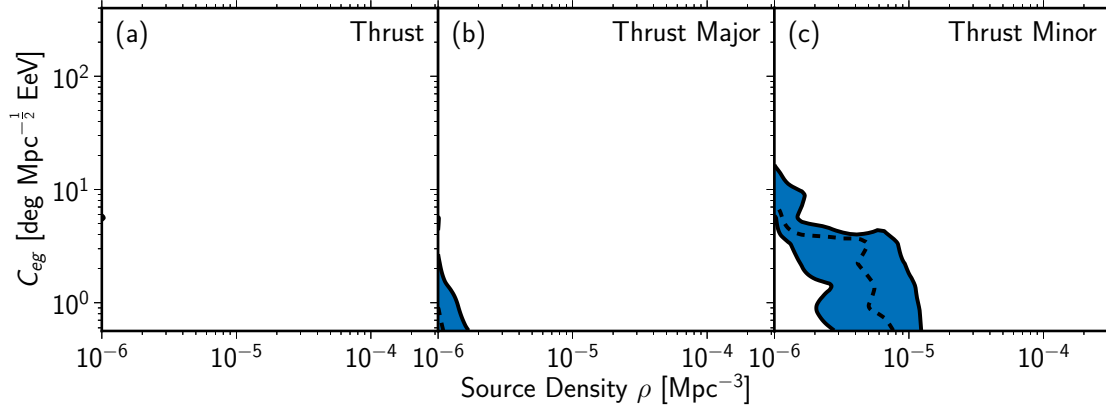
Figure 8.7: Expected exclusion limits on the deflection strength in the extragalactic magnetic field C_{eg} for 46 000 observed UHECR (dashed line) as a function of the source density. Here minimum energy losses of all stable nuclei up to iron resulting in a maximum propagation distance and $Z = 26$ resulting in a maximum deflection in the galactic magnetic field are assumed. The blue shaded area denotes the limits for a $\pm 1\sigma$ fluctuation of the observed likelihood ratio Q.

limits. Future progress in the simulation of UHECR propagation through detailed field models will, however, allow the derivation of robust lower limits on the field strength using this method and the measurement presented in this thesis.

The limits presented above are derived using 23 657 cosmic rays observed with 30 500 km² sr yr accumulated exposure. Up to 2018, the exposure accumulated by the Pierre Auger Observatory is expected to approximately double. In figure 8.7 the limits on the deflection strength in the minimum anisotropic signal model are shown, that are expected from a measurement of the thrust observables using 46 000 cosmic rays. In the analysis, it is assumed that the observables are measured only in the 53 ROI identified using the first 23 000 cosmic rays of the dataset to limit the overlap of the individual regions. If approximately two times the data becomes available, source densities up to $1 \times 10^{-5}\,\mathrm{Mpc}^{-3}$ and deflection strength up two $1\,°\,\mathrm{Mpc}^{-1/2}\,\mathrm{EeV}$ become testable by comparison of a measurement of the thrust minor with simulations of the maximum anisotropy model.

9 Conclusion

Within this work we developed a characterization of the directional energy distribution of UHECR. Our method quantifies the strength of collimation of energy along the system of principal axes of the distribution by adapting the thrust observables known in high energy physics to astroparticle physics. We demonstrated, that the principal axes of the directional energy distribution corresponds to the direction of deflection in cosmic magnetic fields. The distribution of the three thrust observables allows to test the data with respect to anisotropy in the distribution of the UHECR arrival directions based on patterns expected from deflections of cosmic rays in the extragalactic and galactic magnetic field.

The axes and observables have been measured in selected regions of the sky with a high quality sample of the data collected by the Pierre Auger Observatory up to November 2012. The uncertainties of the measurement are understood and allow comparisons of the measurement with results from simulated model scenarios. Before applying our method to data, we optimized the free parameters of the measurement with respect to a maximization of the potential to discover an anisotropic signal using simulations. The measurement of the three thrust observables presented here turned out to be compatible with an isotropic distribution of arrival directions of UHECR.

In addition, we demonstrated that the observed principal axes could still be non-trivial, so that an analysis of the map of axes could reveal information about the structure of cosmic magnetic fields. Here, we tested the non-triviality of the axes based on the reproducibility of the axes in subsets of the data. The axes are not reproducible if the data is split into 12 subsets. Therefore no evidence for the non-triviality of the map has been obtained in this work.

With the non-observation of an anisotropy signal in the measurement of the thrust observables all scenarios that predict anisotropic signal contributions are excluded. For the generation of pseudo experiments in scenarios with different choices of the density of point sources and deflections in the galactic and extragalactic magnetic field we developed the simulation software PARSEC in the course of this work. In the program, deflections in the galactic magnetic field are included using precalculated matrices that act on the probability distributions of the simulations. This technique provides a computationally performant method for the calculation of deflections in the galactic magnetic field in simulations of UHECR propagation, and therefore allows to disentangle deflections in the galactic magnetic field from deflections outside the Milky Way. Propagation outside the Milky Way is based on parametrizations of effects from deflection in the extragalactic magnetic field, energy losses, and cosmological effects. The parametrizations allow to estimate the anisotropic signal contributions as a function of the source density and strength of deflection in the extragalactic magnetic

field.

By comparison of the measured thrust observables with PARSEC simulations, we derived lower limits on the strength of the deflection in the extragalactic magnetic field as function of the density of point sources. Deflections in the galactic magnetic field were modeled with the regular component of the JF2012 model. For source densities compatible with radio loud AGN, we find that deflections stronger than $20\text{-}100\,^\circ\,\mathrm{Mpc}^{-1/2}\,\mathrm{EeV}$ outside the Milky Way are necessary, if the UHECR are protons. Assuming an unstructured extragalactic magnetic field, the field strength in voids has to be larger than $1\,\mathrm{nG}$ which is only marginally compatible with observations of Faraday rotations. This measurement thus suggests that the UHECR flux is not exclusively consisting of protons.

By modeling propagation of a hypothetical particle with $Z = 26$ and the minimum energy losses expected from nuclei, deflections smaller than $\sim 2\,^\circ\,\mathrm{Mpc}^{-1/2}\,\mathrm{EeV}$ in the extragalactic magnetic field can be excluded, if the density of sources is $\sim 1 \times 10^{-6}\,\mathrm{Mpc}^{-3}$ or less. This lower limit is at the edge of the angular resolution of the available Monte Carlo generator and based on conservative assumptions.

Further inferences from the measurement presented in this work will in particular be enabled by improved simulations of UHECR propagation through detailed three-dimensional models of the extragalactic magnetic field, that provide less conservative estimates of the anisotropic signal contributions than assumed here. However, we expect the lower limit resulting from comparison of the thrust minor measurement with the conservative simulations presented here to improve considerably within additional 6 years of operation of the Pierre Auger Observatory. If the sources of UHECR are bright radio loud AGN, a robust lower limit on the deflection strength in the extragalactic magnetic field can then be set following the analysis strategy developed in this work.

Appendices

A Design and Implementation of the PARSEC Software

PARSEC is implemented as C++ code with a Python interface. It is based on the Physics Extension Library (PXL) [293]. PXL is a collection of C++ libraries with a Python interface providing classes and templates for experiment independent high–level physics analysis. The usage of the PXL libraries facilitates modular object-oriented programming and allows graphical steering of the simulation components using the VISPA program [294].

The individual simulation steps are implemented as separate PXL modules which can be individually connected and configured to a simulation chain using the graphical user interface (GUI) of VISPA. A realization of a UHECR scenario is represented by a data container, which is consecutively processed by the following modules.

Source Model

Sources of UHECR are represented as individual objects. They are added to the realization with user defined coordinates in a Python or C++ module. An example module for isotropic source distributions is included in PARSEC. Modules generating sources, e.g. from astronomical catalogues, can be created by the users.

Extragalactic Field Model

From the sources in the simulation the probability vectors for extragalactic propagation are calculated for a user defined discretization of the energies and directions as described in chapter 3. The calculation is separated into C++ classes for the propagation, the energy loss, and the spectral index at the soruces, each based on an abstract interface. The abstract interfaces are implemented as subtypes for the random-walk propagation in turbulent fields, respectively the described energy loss for proton and iron UHECR. This polymorphic design enables users to modify and extend the individual components independently.

Galactic Field Model

For an angular resolution of the discretization better than $\approx 1°$ matrices of about 50000×50000 elements are needed. However, as in typical galactic field models particles from most directions are not distributed over the whole sky, the matrices $\mathcal{L}_i$ are only sparsely populated. The lenses for the galactic fields are consequently implemented using a common linear algebra library which features sparse matrices [295]. This enables calculation of eq. 3.14 with reasonable consumption of resources. PARSEC includes tools for generation of the lenses from backtracking data from the CRT program [53]

and CRPropa [239].

The galactic lenses are independent of the PARSEC module for the extragalactic propagation and can be used to calculate the deflection of individual cosmic rays. Spline interpolation and numeric integration routines used in the program are taken from the GNU Scientific Library [296].

Performance

The example simulation described in section 3.2.4 was performed in 6,690 sec using a single core of a Lenovo Thinkpad T400 notebook with 4 GB RAM and a Intel Core 2 Duo P8600 2.4GHz CPU. The notebook has been benchmarked with a SPECfp_base2006 rate of 12.2 and SPECint_base2006 rate of 15.1 [297]. Peak memory usage of the program was 0.5 GB; the size of the BSS_S magnetic lens on disk is 262 MB.

The individual cosmic ray flux from many sources at large distances to the observer add up to give an almost isotropic contribution. The computation time spent to calculate this background can be eliminated by aborting the calculation for every individual pixel and adding the total isotropic background contribution to every pixel. By this we introduce an error ϵ to $\vec{p}_{eg}^i$. To check if the upcoming contributions are isotropic and decide whether to abort the detailed calculation we proceed as follows: First, we divide the sources into 20 distance bins and calculate the contribution to $\vec{p}_{eg}^i$ from all sources in the first bin. We calculate a factor $a = L_{upc} \cdot (\max \vec{p}_{eg}^i - \min \vec{p}_{eg}^i)/(\max \vec{p}_{eg}^i + \min \vec{p}_{eg}^i)$ with $L_{upc} = \sum f_S$ being the integrated luminosity of all sources further away. If a is lower than a given cut off value, the upcoming luminosity is considered to be isotropic as the contribution from sources further away is more isotropic than from nearer sources. The flux from the upcoming bins is integrated and added once to all pixels in $\vec{p}_{eg}^i$. If a exceeds the selected cut off value, we proceed with
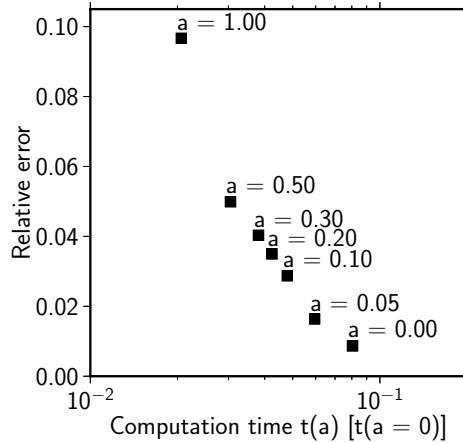
Figure A.1: Computation time for the example scenario and resulting error ϵ for different choices of the cut-off parameter a. Times are given in units of the time needed for the full calculation.

the sources in the next bin. The quantity a thus represents a measure of the strength of the anisotropic signal contribution not considered in the calculation.

In figure A.1 the resulting error $\epsilon = \|\mathbf{p}_{unbiased} - \mathbf{p}_{biased}\|_1$ is displayed as a function of the computation time for various values of the cut-off parameter a. Here, an examplary realization with an isotropic source distribution with density $1 \times 10^{-4}\,\mathrm{Mpc}^{-3}$ up to $1000\,\mathrm{Mpc}$ distance is used. The computation time can be reduced by an order of magnitude for $a = 0.05$ which introduces an uncertainty $\epsilon < 1\%$.

B Uncertainty of the Lenses for the Galactic Magnetic Field

From two realizations of the same model for the galactic magnetic field an upper limit of the introduced error can be derived as follows. For eq. 3.14 it is $\|\mathbf{p}_{obs.}\|_1 \leq 1$ as individual regions of the sky are suppressed. However, from $\boldsymbol{\mathcal{L}} \in \mathbb{R}^{N \times N}$ with $l_{m,n}$ we can generate

$$
\hat{\boldsymbol{\mathcal{L}}} = \begin{pmatrix} l_{1,1} & \cdots & l_{1,N} \\ \vdots & \ddots & \vdots \\ l_{N,1} & \cdots & l_{N,N} \\ s_1 & \cdots & s_N \end{pmatrix} \tag{B.1}
$$

with $\hat{\boldsymbol{\mathcal{L}}} \in \mathbb{R}^{N+1 \times N}$ and $s_n = 1 - \|\mathbf{l}_n\|_1$ such that $\hat{\boldsymbol{\mathcal{L}}} \cdot \mathbf{p}_{eg} = \hat{\mathbf{p}}_o$ with $\hat{\mathbf{p}}_o \in \mathbb{R}^{N+1}$ and $\hat{\mathbf{p}}_o^T = (p_1, \cdots p_N, s)$. s_n represents the suppression the UHECR flux from the extragalactic direction n and $s = \sum s_n$ the total suppression of $\mathbf{p}_{eg}$ by $\boldsymbol{\mathcal{L}}$. By this definitions it is $\|\hat{\mathbf{p}}_o\|_1 = 1$.

Let $\hat{\boldsymbol{\mathcal{L}}}_1$ be a realization of the 'true' lens $\hat{\boldsymbol{\mathcal{L}}}$, then application of $\hat{\boldsymbol{\mathcal{L}}}_1$ in eq. 3.14 introduces an uncertainty $\hat{\delta \mathbf{p}}$

$$
\hat{\boldsymbol{\mathcal{L}}}_1 \cdot \mathbf{p}_{eg} = \hat{\mathbf{p}}_o + \hat{\delta \mathbf{p}} \tag{B.2}
$$

which depends on the extragalactic probability density $\mathbf{p}_{eg}$, or the individual configurations of the source and extragalactic propagation models, respectively.

If $\mathbf{p}_{eg}$ is known, the uncertainty can be calculated, as we can approximate the true lens $\hat{\boldsymbol{\mathcal{L}}}$ by the mean of individual realizations. In the following calculations only two realizations $\hat{\boldsymbol{\mathcal{L}}}_1$ and $\hat{\boldsymbol{\mathcal{L}}}_2$ of $\hat{\boldsymbol{\mathcal{L}}}$ are used in order of clarity.

For two realizations the true lens can be approximated as $\hat{\boldsymbol{\mathcal{L}}} = \frac{1}{2}(\hat{\boldsymbol{\mathcal{L}}}_1 + \hat{\boldsymbol{\mathcal{L}}}_2)$. Using this we substitute $\hat{\boldsymbol{\mathcal{L}}}_1$ in eq. B.2 which yields

$$
\frac{1}{2}\boldsymbol{\delta}\hat{\boldsymbol{\mathcal{L}}} \cdot \mathbf{p}_{eg} = \hat{\delta \mathbf{p}} \tag{B.3}
$$

with $\boldsymbol{\delta}\hat{\boldsymbol{\mathcal{L}}} = \hat{\boldsymbol{\mathcal{L}}}_1 - \hat{\boldsymbol{\mathcal{L}}}_2$.

For

$$
\hat{\delta \mathbf{p}} = \epsilon \cdot \hat{\mathbf{p}}_o \tag{B.4}
$$

resembling a uniform uncertainty on the sky and unknown $\mathbf{p}_{eg}$ we can estimate ϵ by applying the unity norm $\|.\|_1$ to eq. B.3. Using the Cauchy—Schwarz inequality this reads

$$
|\epsilon| \leq \frac{1}{2}\|\boldsymbol{\delta}\hat{\boldsymbol{\mathcal{L}}}\|_1 \tag{B.5}
$$

as $\|\mathbf{p}_{eg}\|_1 = \|\hat{\mathbf{p}}_o\|_1 = 1$.

The definition of the unity norm reads $\|\boldsymbol{\delta}\hat{\boldsymbol{\mathcal{L}}}\|_1 = \max_n \|\hat{\delta \mathbf{l}}_n\|_1$ with $\hat{\delta \mathbf{l}}_n$ being the n-th column vector of $\boldsymbol{\delta}\hat{\boldsymbol{\mathcal{L}}}$.

Using $\boldsymbol{\hat{\delta L}}$ as in eq. B.3 and $\boldsymbol{\hat{L}}$ as in eq. B.1 $\hat{\delta l}_n = (\delta l_{1,n}, \cdots \delta l_{N,n}, \delta s_n)^T$ with $\delta l_{m,n} = l^1_{m,n} - l^2_{m,n}$ being the difference of the elements of the matrices $\boldsymbol{L}_{1,2}$ and $\delta s_n = s^1_n - s^2_n$ being the difference of the corresponding suppression factors. Thus we can write

$$\|\hat{\delta \mathbf{l}_\mathbf{n}}\|_1 = \sum_m |l^1_{m,n} - l^2_{m,n}| + |s^1_n - s^2_n| \tag{B.6}$$

$$= \sum_m \left| l^1_{m,n} - l^2_{m,n} \right| + \left| 1 - |l^1_{m,n}| - 1 + |l^2_{m,n}| \right| \tag{B.7}$$

$$= \|\boldsymbol{\delta L}_n\|_1 + \left| \|\boldsymbol{L}_1\|_1 - \|\boldsymbol{L}_2\|_1 \right| \tag{B.8}$$

using the definitions of the suppression factors. This yields

$$\epsilon \le \frac{1}{2}\|\boldsymbol{\hat{\delta L}}\|_1 = \frac{1}{2} \max_n \left(\|\delta \mathbf{L}_n\|_1 + \left| \|\boldsymbol{L}_1\|_1 - \|\boldsymbol{L}_2\|_1 \right| \right) \tag{B.9}$$

as an upper limit of the uncertainty of the lens.

The formalism can be extended to give an upper limit of the uncertainty in individual directions by substitution of the scalar ϵ in eq. B.5 with a diagonal matrix $\boldsymbol{\mathcal{E}}$ with elements $\epsilon_{m,m}$ being the relative uncertainty of the probability in pixel n. Following the same calculation steps as above this yields

$$\mathbf{e}^T_m \cdot \boldsymbol{\mathcal{E}} \cdot \hat{\mathbf{p}}_o = \frac{1}{2}\mathbf{e}^T_m \cdot \boldsymbol{\hat{\delta L}} \cdot \mathbf{p}_{eg} \tag{B.10}$$

with $\mathbf{e}_m$ beeing the unit vector in direction m. Consequently this transforms to

$$|\epsilon_{m,m}| \le \|\mathbf{e}^T_m \cdot \boldsymbol{\mathcal{E}}\|_1 \tag{B.11}$$

$$\le \frac{1}{2}\|\mathbf{e}^T_m \cdot \boldsymbol{\hat{\delta L}}\|_1 = \frac{1}{2} \max_n \hat{\delta \mathbf{l}}^{\mathbf{T}}_{\mathbf{m}} \tag{B.12}$$

with row vector $\hat{\delta \mathbf{l}}^T_m$ as upper limit of the uncertainty in a specific direction.

From two realizations of the lenses used in section 3.2 we found a maximum uncertainty of 23% for a UHECR energy of $10^{18.5}$ eV with an typical uncertainty for individual pixels of about 2%. The maximum uncertainty above energies of E = $10^{19.5}$ eV is less than 1%.

C Expectation Values of the Thrust Observables

The thrust observables $T_{k=1,2,3}$ have been introduced in eq. 4.1 reading

$$T_k = \max_{\vec{n}_k} \frac{\sum_i |\vec{p}_i \vec{n}_k|}{\sum_i |\vec{p}_i|} \tag{C.1}$$

which is repeated here for conveniance. The expectation value of T_k for N cosmic rays with momenta $\vec{p}_i$ is given by

$$< T_k > = \int d^N\vec{p} \ T_k(\vec{p}_i \cdots \vec{p}_N) F(\vec{p}_1 \cdots \vec{p}_N) \tag{C.2}$$

with probability density function $F(\vec{p}_1 \cdots \vec{p}_N)$ for the distribution of the UHECR momenta and $\int d^N\vec{p}$ denoting N integrations of $\vec{p}_i$ with $i = 1 \cdots N$ over the space of the UHECR momenta.

Without loss of generality, we set the center of the region of interest to the north pole, so that we can write eq. C.2 as

$$< T_k > = \int_0^\beta d^N\alpha \ \int_0^{2\pi} d^N\varphi \ \int_{E_{\min}}^{E_{\max}} d^NE \ \ T_k(\alpha_{1\ldots N}, \varphi_{1\ldots N}, E_{1\ldots N}) \ F(\alpha_{1\ldots N}, \varphi_{1\ldots N}, E_{1\ldots N}) \tag{C.3}$$

with α_i zenith angle, φ_i azimuth angle, E_i energy of the UHECR, and β size of the ROI. The UHECR are independent events, so that

$$F(\alpha_{1\ldots N}, \varphi_{1\ldots N}, E_{1\ldots N}) = \prod_j \hat{f}(\alpha_j, \varphi_j, E_j). \tag{C.4}$$

For an isotropic distribution of UHECR, i.e. energy and arrival directions are uncorrelated

$$\hat{f}(\alpha_j, \varphi_j, E_j) = f(\alpha_j) \cdot f(\varphi_j) \cdot f(E_j) \tag{C.5}$$

and uniformly distributed inside the ROI reading

$$f(\alpha_j) = \frac{\sin \alpha_j}{\int_0^\beta d\alpha_j \sin \alpha_j} = \frac{\sin \alpha_j}{1 - \cos \beta} \qquad \text{and} \qquad f(\varphi_j) = \frac{1}{2\pi}. \tag{C.6}$$

C.1 $< \tilde{T}_1 >$ with $\vec{n}_1$ fixed to the center of the ROI

We first fix $\vec{n}_1$ to the center of the region of interest and calculate the expectation value of eq. C.1, denoted with this $\vec{n}_1$ as $< \tilde{T}_1 >$. In this geometry the integration of the azimuth is trivial and

$$T_k = \frac{\sum_i E_i \cos \alpha_i}{\sum_i E_i}. \tag{C.7}$$

Using eq. C.4 - C.6 the expectation value thus reads

$$< \tilde{T}_1 > = \frac{1}{(1 - \cos \beta)^N} \int_0^\beta d^N\alpha \ \int_{E_{\min}}^{E_{\max}} d^NE \ \frac{\sum_i E_i \cos \alpha_i}{\sum_i E_i} \prod_j \sin \alpha_j f(E_j). \tag{C.8}$$
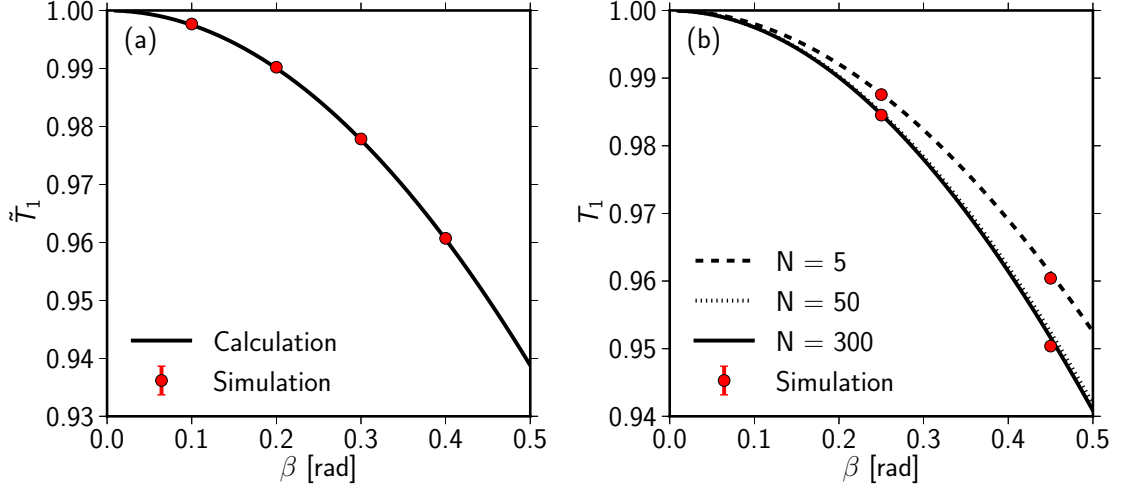
Figure C.1: Expectation value of the thrust observable for isotropic UHECR arrival distribution in dependency on the size of the region of interest β. **(a)** $< \tilde{T}_1 >$ with $\vec{n}_1$ fixed to the ROI center. **(b)** $< T_1 >$ with $\vec{n}_1$ pointing to the barycenter of the energy distribution of N particels with equal energy.

To solve the integral we first integrate over the angles $d\alpha_i$ with indices $i = j$ reading

$$\int_0^\beta \cdots \int_0^\beta d\alpha_i E_i \cos\alpha_i \sin\alpha_i \prod_{j \neq i} \sin\alpha_j = \frac{1}{2} E_i \prod_{j \neq i} \sin\alpha_j \sin^2\beta. \qquad (C.9)$$

Solving the remaining integrations over $d\alpha_i$ with $i \neq j$ yields

$$\int_0^\beta \cdots \int_0^\beta d\alpha_j \frac{1}{2} E_i \prod_{j \neq i} \sin\alpha_j \sin^2\beta = \frac{1}{2} E_i (1 - \cos\beta)^{N-1} \sin^2\beta. \qquad (C.10)$$

Consequently eq. C.8 becomes

$$< \tilde{T}_1 > = \frac{1}{2} \frac{\sin^2\beta (1 - \cos\beta)^{N-1}}{(1 - \cos\beta)^N} \int_{E_{\min}}^{E_{\max}} d^N E \frac{\sum_i E_i}{\sum_i E_i} \prod_j f(E_j). \qquad (C.11)$$

With $\int_{E_{\min}}^{E_{\max}} dE_j f(E_j) = 1$ as definition of the pdf. this reduces to

$$< \tilde{T}_1 > = \frac{1}{2} \frac{\sin^2\beta}{1 - \cos\beta} \qquad (C.12)$$

for the expectation value of the thrust observable with respect to the center of the region of interest. In figure C.1 (a) the expectation value $< \tilde{T}_1 >$ according to equation C.12 is shown as a function of β and compared to the mean of $\tilde{T}_1$ from Monte Carlo simulated isotropic UHECR.

C.2 $< T_1 >$ with $\vec{n}_1$ pointing to barycenter of the directional energy distribution in the ROI

The maximization of T_1 in eq. C.1 can be replaced by the condition that $\vec{n}_1$ points to the barycenter of the energy distributuion in the region of interest reading

$$\vec{n}_1 = \frac{\sum_i \vec{p}_i}{|\sum_i \vec{p}_i|}. \tag{C.13}$$

If the ROI covers less than one semisphere, the thrust can thus be written as

$$T_1 = \frac{\sum_i \left| \vec{p}_i \frac{\sum_j \vec{p}_j}{|\sum_j \vec{p}_j|} \right|}{\sum_j |\vec{p}_j|} \overset{\beta \le \frac{\pi}{2}}{=} \frac{|\sum_i \vec{p}_i|}{(\sum_i E_i)} \tag{C.14}$$

or in spherical coordinates

$$T_1 = \frac{1}{(\sum_i E_i)} \cdot \sqrt{\left(\sum E_i \sin \alpha_i \sin \varphi_i\right)^2 + \left(\sum E_i \sin \alpha_i \cos \varphi_i\right)^2 + \left(\sum E_i \cos \alpha_i\right)^2}. \tag{C.15}$$

The square root in eq. C.15 prohibits a direct integration of the expectation value $< T_1 >$.

To approximate a solution, we set

$$1 + x = \frac{1}{(\sum_i E_i)^2} \left[\left(\sum E_i \sin \alpha_i \sin \varphi_i\right)^2 + \left(\sum E_i \sin \alpha_i \cos \varphi_i\right)^2 + \left(\sum E_i \cos \alpha_i\right)^2 \right]. \tag{C.16}$$

As the right side of eq. C.16 is smaller than one, also $|x| \lesssim 1$ so that the series

$$\sqrt{1 + x} = \sum_{n=0}^{\infty} \binom{2n}{n} \frac{(-1)^n}{(1 - 2n)4^n} x^n \tag{C.17}$$

converges pointwise. The expectation value for the thrust of isotropically distributed UHECR can thus be written as

$$< T_1 > = \sum_{n=0}^{\infty} \binom{2n}{n} \frac{(-1)^n}{(1 - 2n)4^n} \int_{E_{\min}}^{E_{\max}} d^N E \int_0^\beta d^N \alpha \int_0^{2\pi} d^N \varphi \left[\frac{1}{(\sum_i E_i)^2} \left(\left(\sum E_i \sin \alpha_i \sin \varphi_i\right)^2 \right. \right.$$

$$\left. \left. + \left(\sum E_i \sin \alpha_i \cos \varphi_i\right)^2 + \left(\sum E_i \cos \alpha_i\right)^2 \right) - 1 \right]^n \prod_k f(E_k) f(\alpha_k) f(\varphi_k) \tag{C.18}$$

If the sum is truncated, we get an approximation of $< T_1 >$; the approximation is better for small x. Here x is small if all angles α_i are small, which is the case for small regions of interest as $\alpha_i < \beta$.

We truncate terms with $n \geq 2$ yielding

$$
\begin{aligned}
< T_1 > \simeq \frac{1}{2} + \frac{1}{2} \int_{E_{\min}}^{E_{\max}} d^N E \int_0^\beta d^N \alpha \int_0^{2\pi} d^N \varphi \; \frac{1}{(\sum_i E_i)^2} \Bigg[\left(\sum E_i \sin \alpha_i \sin \varphi_i \right)^2 \\
+ \left(\sum E_i \sin \alpha_i \cos \varphi_i \right)^2 + \left(\sum E_i \cos \alpha_i \right)^2 \Bigg] \prod_k f(E_k) f(\alpha_k) f(\varphi_k)
\end{aligned}
\tag{C.19}
$$

$$
= \frac{1}{2}(1 + < T_1^2 >)
$$

as approximation of the expectation value of the thrust observable in a ROI with isotropically distributed UHECR. The calculation of $< T_1^2 >$ is given in the next section of this appendix.

Assuming that all N UHECR in the ROI have the same energy E_c, then $f(E_k) = \delta(E_c - E_k)$ with Dirac delta distribution δ. For this case eq. C.28 reads as

$$
< T_1^2 > = (< \tilde{T}_1 >)^2 + (1 - (< \tilde{T}_1 >)^2) \frac{1}{N}
\tag{C.20}
$$

and $< T_1 >$ can be caluclated. For this example, the expectation value of the thrust observable is displayed together with results from simulations as a function of the size of the ROI β for three choices of N in figure C.1 (b).

C.3 Expectation Value of $< T_1^2 >$

Using eq. C.15 the expectation value of the squared thrust reads

$$
\begin{aligned}
< T_1^2 > = \int_0^\beta \cdots \int_0^\beta d\alpha_i \int_0^{2\pi} \cdots \int_0^{2\pi} d\varphi_i \int_{E_{\min}}^{E_{\max}} \cdots \int_{E_{\min}}^{E_{\max}} dE_i \frac{1}{(\sum_i E_i)^2} \\
\cdot \Bigg[\left(\sum E_i \sin \alpha_i \sin \varphi_i \right)^2 + \left(\sum E_i \sin \alpha_i \cos \varphi_i \right)^2 + \left(\sum E_i \cos \alpha_i \right)^2 \Bigg] \\
\cdot \prod_k f(\alpha_k) \cdot f(\varphi_k) \cdot f(E_k)
\end{aligned}
\tag{C.21}
$$

To simplify eq. C.21 we first integrate over $d\varphi_i$ resulting in

$$
\begin{aligned}
< T_1^2 > = \int_0^\beta \cdots \int_0^\beta d\alpha_i \int_{E_{\min}}^{E_{\max}} \cdots \int_{E_{\min}}^{E_{\max}} dE_i \frac{1}{(\sum_i E_i)^2} \\
\cdot \Bigg[\sum_i E_i^2 \sin^2 \alpha_i + \left(\sum_i E_i \cos \alpha_i \right)^2 \Bigg] \cdot \prod_k^N f(\alpha_k) f(E_k).
\end{aligned}
\tag{C.22}
$$

Using the multinomial theoreme this can be written as

$$
\begin{aligned}
< T_1 > = \int_0^\beta \cdots \int_0^\beta d\alpha_i \int_{E_{\min}}^{E_{\max}} \cdots \int_{E_{\min}}^{E_{\max}} dE_i \frac{1}{(\sum_i E_i)^2} \\
\cdot \Bigg[\sum_i \left(E_i^2 \left(\sin^2 \alpha_i + \cos^2 \alpha_i \right) + E_i \cos \alpha_i \sum_{j \neq i} E_j \cos \alpha_j \right) \Bigg] \\
\cdot \prod_k^N f(\alpha_k) f(E_k).
\end{aligned}
\tag{C.23}
$$

For the integration over α_i we write

$$\sum_i E_i \cos \alpha_i \sum_{j \neq i} E_j \cos \alpha_j \cdot \prod_k^N f(\alpha_k) \sim \tag{C.24}$$

$$\cos \alpha_1 \cos \alpha_2 \sin \alpha_1 \cdot \sin \alpha_2 \cdots + \cos \alpha_1 \cos \alpha_3 \sin \alpha_1 \cdot \sin \alpha_2 \cdots + \cdots$$

which integrates to

$$\frac{1}{2} \sin^2 \alpha_i |_0^\beta \cdot \frac{1}{2} \sin^2 \alpha_j |_0^\beta \cdot \left((-\cos)|_0^\beta \right)^{N-2}. \tag{C.25}$$

Consequently we get

$$< T_1^2 > = \int_{E_{\min}}^{E_{\max}} \cdots \int_{E_{\min}}^{E_{\max}} dE_i \left[\frac{\sum_i E_i^2}{(\sum_i E_i)^2} \right. \\ \left. + \frac{1}{(\sum_i E_i)^2} \left(\left(\frac{1}{2} \frac{\sin^2 \beta}{(1 - \cos \beta)} \right)^2 \sum_i E_i \sum_{j \neq i} E_j \right) \right] \cdot \prod_k^N f(E_k). \tag{C.26}$$

With $\sum_i E_i \sum_{i \neq j} E_j = (\sum E_i)^2 - \sum E_i^2$ and substituting $< \tilde{T}_1 >$ from eq. C.12 the integrand can be written as

$$\frac{1}{(\sum E_i)^2} \left[\sum E_i^2 + (< \tilde{T}_1 >)^2 \cdot \left((\sum E_i)^2 - \sum E_i^2 \right) \right] \\ = \frac{1}{(\sum E_i)^2} \left[(< \tilde{T}_1 >)^2 (\sum E_i)^2 + (1 - (< \tilde{T}_1 >)^2) \sum E_i^2 \right]. \tag{C.27}$$

This finally yields

$$< T_1^2 > = (< \tilde{T}_1 >)^2 + (1 - (< \tilde{T}_1 >)^2) \int_{E_{\min}}^{E_{\max}} d^N E \, \frac{\sum_i E_i^2}{(\sum_i E_i)^2} \prod_k^N f(E_k). \tag{C.28}$$

which cannot simplified further without specifying the energy distribution of the UHECR.

D Probability Distributions of the Thrust Observables in Typical PARSEC Simulations
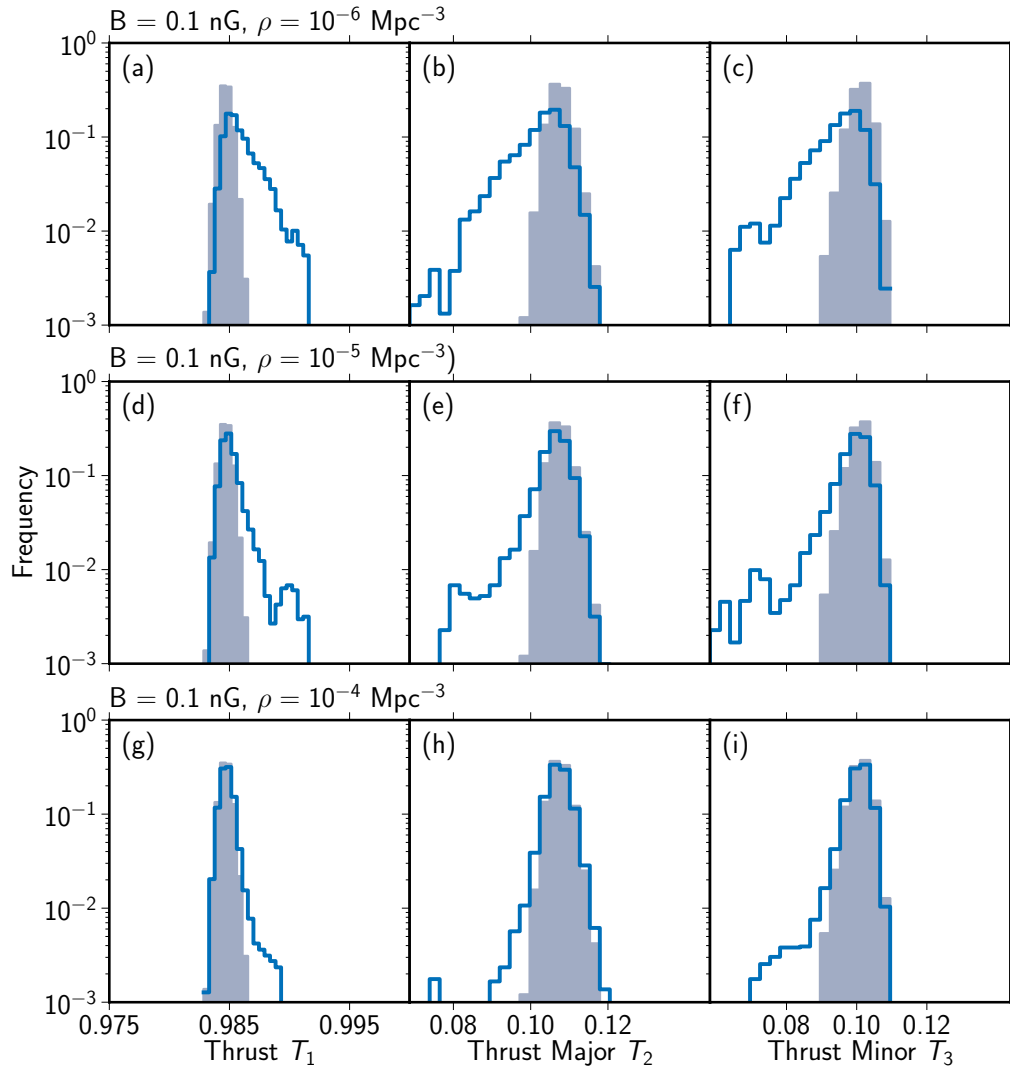
Figure D.1: Probability distribution of the thrust observables $T_{1,2,3}$ in PARSEC simulations with strength of the extragalactic magnetic field B, homogeneously distributed points sources with density ρ, and a JF galactic magnetic field (blue histogram). The gray shaded histogram indicates the isotropic expectation.
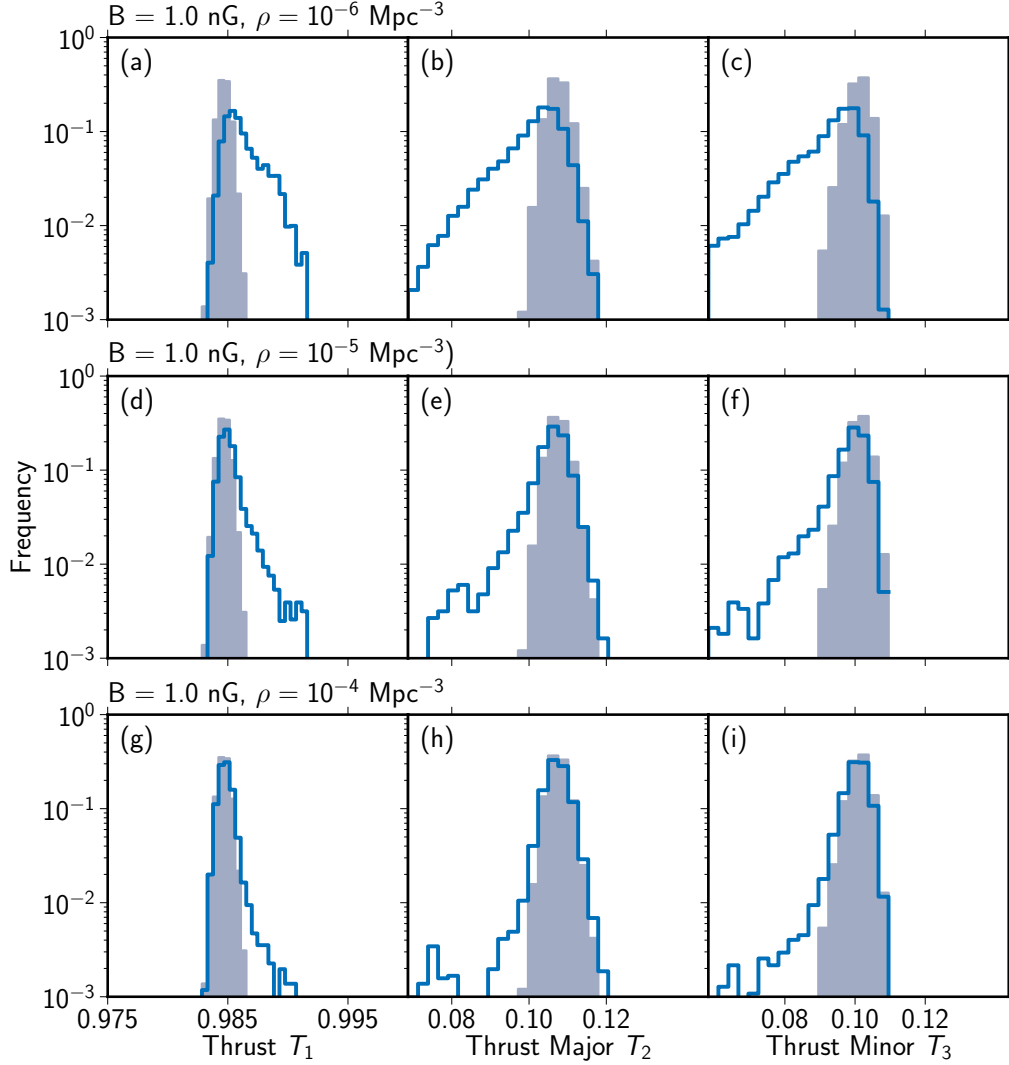
Figure D.2: Probability distribution of the thrust observables $T_{1,2,3}$ in PARSEC simulations with strength of the extragalactic magnetic field B, homogeneously distributed points sources with density ρ, and a JF galactic magnetic field (blue histogram). The gray shaded histogram indicates the isotropic expectation.
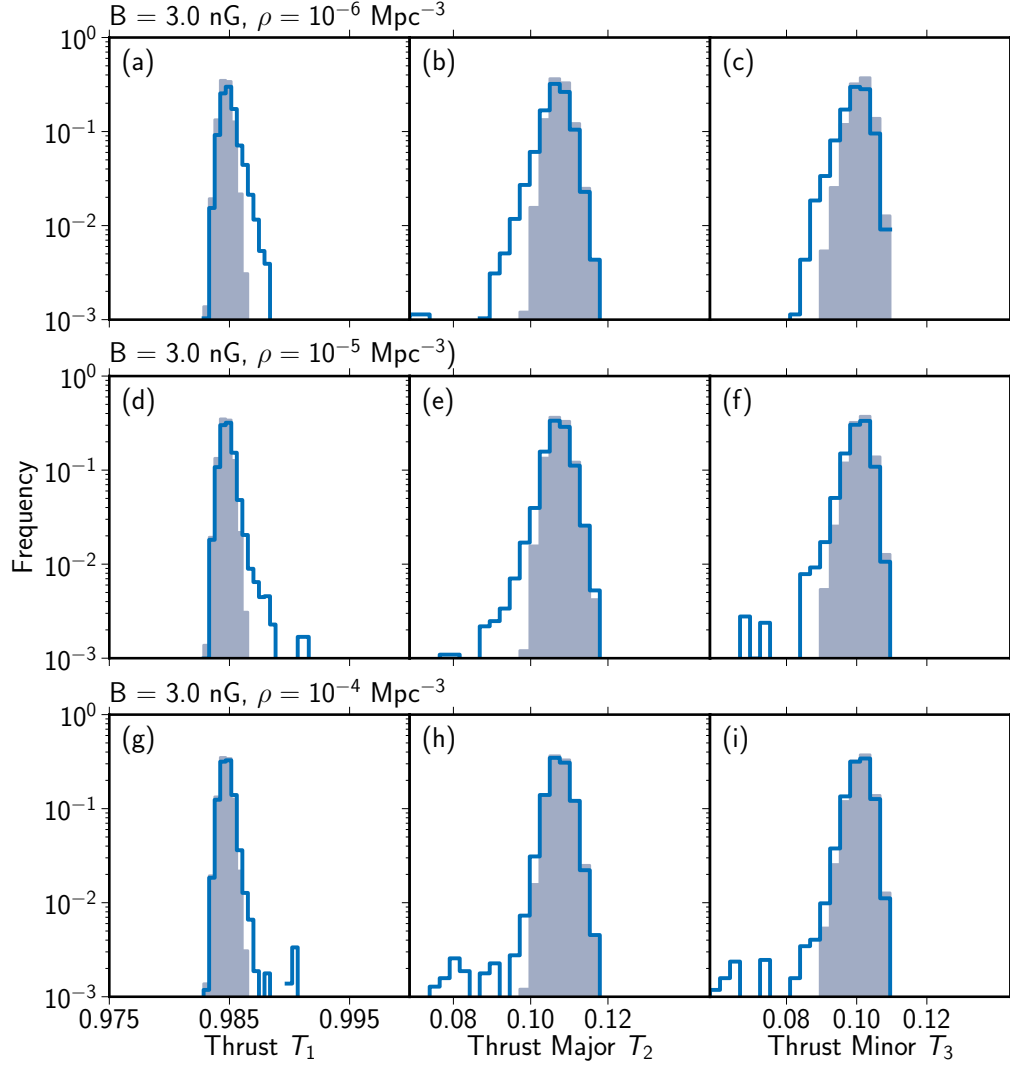
Figure D.3: Probability distribution of the thrust observables $T_{1,2,3}$ in PARSEC simulations with strength of the extragalactic magnetic field B, homogeneously distributed points sources with density ρ, and a JF galactic magnetic field (blue histogram). The gray shaded histogram indicates the isotropic expectation.

E Tests on Structure in the Distribution of $\vec{n}_2$

To investigate methods on the distribution of thrust major axes, we calculated the test power of the method to distinguish between simulations of isotropically distributed UHECR and UHECR from PARSEC simulations with a BSS_S model for the galactic magnetic field, $3\,\mathrm{nG}$ and $7\,\mathrm{nG}$ strength of the extragalactic magnetic field, and a source density of $1 \times 10^{-5}\,\mathrm{Mpc}^{-3}$. We investigated two methods on the global, i.e. all ROI, distribution of axes, and two methods sensitive to local, i.e. ROI on parts of the sphere, deviations from isotropically distributed axes.

E.1 Tests on the Global Distribution of Axes

Coherent deflections in the galactic magnetic field might lead to a global structure in the distributions of thrust major axes. We investigated a preferred angle to the galactic plane, i.e. $\vec{n}_2 \angle \vec{e}_\phi$ with unit vector $\vec{e}_\phi$, using Kuiper's test and also the global distribution of $\vec{n}_2$ with Rayleigh's test.

Kuiper's Test

The Kuiper test is the extension of a rotationally invariant form of the Kolmogorov–Smirnov (KS) test. For the one sided KS-test on compatibility of the observed cumulative distribution $S_n(\theta)$ and the expected cumulative distribution $F(\theta)$,

$$D_n^+ = \max_\theta(S_n(\theta) - F(\theta)) \quad \text{or} \quad D_n^- = \max_\theta(F(\theta) - S_n(\theta)) \tag{E.1}$$

is used as test statistic. In periodic space both $D^\pm$ depend on the choice of the zero direction. In Kuiper's test, $V_n = D_n^+ + D_n^-$ is used as test statistic instead, as it is invariant under rotations [255]. In the investigated simulations, Kuiper's test on the distribution of the angle of the thrust major axis to the galactic plane has no discriminative power.

Rayleigh's Test

Rayleigh's test on spherical distributed data uses the resultant length R given by eq. 4.7 as test statistic. For discrimination between uniform distributed directions as null-Hypothesis and concentrated directions whose distribution follows an unimodal Fisher distribution (cf. eq. 3.7), Rayleigh's test is the uniformly most powerful (UMP) test [255]. No significant deviations from isotropically distributed axes were found in the simulations with Rayleigh's test.

E.2 Tests on Local Distribution of Axes

Structures in the distribution of axes resulting from deflections in the galactic magnetic field are likely not identical on the full sphere, but are localized only in specific regions. Two investigated methods have discriminative power in the investigated simulations. However, all identified anisotropic scenarios are also distinguishable from isotropy by the autocorrelation of events with $E > 60\,\mathrm{EeV}$. Therefore the methods are not primarily sensitive on the distribution of axes, but the clustering of the ROI.

Cluster Search Algorithm

An algorithm to search for cluster of aligned axes is designed as follows. In the first step, as sketched in figure E.1 (a), starting with an arbitrary ROI (magenta), the thrust axes of all other ROI within a search radius r are compared to the one of the initial ROI. If the angle between the axes is smaller than a critical value $\Delta\xi_{\max}$, the ROI are associated (blue lines) with the first ROI. This is repeated for all other ROI (fig. E.1 (b)). Finally, a cluster is defined as set of connected ROI (fig. E.1 (c)). The number of ROI participating in the cluster defines its 'cluster size' C.
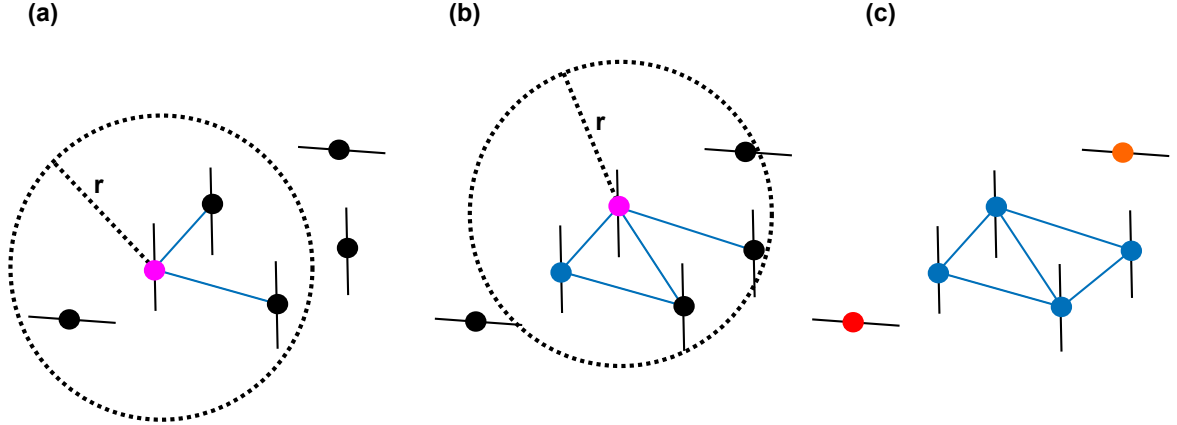
Figure E.1: Illustration of the cluster algorithm described in the text. **(a,b)** Testing of clustering of angles within a search radius around a region. **(c)** Final state of the algorithm.

In the so defined cluster, the angle between two thrust major axes may be larger than $\Delta\xi_{\max}$ as it is only required that the angle between the thrust axes of nearby ROI is small. If no ROI with aligned direction is found, the ROI constitutes a cluster of size $C = 1$. Every individual ROI participates therefore in one and only one cluster.

To compare sets of ROI with this algorithm, we use the distribution of cluster sizes C as test statistic. For several variations of the free parameters of the algorithm, the search radius and the maximum angle between the thrust major axes that are regarded as correlated, no higher test power than using autocorrelation was achieved with this algorithm.

Modified Contiguity Ratio

Spatial autocorrelation of N observations $X_{i,j}$ can be quantified by the contiguity ratio

$$C = \frac{(N-1)\sum_i \sum_j w_{i,j}(X_i - X_j)^2}{2W \sum_i (X_i - \bar{X})} \tag{E.2}$$

where i, j denote the location of the observation and $w_{i,j}$ a weight between the regions with $\sum_{i,j} w_{i,j} = W$, i.e. a degree of contiguity [298]. If the data in neighbouring regions are anti-correlated eq. E.2 yields $-1 < C < 0$ and $0 < C < 1$ otherwise.

We modified eq. E.2 to account for the spherical distribution of observations and the observations of directions reading

$$\tilde{C} = \frac{(N-1)\sum_i \sum_j w_{i,j}(\vec{n}_i - \vec{n}_j)^2}{2W \sum_i (X_i - \bar{X})} \tag{E.3}$$

with weights $w_{i,j} = |\vec{r}_i - \vec{r}_j|^{-1}$ and $\vec{r}_{i,j}$ vector to the center of the ROI. Calculating $\tilde{C}$ from all pair of ROI, no higher test power than using the autocorrelation was achieved with this algorithm..

Mathematical Notation and Symbols

$\vec{a}$	Vector in three dimensional Euclidean space (denoted by a small arrow)
$\mathbf{X}$	Element of arbitrary N-dimensional vector space (printed as bold symbol)
$\mathcal{M}$	Matrix (printed as bold calligraphic symbol)
$\langle x \rangle$	Expectation value of x
$\vec{e}_r, \vec{e}_\phi, \vec{e}_\theta$	Unit vectors of spherical coordinate system
J_0	Bessel function of the first kind and order zero
I_0	Modified Bessel function of the first kind and order zero
$\mathcal{H}_0, \mathcal{H}_\mathbf{X}$	Null-hypothesis, respectively alternative hypothesis parameterized by parameters $\mathbf{X}$
$\mathcal{L}_{\mathcal{H}_0}, \mathcal{L}_{\mathcal{H}_\mathbf{X}}$	Likelihood of the null-hypothesis, respectively the alternative hypothesis parameterized by $\mathbf{X}$
Q	Likelihood ratio $Q = -2 \ln \frac{\mathcal{L}_{\mathcal{H}_{\mathcal{H}_\mathbf{X}}}}{\mathcal{L}_{\mathcal{H}_0}}$

UHECR Propagation

$\mathbf{p}^i_{eg}, \mathbf{p}^i_{obs}$	Probability vectors of the directional UHECR distribution in energy bin i outside the Milky Way and seen by an observer on Earth (p. 38)
L_k	Luminosity of source k (p. 43)
γ	Spectral index of the injection spectrum of an UHECR source (p. 39)
f_S, f_E, f_B	Factors modeling the contribution of a source to the UHECR flux (p. 39)
E_i^l, E_i^r	Left and right edges of the energy bin i at the source (p. 38)
z	Red shift (p. 24)
z_g	Red shift at time of injection of the particle (p. 39)
L_{ad}, L_γ	Energy loss lengths due to adiabatic expansion and photon interaction (p. 25, 26, 39)
B	Rms of the strength of the turbulent extragalactic magnetic field (p. 32, 40)
Λ	Coherence length of the turbulent extragalactic magnetic field (p. 32, 40)
σ	Deflection strength, i.e. rms of the scattering angle of the source for small deflections (p. 32, 40)
κ	Concentration parameter of the Fisher and von Mises distributions (p. 41, 100)

$\mathcal{L}_i$	Matrix describing the deflections in the galactic magnetic field in energy bin i (p. 45)
ρ	Density of point sources (p. 55)

Measurement and Interpretation

$T_{1,2,3}$	Thrust (major, minor) value (p. 58)
$\vec{p}_i$	Momentum of particle with index i (p. 58)
$\vec{n}_{1,2,3}$	Thrust (major, minor) axis (p. 58)
$\xi_{2,3}$	Angle of the thrust major (minor) axis to the unit vector $\vec{e}_\phi$ (p. 59)
β	Size of the regions of interest (p. 58)
C_T	Strength of the energy dependent symetric deflection in the toy model used to simulate effects of turbulent fields (p. 60)
C_C	Strength of the energy dependent directed deflection in the toy model used to simulate effects of coherent fields (p. 61)
E_{seed}	Energy of the seed particle used to define a region of interest (p. 67)
E_{min}	Minimum energy of the particles included in the calculation of the thrust observables (p. 67)
R	Resultant length (p. 63)
V	Circular variance (p. 63)
f_u	Probability density function of the uniform distribution on the circle (p. 98)
f_{CN}	Probability density function of the circular normal (von Mises) distribution (p. 100)
f_C	Combined probability density function of the signal + background model (p. 101)
N, N_S, N_B	Total number of ROI, number of ROI with signal contribution and number of ROI with background only (p. 104)
N_u, N_u^S, N_u^B	Total number of UHECR in a ROI, number of signal UHECR, and number of background UHECR (p. 104)
CL_S	Confidence in the signal hypothesis (p. 108)
C_{eg}	Stength of the deflection in the extragalactic magnetic field (p. 114)

References

[1] D. Pacini, *Penetrating Radiation at the Surface of and in Water*, trans. by A. De Angelis, Nuovo Cimento **6**, 93, arXiv: 1002.1810 (1912).

[2] V. Hess, *Über Beobachtungen der durchdringenden Strahlung bei sieben Freiballonfahrten*, Physikalische Zeitschrift **13**, 1084–1091 (1912).

[3] J. Clay and H. P. Berlage, *Variation der Ultrastrahlung mit der geographischen Breite und dem Erdmagnetismus*, Die Naturwissenschaften **37**, 687 (1932).

[4] T. H. Johnson, *Evidence that protons are the primary particles of the hard component*, Reviews of Modern Physics **11**, 208–210 (1939).

[5] M. Schein, W. P. Jesse, and E. O. Wollan, *The Nature of the Primary Cosmic Radiation and the Origin of the Mesotron*, Physical Review **59**, 615–615 (1941).

[6] P. Freier et al., *Evidence for Heavy Nuclei in the Primary Cosmic Radiation*, Physical Review **74**, 213–217 (1948).

[7] P. Freier et al., *The Heavy Component of Primary Cosmic Rays*, Physical Review **74**, 1818–1827 (1948).

[8] D. J. Bird et al., *Evidence for correlated changes in the spectrum and composition of cosmic rays at extremely high energies*, Physical Review Letters **71**, 3401–3404 (1993).

[9] D. J. Bird et al., *Detection of a cosmic ray with measured energy well beyond the expected spectral cutoff due to cosmic microwave radiation*, Astrophysical Journal **441**, 144–150, arXiv: astro-ph/9410067 (1995).

[10] K.-H. Kampert and A. A. Watson, *Extensive Air Showers and Ultra High-Energy Cosmic Rays: A Historical Review*, European Physical Journal H **37**, 359–412, arXiv: 1207.4827 (2012).

[11] T. Stanev, *Ultrahigh Energy Cosmic Rays: Review of the Current Situation*, arXiv: 1210.0927 (2012).

[12] V. V. Elewyck, *High-Energy Neutrino Astronomy: Status and prospects for cosmic-ray physics*, in Proceedings of the 14th Workshop on Elastic and Diffractive Scattering (EDS Blois Workshop) "Frontiers of QCD: From Puzzles to Discoveries" (2012), arXiv: 1209.3425.

[13] P. Blasi, *Theoretical Challenges in Acceleration and Transport of Ultra High Energy Cosmic Rays: A Review*, Invited Review Talk in UHECR2012 Symposium, CERN, arXiv: 1208.1682 (2012).

[14] A. Letessier-Selvon and T. Stanev, *Ultrahigh Energy Cosmic Rays*, Reviews of Modern Physics **83**, 907–942, arXiv: 1103.0031 (2011).

References

[15] G. Sigl, *Interdisciplinary Aspects of High-Energy Astrophysics*, in *Astronomy at the Frontiers of Science*, edited by J.-P. Lasota, Springer (Heidelberg) 2011, Chap. 4. arXiv: 1102.1436.

[16] K. Kotera and A. V. Olinto, *The Astrophysics of Ultrahigh Energy Cosmic Rays*, Annual Review of Astronomy and Astrophysics **49**, 119–153, arXiv: 1101.4256 (2011).

[17] R. L. Diehl, *Particle acceleration in cosmic sites*, The European Physical Journal D **55**, 509–518, arXiv: 0902.4795 (2009).

[18] T. Suomijärvi (For the Pierre Auger Collaboration), *Performance and operation of the Surface Detector of the Pierre Auger Observatory*, in Proceedings of the 31st ICRC, Łódź (2009).

[19] J. Abraham et al. (The Pierre Auger Collaboration), *Trigger and aperture of the surface detector array of the Pierre Auger Observatory*, Nuclear Instruments and Methods in Physics Research Section A **A613**, 29–39, arXiv: 1111.6764 (2010).

[20] L. Evans and P. Bryant, *LHC Machine*, Journal of Instrumentation **3**, S08001 (2008).

[21] R. M. Kulsrud and E. G. Zweibel, *On the origin of cosmic magnetic fields*, Reports on Progress in Physics **71**, 046901, arXiv: 0707.2783 (2008).

[22] D. G. Yamazaki et al., *The search for a primordial magnetic field*, Physics Reports, 141–167, arXiv: 1204.3669 (2012).

[23] L. Widrow et al., *The First Magnetic Fields*, Space Science Reviews **166**, 37–70, arXiv: 1109.4052 (2012).

[24] D. Ryu et al., *Magnetic fields in the Large-Scale Structure of the Universe*, Space Science Reviews **166**, 1–35, arXiv: 1109.4055 (2012).

[25] J. Aublin (For the Pierre Auger Collaboration), *Discriminating models of UHECR sources with a log likelihood method*, Nuclear Physics B (Proc. Suppl.) **190**, 94–98 (2009).

[26] A. Cuoco et al., *Clustering Properties of Ultra-High-Energy Cosmic Rays and the Search for Their Astrophysical Sources*, Astrophysical Journal **676**, 807, arXiv: 0709.2712 (2008).

[27] M. Erdmann and P. Schiffer, *A Method of Measuring Cosmic Magnetic Fields with Ultra High Energy Cosmic Ray Data*, Astroparticle Physics **33**, 201–205, arXiv: 0904.4888 (2010).

[28] G. Golup et al., *Source position reconstruction and constraints on the galactic magnetic field from ultra-high energy cosmic rays*, Astroparticle Physics **32**, 269–277, arXiv: 0902.1742 (2009).

[29] G. Giacinti and D. V. Semikoz, *Search for Individual UHECR Sources in the Future Data*, in Proceedings of the 31st ICRC, Łódź (2009), arXiv: 1107.2356.

[30] S. Schulte, *Autocorrelation studies of the arrival directions of UHECRs measured by the surface detector of the Pierre Auger Observatory*, PhD thesis RWTH Aachen University, 2011.

[31] M. Grigat, *Large scale anisotropy studies of ultra high energy cosmic rays using data taken with the surface detector of the Pierre Auger Observatory*, PhD thesis RWTH Aachen University, 2011.

[32] P. Younk, *A method to constrain the characteristic angular size of the brightest cosmic-ray sources observed above 57×10^{18} eV*, Astrophysics and Space Sciences Transactions **7**, 403–410, arXiv: 0909.3483 (2011).

[33] P. Abreu et al. (The Pierre Auger Collaboration), *Search for signatures of magnetically-induced alignment in the arrival directions measured by the Pierre Auger Observatory*, Astroparticle Physics **35**, 354–361, arXiv: 1111.2472 (2012).

[34] P. Abreu et al. (The Pierre Auger Collaboration), *A search for anisotropy in the arrival directions of ultra high energy cosmic rays recorded at the Pierre Auger Observatory*, Journal of Cosmology and Astroparticle Physics **4**, 040, arXiv: 1210.3602 (2012).

[35] P. Abreu et al. (The Pierre Auger Collaboration), *Large scale distribution of arrival directions of cosmic rays detected above 10^{18} eV at the Pierre Auger Observatory*, The Astrophysical Journal Supplement Series **203**, 34, arXiv: 1210.3736 (2012).

[36] P. Abreu et al. (The Pierre Auger Collaboration), *Anisotropy and chemical composition of ultra-high energy cosmic rays using arrival directions measured by the Pierre Auger Observatory*, Journal of Cosmology and Astroparticle Physics **1106**, 022, arXiv: 1106.3048 (2011).

[37] P. Abreu et al. (The Pierre Auger Collaboration), *Search for First Harmonic Modulation in the Right Ascension Distribution of Cosmic Rays Detected at the Pierre Auger Observatory*, Astroparticle Physics **34**, 627–639, arXiv: 1103.2721 (2011).

[38] G. Sigl, M. Lemoine, and P. Biermann, *Ultra-high energy cosmic ray propagation in the local supercluster*, Astroparticle Physics **10**, 141–156, arXiv: astro-ph/9806283 (1999).

[39] T. Stanev et al., *Propagation of ultrahigh energy protons in the nearby universe*, Physical Review D **62**, 093005, arXiv: astro-ph/0003484 (2000).

[40] C. Isola, M. Lemoine, and G. Sigl, *Centaurus A as the Source of ultra-high energy cosmic rays?*, Physical Review D **65**, 023004, arXiv: astro-ph/0104289 (2002).

[41] T. Stanev, D. Seckel, and R. Engel, *Propagation of ultrahigh energy protons in regular extragalactic magnetic fields*, Physical Review D **68**, 103004, arXiv: astro-ph/0108338 (2003).

References

[42] G. Sigl, F. Miniati, and T. Ensslin, *Ultra-High Energy Cosmic Ray Probes of Large Scale Structure and Magnetic Fields*, Physical Review D **70**, 043007, arXiv: `astro-ph/0401084` (2004).

[43] K. Dolag et al., *Mapping deflections of extragalactic ultrahigh energy cosmic rays in magnetohydrodynamic simulations of the Local Universe*, Journal of Experimental and Theoretical Physics Letters **79**, 719–723, arXiv: `astro-ph/0310902` (2004).

[44] H. Yoshiguchi et al., *Small-Scale Clustering in the Isotropic Arrival Distribution of Ultra-High-Energy Cosmic Rays and Implications for Their Source Candidates*, Astrophysical Journal **586**, 1211, arXiv: `astro-ph/0909.3483` (2003).

[45] H. Yoshiguchi, S. Nagataki, and K. Sato, *Statistical Significance of Small-Scale Anisotropy in Arrival Directions of Ultra-High-Energy Cosmic Rays*, Astrophysical Journal **614**, 43, arXiv: `astro-ph/0404411` (2004).

[46] K. Dolag et al., *Constrained simulations of the magnetic field in the local Universe and the propagation of ultrahigh energy cosmic rays*, Journal of Cosmology and Astroparticle Physics **01**, 009, arXiv: `astro-ph/0410419` (2005).

[47] H. Takami, H. Yoshiguchi, and K. Sato, *Propagation of Ultra-High-Energy-Cosmic Rays above $10^{19}\,eV$ in a structured extragalactic magnetic field and galactic magnetic field*, Astrophysical Journal **639**, 803–815, arXiv: `astro-ph/0506203` (2006).

[48] E. Armengaud et al., *CRPropa: A Numerical Tool for the Propagation of UHE Cosmic Rays, Gamma-rays and Neutrinos*, Astroparticle Physics **28**, 463–471, arXiv: `astro-ph/0603675` (2007).

[49] D. De Marco, P. Blasi, and T. Stanev, *Numerical propagation of high energy cosmic rays in the Galaxy: I. Technical issues*, Journal of Cosmology and Astroparticle Physics **6**, 027, arXiv: `0705.1972` (2007).

[50] S. Das et al., *Propagation of Ultra-High-Energy Protons through the Magnetized Cosmic Web*, Astrophysical Journal **682**, 29, arXiv: `0801.0371` (2008).

[51] N. Globus, D. Allard, and E. Parizot, *Propagation of high-energy cosmic rays in extragalactic turbulent magnetic fields: resulting energy spectrum and composition*, Astronomy and Astrophysics **479**, 97–110, arXiv: `0709.1541` (2008).

[52] D. Hooper and A. M. Taylor, *On the heavy chemical composition of the ultra-high energy cosmic rays*, Astroparticle Physics **33**, 151–159, arXiv: `0910.1842` (2010).

[53] M. S. Sutherland, B. M. Baughman, and J. J. Beatty, *CRT: A numerical tool for propagating ultra-high energy cosmic rays through Galactic magnetic field models*, Astroparticle Physics **34**, 198–204, arXiv: `1010.3172` (2010).

[54] K. Dolag et al., *A new Monte Carlo Generator of Ultra High Energy Cosmic Rays from the Local and Distant Universe*, in Proceedings of the 32nd ICRC, Beijing (2011), arXiv: `1202.3005`.

[55] E. Battaner, J. Castellano, and M. Masip, *Cosmic magnetic lenses*, Astronomy and Astrophysics **527**, A79, arXiv: 1006.2346 (2011).

[56] H. Dembinski, *Measurement of the ultra-high energy cosmic ray flux using data from very inclined air showers at the Pierre Auger Observatory*, PhD thesis RWTH Aachen University, 2009.

[57] B. G. Keilhauer, *Investigation of Atmospheric Effects on the Development of Extensive Air Showers and their detection with the Pierre Auger Observatory*, PhD thesis Universität Karlsruhe (TH), 2003.

[58] M. Nagano and A. A. Watson, *Observations and implications of the ultrahigh-energy cosmic rays*, Reviews of Modern Physics **72**, 689–732 (2000).

[59] J. Blümer, R. Engel, and J. R. Hörandel, *Cosmic Rays from the Knee to the Highest Energies*, Progress in Particle and Nuclear Physics **63**, 293–338, arXiv: 0904.0725 (2009).

[60] J. Beringer et al. (The Particle Data Group), *Review of Particle Physics*, Physical Review D **86**, 010001 (2012).

[61] P. Billoir, *Phenomenology of Ultra-High-Energy Atmospheric Showers*, in *Physics and Astrophysics of Ultra-High-Energy-Cosmic Rays*, edited by M. Lemoine and G. Sigl, Springer (Berlin, Heidelberg) 2001.

[62] W. Heitler, *The quantum theory of radiation*, in, (Original work from 1954), Clarendon Press (Oxford) 1960.

[63] J. Matthews, *A Heitler model of extensive air showers*, Astroparticle Physics **22**, 387–397 (2005).

[64] T. K. Gaisser, *Cosmic Rays and Particle Physics*, Cambridge University Press (Cambridge, New-York, Melbourne) 1990.

[65] E. S. Seo et al., *Measurement of cosmic-ray proton and helium spectra during the 1987 solar minimum*, Astrophysical Journal **378**, 763–772 (1991).

[66] I. P. Ivanenko et al., *Energy Spectra of Cosmic Rays above 2 TeV as Measured by the 'SOKOL' Apparatus*, in Proceedings of the 23 ICRC, Calgary (1993), p. 17.

[67] N. L. Grigorov et al., *Energy Spectrum of Primary Cosmic Rays in the 10^{11}-10^{15} eV According to the Data of Proton-4 Measurements. (Abstract)*, in Proceedings of the 12 ICRC, Vol. 1, Reference for the data of the Proton experiment used in the spectrum shown in [78], Hobart (1971), p. 170.

[68] M. Amenomori et al. (The Tibet AS gamma Collaboration), *The Cosmic ray energy spectrum between 10**14.5-eV and 10**16.3-eV covering the 'knee' region*, Astrophysical Journal **461**, 408–414 (1995).

[69] M. Nagano et al., *Energy spectrum of primary cosmic rays between $10^{14.5}$ and 10^{18} eV*, Journal of Physics G: Nuclear Physics **10**, 1295 (1984).

[70] M. Glasmacher et al., *The cosmic ray energy spectrum between 10^{14} and 10^{16} eV*, Astroparticle Physics **10**, 291–302 (1999).

References

[71] R. Abbasi et al. (The IceCube Collaboration), *All-particle cosmic ray energy spectrum measured with 26 IceTop stations*, Astroparticle Physics **44**, 40–58, arXiv: 1202.3039 (2013).

[72] T. Antoni et al. (The KASCADE Collaboration), *KASCADE measurements of energy spectra for elemental groups of cosmic rays: Results and open problems*, Astroparticle Physics **24**, 1–25, arXiv: astro-ph/0505413 (2005).

[73] W. Apel et al. (The KASCADE-Grande Collaboration), *The spectrum of high-energy cosmic rays measured with KASCADE-Grande*, Astroparticle Physics **36**, 183–194, arXiv: 1206.3834 (2012).

[74] M. Ave et al., *The Energy spectrum of cosmic rays above 3 x 10**17-eV as measured with the Haverah Park array*, Astroparticle Physics **19**, 47–60, arXiv: astro-ph/0112253 (2003).

[75] R. Abbasi et al. (The HiRes Collaboration), *First observation of the Greisen-Zatsepin-Kuzmin suppression*, Physical Review Letters **100**, 101101, arXiv: astro-ph/0703099 (2008).

[76] D. Ivanov, *Energy Spectrum Measured by the Telescope Array Surface Detector*, PhD thesis Rutgers, The State University of New Jersey, 2012.

[77] F. Salamida for the Pierre Auger Collaboration (For the Pierre Auger Collaboration), *Update on the measurement of the CR energy spectrum above 10^{18} eV made using the Pierre Auger Observatory*, in Proceedings of the 32nd ICRC, Beijing (2011), arXiv: 1107.4809.

[78] J. Cronin, T. Gaisser, and S. Swordy, *Cosmic Rays at the Energy Frontier*, Scientific American **276**, 44 (1997).

[79] J. Simpson, *Elemental and isotopic composition of the galactic cosmic rays*, Annual Review of Nuclear and Particle Science **33**, 323–382 (1983).

[80] D. Harari, S. Mollerach, and E. Roulet, *The toes of the ultra high energy cosmic ray spectrum*, Journal of High Energy Physics **08**, 22, arXiv: astro-ph/9906309 (1999).

[81] M. Nagano et al., *Energy spectrum of primary cosmic rays above 10 17.0 eV determined from extensive air shower experiments at Akeno*, Journal of Physics G **18**, 423 (1992).

[82] W. D. Apel et al. (The KASCADE-Grande Collaboration), *Kneelike Structure in the Spectrum of the Heavy Component of Cosmic Rays Observed with KASCADE-Grande*, Physical Review Letters **107**, 171104, arXiv: 1107.5885 (2011).

[83] C. Di Giulio (For the Pierre Auger Collaboration), *Energy calibration of data recorded with the surface detectors of the Pierre Auger Observatory*, in Proceedings of the 31st ICRC, Łódź (2009).

[84] J. Abraham et al. (The Pierre Auger Collaboration), *Observation of the suppression of the flux of cosmic rays above $4 \times 10^{19} eV$*, Physical Review Letters **101**, 061101, arXiv: 0806.4302 (2008).

[85] R. U. Abbasi et al. (The High Resolution Fly's Eye Collaboration), *Indications of Proton-Dominated Cosmic-Ray Composition above 1.6 EeV*, Physical Review Letters **104**, 161101, arXiv: 0910.4184 (2010).

[86] J. Abraham et al. (The Pierre Auger Collaboration), *Measurement of the Depth of Maximum of Extensive Air Showers above 10^{18} eV*, Physical Review Letters **104**, 091101, eprint: 1002.0699 (2010).

[87] Y. Tsunesada (For the Telescope Array Collaboration), *Highlights from Telescope Array*, in Proceedings of the 32nd ICRC Conference, Beijing (2011), arXiv: 1111.2507.

[88] P. Abreu et al. (The Pierre Auger Collaboration), *Interpretation of the Depths of Maximum of Extensive Air Showers Measured by the Pierre Auger Observatory*, Journal of Cosmology and Astroparticlephysics **1302**, 026, arXiv: 1301.6637 (2013).

[89] A. Abdo et al. (The Milagro Collaboration), *Discovery of Localized Regions of Excess 10-TeV Cosmic Rays*, Physical Review Letters **101**, 221101, arXiv: 0801.3827 (2008).

[90] R. U. Abbasi, P. Desiati, and J. C. D. Velez (For the IceCube Collaboration), *Large Scale Cosmic Rays Anisotropy With IceCube*, in Proceedings of the 31st ICRC, Łódź (2009), arXiv: 0907.0498.

[91] R. Abbasi et al. (The IceCube Collaboration), *Measurement of the Anisotropy of Cosmic Ray Arrival Directions with IceCube*, Astrophysical Journal **718**, L194, arXiv: 1005.2960 (2010).

[92] R. Iuppa et al. (on behalf of the ARGO-YBJ Collaboration), *Anisotropies in the cosmic radiation observed with ARGO-YBJ*, in Proceedings of the 2011 Fermi Symposium (2011), arXiv: 1112.2375.

[93] M. Aartsen et al. (The IceCube Collaboration), *Observation of Cosmic Ray Anisotropy with the IceTop Air Shower Array*, arXiv: 1210.5278 (2012).

[94] A. Tamburro, *Measurements of Cosmic Rays with IceTop/IceCube: Status and Results*, Modern Physics Letter A **27**, 1230038, arXiv: 1210.1832 (2012).

[95] M. Aglietta et al. (The Pierre Auger Collaboration), *Anisotropy studies around the Galactic Centre at EeV energies with the Auger Observatory*, Astroparticle Physics **27**, 244–253, arXiv: astro-ph/0607382 (2007).

[96] J. Abraham et al. (The Pierre Auger Collaboration), *Correlation of the highest energy cosmic rays with nearby extragalactic objects*, Science **318**, 938–943, arXiv: 0711.2256 (2007).

[97] J. Abraham et al. (The Pierre Auger Collaboration), *Correlation of the highest-energy cosmic rays with the positions of nearby active galactic nuclei*, Astroparticle Physics **29**, 188–204, arXiv: 0712.2843 (2008).

References

[98] P. Abreu et al. (The Pierre Auger Collaboration), *Update on the correlation of the highest energy cosmic rays with nearby extragalactic matter*, Astroparticle Physics **34**, 314–326, arXiv: 1009.1855 (2010).

[99] R. Abbasi et al. (The High Resolution Fly's Eye Collaboration), *Search for Correlations between HiRes Stereo Events and Active Galactic Nuclei*, Astroparticle Physics **30**, 175–179, arXiv: 0804.0382 (2008).

[100] T. Abu-Zayyad et al. (The Telescope Array Collaboration), *Search for Anisotropy of Ultra-High Energy Cosmic Rays with the Telescope Array Experiment*, Astrophysical Journal **757**, 26, arXiv: 1205.5984 (2012).

[101] A. Cuoco, G. Miele, and P. Serpico, *Astrophysical interpretation of the medium scale clustering in the ultrahigh energy sky*, Physics Letters B **660**, 307–314, arXiv: 0706.2864 (2008).

[102] P. Schiffer, *Constraining Cosmic Magnetic Fields by a Measurement of Energy-Energy-Correlations with the Pierre Auger Observatory*, PhD thesis RWTH Aachen University, 2011.

[103] P. Schiffer (For the Pierre Auger Collaboration), *Measurement of Energy-Energy-Correlations with the Pierre Auger Observatory*, in Proceedings of the 32th ICRC, Beijing (2011).

[104] P. Blasi, *Origin of Galactic Cosmic Rays*, Nuclear Physics B: Proceedings Supplements **239–240**, 140–147, arXiv: 1211.4799 (2012).

[105] J. R. Hörandel, *On the knee in the energy spectrum of cosmic rays*, Astroparticle Physics **19**, 193–220, arXiv: astro-ph/0210453 (2003).

[106] J. R. Hörandel, N. Kalmykov, and A. Timokhin, *The end of the galactic cosmic-ray energy spectrum — a phenomenological view*, Journal of Physics: Conference Series **47**, 132–141, arXiv: astro-ph/0508015 (2006).

[107] J. R. Hörandel, *Models of the knee in the energy spectrum of cosmic rays*, Astroparticle Physics **21**, 241–265, arXiv: astro-ph/0402356 (2004).

[108] M. Pohl and D. Eichler, *Understanding TeV-band cosmic-ray anisotropy*, Astrophysical Journal **766**, 4, arXiv: 1208.5338 (2012).

[109] D. Allard et al., *UHE nuclei propagation and the interpretation of the ankle in the cosmic-ray spectrum*, Astronomy and Astrophysics **443**, L25, arXiv: astro-ph/0505566 (2005).

[110] D. Allard, E. Parizot, and A. Olinto, *On the transition from galactic to extragalactic cosmic-rays: spectral and composition features from two opposite scenarios*, Astroparticle Physics **27**, 61–75, arXiv: astro-ph/0512345 (2007).

[111] V. S. Berezinsky and S. I. Grigoreva, *A bump in the ultra-high energy cosmic ray spectrum*, Astronomy and Astrophysics **199**, 1 (1988).

[112] V. Berezinsky, A. Gazizov, and S. Grigorieva, *On astrophysical solution to ultrahigh energy cosmic rays*, Physical Review D **74**, 043005, arXiv: hep-ph/0204357 (2006).

[113] W. A. Terrano, I. Zaw, and G. R. Farrar, *Chandra observations and classification of AGN-candidates correlated with Auger UHECRs*, Astrophysical Journal **754**, 142, arXiv: 1207.3186 (2012).

[114] R. S. Nemmen, C. Bonatto, and T. Storchi-Bergmann, *A Correlation Between the Highest Energy Cosmic Rays and Nearby Active Galactic Nuclei Detected by Fermi*, Astrophysical Journal **722**, 281, arXiv: 1007.5317 (2010).

[115] P. Bhattacharjee and G. Sigl, *Origin and propagation of extremely high-energy cosmic rays*, Physics Reports **327**, 109–247, arXiv: astro-ph/9811011 (2000).

[116] J. Abraham et al. (The Pierre Auger Collaboration), *An upper limit to the photon fraction in cosmic rays above 10^{19}-eV from the Pierre Auger Observatory*, Astroparticle Physics **27**, 155–168, arXiv: astro-ph/0606619 (2007).

[117] J. Abraham et al. (The Pierre Auger Collaboration), *Upper limit on the cosmic-ray photon flux above 10^{19} eV using the surface detector of the Pierre Auger Observatory*, Astroparticle Physics **29**, 243–256, arXiv: 0712.1147 (2008).

[118] S. Colgate, *Acceleration in astrophysics*, Physica Scripta **T52**, 96–105 (1994).

[119] E. Fermi, *On the Origin of the Cosmic Radiation*, Physical Review **75**, 1169 (1949).

[120] C. D. Dermer, *Maximum Particle Energies by Fermi Acceleration in Nonrelativistic and Relativistic Flows*, in Proceedings of the 27th, Hamburg (Aug. 2001), p. 2039, arXiv: astro-ph/0012490.

[121] R. Blandford and D. Eichler, *Particle Acceleration at Astrophysical Shocks: A Theory of Cosmic Ray Origin*, Physics Reports **154**, 1–75 (1987).

[122] A. Achterberg et al., *Particle acceleration by ultrarelativistic shocks: Theory and simulations*, Monthly Notices of the Royal Astronomical Society **328**, 393, arXiv: astro-ph/0107530 (2001).

[123] F. M. Rieger, V. Bosch-Ramon, and P. Duffy, *Fermi acceleration in astrophysical jets*, Astrophysics and Space Science **309**, 119–125, arXiv: astro-ph/0610141 (2007).

[124] R. van Weeren et al., *Particle Acceleration on Megaparsec Scales in a Merging Galaxy Cluster*, Science **330**, 347, arXiv: 1010.4306 (2010).

[125] L. O. Drury, *Origin Of Cosmic Rays*, Astroparticle Physics **39–40**, 52–60, arXiv: 1203.3681 (2012).

[126] A. M. Hillas, *The Origin of Ultra-High-Energy Cosmic Rays*, Annual Review of Astronomy and Astrophysics **22**, 425–44 (1984).

[127] K. V. Ptitsyna and S. V. Troitsky, *Physical conditions in potential accelerators of ultra-high-energy cosmic rays: updated Hillas plot and radiation-loss constraints*, Physics-Uspekhi **53**, 691, arXiv: 0808.0367 (2010).

References

[128] D. F. Torres and L. A. Anchordoqui, *Astrophysical origins of ultrahigh energy cosmic rays*, Reports on Progress in Physics **67**, 1663–1730, arXiv: astro-ph/0402371 (2004).

[129] N. Shaham and T. Piran, *Implications of the Penetration Depth of Ultrahigh-Energy Cosmic Rays on Physics at 100 TeV*, Physical Review Letters **110**, 021101, arXiv: 1204.1488 (2013).

[130] J. Lattimer and M. Prakash, *The physics of neutron stars*, Science **304**, 536–542, arXiv: astro-ph/0405262 (2004).

[131] N. Rea, *Magnetars: neutron stars with huge magnetic storms*, in Proceedings of IAUS 291 "Neutron Stars and Pulsars: Challenges and Opportunities after 80 years", edited by J. van Leeuwen (2012), arXiv: 1211.2086.

[132] J. Arons, *Magnetars in the metagalaxy: an origin for ultrahigh-energy cosmic rays in the nearby universe*, Astrophysical Journal **589**, 871–892, arXiv: astro-ph/0208444 (2003).

[133] A. Olinto, R. Epstein, and P. Blasi, *Galactic ultrahigh-energy cosmic rays*, in Proceedings of the 26th ICRC, Salt Lake City (1999), arXiv: astro-ph/9906338.

[134] K. Fang, K. Kotera, and A. V. Olinto, *Newly-born pulsars as sources of ultrahigh energy cosmic rays*, Astrophysical Journal **750**, 118, arXiv: 1201.5197 (2012).

[135] C. Hernández-Monteagudo, F. Atrio-Barandela, and J. P. Mücket, *On the Number Density of Sunyaev-Zeldovich Clusters of Galaxies*, Astrophysical Journal **528**, L69–L72, arXiv: 9911121 (2000).

[136] B. D. Metzger, D. Giannios, and S. Horiuchi, *Heavy nuclei synthesized in gamma-ray burst outflows as the source of ultrahigh energy cosmic rays*, Monthly Notices of the Royal Astronomical Society **415**, 2495–2504, arXiv: 1101.4019 (2011).

[137] N. Gehrels and P. Meszaros, *Gamma Ray Bursts*, Science **337**, 932, arXiv: 1208.6522 (2012).

[138] E. Waxman, *Cosmological Gamma-Ray Bursts and the Highest Energy Cosmic Rays*, Physical Review Letters **75**, 386–389, arXiv: astro-ph/9505082 (1995).

[139] R.-Y. Liu, X.-Y. Wang, and Z.-G. Dai, *Nearby low-luminosity gamma-ray bursts as the sources of ultra-high-energy cosmic rays revisited*, Monthly Notices of the Royal Astronomical Society **418**, 1382–1391, arXiv: 1108.1551 (2011).

[140] K. Z. Stanek et al., *Protecting life in the Milky Way: Metals keep the GRBs away*, Acta Astronomica **56**, 333, arXiv: astro-ph/0604113 (2006).

[141] H. Yüksel and M. D. Kistler, *Enhanced cosmological GRB rates and implications for cosmogenic neutrinos*, Physical Review D **75**, 083004, arXiv: astro-ph/0610481 (2007).

[142] G. Gavazzi, G. Savorgnan, and M. Fumagalli, *The complete census of optically selected AGNs in the Coma Supercluster: the dependence of AGN activity on the local environment*, Astronomy and Astrophysics **534**, A31, arXiv: 1107.3702 (2011).

[143] K. Kellermann et al., *VLA observations of objects in the Palomar Bright Quasar Survey*, The Astronomical Journal **98**, 1195–1207 (1989).

[144] R. Antonucci, *Unified models for active galactic nuclei and quasars*, Annual Review of Astronomy and Astrophysics **31**, 473–521 (1993).

[145] C. M. Urry and P. Padovani, *Unified schemes for radio-loud active galactic nuclei*, Publications of the Astronomical Society of the Pacific **107**, 803, arXiv: astro-ph/9506063 (1995).

[146] J. V. Wall et al., *The Parkes quarter-Jansky flat-spectrum sample. 3. Space density and evolution of QSOs*, Astronomy and Astrophysics **434**, 133–148, arXiv: astro-ph/0408122 (2004).

[147] A. Neronov, D.Semikoz, and I.Tkachev, *Ultra-High Energy Cosmic Ray production in the polar cap regions of black hole magnetospheres*, New Journal of Physics **11**, 065015, arXiv: 0712.1737 (2009).

[148] F. Hamann and G. Ferland, *Elemental abundances in quasistellar objects: star formation and galactic nuclear evolution at high redshifts*, Annual Review of Astronomy and Astrophysics **37**, 487–531, arXiv: astro-ph/9904223 (1999).

[149] V. Wild et al., *Post-starburst galaxies: more than just an interesting curiosity*, Monthly Notices of the Royal Astronomical Society **395**, 144–159, arXiv: 0810.5122 (2009).

[150] L. A. Anchordoqui, G. E. Romero, and J. A. Combi, *Heavy nuclei at the end of the cosmic ray spectrum?*, Physical Review D **60**, 103001, arXiv: astro-ph/9903145 (1999).

[151] P. J. E. Peebles, *Principles of physical cosmology*, Princeton University Press (New Jersey) 1993.

[152] B. W. Carroll and D. A. Ostile, *An introduction to modern astrophysics*, 2nd edition, Pearson (San Francisco) 2007.

[153] D. N. Spergel et al. (The WMAP Collaboration), *First Year Wilkinson Microwave Anisotropy Probe (WMAP) Observations: Determination of Cosmological Parameters*, Astrophysical Journal, arXiv: astro-ph/0302209 (2003), 10.1086/377226.

[154] M. Ahlers, L. A. Anchordoqui, and S. Sarkar, *Neutrino diagnostics of ultra-high energy cosmic ray protons*, Physical Review D **79**, 083009, arXiv: 0902.3993 (2009).

[155] D. Coward, R. Burman, and D. Blair, *Statistical characteristics of a stochastic background of gravitational waves from neutron star formation*, Classical and Quantum Gravity **19**, 1303–1307 (2002).

[156] A. M. Hopkins and J. F. Beacom, *On the normalisation of the cosmic star formation history*, Astrophysical Journal **651**, 142–154, arXiv: astro-ph/0601463 (2006).

References

[157] G. Hasinger, T. Miyaji, and M. Schmidt, *Luminosity-dependent evolution of soft x-ray selected AGN: New Chandra and XMM-Newton surveys*, Astronomy and Astrophysics **441**, 417–434, arXiv: `astro-ph/0506118` (2005).

[158] J. P. Rachen, *Interaction Processes and Statistical Properties of the Propagation of Cosmic Rays in Photon Backgrounds*, PhD thesis Universität Bonn, 1996.

[159] R. Aloisio, *Ultra High Energy Cosmic Rays Propagation and Spectrum*, AIP Conference Proceedings **1367**, 114–119, arXiv: `1104.0329` (2011).

[160] D. Allard, *Extragalactic propagation of ultrahigh energy cosmic-rays*, Astroparticle Physics **39–40**, 33–43, arXiv: `1111.3290` (2011).

[161] H. Dole et al., *The cosmic infrared background resolved by spitzer. contributions of mid-infrared galaxies to the far-infrared background*, Astronomy and Astrophysics **451**, 417–429, arXiv: `astro-ph/0603208` (2006).

[162] A. Kashlinsky, *Cosmic infrared background and early galaxy evolution*, Physics Reports **409**, 361–438, arXiv: `astro-ph/0412235` (2005).

[163] E. Dwek and F. Krennrich, *The Extragalactic Background Light and the Gamma-ray Opacity of the Universe*, Astroparticle Physics **43**, arXiv: `1209.4661` (2013), `10.1016/j.astropartphys.2012.09.003`.

[164] S. Yoshida and M. Teshima, *Energy Spectrum of Ultra-high Energy Cosmic Rays with Extra-Galactic Origin*, Progress of Theoretical Physics **89**, 833–845 (1993).

[165] R. J. Protheroe and P. Johnson, *Propagation of ultra high energy protons and gamma rays over cosmological distances and implications for topological defect models*, Astroparticle Physics **4**, 253, arXiv: `astro-ph/9506119` (1996).

[166] L. A. Anchordoqui et al., *Effect of the 3 K background radiation on ultrahigh energy cosmic rays*, Physical Review D **55**, 7356–7360, arXiv: `hep-ph/9704387` (1997).

[167] V. Berezinsky, A. Gazizov, and M. Kachelriess, *Second dip as a signature of ultrahigh energy proton interactions with cosmic microwave background radiation*, Physical Review Letters **97**, 231101, arXiv: `astro-ph/0612247` (2006).

[168] D. Hooper, S. Sarkar, and A. M. Taylor, *Intergalactic propagation of ultrahigh energy cosmic ray nuclei: An analytic approach*, Physical Review D **77**, 103007, arXiv: `0802.1538` (2008).

[169] R. Aloisio, *Ultra High Energy Nuclei Propagation*, Nuovo Cimento B **123**, 915–917, arXiv: `0807.0151` (2008).

[170] M. Ahlers and A. M. Taylor, *Analytic solutions of ultrahigh energy cosmic ray nuclei revisited*, Physical Review D **82**, 123005, arXiv: `1010.3019` (2010).

[171] R. Aloisio, V. Berezinsky, and S. Grigorieva, *Analytic calculations of the spectra of ultra-high energy cosmic ray nuclei. I. The case of CMB radiatio*, Astroparticle Physics **41**, 73–93, arXiv: `0802.4452` (2013).

[172] R. Aloisio, V. Berezinsky, and S. Grigorieva, *Analytic calculations of the spectra of ultra high energy cosmic ray nuclei. II. The general case of background radiation*, Astroparticle Physics **41**, 94–107, arXiv: 1006.2484 (2013).

[173] G. R. Blumenthal, *Energy Loss of High-Energy Cosmic Rays in Pair-Producing Collisions with Ambient Photons*, Physical Review D **1**, 1596–1602 (1970).

[174] F. W. Stecker, *Effect of Photomeson Production by the Universal Radiation Field on High-Energy Cosmic Rays*, Physical Review Letters **21**, 1016–1018 (1968).

[175] K. Greisen, *End to the Cosmic-Ray Spectrum?*, Physical Review Letters **16**, 748–750 (1966).

[176] G. T. Zatsepin and V. Kuzmin, *Upper Limit on the Spectrum of Cosmic Rays*, Soviet Physics JETP Letters **4**, 78–80 (1966).

[177] D. Hooper, S. Sarkar, and A. M. Taylor, *The intergalactic propagation of ultra-high energy cosmic ray nuclei*, Astroparticle Physics **27**, 199–212, arXiv: astro-ph/0608085 (2007).

[178] M. J. Chodorowski, A. A. Zdziarski, and M. Sikora, *Reaction rate and energy-loss rate for photopair production by relativistic nuclei*, Astrophysical Journal **400**, 181–185 (1992).

[179] F. W. Stecker, *Photodisintegration of Ultrahigh-Energy Cosmic Rays by the Universal Radiation Field*, Physical Review **180**, 1264–1266 (1969).

[180] J. L. Puget, F. W. Stecker, and J. H. Bredekamp, *Photonuclear interactions of ultrahigh energy cosmic rays and their astrophysical consequences*, Astrophysical Journal **205**, 638–654 (1976).

[181] F. W. Stecker and M. H. Salamon, *Photodisintegration of Ultra-High-Energy Cosmic Rays: A New Determination*, Astrophysical Journal **512**, 521, arXiv: astro-ph/9808110 (1999).

[182] K.-H. Kampert et al., *CRPropa 2.0 – a Public Framework for Propagating High Energy Nuclei, Secondary Gamma Rays and Neutrinos*, Astroparticle Physics **42**, 41–51, arXiv: 1206.3132 (2013).

[183] A. M. Taylor, *The Propagation of Ultra High Energy Cosmic Rays*, PhD thesis University of Oxford, 2006.

[184] J. Valleé, *Observations of the Magnetic Fields inside and outside the Milky Way, starting with Globules (∼ 1 parsec), Filaments, Clouds, SuperBubbles, Spiral Arms, Galaxies, Superclusters, and ending with the Cosmological Universe's Background Surface (at ∼ 8 Teraparsecs)*, Fundamentals of Cosmic Physics **19**, 1–89 (1997).

[185] J.-L. Han and R. Wielebinski, *Milestones in the Observations of Cosmic Magnetic Fields*, Chinese Journal of Astronomy and Astrophysics **2**, 293–324, arXiv: astro-ph/0209090 (2002).

References

[186] L. M. Widrow, *Origin of Galactic and Extragalactic Magnetic Fields*, Reviews of Modern Physics **74**, 775–823, arXiv: astro-ph/0207240 (2002).

[187] M. Giovannini, *The Magnetized Universe*, International Journal of Modern Physics D **13**, 391–502 (2004).

[188] R. Beck, *Galactic and Extragalactic Magnetic Fields*, AIP Conference Proceedings **1085**, 83–96, arXiv: 0810.2923 (2009).

[189] R. Beck, *Cosmic Magnetic Fields: Observations and Prospects*, in 25th Texas Symposium on Relativistic Astrophysics and Cosmology, Vol. 1381 (2011), pp. 117–136, arXiv: 1104.3749.

[190] A. Kandus, K. E. Kunze, and C. G. Tsagas, *Primordial magnetogenesis*, Physics Reports **505**, 1–58, arXiv: 1007.3891 (2011).

[191] R. Kulsrud et al., *Dynamos and cosmic magnetic fields*, Physics Reports **283**, 213–226 (1997).

[192] S. R. Furlanetto and A. Loeb, *Intergalactic Magnetic Fields from Quasar Outflows*, Astrophysical Journal **556**, 619, arXiv: astro-ph/0102076 (2001).

[193] H. J. Völk and A. M. Atoyan, *Early Starbursts and Magnetic Field Generation in Galaxy Clusters*, Astrophysical Journal **541**, 88, arXiv: astro-ph/0005185 (2000).

[194] P. P. Kronberg, H. Lesch, and U. Hopp, *Magnetization of the Intergalactic Medium by Primeval Galaxies*, Astrophysical Journal **511**, 56 (1999).

[195] S. Matarrese et al., *Large-scale magnetic fields from density perturbations*, Physical Review D **71**, 043502, arXiv: astro-ph/0410687 (2005).

[196] T. S. Koivisto and F. R. Urban, *Cosmic magnetization in three-form inflation*, Physical Review D **85**, 083508, arXiv: 1112.1356 (2012).

[197] J. C. N. de Araujo and R. Opher, *A Possible Dynamical Effect of a Primordial Magnetic Field*, Astrophysical Journal **490**, 488, arXiv: astro-ph/9707303 (1997).

[198] E. Battaner, E. Florido, and J. Garcia-Ruiz, *Magnetic fields and large scale structure in a hot Universe III. The polyhedric network*, Astronomy and Astrophysics **327**, 8–10, arXiv: astro-ph/9710074 (1997).

[199] E. Battaner, E. Florido, and J. Jiménez-Vicente, *Magnetic fields and large scale structure in a hot universe I. General equations*, Astronomy and Astrophysics **326**, 13–22, arXiv: astro-ph/9602097 (1997).

[200] E. Florido and E. Battaner, *Magnetic fields and large-scale structure in a hot universe II. Magnetic flux tubes and filamentary structure*, Astronomy and Astrophysics **327**, 1–7, arXiv: astro-ph/9710196 (1997).

[201] E. Siegel and J. Fry, *Cosmological Structure Formation Creates Large-Scale Magnetic Fields*, Astrophysical Journal **651**, 627–634, arXiv: astro-ph/0604526 (2006).

[202] V. Semikoz, D. Sokoloff, and J. Valle, *Is the baryon asymmetry of the Universe related to galactic magnetic fields?*, Physical Review D **80**, 083510, arXiv: 0905.3365 (2009).

[203] T. Suyama and J. Yokoyama, *Metric perturbation from inflationary magnetic field and generic bound on inflation models*, Physical Review D **86**, 023512, arXiv: 1204.3976 (2012).

[204] T. Fujita and S. Mukohyama, *Universal upper limit on inflation energy scale from cosmic magnetic field*, Journal of Cosmology and Astroparticle Physics **1210**, 034, arXiv: 1205.5031 (2012).

[205] D. Grasso and H. Rubinstein, *Magnetic Fields in the Early Universe*, Physics Reports **348**, 163–266, arXiv: astro-ph/0009061 (2001).

[206] S. Lee, A. V. Olinto, and G. Sigl, *Extragalactic Magnetic Field and the Highest Energy Cosmic Rays*, Astrophysical Journal **455**, L21–L24, arXiv: astro-ph/9508088 (1995).

[207] M. Lemoine et al., *Ultra-high-Energy Cosmic-Ray Sources and Large-Scale Magnetic Fields*, Astrophysical Journal **486**, L115–L118, arXiv: astro-ph/9704203 (1997).

[208] M. S. Sutherland, B. M. Baughman, and J. J. Beatty, *A Method for Constraining Cosmic Magnetic Field Models Using Ultra-High Energy Cosmic Rays: The Field Scan Method*, Astroparticle Physics **37**, arXiv: 1207.1654 (2012).

[209] C. L. Carilli and G. B. Taylor, *Cluster Magnetic Fields*, Annual Review of Astronomy and Astrophysics **40**, 319–348, arXiv: astro-ph/0110655 (2002).

[210] K.-T. Kim et al., *Discovery of intergalactic radio emission in the Coma-A1367 supercluster*, Nature **341**, 720 (1989).

[211] A. Neronov and D. Semikoz, *Sensitivity of γ-ray telescopes for detection of magnetic fields in the intergalactic medium*, Physical Review D **80**, 123012, arXiv: 0910.1920 (2009).

[212] K. Takahashi et al., *Lower Bounds on Intergalactic Magnetic Fields from Simultaneously Observed GeV-TeV Light Curves of the Blazar Mrk 501*, Astrophysical Journal **744**, L7, arXiv: 1103.3835 (2012).

[213] P. Blasi, S. Burles, and A. V. Olinto, *Cosmological magnetic fields limits in an inhomogeneous universe*, Astrophysical Journal **514**, L79–L82, arXiv: astro-ph/9812487 (1999).

[214] D. G. Yamazaki et al., *Constraints on the Evolution of the Primordial Magnetic Field from the Small-Scale Cosmic Microwave Background Angular Anisotropy*, Astrophysical Journal **646**, 719, arXiv: astro-ph/0602224 (2006).

[215] I. Vovk et al., *Fermi/LAT observations of 1ES 0229+200: implications for extragalactic magnetic fields and background light*, Astrophysical Journal **747**, L14, arXiv: 1112.2534 (2012).

References

[216] A. M. Taylor, I. Vovk, and A. Neronov, *Extragalactic magnetic fields constraints from simultaneous GeV-TeV observations of blazars*, Astronomy and Astrophysics **529**, A144, arXiv: 1101.0932 (2011).

[217] A. Neronov and I. Vovk, *Evidence for strong extragalactic magnetic fields from Fermi observations of TeV blazars*, Science **328**, 73–75, arXiv: 1006.3504 (2010).

[218] F. Tavecchio et al., *The intergalactic magnetic field constrained by Fermi/LAT observations of the TeV blazar 1ES 0229+200*, Monthly Notices of the Royal Astronomical Society **406**, L70–L74, arXiv: 1004.1329 (2010).

[219] C. D. Dermer et al., *Time Delay of Cascade Radiation for TeV Blazars and the Measurement of the Intergalactic Magnetic Field*, Astrophysical Journal **733**, L21, arXiv: 1011.6660 (2011).

[220] S. Ando and A. Kusenko, *Evidence for Gamma-Ray Halos Around Active Galactic Nuclei and the First Measurement of Intergalactic Magnetic Fields*, Astrophysical Journal **722**, L39, arXiv: 1005.1924 (2010).

[221] H. Xu et al., *Turbulence and Dynamo in Galaxy Cluster Medium: Implications on the Origin of Cluster Magnetic Fields*, Astrophysical Journal **698**, L14, arXiv: 0905.2196 (2009).

[222] D. Ryu, H. Kang, and P. Biermann, *Cosmic magnetic fields in large scale filaments and sheets*, Astronomy and Astrophysics **335**, 19–25, arXiv: astro-ph/9803275 (1998).

[223] D. Harari et al., *Lensing of ultra-high energy cosmic rays in turbulent magnetic fields*, Journal of High Energy Physics **0203**, 045, arXiv: astro-ph/0202362 (2002).

[224] A. Achterberg et al., *Intergalactic Propagation of UHE Cosmic Rays*, in 19th Texas Symposium on Relativistic Astrophysics and Cosmology, Paris, France (1998), arXiv: astro-ph/9907060.

[225] V. Berezinsky and A. Z. Gazizov, *Diffusion of Cosmic Rays in the Expanding Universe. I.* Astrophysical Journal **643**, 8, arXiv: astro-ph/0512090 (2006).

[226] V. Berezinsky and A. Z. Gazizov, *Diffusion of Cosmic Rays in the Expanding Universe. II. Energy Spectra of Ultra-High Energy Cosmic Rays*, Astrophysical Journal **669**, 684, arXiv: astro-ph/0702102 (2007).

[227] R. Aloisio and V. Berezinsky, *Diffusive propagation of UHECR and the propagation theorem*, Astrophysical Journal **612**, 900–913, arXiv: 0403095v3 (2004).

[228] O. Deligny, A. Letessier-Selvon, and E. Parizot, *Magnetic horizons of UHECR sources and the GZK feature*, Astroparticle Physics **21**, 609–615, arXiv: astro-ph/0303624 (2004).

[229] J. Han, *Magnetic structure of our Galaxy: A review of observations*, in Proceedings of the IAU Symposium No. 259, Cosmic Magnetic Fields: From Planets, to Stars and Galaxies, edited by K. Strassmeier, A. Kosovichev, and J. Beckman, Puerto Santiago, Tenerife, Spain (2009), p. 455, arXiv: 0901.1165.

[230] S. Nishiyama et al., *Magnetic Field Configuration at the Galactic Center Investigated by Wide Field Near - Infrared Polarimetry*, Astrophysical Journal **690**, 1648, arXiv: 0809.3089 (2009).

[231] R. M. Crocker et al., *A lower limit of 50 microgauss for the magnetic field near the Galactic Centre*, Nature **468**, 65–67, arXiv: 1001.1275 (2010).

[232] T. Stanev, *Ultra-high-energy cosmic rays and the large-scale structure of the galactic magnetic field*, Astrophysical Journal **479**, 290–295, arXiv: astro-ph/9607086 (1997).

[233] H. Men, K.Ferriere, and J. Hannesson, *Observational Constraints on models for interstellar magnetic field in the Galactic Disk*, Astronomy and Astrophysics **486**, 819–828, arXiv: 0805.3454 (2008).

[234] T. R. Jaffe et al., *Modelling the Galactic Magnetic Field on the Plane in 2D*, Monthly Notices of the Royal Astronomical Society **401**, 1013–1028, arXiv: 0907.3994 (2009).

[235] R. Jansson et al., *Constraining models of the large scale Galactic magnetic field with WMAP5 polarization data and extragalactic rotation measure sources*, Journal of Cosmology and Astroparticle Physics **7**, 21, arXiv: 0905.2228 (2009).

[236] M. S. Pshirkov et al., *Deriving the Global Structure of the Galactic Magnetic Field from Faraday Rotation Measures of Extragalactic Sources*, Astrophysical Journal **738**, 192, 192, arXiv: 1103.0814 (2011).

[237] R. Jansson and G. R. Farrar, *A New Model of the Galactic Magnetic Field*, Astrophysical Journal **757**, 14, arXiv: 1204.3662 (2012).

[238] R. Jansson and G. R. Farrar, *The Galactic Magnetic Field*, Astrophysical Journal **761**, L11, arXiv: 1210.7820 (2012).

[239] The CRPRopa Team, *CRPropa 3 (Development Version)*, (2013) https://crpropa.desy.de.

[240] H. Yoshiguchi, S. Nagataki, and K. Sato, *A New Method for Calculating Arrival Distribution of Ultra-High-Energy Cosmic Rays above 10^{19} eV with Modifications by the Galactic Magnetic Field*, Astrophysical Journal **596**, 1044–1052, arXiv: astro-ph/0307038 (2003).

[241] K. M. Górski et al., *HEALPix: A Framework for High-Resolution Discretization and Fast Analysis of Data Distributed on the Sphere*, Astrophysical Journal **622**, 759–771, arXiv: 0409513 (2005).

[242] R. Fisher, *Dispersion on a Sphere*, Proceedings of the Royal Society A **217**, 295–305 (1953).

[243] I. Wolfram Research, *Mathematica*, Version 8.0, Wolfram Research, Inc. (Champaign, Illinois) 2010.

[244] D. Harari, S. Mollerach, and E. Roulet, *Signatures of galactic magnetic lensing upon ultra high energy cosmic rays*, Journal of High Energy Physics **2000**, 035, arXiv: astro-ph/0001084 (2000).

References

[245] G. Lemaitre and M. S. Vallarta, *On Compton's Latitude Effect of Cosmic Radiation*, Physical Review **43**, 87–91 (1933).

[246] W. Swann, *Application of Liouville's Theorem to Electron Orbits in the Earth's Magnetic Field*, Physical Review **44**, 224–227 (1933).

[247] D. Harari, S. Mollerach, and E. Roulet, *Magnetic lensing of Extremely High Energy Cosmic Rays in a Galactic wind*, Journal of High Energy Physics **0010**, 047, arXiv: astro-ph/0005483 (2000).

[248] J. Abraham et al. (The Pierre Auger Collaboration), *Measurement of the energy spectrum of cosmic rays above 10^{18} eV using the Pierre Auger Observatory*, Physics Letters B **685**, 239–246, arXiv: 1002.1975 (2010).

[249] V. Berezinsky, A. Gazizov, and S. Grigorieva, *Dip in UHECR spectrum as signature of proton interaction with CMB*, Physics Letters B **612**, 147–153, arXiv: astro-ph/0502550 (2005).

[250] M. K. E. Parizot and D. V. Semikoz, *The GZK Horizon and Constraints on the Cosmic Ray Source Spectrum from Observations in the GZK Regime*, Journal of Experimental and Theoretical Physics Letters **88**, 553–557, arXiv: 0711.3635 (2008).

[251] M.-P. Véron-Cetty and P. Véron, *A catalogue of quasars and active nuclei: 12th edition*, Astronomy and Astrophysics **455**, 776 (2006).

[252] P. Sommers, *Cosmic Ray Anisotropy Analysis with a Full-Sky Observatory*, Astroparticle Physics **14**, 271–286, arXiv: astro-ph/0004016 (2001).

[253] S. Brandt et al., *The principal axis of jets — an attempt to analyse high-energy collisions as two-body processes*, Physics Letters **12**, 57–61 (1964).

[254] E. Farhi, *Quantum Chromodynamics Test for Jets*, Physical Review Letters **39**, 1587–1588 (1977).

[255] K. V. Mardia, *Statistics of Directional Data*, Academic Press (London) 1972.

[256] S. R. Jammalamadaka and A. SenGupta, *Topics in Circular Statistics*, Vol. 5, Series on multivariate analysis, World Scientific (Singapore) 2001.

[257] J. Abraham et al. (The Pierre Auger Collaboration), *Properties and performance of the prototype instrument for the Pierre Auger Observatory*, Nuclear Instruments and Methods in Physics Research Section A **523**, 50 (2004).

[258] I. Allekotte et al. (The Pierre Auger Collaboration), *The Surface Detector System of the Pierre Auger Observatory*, Nuclear Instruments and Methods in Physics Research Section A **586**, 409–420, arXiv: 0712.2832 (2008).

[259] J. Abraham et al. (The Pierre Auger Collaboration), *The Fluorescence Detector of the Pierre Auger Observatory*, Nuclear Instruments and Methods in Physics Research Section A **620**, 227–251, arXiv: 0907.4282 (2010).

[260] J. D. Hunter, *Matplotlib: A 2D graphics environment*, Computing In Science & Engineering **9**, 90–95 (2007).

[261] The Open Street Map Community, *OpenStreetMap*, (Nov. 21, 2012) http://www.openstreetmap.org.

[262] C. Amante and B. W. Eakins, *ETOPO1 1 Arc-Minute Global Relief Model: Procedures, Data Sources and Analysis*, tech. rep., Image distributed with the matplotlib package [260] NOAA, 2009, p. 19.

[263] D. A. Hastings et al. (The GLOBE Task Team), *The Global Land One-kilometer Base Elevation (GLOBE) Digital Elevation Model*, version 1.0, National Oceanic and Atmospheric Administration, 1999.

[264] M. Straub, Private Communication, 2012.

[265] P. Abreu et al. (The Pierre Auger Collaboration), *Antennas for the Detection of Radio Emission Pulses from Cosmic-Ray*, Journal of Instrumentation **7**, P10011, arXiv: 1209.3840 (2012).

[266] M. Kleifges (For the Pierre Auger Collaboration), *Extension of the Pierre Auger Observatory using high-elevation fluorescence telescopes (HEAT)*, in Procceedings of the 31st ICRC, Łódź (2009).

[267] A. Etchegoyen (For the Pierre Auger Collaboration), *AMIGA, Auger Muons and Infill for the Ground Array*, in Proceedings of the 30th ICRC, Merida (2008), arXiv: 0710.1646.

[268] J. L. Kelley (For the Pierre Auger Collaboration), *AERA: the Auger Engineering Radio Array Auger Engineey*, in Proceedings of the 32nd ICRC, Beijing (2011), arXiv: 1107.4807.

[269] P. Allison (For the Pierre Auger Collaboration), *Microwave detection of cosmic ray showers at the Pierre Auger Observatory*, in Proceedings of the 32nd ICRC, Beijing (2011), arXiv: 1107.4807.

[270] J. Blümer (For the Pierre Auger Collaboration), *Status And Perspectives Of The Pierre Auger Observatory*, in Proceedings of the 28th ICRC, Tsukuba (2003), pp. 1–10.

[271] D. Kuempel, K.-H. Kampert, and M. Risse, *Geometry reconstruction of fluorescence detectors revisited*, Astroparticle Physics **30**, 167–174 (2008).

[272] T. K. Gaisser and A. M. Hillas, *Reliability of the method of constant intensity cuts for reconstructing the average development of vertical showers*, in Proceedings of the 15th ICRC, Plovdiv (1977), pp. 353–357.

[273] R. Pesce (For the Pierre Auger Collaboration), *Energy calibration of data recorded with the surface detectors of the Pierre Auger Observatory: an update*, in Proceedings of th 32nd ICRC, Beijing (2011), arXiv: 1107.4809.

[274] X. Bertou et al. (The Pierre Auger Collaboration), *Calibration of the surface array of the Pierre Auger Observatory*, Nuclear Instruments and Methods in Physics Research Section A **A568**, 839–846 (2006).

References

[275] S. Argiro et al., *The Offline Software Framework of the Pierre Auger Observatory*, Nuclear Instruments and Methods in Physics Research Section A **580**, 1485–1496, arXiv: 0707.1652 (2007).

[276] I. C. Mariş, *Measurement of the Ultra High Energy Cosmic Ray Flux using Data of the Pierre Auger Observatory*, PhD thesis Universität Karlsruhe, 2008.

[277] K. Kamata and J. Nishimura, *The Lateral and the Angular Structure Functions of Electron Showers*, Progress of Theoretical Physics Supplement **6**, 93–155 (1958).

[278] K. Greisen, *The Extensive Air Showers*, in *Progress in Cosmic Ray Physics*, Vol. III, edited by J. Wilson, North-Holland (Amsterdam) 1958.

[279] D. Veberič, M. Roth, and H. Dembinski, *Offline Reference Manual - SD Reconstruction*, version 0.8, Updated version of the Auger internal note GAP-2005-035 shipped with the Offline source code (2005).

[280] D. Newton, J. Knapp, and A. Watson, *The Optimum Distance at which to Determine the Size of a Giant Air Shower*, Astroparticle Physics **26**, 414–419, arXiv: astro-ph/0608118 (2007).

[281] C. Bonifazi for the Pierre Auger Collaboration, *The angular resolution of the Pierre Auger Observatory*, Nuclear Physics Proceeding Supplement **190**, 20–25, arXiv: 0901.3138 (2009).

[282] P. Ghia, I. Lhenry-Yvon, and H. Rivera, *Study of the consistency of T2 files with SD and infill event rate*, Internal Note of the Pierre Auger Collaboration, GAP-2012-026 (2012).

[283] R. Piessens, E. D. Doncker-Kapenga, and C. W. Überhuber, *QUADPACK: a subroutine package for automatic integration*, Springer (Berlin, Heidelberg) 1983.

[284] *SciPy: Scientific Library for Python*, (July 23, 2012) http://scipy.org.

[285] R. E. von Mises, *Über die "Ganzzahligkeit" der Atomgewichte und verwandte Fragen*, Physikalische Zeitschrift **19**, as quoted by [255], 490–500 (1918).

[286] A. L. Read, *Modified frequentist analysis of search results (the CL_s method)*, in 1st Workshop on Confidence Limits, Geneva, Switzerland (CERN, 2000), pp. 81–101.

[287] A. L. Read, *Presentation of search results: the CL_s technique*, Journal of Physics G **28**, 2693–2704 (2002).

[288] R. Barate et al. (The LEP Working Group for Higgs boson searches, the ALEPH Collaboration, the DELPHI Collaboration, the L3 Collaboration, and the OPAL Collaboration), *Search for the standard model Higgs boson at LEP*, Physics Letters B **565**, 61–75, arXiv: hep-ex/0306033 (2003).

[289] T. Aaltonen et al. (The CDF and D0 Collaborations), *Combination of Tevatron searches for the standard model Higgs boson in the W+W- decay mode*, Physical Review Letters **104**, 061802, arXiv: 1001.4162 (2010).

[290] G. Aad et al. (The ATLAS Collaboration), *Combined search for the Standard Model Higgs boson in pp collisions at $\sqrt{s} = 7$ TeV with the ATLAS detector*, Physical Review D **86**, 032003, arXiv: 1207.0319 (2012).

[291] S. Chatrchyan et al. (The CMS Collaboration), *Combined results of searches for the standard model Higgs boson in pp collisions at $\sqrt{s} = 7$ TeV*, Physics Letters B **710**, 26–48, arXiv: 1202.1488 (2012).

[292] B. Efron, *An introduction to the Bootstrap*, reprint 1998, Chapman & Hall (Boca Raton) 1993.

[293] M. Brodski et al., *VISPA - Visual Physics Analysis on Linux, Mac OS X and Windows*, in Proceedings of the EPS-HEP Conference, Krakow, Poland (2009), p. 447.

[294] H.-P. Bretz et al., *A Development Environment for Visual Physics Analysis*, Journal of Instrumentation **7**, T08005, arXiv: 1205.4912 (2012).

[295] J. Walter, M. Koch, and G. Winkler, *uBLAS – Boost Basic Linear Algebra*, http://www.boost.org/libs/numeric/ublas/doc/index.htm.

[296] M. Galassi et al., *GNU Scientific Library Reference Manual*, edited by B. Gough, Network Theory Limited (Godalming) 2009.

[297] The Standard Performance Evaluation Corporation, (Jan. 15, 2011) http://www.spec.org.

[298] R. C. Geary, *The Contiguity Ratio and Statistical Mapping*, The Incorporated Statistician **5**, 115–146 (1954).

[299] H.-P. Bretz et al., *PARSEC: A Parametrized Simulation Engine for Ultra-High Energy Cosmic Ray Protons*, submitted to Astroparticle Physics, arXiv: 1302.3761 (2013).

[300] M. Erdmann and T. Winchen, *Proposed Test for Anisotropy using the Principal Axes of the Energy Distribution around the Highest Energetic Events*, Internal Note of the Pierre Auger Collaboration, GAP-2012-116 (2012).

[301] M. Erdmann and T. Winchen, *Detecting Local Deflection Patterns of Ultra-high Energy Cosmic Rays using the Principal Axes of the Directional Energy Distribution*, in Proceedings of the 33rd ICRC, Rio de Janeiro (2013), arXiv: 1307.8273.

[302] P. Abreu et al. (The Pierre Auger Collaboration), *Characterization of the UHECR Distribution in Regions around Events with $E > 60$ EeV observed with the Pierre Auger Observatory*, in preparation (2013).

Declaration of Pre-released Extracts

The following publications and internal notes of the Pierre Auger Collaboration contain pre-released extracts of this work. The text of the publications has been written by the author of this thesis and was revised and copy-edited by the co-authors of the publications.

- H.-P. Bretz et al., *PARSEC: A Parametrized Simulation Engine for Ultra-High Energy Cosmic Ray Protons*, submitted to Astroparticle Physics, arXiv: 1302.3761 (2013)
  The publication contains parts of chapter 3, appendix A and appendix B. The software discussed in the article is joint work of the authors of the publication.

- K. Dolag et al., *A new Monte Carlo Generator of Ultra High Energy Cosmic Rays from the Local and Distant Universe*, in Proceedings of the 32nd ICRC, Beijing (2011), arXiv: 1202.3005
  The article contains parts of chapter 3.

- M. Erdmann and T. Winchen, *Proposed Test for Anisotropy using the Principal Axes of the Energy Distribution around the Highest Energetic Events*, Internal Note of the Pierre Auger Collaboration, GAP-2012-116 (2012)
  The internal note of the Pierre Auger Collaboration contains parts of chapter 4, chapter 7, and appendix C.

- M. Erdmann and T. Winchen, *Detecting Local Deflection Patterns of Ultra-high Energy Cosmic Rays using the Principal Axes of the Directional Energy Distribution*, in Proceedings of the 33rd ICRC, Rio de Janeiro (2013), arXiv: 1307.8273
  The publication contains parts of chapter 4, chapter 7, and chapter 8.

The photo shown in figure 5.2 has been published online and is used to illustrate the Wikipedia article on the Pierre Auger Observatory. Permission has been given to use the picture to illustrate an article of the Dutch popular-science magazine 'KIJK'.

The following publications based on work presented in this thesis are in preparation.

- P. Abreu et al. (The Pierre Auger Collaboration), *Characterization of the UHECR Distribution in Regions around Events with $E > 60$ EeV observed with the Pierre Auger Observatory*, in preparation (2013)
  The publication will contain parts of chapter 4, chapter 6, chapter 7, and chapter 8.

Acknowledgements

Although a doctoral thesis is published by a single author, creating it is impossible without the help of many people. From all the people I had the opportunity to work with, I am in particular grateful to my doctoral advisor Martin Erdmann not only for giving me this opportunity, but also for his guidance, feedback, and constant motivation.

This thesis would be unthinkable without the work of all members of the Pierre Auger Collaboration. I particularly appreciate the valuable discussions on UHECR propagation with Brian Boughman, Manlio DeDomenico, Diego Harari, Haris Lyberis, Günther Sigl, and Michael Sutherland, and the ongoing discussion of the thrust observables with Olivier Deligny, Karl-Heinz Kampert, and Paul Sommers.

Before any part of this work has been presented to the collaboration, it has been tempered in countless meetings and discussions in the astrophysics group of the III. Physikalisches Institut A. For all the ideas that have been developed or discarded on the whiteboard, I thank all current and former members of the astrophysics group and also the VISPA team. I am also grateful to the administrative and technical staff of the institute for keeping the bureaucracy at bay and the computers running. So many people have now worked in all these groups that the list of names is too long to be given here — I thank you all for creating the thriving atmosphere at the institute which made the long hours not only fruitful but also fun.

I am grateful to Martin Erdmann, Daniel Kümpel, Maurice Stephan, and David Walz for critical comments to the manuscript of this thesis, and to Martin Urban and Marcel Rieger for carefully checking the calculations in appendix C.

For help wrestling with the references, tackling typos, and more support than one could have wished for I thank Julia Maria Mönig. I am grateful for all the support received from my family and friends.

With few unfortunately unavoidable exceptions, all computer software used and developed to create this thesis is free software. I gratefully acknowledge the work of the countless programmers who have created and shared the tools this work is built with.